University of Padova
Department of Information Engineering

Ph.D. School in Information Engineering
Section: Bioengineering
Series: XXVII

MATHEMATICAL MODELING OF ELECTRICAL ACTIVITY AND EXOCYTOSIS IN INTESTINAL L-CELLS AND PANCREATIC BETA-CELLS

School director: Ch.mo Prof. Matteo Bertocco
Coordinator: Prof. Giovanni Sparacino
Advisor: Dott. Morten Gram Pedersen

Ph.D. Candidate: Ing. Michela Riz

2015

❧ to my loving family and my patient boyfriend...
...per avermi aiutato a non mollare mai ❧

"Ever Tried..Ever Failed..No Matter!
Try Again..Fail Again..Fail Better!"

Samuel Beckett

Contents

Summary

In healthy subjects, glucose concentration is tightly kept in a limited range around its basal value thanks to complex regulatory mechanisms. Impairment of this regulatory system is the cause of several metabolic disorders, such as diabetes, characterized by chronic hyperglycemia, which leads to severe micro- and macro-vascular complications.

Different hormones are involved in this regulation, with insulin being one of the most important and well studied. It is physiologically secreted at every meal by pancreatic β-cells in response to increased blood glucose levels, in order to lower glucose concentration. Other substances can stimulate insulin secretion, for example glucagon-like peptide-1 (GLP-1) is an insulinotropic hormone released from intestinal L-cells in response to food ingestion. It is, together with other hormones, responsible for the so-called incretin effect, i.e., the fact that glucose ingested orally elicits a greater insulin response than glucose administered intravenously, even when glucose concentrations in plasma are matched. In type-2 diabetes, both insulin and GLP-1 secretion is impaired. In this context, a combination of experimental data and mathematical modeling could help in getting a deeper insight into the cellular mechanisms leading to the secretion of both hormones.

In most of the excitable cells, the steps leading to secretion are quite similar: a trigger initiates the electrical activity in the cell, which leads to the opening of voltage gated calcium channels and a subsequent calcium influx inside the cell; the increase in calcium levels allows the vesicles to fuse with the plasma membrane and to release their content outside the cell.

In this work, the different steps leading to secretion will be analyzed by means of a combination of both experimental data and mathematical modeling, with reference to the intestinal L-cells and the pancreatic β-cells.

Regarding the intestinal L-cells, a mathematical model of electrical activity was built to investigate the stimulus-secretion pathway, which is still poorly understood.

However, two glucose-sensing mechanisms are known to contribute in the sensing of luminal glucose: the sodium-glucose cotransporters (SGLT) and ATP-sensitive K^+-channels (K(ATP)-channels). The results showed how the two glucose-sensing mechanisms interact, and suggested that the depolarizing effect of SGLT currents is modulated by K(ATP)-channels activity.

On the other hand, the stimulus-secretion pathway in pancreatic β-cells is well established. SK-channels and Ca^{2+} dynamics were included in a previous mathematical model of electrical activity in human beta-cells to investigate the heterogeneous and non-intuitive electrophysiological responses to ion channel antagonists. By using our model we also studied paracrine signals, and simulated slow oscillations by adding a glycolytic oscillatory component to the electrophysiological model. The model was further developed by including Kir channels, which play a critical role in the cardiac cells, by determining the shape of cardiac action potential. The inclusion of the Kir2.1 current in the model resulted in a clear improvement of the model behavior, by slowing down the spiking dynamics, thanks to the small outward Kir2.1 current, which tends to stabilize the inter-spike membrane potential.

As a result of the β-cell electrical depolarization, Ca^{2+}-channels open, leading to an influx and a subsequent diffusion of calcium inside the cell, which in turn triggers exocytosis. Hence, from the electrical activity analysis, we moved to the investigation of the relationship between insulin granule exocytosis, calcium levels, distance from Ca^{2+}-channels and channel clustering in β-cells.

This subproject is based on Total Internal Reflection Fluorescence (TIRF) microscopy, consisting in simultaneous visualization of two different fluorophores. The first fluorophore is used to label insulin-containing vesicles, and to differentiate them into two groups: the ones that undergo exocytosis in response to depolarization, and the ones that do not. The second fluorophore, a genetically encoded Ca^{2+} indicator (R-GECO), is attached to the plasma membrane and permits visualizing calcium levels during the stimulus. Simulations were performed using the modeling program CalC, which implements calcium diffusion and buffering. Simulated calcium levels and the corresponding R-GECO signal were evaluated at different distances from the channel. The comparison of the simulations to the TIRF microscopy data allowed estimating the average distance from the channel of the granules that undergo exocytosis.

Calcium diffusion simulations were coupled to a simple model for insulin granule

exocytosis to investigate different pools of granules, in terms of vicinity to the Ca^{2+}-channel and calcium affinity. Furthermore, the fusion probability was evaluated both in a single channel, and in a cluster-of-channels context. Simulations confirmed that the hypothesis of a cluster significantly increases the fusion probability and a certain dependence between the channels in the cluster is functional advantageous.

So far we analyzed cellular mechanisms, which translate in insulin secretion. Hence, the natural step was to move from a cellular point of view to a bigger scale considering the whole pancreas. In this context, the so called minimal model approach might become useful, by allowing the determination of indexes to assess β-cell function in different experimental groups. A minimal model specific for the perfused pancreas experimental setting was built adapting the C-peptide minimal model previously applied to the intravenous glucose tolerance test. The model was initially applied to untreated pancreata and afterward used for the assessment of pharmacologically relevant agents (GLP-1, the GLP-1 receptor agonist lixisenatide, and a GPR40/FFAR1 agonist, SAR1) to quantify and differentiate their effect on insulin secretion. Model application showed that lixisenatide reaches improvement of β-cell function similarly to GLP-1 and demonstrated that SAR1 leads to an additional improvement of β-cell function in the presence of postprandial GLP-1 levels.

In conclusion, in this work different aspects of GLP-1 and insulin secretion were investigated by means of a combination of experimental data and mathematical models. Starting from the modeling of electrical activity in both L-cells and β-cells, we moved to the calcium diffusion and exocytosis of insulin vesicles, concluding with a minimal model of insulin secretion.

Sommario

In soggetti sani, il controllo della glicemia si basa su un complesso sistema di regolazione che permette di mantenere il livello di glucosio nel sangue all'interno di un range ristretto che oscilla attorno al suo valore basale. Malfunzionamenti in questo sistema di regolazione causano diversi disordini metabolici, tra cui il diabete, caratterizzato da una iperglicemia cronica, che può portare a gravi complicanze micro- e macro-vascolari.

Diversi ormoni fanno parte di questo sistema di regolazione. L'insulina, che è uno dei più importanti e maggiormente studiati, è fisiologicamente secreta ad ogni pasto dalle β-cellule pancreatiche, a seguito dell'aumento dei livelli di glucosio per diminuirli. Altre sostanze stimolano la secrezione di insulina, ad esempio il Glucagon-like Peptide-1 (GLP-1) è un ormone insulinotropico rilasciato dalle L-cellule intestinali in risposta all'assunzione di cibo. Assieme ad altri ormoni, è responsabile del cosiddetto effetto incretinico, ovvere la risposta insulinica maggiore per l'assunzione di glucosio orale rispetto alla somministrazione di glucosio endovenoso, anche nel caso in cui le concentrazioni nel plasma siano le stesse. Nel diabete di tipo 2 è ridotta sia la secrezione di insulina che di GLP-1. In questo contesto, i modelli matematici in combinazione con i dati sperimentali posso aiutare nell'ottenere una visione più approfondita dei meccanismi cellulari che portano alla secrezione di entrambi gli ormoni.

Nella maggior parte delle cellule eccitabili, le fasi che portano alla secrezione sono piuttosto simili: l'attività elettrica, indotta da uno stimolo esterno, fa aprire i canali di calcio voltaggio dipendenti e causa un influsso di calcio all'interno della cellula; l'aumento dei livelli di calcio permette ai granuli di fondersi con la membrana plasmatica e rilasciare il loro contenuto all'esterno della cellula.

In questo lavoro, le diverse fasi che portano alla secrezione verranno analizzate attraverso una combinazione di dati sperimentali e modelli matematici, in riferimento alle L-cellule intestinali e le β-cellule pancreatiche.

Riguardo alle L-cellule intestinali, è stato sviluppato un modello matematico dell'attività elettrica per indagare il pathway stimolo-secrezione, che è ancora poco compreso. Tuttavia, è noto che due sono i meccanismi ritenuti responsabili della percezione del glucosio intestinale: il cotrasportatore sodio-glucosio (SGLT) e i canali potassio sensibili all'ATP (canali-K(ATP)). I risultati ottenuti hanno mostrato come i due meccanismi di percezione del glucosio interagiscono e suggeriscono che l'effetto depolarizzante delle correnti dovute ad SGLT è modulato dall'attività dei canali-K(ATP) .

Invece, il pathway stimolo-secrezione delle β-cellule pancreatiche è noto. Per investigare alcune risposte elettrofisiologiche eterogenee e non intuitive ad antagonisti dei canali ionici, in un precedente modello matematico dell'attivià elettrica nelle β-cellule umane sono stati inseriti i canali SK e la dinamica del calcio. Utilizzando il modello sono stati studiati anche i segnali paracrini e, aggiungendo un oscillatore glicolitico al modello elettrofisiologico, sono state simulate anche le oscillazioni lente. Il modello è stato ulteriormente sviluppato includendo i canali Kir2.1, che svolgono un ruolo fondamentale nelle cellule cardiache, determinandone la forma dei potenziali d'azione. L'inserimento di questa corrente nel modello ne ha migliorato il comportamento rallentandone la dinamica.

A seguito della depolarizzazione elettrica delle β-cellule i canali di calcio si aprono permettendo l'influsso e la diffusione del calcio all'interno della cellula, che a sua volta causa l'esocitosi dei granuli di insulina. Per questo motivo, dall'analisi dell'attività elettrica, siamo passati allo studio nelle β-cellule della relazione tra l'esocitosi dei granuli di insulina, i livelli di calcio, la distanza dai canali di calcio ed il clustering dei canali.

Questo sotto-progetto è basato su dati di microscopia per fluorescenza a riflessione interna totale (TIRF), che consiste nella visualizzazione simultanea di due differenti fluorofori. Il primo è utilizzato per differenziare i granuli contenenti insulina in due gruppi, quelli che vanno incontro ad esocitosi e quelli che non lo fanno. Il secondo fluoroforo, un indicatore del calcio geneticamente codificato (R-GECO), è connesso con la membrana plasmatica e permette di visualizzare i livelli di calcio in quell'area durante lo stimolo. Le simulazioni sono state effettuate utilizzando il programma CalC, che permette di implementare la diffusione ed il buffering del calcio. Il confronto delle simulazioni con i dati di microscopia TIRF ha permesso di stimare la distanza media dai canali di calcio a cui si trovano i granuli che vanno

incontro ad esocitosi.

Le simulazioni di diffusione del calcio sono state accoppiate ad un modello dell'esocitosi per studiare i differenti gruppi di granuli, in termini di vicinanza ai canali di calcio ed affinità al calcio stesso. In questo contesto, la cinetica dei canali di calcio durante la depolarizzazione è stata simulata attraverso un sequenza stocastica ed un setup a canale singolo è stato confrontato con un setup di tre canali clusterizzati indipendenti o sincronizzati. Le simulazioni hanno confermato che l'ipotesi di un cluster di canali aumenta in modo significativo la probabilità di fusione e una certa dipendenza tra i canali risulterebbe funzionalmente vantaggiosa.

Fino a questo momento, sono stati analizzati meccanismi cellulari, che si traduco nella secrezione di insulina. Quindi, un ulteriore passo è stato quello di spostarsi ad una scala maggiore considerando l'intero pancreas. In questo contesto, i cosiddetti modelli minimi possono essere un utile approccio, in quanto permettono di determinare degli indici per valutare la funzionalità β-cellulare in differenti gruppi sperimentali. A partire dal modello minimo del C-peptide precedentemente applicato al test endovenoso di tolleranza al glucosio, è stato sviluppato un modello minimo specifico per il setup del pancreas perfuso. Il modello è stato inizialmente applicato a pancreas non trattati e, successivamente, utilizzato per la valutazione di importanti agenti farmacologici (GLP-1, lixisenatide, un agonista del recettore del GLP-1, e SAR1, un agonista del recettore GPR40/FFAR1), quantificando e differenziando il loro effetto sulla secrezione di insulina. I risultati hanno mostrato che lixisenatide ottiene un miglioramento della funzione β-cellulare simila al GLP-1 e che SAR1 porta ad un miglioramento ulteriore della funzionalità β-cellulare in presenza di livelli post-prandiali di GLP-1.

In conclusione, in questo lavoro diversi aspetti della secrezione di GLP-1 e di insulina sono stati studiati con una combinazione di dati sperimentali e modelli matematici. Iniziando dai modelli dell'attività elettrica sia nella L-cellule che nelle β-cellule, siamo passati alla diffusione del calcio e all'esocitosi dei granuli di insulina, concludendo con un modello minimo della secrezione di insulina.

1

Introduction

This introductory Chapter has the aim to outline the context within the present Thesis is embedded. Therefore, a brief description about metabolic processes connected with regulation of glucose concentration will be first presented in order to define diabetes. A short description of the main regulatory hormones will follow. Finally, the different steps of exocytosis will be presented. The Thesis outline will conclude the Chapter.

1.1 Experiments and the Modeling Contribution

In this Thesis, a combination of experimental data and mathematical modeling is used to help in getting a deeper insight into the cellular mechanisms involved in insulin and GLP-1 secretion. As a consequence, before introducing the background in which the Thesis is embedded, I would like to highlight the relationship between experiment and modeling.

The modeling process itself is strictly connected to the available experiments. In fact, in the first phase it is necessary to focus on the most plausible mechanisms based on the experiments. Then, after creating a schematic representation of the biological process, the basics laws of physics and chemistry are applied to get mathematical equations and expressions. These equations are combined together using differential equations to obtain a dynamic mathematical model. Finally, the model is used to simulate the experiments and the results are compared to the initial (or new) data.

After the comparison, the entire process is repeated in order to adjust the behavior of the model to reproduce better the experiments.

Once the model has been built and tested against the available data, it can be used in different ways. For example, it can be used to test hypothesis, which for some reasons are hard or even impossible to test experimentally. The model simulations can support the interpretation of the experimental data, especially when the result are non intuitive and heterogeneous between cells. Finally, the model might allow to get access to variables of the systems that can not be observed or measured experimentally.

1.2 Background

The human body is a complex system that is controlled in an extremely accurate way; its regulatory system produces many substances, which have the aim to keep parameters, like body temperature, blood pressure and substrate concentration, in a physiological range. A defect in this organization causes different kinds of disease. Glucose is a substrate that is essential for the correct working of many organs and tissues, since it is their principal energy provider.

In healthy subjects, glucose concentration is tightly kept in a limited range around its basal value (i.e. 70-120 mg/dl) thanks to complex regulatory mechanisms. Impairment of this regulatory system is the cause of several metabolic disorders, such as diabetes, characterized by chronic hyperglycemia, which leads to severe micro- and macro-vascular complications [1].

1.2.1 Glucose Complex Regulatory Mechanism

In the 1920s *insulin* was identified as a potent hormonal regulator of both glucose appearance and disappearance in the blood circulation. As a consequence, diabetes was initially viewed as a mono-hormonal disorder characterized by absolute or relative insulin deficiency. Afterwards, in the 1950s *glucagon* was characterized as a major stimulus of hepatic glucose production. This discovery led to a bi-hormonal definition of diabetes [2]. Finally, In the 1970s the gut hormone GLP-1 was identified as another player in the glucose regulatory mechanism. Consequently, the more recent view of glucose homeostasis is represented by a multi-hormonal and complex network (Fig. 1.1) [3].

In healthy subjects glucose concentration in blood, the glycaemia, is the balance between glucose entering the circulation and glucose removed from it. Glucose appearance is the sum of different components:

- intestinal absorption during the fed state, determined by gastric emptying;
- glycogenolysis, i.e. the breakdown of glycogen, which is the storage form of glucose in the liver;
- gluconeogenesis, a metabolic pathway that results in the generation of glucose from non-carbohydrate substrates such as pyruvate, lactate, glycerol, and glucogenic amino acids.

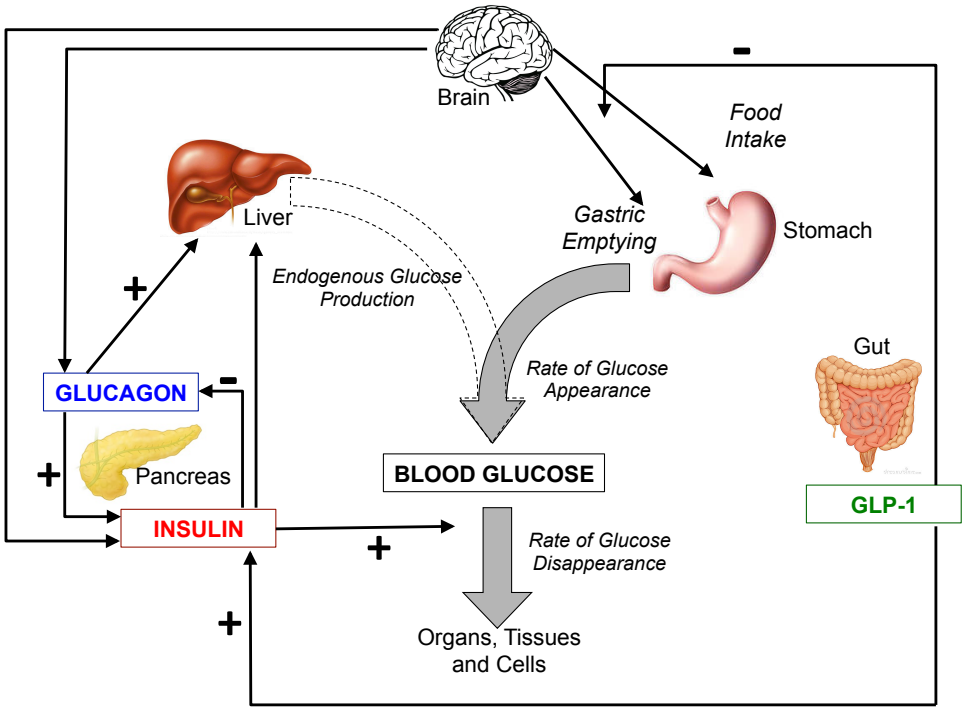

Figure 1.1: Simplified scheme of the complex glucose regulatory mechanisms. Adapted from [4].

Glucose is used by many organs, tissues and cells in different ways. Some, like brain or red blood cells, consume glucose continuously and independently of insulin and the interruption of this supplying may cause severe damages. For muscles, fatty tissue and liver the absorption of glucose is proportional to insulin concentration. In fact, insulin must be present in order to transport glucose from bloodstream into cells, where it is used for growth and energy.

In the fasting state, glucose disappears from the circulation at a constant rate. To balance this loss, endogenous glucose production is necessary. Its main source is the liver. However, in cases of extreme starvation, renal gluconeogenesis contributes substantially to the glucose production [5].

After a meal, blood glucose reaches a peak and slowly goes back down to the fasting levels. In this period, glucose removal into skeletal muscles and adipose tissue is mainly driven by insulin. Simultaneously, endogenous glucose production is suppressed by direct action of insulin, and as a result of glucagon suppression.

Insulin

Insulin is released by the pancreatic β-cells of the islet of Langerhans in response to increased blood glucose levels, in order to lower glucose concentration and bring it back within the physiological range. This action is achieved by three different ways. First, insulin stimulates insulin-sensitive peripheral tissue and increases their uptake of glucose. Second, insulin promotes glucose storage in the liver in the form of glycogen [6]. Third, insulin inhibits glucagon secretion from pancreatic α-cells, which has the effect of decreasing the endogenous glucose production [7].

Other actions of insulin include the stimulation of fat synthesis, promotion of triglyceride storage in fat cells, promotion of protein synthesis in the liver and muscles, and proliferation of cell growth [6].

In response to a glucose step, insulin is secreted in two phases [8]: an initial rapid release attributable to granules already residing at the membrane, followed by a sustained second phase, caused by the recruitment of new granules from a reserve pool.

While glucose is the most important stimulus for insulin secretion, it can be modulated by additional stimuli such as somatostatin, adrenaline, some amino acids, the gut hormone GLP-1, and neuronal stimulation [9].

In type 2 diabetes the amount of insulin secreted during the first phase, in particular, is severely reduced [10]. It is now generally accepted that deficient insulin secretion plays a crucial role in the pathogenesis of diabetes [11].

Glucagon

Glucagon is secreted by the pancreatic α-cells of the islet of Langerhans and plays a major role in sustaining plasma glucose during fasting conditions by stimulating the hepatic glucose production.

When plasma glucose falls below normal range, glucagon secretion increases, resulting in an increased hepatic glucose production, which helps in bringing back plasma glucose to normal range. This endogenous source is not needed after a meal, and in fact glucagon secretion is suppressed in the fed state [12].

In the bi-hormonal definition of diabetes, glucagon excess plays an important role in diabetes etiology. In a diabetic subject, the inadequate concentrations of insulin and the elevated concentrations of glucagon, cause an excess in glucagon's actions and contributes to an unnecessary supply of glucose in the fed state.

GLP-1

GLP-1 is an insulinotropic hormone released from intestinal L-cells in response to food ingestion [13]. It is, together with other hormones, responsible for the so-called incretin effect, i.e., the fact that glucose ingested orally elicits a greater insulin response than glucose administered intravenously, even when glucose concentrations in plasma are matched. In addition, GLP-1 inhibits glucagon secretion, slows gastric emptying, regulates appetite and food intake, stimulates β-cell neogenesis, proliferation and promotes cell survival both in vitro and in vivo [13].

In particular, GLP-1 stimulates insulin secretion when plasma glucose concentrations are high, but not when they approach or fall below the normal range.

Animal studies have demonstrated that the action of GLP-1 occurs directly through activation of GLP-1 receptors on the pancreatic β-cells and indirectly through sensory nerves [14]. GLP-1 has a very short plasma half-time ($\sim$2 minutes), since it is rapidly degraded by the enzyme dipeptidyl peptidase-IV.

In advanced type 2 diabetes, GLP-1 secretion is attenuated [13], and deficient incretin signaling has been suggested to be a major reason of insufficient insulin release and excessive glucagon release in type 2 diabetics [15]. Further highlighting the importance of GLP-1 in diabetes, changes in GLP-1 secretion have been suggested to contribute to the dramatic anti-diabetic effects of gastric bypass surgery [16].

1.2.2 Diabetes

Traditionally diabetes is differentiated into two types.

"Type 1 diabetes" is mainly characterized by loss of the pancreatic β-cells leading to insulin deficiency. As a result, postprandial glucose concentration rise due to lack of insulin-stimulated glucose disappearance and poorly regulated hepatic glucose production. In most cases type 1 diabetes has an autoimmune origin and affects children or young adults, and in fact it is also called "juvenile diabetes".

In "Type 2 diabetes" tissues are unable to appropriately utilize glucose because of insulin resistance, and insulin secretion cannot compensate for this. It is frequently associated with obesity and a sedentary lifestyle. Type 2 is the most common diabetes type (90 % of cases) and mostly affects adult people.

Fail of the glucose counter regulatory system in diabetic people causes blood glucose levels to go out of the correct range. This situation might lead to short (hypoglycaemia) and long (hyperglycaemia) term complications.

Hyperglycaemia, high glucose levels, does not have an immediate damaging consequence on organism, but, if this state is frequent and persists for long time, it can lead to several invalidating complications like neuropathy, nephropathy, retinopathy, heart disease, strokes and peripheral vascular disease [17].

On the other hand, hypoglycemia, low glucose levels, affects the brain, given its continuous glucose demand. Therefore, when glucose levels fall, brain functions diminish and people may lose cognitive abilities and even enter a coma condition.

For the past 80 years, insulin therapy has been the only pharmacological alternative. However, it substitutes only one of the hormones involved in glucose regulation.

The close relationship between insulin and glucagon has suggested additional areas for treatment. Based on preclinical data, several glucagon receptor antagonists have been put forth into clinical development. However, they have been abandoned because of safety issues [18]. To date, no pharmacological means of regulating glucagon exist and the need to decrease postprandial glucagon secretion remains a clinical target for future therapies.

Recently, the importance of incretin hormones has become clearer. However, replacing GLP-1 is challenging. In clinical trials, continuous infusion was superior to single or repeated injections of GLP-1 because of its rapid degradation [19]. To avoid this intensive mode of treatment GLP-1 mimetics, which last longer than native GLP-1, and inhibitors of GLP-1 degradation, have been investigated and

are already available [20]. Alternative treatments, aiming at enhancing endogenous GLP-1 secretion from the intestinal L-cells directly, are under investigation [21, 22].

These new classes of investigational compounds have the potential to enhance insulin secretion and suppress prandial glucagon secretion in a glucose-dependent manner, regulate gastric emptying, and reduce food intake. Lastly, incretin mimetics may also play a role in preservation of β-cell function and proliferation.

1.2.3 Exocytosis Process in Excitable Cells

From the cellular point of view, hormone secretion is the result of regulated exocytosis, the process with which internal vesicles fuse with the plasma membrane releasing their content into the capillary blood. Exocytosis machinery is still an open research area. The Nobel Prize in Physiology or Medicine 2013 was awarded jointly to James E. Rothman, Randy W. Schekman and Thomas C. Südhof "for their discoveries of machinery regulating vesicle traffic, a major transport system in our cells" [23].

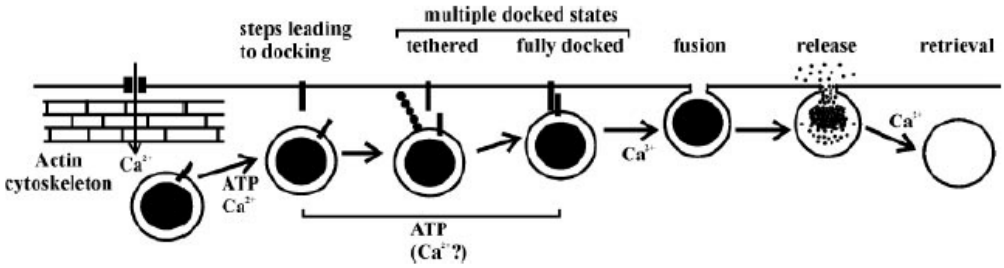

Figure 1.2: Schematic representation of the steps leading to granule exocytosis. From [24].

Regulated exocytosis has been extensively studied in synapses, where it is the mechanism by which neurotransmitters are very rapidly released in a controlled manner from synaptic vesicles. However, a wide range of non-neuronal cell types contain similar regulated secretory granules, the contents of which serve a diverse range of physiological functions. These include cells specialized to secrete large amounts of secretory products, like intestinal L-cells and pancreatic β-cells, whose exocytosis is Ca^{2+}-regulated.

Thanks to different experimental procedures, regulated exocytosis has been functionally dissected into a number of stages (Fig. 1.2) from being non-releasable, they might becomes releasable following a recruitment step, and become part of a so-

called “ready-releasable” pool that can undergo exocytosis within tens of milliseconds. The pool of secretory granules may be fully releasable, but in many cell types, a large reserve pool exists and only a small portion of the granules (∼3 %) are initially rapidly releasable [8, 25, 26].

The functionally defined, sequential stages within the exocytotic pathway have been shown to involve ATP-dependent priming steps, physical movement of vesicles to the submembrane region of the cell, tethering and then docking at release sites on the plasma membrane, conversion to a fully releasable state, triggered membrane fusion, release of granule contents, and finally retrieval of the granule membrane. In the case of Ca^{2+}-triggered exocytosis, calcium may stimulate multiple stages before membrane fusion as well as fusion itself and membrane retrieval by endocytosis [27].

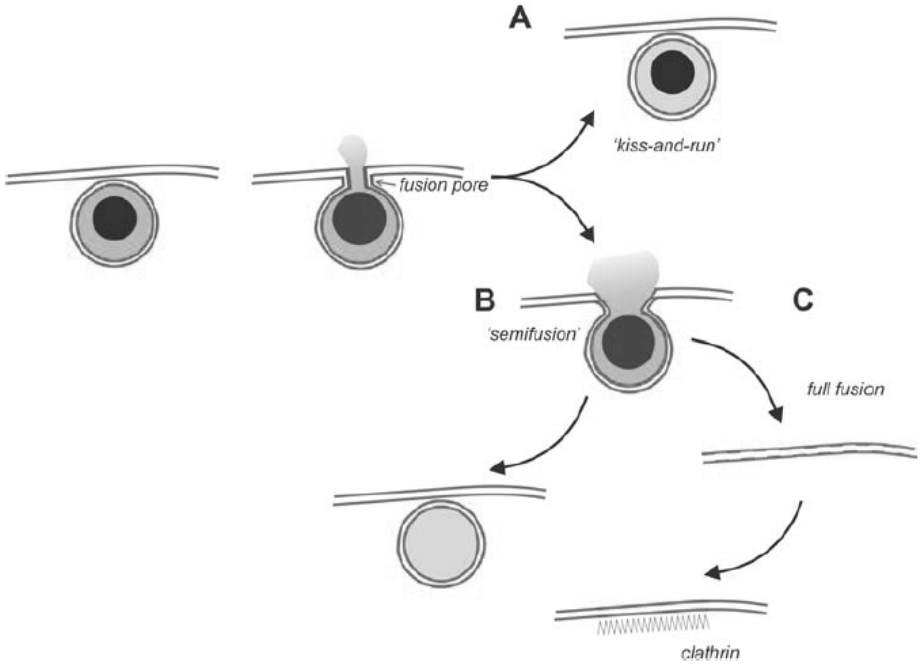

Figure 1.3: Alternative events after fusion-pore formation: kiss-and-run exocytosis (A), semifusion (B) and full fusion (C). From [8].

The precise events that initiate and complete membrane fusion are not understood, although many of the proteins involved have been identified [28]. However, it has been established through biophysical measurements, that fusion begins with the formation of a fusion pore that can open transiently and, potentially rapidly reclose.

After the fusion pore is formed, three alternative events can take place [8]. In the first type called “kiss-and-run” the fusion pore could close even before emptying

the granule interior completely and without mixing of the granule membrane with the plasma membrane (Fig. 1.3A). Alternatively, in case of complete fusion the granule membrane is integrated into the plasma membrane, and then recaptured by clathrin-mediated endocytosis (Fig. 1.3C). The last case, called "semifusion", is an intermediate between the previous two. It consists in a large opening between the granule lumen and the extracellular space, but the granule remains structurally intact (Fig. 1.3B). One physiological consequence of fusion through a reversible fusion pore is that it could allow to control the amount of release that occurs per secretory granule.

In cells where a rise in intracellular Ca^{2+} is the main (or the only) trigger for the initiation of regulated exocytosis, Ca^{2+} elevation can occur via a variety of entry mechanisms including second messenger-operated, voltage-operated, receptor-activated, and Ca^{2+} release-activated Ca^{2+}-channels. Many features can modify the extent and duration of an effective Ca^{2+} signal for exocytosis, including buffering and Ca^{2+} uptake into organelles. Another factor that affects Ca^{2+}-regulated exocytosis in particular cell types is the spatial distribution of channels, which can be associated with secretory granules location [29, 30].

Considerable effort has been made in the determination of the Ca^{2+} sensitivity of the exocytotic machinery in a wide range of cell types [31]. This information is required for the interpretation of the relationship between the observed physiological Ca^{2+} signals and the efficiency of activation of exocytosis, and also provides clues regarding the physiologically relevant properties of the Ca^{2+}-sensor.

Within experimental error, the Ca^{2+}-dependency of Ca^{2+}-triggered granule exocytosis is similar in many cell types, suggesting the existence of a common Ca^{2+}-sensor or a closely related family of Ca^{2+}-binding proteins. However, there are some notable differences, and in certain cell types vesicles have distinct Ca^{2+}-dependencies allowing differential control of their release.

Despite considerable similarities in the process of regulated exocytosis in most cell types, differences are evident that reflect the physiological function of the particular cells. These include variations in the rate of exocytosis, the lag time before it begins, its time course, the proportion of vesicles that undergo fusion in response to stimulation and the presence of single or multiple granule types.

1.3 Thesis Outline

In the previous Subsection, we have briefly described the common steps of exocytosis in excitable cells. In this Thesis the focus will be on modeling secretion of two hormones involved in glucose regulation, i.e. insulin, secreted by pancreatic β-cells, and GLP-1, secreted by intestinal L-cells.

Electrical activity plays a pivotal role both in β-cells and L-cells by coupling the increase in the blood glucose to insulin and GLP-1 secretion respectively. In the next Chapter, some basic concepts required for the modeling of cellular electrical activity will be presented. In particular, after a brief overview of the cell components, attention will be given to the description of the cell membrane and the different means of transporting ions across the membrane. The biological concepts will be followed by the respective mathematical models. The Chapter will be concluded by the pioneering model by Hodgkin and Huxley of electrical activity in the squid giant axon.

In Chapter 3 a mathematical model of electrical activity in primary L-cell and in the GLP-1 secreting GLUTag cell line will be presented. By using the model, the interaction between two glucose-sensing mechanisms underlying electrical activity and GLP-1 secretion will be analyzed.

Chapter 4 will be dedicated to the modeling of electrical activity in human pancreatic β-cells. Initially, the first model of human β-cells will be described, followed by my contribution to the further development of the model, which was used to investigate the heterogeneous response of β-cells to different channel blockers. The Chapter will be concluded with an additional development of the model, which led to interesting but mostly speculative results.

As previously described, exocytosis in both cells is triggered by intracellular calcium elevation as a consequence of electrical activity and calcium channel opening. Hence, it was natural to move from the modeling of electrical activity to the modeling of calcium diffusion and buffering. This and the following parts of the Thesis will refer to pancreatic β-cells only. The first part is based on TIRF microscopy data. An overview of this technique and its application will be given at the beginning of Chapter 5. The Chapter will continue with an introduction of the basic concepts of calcium diffusion and buffering in cells. Also in this case, the biological description will be followed by the mathematical modeling equations. Then, after describing the main features of the modeling program used to simulate calcium diffusion and

buffering, the simulation results will be compared to the data. The Chapter will be concluded with some discussion on the obtained results.

The simulations of calcium diffusion and buffering were coupled to a simple model that describes the different exocytosis steps of a secretory granule. The model description and the results will be presented in Chapter 6.

Finally, from a cellular point of view, the Thesis will move to a bigger scale, in which the whole pancreas will be considered and the insulin secretion as a result of a stimulated perfused rat pancreas will be modeled. In this case, the model was used to quantify the effect of different pharmacologically relevant agents. The model and its application will be presented in Chapter 7.

2

Basic Concepts for Modeling Cellular Electrical Activity

The aim of this Chapter is to give the background knowledge required to understand the next two Chapters, in which the modeling of electrical activity in intestinal L-cells and pancreatic β-cells will be presented. This Chapter is a mixture between biological and mathematical concepts. First a brief description of the cell will be introduced, focusing in particular on the cell membrane. Afterwards, a complete overview of the structures and mechanisms of transport across the membrane will be presented. The Chapter will be concluded by the pioneering model of electrical activity in the squid giant axon by Hodgkin and Huxley.

2.1 Cells: a Small and Complex "Organism"

The cell is the basic structural, functional, and biological unit of all known living organisms. Cells are the smallest unit of life that can replicate independently, and are often called the "building blocks of life".

An eukariotic cells is enclosed within a membrane and subdivided into membrane bound compartments, in which specific metabolic activities take place. Its nucleus is surrounded by a double membrane, called nuclear envelope, with pores that allow material to move in and out. The intracellular space where most of the cellular activities occur is called cytoplasm.

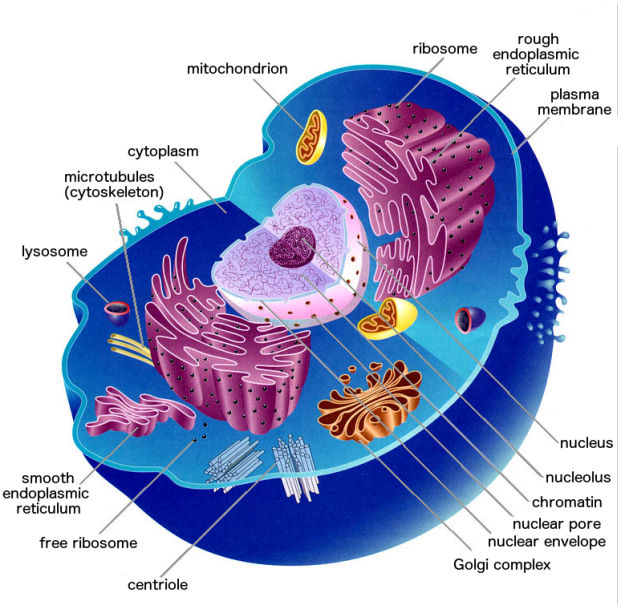

Figure 2.1: Scheme of an eukariotic cell. The nucleus components and various membrane bound compartments are shown.

The cytoplasm comprises the cytosol and the organelles, the cellular internal substructures adapted and/or specialized for carrying out one or more vital functions, analogous to the organs of the human body. The cytosol consists mostly of water, dissolved ions, small and large water-soluble molecules. Its viscosity is roughly the same as pure water, although diffusion of small molecules through this liquid is about fourfold slower than in pure water, due mostly to collisions with the large numbers of macromolecules [32].

A brief overview of the most important cell components will be given in the following (see Figure 2.1).

The *cytoskeleton* is a network of microfilaments, intermediate filaments and microtubules, which have the function of organizing and maintaining the cell shape. It anchors organelles in place, helps during endocytosis and moves parts of the cell in processes of growth and mobility.

The *mitochondria* are the so called "power generators", playing a fundamental role in producing energy in the cell. In particular, they synthesize ATP by electron transport and oxidative phosphorylation .

The *Endoplasmic Reticulum (ER)* is a transport network for molecules targeted for certain modifications and specific destinations. The ER has two forms: the rough ER, which has *ribosomes* on its surface that secrete proteins into the ER, and the

smooth ER, which lacks ribosomes and plays a role in calcium sequestration and release.

The *Golgi apparatus* processes and packages the macromolecules, such as proteins and lipids, before sending them to their destination.

The *lysosomes* contain digestive enzymes, to degrade excess or worn-out organelles, food particles, and engulfed viruses or bacteria.

The *centrioles* are involved in organizing microtubules in the cytoplasm. Its position determines the position of the nucleus and plays a crucial role in the spatial arrangement of the cell.

2.2 The Cell Membrane

The cell membrane, also called plasma membrane, separates the interior of all cells from the outside extracellular environment. It consists of a phospholipid bilayer with embedded proteins. Besides protecting the cell from its surroundings, cell membranes are involved in a variety of cellular processes such as cell adhesion, ion conductivity and cell signaling, and serve as the attachment surface for several extracellular structures.

The cell membrane is selectively permeable and able to regulate what enters and exits the cell, thus facilitating the transport of materials needed for survival. The movement of substances across the membrane can be either "passive", occurring without the input of cellular energy, or "active", requiring the cell to expend energy in transporting it.

Some substances, such as small molecules and ions (CO_2, O_2, ...), can move across the plasma membrane by simple diffusion. Others diffuse passively through protein channels in facilitated diffusion or are pumped across the membrane by transmembrane transporters.

Other transport mechanisms, that involve the plasma membrane, are endocytosis and exocytosis. Endocytosis is the process in which cells absorb molecules by engulfing them. The plasma membrane creates a small deformation inward, called an invagination, in which the substance to be transported is captured. The deformation then pinches off from the membrane on the inside of the cell, creating a vesicle containing the captured substance. Since endocytosis requires energy, it is a form of active transport.

Similarly, using exocytosis the membrane of internal vesicles can fuse with the plasma membrane, releasing its contents to the surrounding medium. Exocytosis occurs in various cells to remove undigested residues of substances brought in by endocytosis, and to secrete substances such as hormones and enzymes.

As said before, cell membrane is a selective filter, allowing the concentrations of ions in the cytosol to be different from those in the extracellular fluid.

Ion	**Intracellular Concentration (mM)**	**Extracellular Concentration(mM)**
K^+	139	4
Na^+	12	145
Cl^-	4	116
HCO3-	12	29
Mg^{2+}	0.8	1.5
Ca^{2+}	<0.0002	1.8

Table 2.1: Typical intra end extracellular ion concentrations in mammalian cells [33].

Table 2.1 shows that typically cytosol has a high concentration of potassium ions and a low concentration of sodium ions compared to extracellular fluid. This difference create a voltage difference between the two sides of the membrane. Moreover, the low concentration of calcium in the cytosol allows Ca^{2+} to function as a second messenger in signaling. A trigger, such as a hormone or an action potential, allows calcium to flow into the cytosol by opening calcium channels. This sudden increase in cytosolic calcium can activate other signaling molecules or trigger exocytosis.

2.2.1 Model of the Cell Membrane

To exemplify what a selective filter means and how the membrane potential is created, consider the case where two ions, K^+ and any monovalent anion A^-, are in solution such that the concentration is different across an impermeable membrane, but is equal on the same side of the membrane. In that case, there is no potential difference across the membrane, because the charge between the K^+ ions and the A^- ions is balanced on each side due to the equivalent concentrations. If a ion-selective pore is inserted, allowing only the passage of K^+, this ion diffuses through the pore driven by the concentration gradient. However, since the membrane is not permeable to the anion A^-, each K^+ ion that passes down the concentration gradient

is not balanced by an accompanying A^-. The transfer of these charges establishes an electrical potential gradient, and K^+ ions continue to move from high concentrations to low until the force due to the electrical potential difference is balanced by the opposite force generated by the concentration difference, called osmotic force.

Nernst Potential

The equilibrium potential, where the electrical and osmotic forces are balanced is given by the Nernst equation. It is what the membrane potential would be if a particular ion were at equilibrium across a membrane. The Nernst equation is derived from the expression for the change in Gibbs free energy, when one mole of an ion of valence z is moved across a membrane:

$$\Delta G = -RT \ln \frac{[\text{ion}]_{\text{out}}}{[\text{ion}]_{\text{in}}} + \Delta V z F. \tag{2.1}$$

Nernst potential is obtained by setting ΔG to zero, which corresponds to the equilibrium state:

$$\Delta V = V_{\text{Nernst}} = \frac{RT}{zF} \ln \frac{[\text{ion}]_{\text{out}}}{[\text{ion}]_{\text{in}}}, \tag{2.2}$$

where R is the gas constant, F the Faraday's constant and T the temperature.

Because the Nernst potential represents the thermodynamic equilibrium of the system, the potential difference evolves to this value driven by the Nernst equation regardless of the initial starting point. In electrophysiology and in this Thesis, the equilibrium potential will be called the reversal potential, because it corresponds to the point at which the current flux changes its direction, and consequently its sign.

While the Nernst potential is the equilibrium potential for one permeant ion, in a cell there are various channels selective for different ions. To consider the general case with multiple conductances ($g = 1/R$), the following weighted sum formalism can be used for calculating the resting membrane potential of a cell:

$$V_m = \frac{\sum_i (V_i \cdot g_i)}{\sum_i g_i}, \tag{2.3}$$

where V_i is the reversal potential, calculate from the Nernst equation, for ion i. For example, the membrane potential for a cell containing Na^+, K^+, and Cl^- ions would be:

$$V_m = \frac{(V_{Na} \cdot g_{Na}) + (V_K \cdot g_K) + (V_{Cl} \cdot g_{Cl})}{g_{Na} + g_K + g_{Cl}}. \tag{2.4}$$

Since the resting membrane potential is the weighted average of Nernst potentials for the various ion, the ion with the greatest conductance contributes the most.

Membrane Model

Now that we have introduced the concepts of the equilibrium potential, we can move to the description of the membrane model, which is used to describe how the systems evolves to the steady state.

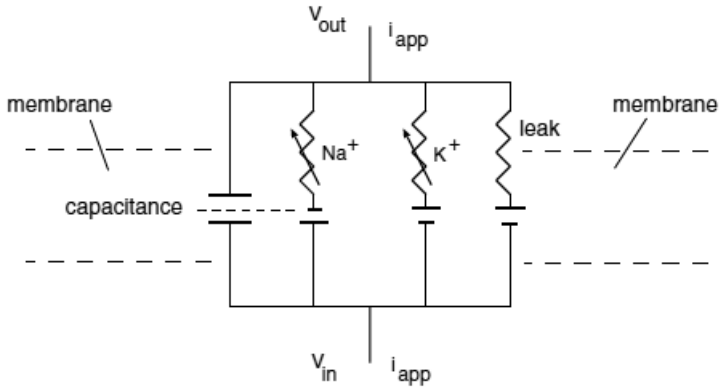

Figure 2.2: **The equivalent electrical circuit for an electrically active membrane.** The capacitance is due to the phospholipid bilayer separating the ions on the inside from the outside of the cell. The three ionic currents, one for Na^+, one for K^+, and one for a non-specific leak, are indicated by resistances. From [34].

The notion that a cell membrane could be compared to an electrical circuit comes from the pioneering work of K.S. Cole [35]. In his model, the base circuit elements are:

- the phospholipid bilayer, which act as a *capacitor* in which the ionic charge accumulates as the electrical potential across the membrane changes;
- the ionic channels of the membrane, which act as *resistors* in an electronic circuit;
- the electrochemical driving forces, which act as *batteries* driving the ionic currents.

The ionic and the capacitive currents are arranged in a parallel circuit, as shown in Figure 2.2.

As a consequence to analyze the system evolution, we need to study the dynamics of the various currents that flow in and out of the cell. Kirchoff's law is used to translate the electric circuit diagram in Figure 2.2 into differential equations. Kirchoff's law says that the capacitive current must balance with the ionic currents

and any currents that might be applied through experimental manipulation. This implies that

$$I_{\text{cap}} = I_{\text{ion}} + I_{\text{app}}. \tag{2.5}$$

Since we assume that the membrane acts as a capacitor, the capacitive current across the membrane can be written as

$$I_{\text{cap}} = C\frac{dV}{dt}, \tag{2.6}$$

where C is the capacitance of the membrane and V is the membrane potential.

Taking an example for the ionic currents and assuming that the reversal potential stays constant, the current flowing through K^+-channels is:

$$I_K = -g_K\left(V - V_K\right). \tag{2.7}$$

where g_K is the conductance of the K^+-channels. The negative sign is necessary because, by convention, the membrane potential V is the difference between the outside and the inside voltage ($V_{\text{out}} - V_{\text{in}}$). V_K is the K^+ reversal potential determined by the Nernst equation, and $V - V_K$ represents the driving force across the membrane provided by the ionic battery. The reversal potential for a given ion is assumed to remain constant, which means that restorative mechanisms such as ionic pumps prevent the ionic battery from running down. This is a reasonable assumption for a large cell, where the ion transfer has a negligible effect on the intracellular ionic concentration.

Numerous ions are responsible for the electrical behavior in a cell, thus the total current is the sum of the individual ionic currents:

$$I_{\text{ion}} = \sum I_i = \sum -g_i(V - V_i) = -g_K(V - V_K) - g_{Na}(V - V_{Na}) - \dots. \tag{2.8}$$

Summarizing the expressions Eq. 2.5, Eq. 2.6 and Eq. 2.8, one gets:

$$C\frac{dV}{dt} = -\sum_i g_i(V - V_i) + I_{\text{app}}. \tag{2.9}$$

To solve this differential equation for voltage, we must know how the gated conductances g_i depend on V (and possibly time). In general, the g_i will not be linear functions of V. In the next Sections, we will describe different ion transport mechanism, along with the model of the associated current.

2.3 The Cell Membrane Population

Each cell membrane has a set of specific membrane proteins with different functions: transport of nutrients, passage of water, selective transport of molecules, reception of signals from the extracellular environment, physical and functional connection with other cells or the extracellular matrix. The ability of cells to generate electrical signals is entirely dependent on the evolution of ion-specific pumps and pores that allow the transfer of charge up and down gradients.

The membrane proteins can be divided into two categories: the integral membrane proteins and the peripheral ones. The integral membrane protein is permanently attached to the biological membrane. They include transporters, linkers, channels, receptors, enzymes, proteins responsible for cell adhesion, ect. The peripheral membrane proteins instead adhere only temporarily to the biological membrane and do not interact with the hydrophobic core of the bilayer. They are often associated with integral membrane proteins acting as regulatory protein subunits.

2.3.1 Ion Channels

Basic Biology

An example of integral membrane protein, responsible for the selective transport of ions are the channels. The ion channels are small highly selective pores in the cell membrane that open and close in a regulated manner, allowing the passage of ions following the driving force that is a combination of electrical potential and chemical ionic concentrations. They are an example of passive transport, since ions flow from high to low concentration and no energy is used. The average rate of transport is pretty fast ($\sim 10^7$ ions/s) [33, 36].

Besides the transport function, the ion channels regulate the membrane potential and signaling. As a consequence, they are responsible for processes as heart beat, muscle contraction, sensory signals, cognition and hormone secretion.

Each cell type expresses a different set of channel proteins depending on its function. However, their expression can be regulated by growth factors, inflammatory mediators, hormones, etc.

In a shorter term, the ion channel activity is regulated by gating, which sets how long on average a channel is open. Some channels exhibit only two discrete states (e.g. K^+-channels): open, when it is conducting, or closed (Figure 2.3). Others, like

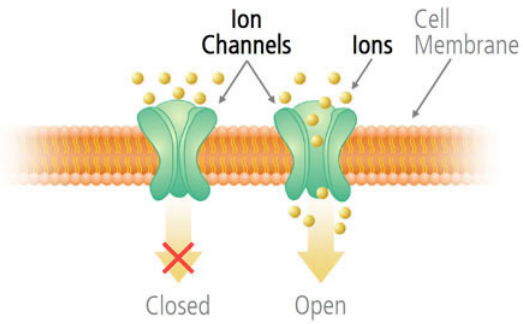

Figure 2.3: Scheme of two-state ion channel.

Ca^{2+}-channels can also reach an inactive state, that corresponds to an open channel that is not conducting [37]. This happens when part of the channel structure or some external particles block the otherwise open channel.

Different mechanisms can regulate channel gating, for example the voltage across the cell membrane producing *voltage-gated channels*, a chemical ligand producing *ligand-gated channels* or a mechanical stimulus producing *stretch-gated channels*. The gating source gives the required energy to switch the channel protein between two different 3D conformation shapes, corresponding to the opening and closing of the pore.

Models of Voltage-Dependent Gating

Even if using special techniques it is possible to measure transition between closed and open states for a single channel, we will focus on the average change for the entire ensamble of channels, since it determines the cellular dynamics.

The mathematical description of voltage-dependent activation and inactivation gates is based on the mechanism

$$C \underset{k^-}{\overset{k^+}{\rightleftharpoons}} O, \tag{2.10}$$

where C corresponds to the closed state, O to the open state of the channel and the arrows stand for reversible elementary molecular processes, representing the conformation changes. k^- is the rate constant $[s^{-1}]$ for the transition from state O to state C, while k^+ is the rate constant $[s^{-1}]$ for the reverse reaction.

Hence, the rate of the transition from state O to state C is

$$j_- = k^- f_O, \tag{2.11}$$

where f_O represents the fraction of open channels N_O/N, being N the total number of channels and N_O the open channels. Similarly for the reverse reaction from closed to open ($C \xrightarrow{k^+} O$).

Because the kinetic model (2.10) involves only interconversion of channel states, the total number of channels should be preserved, $N = N_O + N_C$. As a consequence, one differential equation is sufficient to describe the changes in the fraction of open channels and the fraction of closed channels can be simply calculated as $f_C = 1 - f_O$.

The change in f_O over time corresponds to the difference between the fraction of closed channels that open and the fraction of open channels that close:

$$\frac{df_O}{dt} = j_+ - j_- = k^+(1 - f_O) - k^- f_O. \tag{2.12}$$

Rearranging

$$\frac{df_O}{dt} = -(k^- + k^+)\left(f_O - \frac{k^+}{(k^- + k^+)}\right), \tag{2.13}$$

and defining $\tau = 1/(k^- + k^+)$ and $f_\infty = k^+/(k^- + k^+)$, one gets

$$\frac{df_O}{dt} = -\frac{(f_O - f_\infty)}{\tau}. \tag{2.14}$$

It means, that at steady state the fraction of open channel f_O is equal to f_∞ and that the steady state would be reached with τ as time constant.

Because ionic channels are composed of proteins with charged amino acid side chains, the potential difference across the membrane can influence the rate at which the transitions from the open to the closed state occur. According to the Arrhenius expression for the rate constants, the membrane potential V contributes to the energy barrier for these transitions. Hence, the rate constants will have the form

$$k^+ = k_0^+ \exp(-\alpha V) \quad \text{and} \quad k^- = k_0^- \exp(-\beta V), \tag{2.15}$$

where both k_0^+ and k_0^- are independent of V. Substituting the relationship (2.15) into the expression for f_∞:

$$\begin{aligned} f_\infty &= \frac{k_0^+ \exp(-\alpha V)}{(k_0^+ \exp(-\alpha V) + k_0^- \exp(-\beta V))} \\ &= \frac{1}{1 + k_0^-/k_0^+ \exp((\alpha - \beta)V)}. \end{aligned} \tag{2.16}$$

Similarly for τ:

$$\begin{aligned} \tau &= \frac{1}{(k_0^+ \exp(-\alpha V) + k_0^- \exp(-\beta V))} \\ &= \frac{1}{k_0^+ \exp(-\alpha V)} \cdot \frac{1}{1 + k_0^-/k_0^+ \exp((\alpha - \beta)V)}. \end{aligned} \tag{2.17}$$

Now, defining

$$V_0 = -\frac{\ln(k_0^-/k_0^+)}{\alpha - \beta} \quad \text{and} \quad n_0 = \frac{1}{\alpha - \beta}, \tag{2.18}$$

and substituting into (2.16) and (2.17), one finally gets

$$f_\infty = \frac{1}{1 + \exp((V - V_0)/n_0)}, \tag{2.19}$$

$$\tau = \frac{\exp(\alpha V)}{k_0^+} \cdot \frac{1}{1 + \exp((V - V_0)/n_0)}. \tag{2.20}$$

It is worth noting that n_0 determines the steepness of the dependence of f_∞ on V, whereas V_0 corresponds to the voltage at which half of the channels are open.

An activation gate tends to open when the membrane is depolarized, while an inactivation gate tends to close. Whether a gate activates or inactivates with depolarization is determined by the sign of n_0: a negative sign implies activation and a positive sign inactivation.

Voltage Clamp

In order to measure the voltage dependence of the activation and the inactivation of ion conductances, a technique called voltage clamp is used. An electronic feedback device adjusts the applied current, I_{app}, to counter the membrane currents such that the membrane voltage is held constant. Now, consider a membrane with a single gated ionic current. If we assume that the total conductance is the result of the activation of many channels, the conductance g that we have used above can be defined as the product of the maximum possible conductance $\bar{g}$ and the fraction of open channels f_0:

$$g = f_0 \bar{g}. \tag{2.21}$$

We can include this new relationship in the differential equation for membrane potential:

$$C\frac{dV}{dt} = -f_0 \bar{g}(V - V_{\text{rev}}) + I_{\text{app}}. \tag{2.22}$$

If we apply a current that is equal and opposite to the current flowing through the membrane,

$$I_{\text{app}} = \xi \bar{g}(V - V_{\text{rev}}), \tag{2.23}$$

then the right-hand side of Eq. 2.22 is zero and the voltage must be constant. Because V is constant, $\xi = f_0$ and the time dependence of the applied current follows the

one of f_0 as determined by the gating equation:

$$\frac{d\xi}{dt} = -\frac{f - f_0}{\tau}. \tag{2.24}$$

Thus the time dependence of the applied current provides a direct measurement of the gated current at a fixed voltage. To carry out a voltage clamp measurement like this it is necessary to block all but a single type of current. While this is not always possible, specific toxins and pharmacological agents have proven useful.

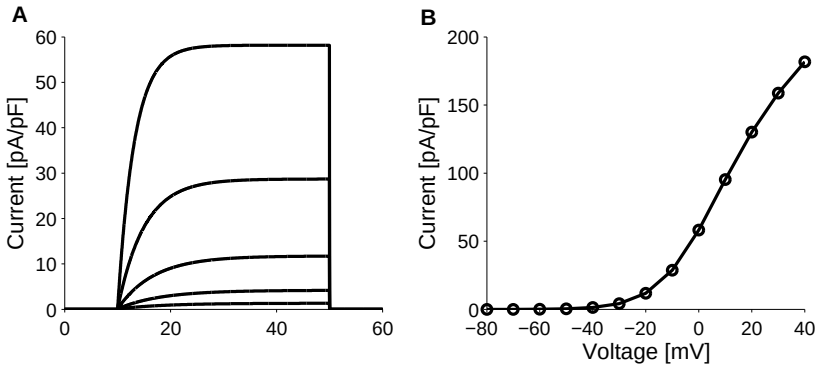

Figure 2.4: **Simulation of voltage clamp experiment.** A) Current simulations resulting from 40 ms depolarizations from the holding potential of -70 mV to different test potentials from -40 mV to 10 mV (step 10 mV). B) The maximum (steady state) current as a function of test potential.

The simulation shown in Figure 2.4A represents a typical set of experiments in which the membrane potential is clamped at a holding potential (-70 mV), then changed to various test potentials for a fixed interval (40 ms), and finally returned to the holding potential. To simplify the interpretation, the value of the holding potential generally is chosen so that the current through the channel is negligible. Figure 2.4A shows the current that develops during this protocol for 5 test voltages V_{test}. The increase in current when the potential is clamped at the test values is governed by the exponential increase in f_0 with characteristic time $\tau(V_{\text{test}})$. When the potential is clamped again at the holding potential, the resulting current is called the tail current. Figure 2.4B gives a plot of the steady-state current as a function of the test voltage.

2.3.2 Pumps and Transporters

Biology

In addition to ion channels, there are numerous specific pumps, cotransporters and exchangers that allow ions and small molecules to be transported selectively into internal compartments or out of the cell.

Unlike ionic channels, most transporter and pumps expend considerable energy. Furthermore, contrarily to the ion channel passive transport, the pumps is a very slow mechanism (i.e. ∼100 molecules/s) [33, 36].

The pumps are the primary active transporters, since they generate chemical or electrical gradient and later they transport against the same gradient. Usually pumps use ATP, light, redox potential or decarboxylation to transport against the driving forces. The ATP-driven pumps are also called ATPases. For example the Sarco-Endoplasmatic Reticulum Ca^{2+} ATPase (SERCA) pump is found in the ER, where it is used to maintain the calcium reserve. The calcium release from the ER is involved in cardiac contraction, in stimulating hormone secretion and other intracellular signaling cascades [38].

Besides the pumps, secondary transporters use the gradients created by the primary transporters as energy. Similarly to the pumps, they are selective for the transported molecule, have low transport rate and are reversible.

Their working mechanism consist in these steps: the substrate binds on one side of the membrane, the binding site reorients and finally the substrate is released on the other side. As a consequence, they are subject to significant conformational changes and they can be open only to one side of the membrane.

There are three types of transporters: the uniporters, the co-transporters, which can be either symporters or antiporters.

The uniporters transport only a single substrate. Their mechanism consist in a facilitated "low resistance" diffusion, since they transport down the concentration gradient, by accelerating a reaction that is already thermodinamically favored. The rate of movement is

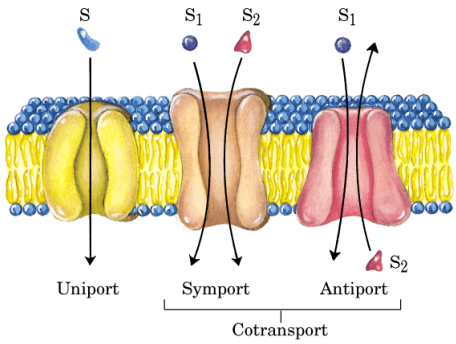

Figure 2.5: Examples of Transporters. From [39].

much higher than the passive diffusion, since the molecule never comes in contact with the hydrophobic core of the cell membrane. Since the transport occurs via a limited number of uniporters, it is easily saturable.

Example of uniporters, are the GLUT transporters. GLUTs transport glucose and each isoform plays a specific role in glucose metabolism determined by substrate specificity, transport kinetics, and regulated expression in different physiological conditions. They are expressed by renal tubular cells, small intestinal epithelial cells, liver cells and pancreatic β-cells.

On the other hand the co-transporters couple movement of one substrate down the gradient to the movement of another substrate against the gradient. It is a symporter, if both substrates are transported in the same direction. Otherwise, the co-transporters is called antiporter.

An example of a symporter is the Sodium-Glucose Linked Transporter (SGLT): a family of glucose transporter found in the intestinal mucosa of the small intestine and the proximal tubule of the nephron. They contribute to renal glucose reabsorption. In the kidneys, 100% of the filtered glucose in the glomerulus has to be reabsorbed along the nephron. In case of too high plasma glucose concentration, glucose is excreted in urine, because SGLT are saturated.

An example of antiporter is the Na^+-Ca^{2+}-eXchanger (NCX), which is considered one of the most important cellular mechanisms for removing calcium from cells. It uses the energy that is stored in the electrochemical gradient of sodium by allowing Na^+ to flow down its gradient across the plasma membrane in exchange for the countertransport of calcium ions. The NCX removes a single Ca^{2+} in exchange for the import of three Na^+. The exchanger is usually found in the plasma membranes, the mitochondria and th ER of excitable cells.

Models of Transporters

To exemplify the mathematical description of the transporters model, GLUT2 will be considered.

The transport is modeled as a four state process (Fig. 2.6) [40]. State S_1 represents the empty carrier, with the glucose binding site exposed to the exterior of the cell. When glucose binds to this state, the transporter makes a transition to state S_2 with glucose bound and facing exterior. The third step corresponds to the translocation of the glucose from outside to inside the cell (state S_3). When glucose

dissociates from GLUT and ends up inside the cell, the transporter is left in state S_4. Finally, the cycle can repeat if S_4 makes the conformational transition back to S_1. All these processes are reversible.

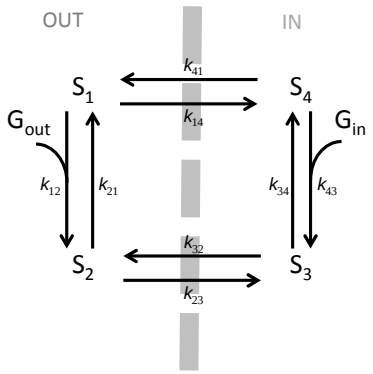

Figure 2.6: Four-state kinetic diagram of a GLUT transporter.

From the diagram in Figure 2.6, it is easy to verify that the transition from S_1 and S_2 is a bimolecular process, because it requires the interaction of a glucose molecule (G_{out}) and the GLUT transporter in state S_1. While the reverse transition (from S_2 to S_1) is an unimolecular process and involves the GLUT molecule only.

Similarly to the ion channels, the rate of the transition from S_1 to S_2 is given by

$$J_{12} = k_{12}\mathrm{G}_{out}x_1, \tag{2.25}$$

where x_1 represents the fraction of the GLUT molecules in S_1 ($x_1 = N_1/N$). The factor k_{12} is the rate constant, in this case bimolecular, with units [$s^{-1}mM^{-1}$]. Similarly for the reverse unimolecular reaction from S_2 to S_1, the rate is given by

$$J_{21} = k_{21}x_2, \tag{2.26}$$

with k_{21} a unimolecular rate constant [s^{-1}].

It is possible to write the differential equations that the diagram 2.6 represents, by tracking the changes for the fraction of GLUT molecules in each state:

$$\begin{aligned}
\frac{dx_1}{dt} &= -k_{12}\mathrm{G}_{out}x_1 + k_{21}x_2 + k_{41}x_4 - k_{14}x_1, \\
\frac{dx_2}{dt} &= k_{12}\mathrm{G}_{out}x_1 - k_{21}x_2 - k_{23}x_2 + k_{32}x_3, \\
\frac{dx_3}{dt} &= k_{23}x_2 - k_{32}x_3 - k_{34}x_3 - k_{43}\mathrm{G}_{in}x_4, \\
\frac{dx_4}{dt} &= k_{34}x_3 - k_{43}\mathrm{G}_{in}x_4 - k_{41}x_4 + k_{14}x_1.
\end{aligned} \tag{2.27}$$

Similarly to the ion channels, the total number of transporters should be preserved

$$x_1 + x_2 + x_3 + x_4 = 1, \tag{2.28}$$

and one of the dependent variables can be eliminated using the conservation law, for example:

$$\begin{aligned}
\frac{dx_1}{dt} &= -(k_{12}\mathrm{G}_{\mathrm{out}} + k_{14} + k_{41})x_1 + (k_{21} - k_{41})x_2 - k_{41}x_3 + k_{41}, \\
\frac{dx_2}{dt} &= k_{12}\mathrm{G}_{\mathrm{out}}x_1 - (k_{21} + k_{23})x_2 + k_{32}x_3, \\
\frac{dx_3}{dt} &= -k_{43}\mathrm{G}_{\mathrm{in}}x_1 + (k_{23} - k_{43}\mathrm{G}_{\mathrm{in}})x_2 - (k_{32} + k_{34} + k_{43}\mathrm{G}_{\mathrm{in}})x_3 - k_{43}\mathrm{G}_{\mathrm{in}}, \\
x_4 &= 1 - x_1 - x_2 - x_3.
\end{aligned} \tag{2.29}$$

To illustrate how a complete model of a transporter is created, we will consider the SGLT1 from intestinal epithelials cells. This transporter utilizes a concentration gradient of Na^+ to transport glucose from the intestine into the epithelial cells that line the gut.

A model of any transporter must incorporate a number of basic experimental facts [41]. One of these is stoichiometry, which for the co-transporter is the number of Na^+ ions transported per glucose molecule. Experimental measurements on the SGLT1 cotransporter from intestine yields a stoichiometry of 2 Na^+ to 1 glucose. Another important fact about the cotransporter is the absolute requirement for Na^+. If Na^+ is absent from the external medium, glucose is not transported. In addition, the co-transporter is electrogenic, because transport generates an electrical current due to the transport of Na^+.

These observations require 2 Na^+ and 1 glucose ordered association/dissociation steps on each side of the membrane. It would be possible that the second sodium binds after the glucose. However, this can be ruled out if the states with Na^+ and glucose bound from the outside are connected by conformational transitions to comparable states inside. In that case the six state cycle would transport only a single Na^+ for every glucose molecule, implying a stoichiometry at steady state less than 2:1. Alternatively, glucose could bind first. This is ruled out, since the cotransporter supports Na^+ currents even in the absence of glucose.

Now, there are different possibilities for connecting the outside to the inside of the cell. The conformational change must occur after the glucose binding, otherwise no glucose would be transported. The cycle must end after the second Na^+ is released

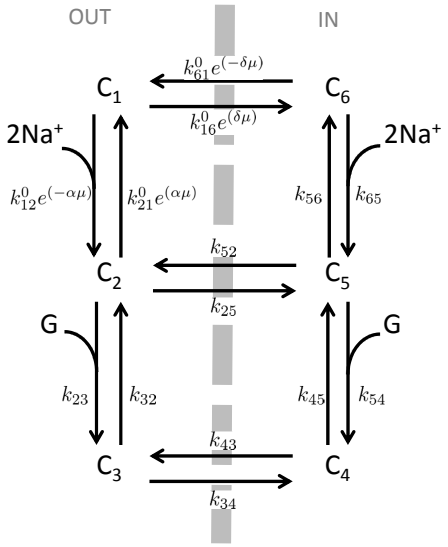

Figure 2.7: Six-state model of sodium/glucose cotransporter SGLT1. Adapted from [42].

inside the cell, to have the right stoichimetry. Finally a single cycle cannot explain the Na^+ current even in absence of glucose. The other possibilities, that are compatible with the experimental evidence, can all be reduced to a six-state diagram.

The six state model (Fig. 2.7) [42] starts with the empty carrier outside the cell (state 1). The first step is the association of two sodium ions with the carrier (state 2), that allows the subsequent association of glucose (state 3), the third step corresponds to the translocation of the carrier from outside to inside the cell (state 4), symmetrical steps take place inside the cell consisting in successive dissociation of glucose (state 5) and sodium (state 6), a final step bring the empty carrier back the initial state outside the cell.

Models of Pumps

As example of pumps models, the SERCA pump will be presented. The rate at which it pumps Ca^{2+} has a sigmoidal dependence on intracellular Ca^{2+} with Hill coefficient close to two,

$$R = \frac{R_{\max}[\mathrm{Ca}^{2+}]_\mathrm{i}^2}{K^2 + [\mathrm{Ca}^{2+}]_\mathrm{i}^2}. \tag{2.30}$$

The Hill coefficient is related to the stoichiometry of the SERCA pump, which is known to be 2 Ca^{2+}:1 ATP [43]. Experiments confirmed the presence of two binding sites for Ca^{2+}.

A simple model that is consistent with the Ca^{2+} dependence of the pump rate can be constructed using only two states; from an inactive state I, it reaches an active state A via the binding of two Ca^{2+} ions. This model is consistent with equation (2.30) assuming that the two states rapidly equilibrates and that the active state allows Ca^{2+} release inside the cell.

Rapid equilibration implies the balance of the forward and the reverse rates, leading to this condition

$$k^-/k^+ = K_{\text{eq}} = \frac{[\text{Ca}^{2+}]_{\text{i}}^2[I]}{[A]}, \tag{2.31}$$

where $[I]$ and $[A]$ are the per unit area concentration of inactive and active SERCA pumps respectively, and K_{eq} is the ratio of the rate constants. Solving for $[I]$ and substituting that expression into the conservation condition $[I]+[A]=N$, one gets

$$\frac{K_{\text{eq}}[A]}{[\text{Ca}^{2+}]_{\text{i}}^2} + [A] = N, \tag{2.32}$$

then solving for $[A]$

$$[A] = \frac{N[\text{Ca}^{2+}]_{\text{i}}^2}{K^2 + [\text{Ca}^{2+}]_{\text{i}}^2}, \tag{2.33}$$

where $K = \sqrt{K_{\text{eq}}}$. It has the same units of concentration, and equals the concentration of Ca^{2+} at which half of the SERCA are in the active state. A small value of K corresponds to a high affinity for the binding site. If the rate constant for the Ca^{2+} release inside the cell is k, then from (2.33), one gets

$$R = kA = \frac{R_{\text{max}}[\text{Ca}^{2+}]_{\text{i}}^2}{K^2 + [\text{Ca}^{2+}]_{\text{i}}^2}, \tag{2.34}$$

with $R_{\text{max}} = kN$.

2.4 Hodgkin-Huxley Model

Now that we have all the basic concepts, the famous model of electrical activity in the squid giant axon developed by Hodgkin and Huxley will be presented [44].

The Hodgkin-Huxley model is empirical. Many voltage clamp experiments were performed by Hodgkin and Huxley, and their data were fit to expressions that they incorporated into the model without consideration of an underlying mechanism for the channel gates. However, it is possible to derive the gating expression used in the Hodgkin-Huxley model using mechanistic models.

From the knowledge of the individual currents, one can obtain the conductances as

$$g_{Na} = \frac{I_{Na}}{(V - V_{Na})}, \qquad g_K = \frac{I_K}{(V - V_{K)}}. \tag{2.35}$$

Figure 2.8 shows the plot of the ionic conductance as function of time following a step increase or decrease in the membrane potential. It is important to notice that with voltages fixed, the conductances are time dependent.

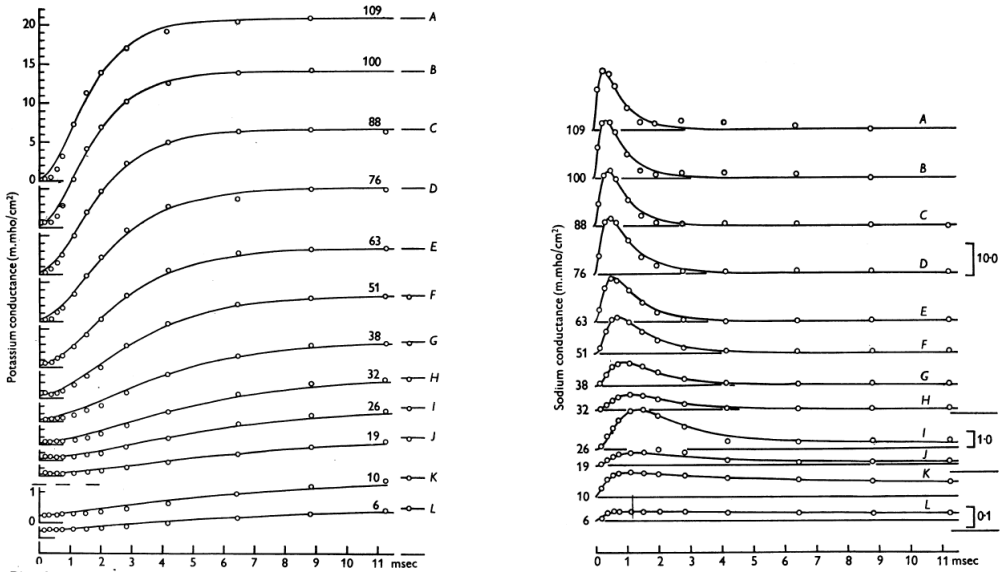

Figure 2.8: Hodgkin-Huxley voltage clamp experiments. From[44].

Considering the potassium conductance, it increases over time to a final steady level. In particular, g_K increases in a sigmoidal fashion, i.e. with a slope that first increases and then decreases.

This leads Hodgkin and Huxley to the idea that g_K had a single activation gate, which can be modeled as some power of a different variable, that satisfies a first order differential equation:

$$g_K(V) = \bar{g}_K n^4, \tag{2.36}$$

$$\frac{dn}{dt} = -\frac{n - n_\infty(V)}{\tau_n(V)}, \tag{2.37}$$

the fourth power was chosen not for physiological reasons, but because it was the smallest exponent that gave acceptable agreement with the experimental data. The function $n(t)$ is called the potassium activation, since at elevated potentials it increases monotonically and exponentially towards its resting value. Furthermore,

since the Nernst potential is below the resting potential, the potassium current is an outward current at potential greater than rest.

Suppose to increase the membrane potential from 0 to V_0 and that initially $n = 0$. The solution of Eq. 2.37 is

$$n(t) = n_\infty(V_0)\left[1 - \exp\left(\frac{-t}{\tau_n(V_0)}\right)\right]. \tag{2.38}$$

By fitting Eq. 2.38 to experimental data, it is possible to estimate n_∞ and τ_n for any given voltage step. To obtain a complete description of g_K, Hodgkin and Huxley fitted a smooth curve through the data points. The functional form of the smooth curve has no physiological significance, but it is a convenient way of providing a continuous description of n_∞ and τ_n.

Now, considering the sodium conductance g_{Na}. Following a step increase in the voltage, it first increases, but then decreases again. This observation suggested that the sodium conductance involved two voltage-dependent "gates", an activation gate and an inactivation gate. Hodgkin and Huxley proposed that the sodium conductance is of the form

$$g_{Na}(V) = \bar{g}_{Na} m^3 h, \tag{2.39}$$

and they fit the time-dependent behavior of m and h to exponentials dynamics similar to n:

$$\frac{dm}{dt} = -\frac{m - m_\infty(V)}{\tau_m(V)}, \tag{2.40}$$

$$\frac{dh}{dt} = -\frac{h - h_\infty(V)}{\tau_h(V)}. \tag{2.41}$$

Since m is small at rest and increases at higher potentials, it is called the sodium activation, while h that shots down, is called the sodium inactivation.

Hodgkin-Huxley equations assumed that Na^+-channels consist of three m gates and one h gate, each of which can be either closed or open. If the gates operate independently, then the fraction of open Na^+-channels is m^3h, where m and h obey the equation of the two-state model. Similarly, if there are four n gates per potassium channel, all of which must be open for potassium to flow, then the fraction of open K^+-channels is n^4. In Figure 2.9 the gating variables and the corresponding time constants are shown as a function of voltage.

Putting together the differential equations for the gating variables one gets the

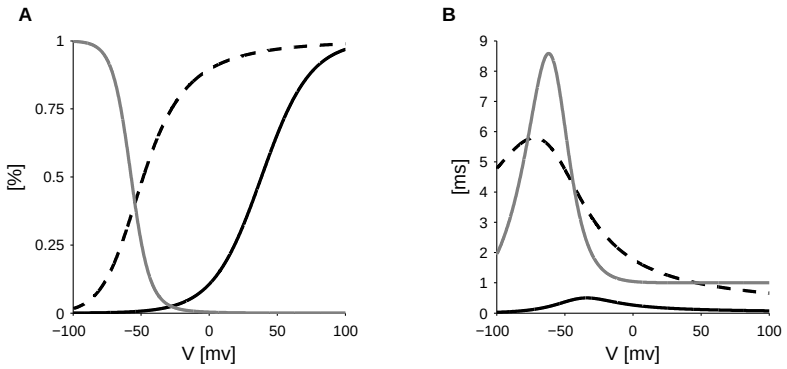

Figure 2.9: **Voltage dependence of Hodgkin-Huxley model parameters.** A) Voltage dependence of the gating variables: n (dashed line), m (black solid) and h (grey solid). B) Voltage dependence of the time constants: τ_n (dashed line), τ_m (black solid) and τ_h (grey solid).

primary equations for the Hodgkin-Huxley model:

$$C\frac{dV}{dt} = -\bar{g}_{Na}m^3h(V - V_{Na}) - \bar{g}_K n^4(V - V_K) + \\ - \bar{g}_{\text{leak}}(V - V_{\text{leak}}) + I_{\text{app}}, \tag{2.42}$$

$$\frac{dm}{dt} = -\frac{m - m_\infty}{\tau_m}, \tag{2.43}$$

$$\frac{dh}{dt} = -\frac{h - h_\infty}{\tau_h}, \tag{2.44}$$

$$\frac{dn}{dt} = -\frac{n - n_\infty}{\tau_n}. \tag{2.45}$$

They added the conductance $\bar{g}_{\text{leak}}$ to their voltage equation, to account for a small voltage-independent conductance that they attributed to a leak in the membrane, possible through their microelectrode. All the voltage-dependent terms in the gating equations are non linear functions of V.

One wonders whether these equations reproduce a realistic action potential, and which is the mechanism of the produced action potential .

The actual sequence of events is determined by the dynamics of m, n, and h. The first useful observation is that $\tau_m(V)$ is much smaller than either $\tau_n(V)$ or $\tau_h(V)$ (Fig. 2.9B). As a consequence, $m(t)$ responds much more quickly to changes in V than either n or h. If the potential V is raised slightly by a small stimulating current, the sodium activation m is tracking the increased $m_\infty(V)$. If the stimulating current is large enough to raise the potential, and therefore $m_\infty(V)$, to a high enough level (above its threshold), then m will increase sufficiently to change the sign of the net

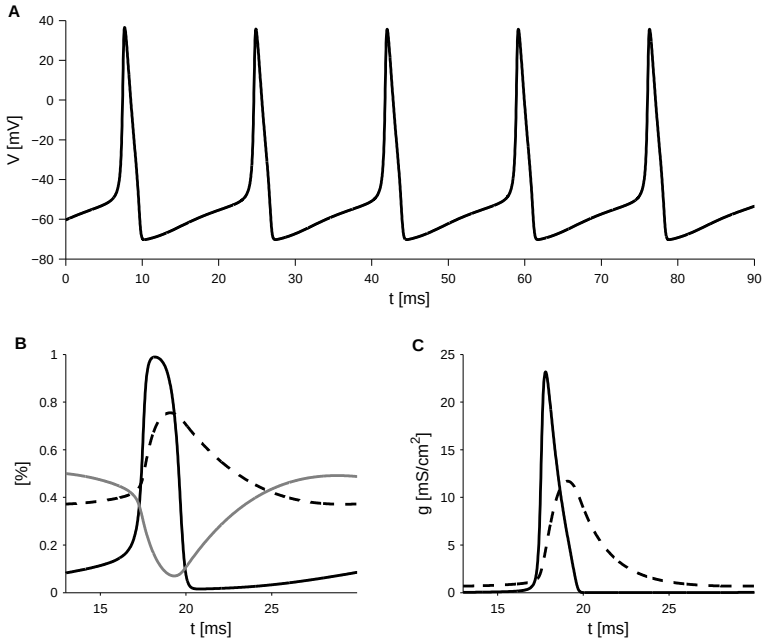

Figure 2.10: **Hodgkin-Huxley model simulations.** A) Sequence of action potentials as a result of a depolarizing current stimulus. B) Gating variables during one single action potential: n (dashed line), m (black solid) and h (grey solid). C) g_K (dashed) and g_{Na} (solid) during one single action potential.

current. Now, as the potential rises, m continues to rise, and the inward sodium current is increased, further adding to the rise of the potential.

If nothing further were to happen, the potential would be driven to a new equilibrium at V_{Na}. However, as the potential increases, h_∞ decreases toward zero (it was about 0.6 at resting potential), and as h approaches zero, the sodium current inactivates. However, because the time constant $\tau_h(V)$ is much larger than $\tau_m(V)$, there is a considerable delay between turning on the sodium current when m increases and turning it off when h decreases.

At about the same time that the sodium current is inactivated, the outward potassium current is activated. This is because of the similarity of the time constants $\tau_n(V)$ and $\tau_h(V)$ (Fig. 2.9B). Activation of the potassium current drives the potential below rest toward V_K. When V is negative, n declines, and the whole process can start again. In Figure 2.10A a plot of the potential $V(t)$ during a sequence of action potentials following a superthreshold stimulus is shown. In Figure 2.10B, $m(t)$, $n(t)$, and $h(t)$ during one single action potential are shown. Finally, in Figure 2.10C, g_K and g_{Na} during one single action potential are shown.

3

Modeling Electrical Activity in Intestinal L-Cells

As said in the introductory Chapter, glucose sensing by a variety of specialized cells plays a crucial role in the control of body weight and blood glucose levels, and dysfunctional glucose sensing is involved in the development of obesity and diabetes [45]. The various glucose-sensing cells rely on different molecular mechanisms for monitoring glucose levels. The prototype mechanism operating in pancreatic β-cells, that will be analyzed in the next Chapters, involves closure of K(ATP)-channels, which leads to cell depolarization and action potential firing with subsequent insulin release [46]. However, the stimulus-secretion pathway in intestinal L-cells is still poorly understood.

Due to the low number of L-cells in the intestinal wall and their resemblance with neighbouring enterocytes, the GLP-1 secreting cell line GLUTag [47] has been widely used to obtain insight into the cellular mechanisms leading to GLP-1 release. These studies have clarified that GLUTag cells use the electrogenic SGLT1 [48] and K(ATP)-channels [49] to sense glucose. Electrical activity consisting of action potential firing driven by Na^+- and Ca^{2+}-channels then promote Ca^{2+} influx and release of GLP-1 [50].

Subsequent studies using transgenic mice with fluorescent L-cells [51] confirmed that primary L-cells rely on similar mechanisms to transduce glucose sensing to GLP-1 secretion [51, 52]. However, differences in the electrophysiological properties of GLUTag [50] and primary L-cells [53] have emerged, which could underlie the

variation in secretory responses in GLUTag versus L-cells. In particular, primary L-cells appear to rely mainly on SGLT1 for glucose sensing, in contrast to GLUTag cells, which use both SGLT1 and K(ATP)-channels to transduce glucose stimuli into GLP-1 secretion [54–57].

This particular glucose-sensing arrangement with glucose triggering both a depolarizing SGLT current as well as leading to closure of the hyperpolarizing K(ATP) current is of more general interest for our understanding of glucose-sensing cells.

To dissect the interactions of these two glucose-sensing mechanisms, a mathematical model of electrical activity underlying GLP-1 secretion was built and will be described in this Chapter. In particular, two sets of model parameters will be presented: one set represents primary mouse colonic L-cells; the other set is based on data from GLUTag cell line. The model will then be used to obtain insight into the differences in glucose-sensing between primary L-cells and GLUTag cells. The results presented here will illuminate how the two glucose-sensing mechanisms interact, and should be useful for further basic, pharmacological and theoretical investigations of the cellular signal underlying endogenous GLP-1 and peptide YY release.

3.1 Mathematical Modeling

A single mathematical Hodgkin-Huxley-type model that, depending of the parameters, describes electrical activity in mouse L-cells or in the GLP-1 secreting cell line GLUTag [47] was developed. The model and the two parameter sets were based on patch clamp data from primary colonic L-cells [53] and GLUTag cells [50], respectively. The model includes ATP-sensitive K^+-channels (K(ATP)-channels), voltage-gated Na^+-, K^+- and Ca^{2+}-channels, and the electrogenic sodium glucose co-transporter SGLT1.

The evolution of the membrane potential V is driven by the contribution from the different currents (normalized by cell capacitance) to be described in details below,

$$\frac{dV}{dt} = -\left(I_{Na} + I_{CaT} + I_{CaHVA} + I_{Kv} + I_{KA} + I_{K,hyper} + I_{SGLT} + I_{K(ATP)}\right). \quad (3.1)$$

Voltage-gated membrane currents are modeled as

$$I_X = g_X m_X h_X \left(V - V_X\right), \quad (3.2)$$

where X stands for the channel type, V_X is the associated reversal potential, g_X the maximal whole-cell channel conductance, and m_X and h_X describe activation and inactivation of the channel, respectively.

Activation (similarly inactivation) is described by

$$\frac{dm}{dt} = \frac{m_{X,\infty}(V) - m_X}{\tau_{mX}}, \tag{3.3}$$

where $m_{X,\infty}$ is the steady-state voltage-dependent activation function, and τ_{mX} is the time-constant of activation, which in some cases depends on the membrane potential. Steady-state voltage-dependent activation (inactivation) functions were described by the Boltzmann equation

$$m_{X,\infty} = \frac{1}{1 + e^{(V - V_{mX})/k_{mX}}}. \tag{3.4}$$

Parameters can be found in Table 3.1.

Voltage-gated Sodium-channels

In GLUTag cells, voltage steps triggered rapidly inactivating currents at potentials higher than -40 mV. Inactivation parameters were used from [50] without modification, with an estimated time constant of 1.5 ms based on reported voltage clamp traces. Channel conductance and activation function were obtained from fits to the current-voltage (I-V) relationship in [50]. Given the rapid activation, Na^+-channel were assumed to activate instantaneously.

In primary murine L-cells, Na^+-currents (I_{Na}) were reported to have fast activation and to undergo large and rapid inactivation. Hence, they were assumed to activate instantaneously, while the inactivation kinetics was estimated by simulating voltage clamp experiments [53] ($\tau_{hNa} \approx 3$ ms). Activation and inactivation parameters were used without modification from [53]. The conductance value was slightly ($\sim$10%) increased compared to the value reported in [53], but the resulting I-V relationship was the within errorbars in [53]. Compared to GLUTag cells, primary L-cells have a bigger sodium current with activation function is left-shifted by $\sim$10 mV.

Voltage-activated Calcium-channels

The calcium I-V relationship in GLUTag cells exhibit a single peak [50], probably due to the lack of the low voltage activated T-type Ca^{2+}-channels in the cell line [53].

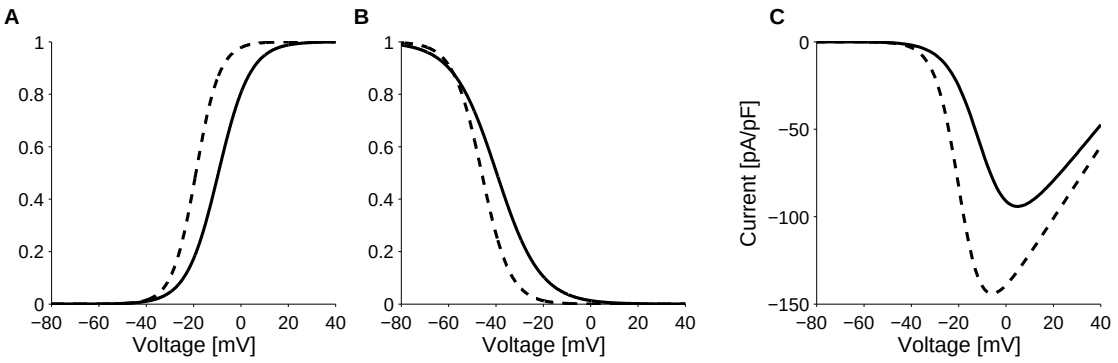

Figure 3.1: **Sodium currents.** Comparison of Na^+ current (I_{Na}) activation function (A), inactivation function (B) and I-V relationship (C) between GLUTag (solid line) and primary L-cells (dashed line).

Hence, the Ca^{2+} current in GLUTag was modeled as a single high voltage activated (HVA) current (I_{CaT} = 0 pA/pF in Eq. 3.1). Since half of the current inactivates [50], inactivation function was modeled as:

$$h_{CaHVA,\infty} = (1 - A) + A h^*_{CaHVA,\infty}, \tag{3.5}$$

with $A = 0.5$ and $h^*_{CaHVA,\infty}$ as in Eq. 3.4. Inactivation parameters were used without modification from [50] and an estimated time constant of ∼40 ms compatible with voltage clamp experiments. Channel conductance and activation function were obtain from the I-V relationship reported by [50].

In primary murine L-cells, Ca^{2+}-currents have fast activation and approximately half of the total Ca^{2+} current inactivates. Moreover, voltage dependence of the peak current presents a clear shoulder around −30 mV, suggesting the presence of low (T-type, I_{CaT}) and high (L- and Q-type, I_{CaHVA}) voltage-activated Ca^{2+} currents [53]. We assumed instantaneous activation of the Ca^{2+}-currents.

The T-type Ca^{2+}-channels were assumed to inactivate completely. Accordingly the I-V relationship for the steady state Ca^{2+}-current lacks the shoulder around −30 mV of the peak current [53]. The high voltage activated Ca^{2+}-channels likely correspond to a combination of L-type and Q-type [53], which in neuronal cells have similar inactivation kinetics [58]. Barium and calcium inactivated the Ca^{2+}-current to a similar degree [53], suggesting that inactivation was voltage-dependent. Given the complete inactivation of T-type Ca^{2+}-channels, the residual current is due to HVA Ca^{2+}-channels only. As a consequence their inactivation function was modeled as in Eq. 3.5, with A=0.38 and $h^*_{CaHVA,\infty}$ estimated as described below.

To differentiate between inactivation of low- and high-voltage-activated Ca^{2+}-channels, we fitted all parameters simultaneously (activation, inactivation and conductance) using I-V relationship for peak and steady state Ca^{2+}-current along with the overall inactivation function reported in [53]. The resulting activation parameters and conductance were in good agreement with the ones reported by [53], which fitted the I-V relationship for the peak Ca^{2+}-current only, and we used as initial values for the fitting procedure. Ca^{2+}-currents exhibits slower inactivation in correspondence to voltage pulse evoking of maximal peak current, where HVA Ca^{2+}-channel represent the dominant component [53]. As consequence, we assumed that the time-constant of T-type Ca^{2+}-channels inactivation was faster (∼20 ms) compared to the HVA Ca^{2+}-channel inactivation (∼100 ms).

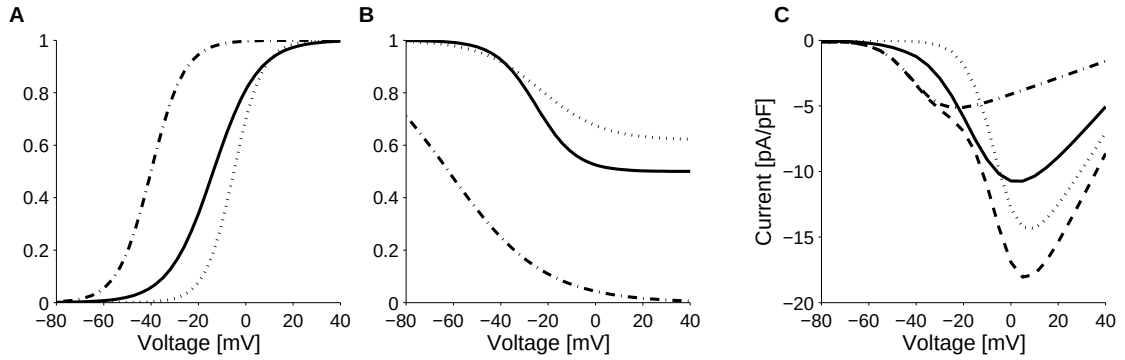

Figure 3.2: **Calcium currents.** Comparison of HVA Ca^{2+} current (I_{CaHVA}) activation function (A), inactivation function (B) and I-V relationship (C) between GLUTag (solid line) and primary L-cells (dotted line). Superimposed T-type Ca^{2+} current (dot-dashed line) and total Ca^{2+} current (dashed line) in primary L-cells.

Voltage-dependent Potassium-channels

A detailed characterization of K^+-channels in GLUTag cells was reported in [50]. Depolarization steps resulted in voltage-dependent currents, which showed partial inactivation. The dominant component of this current was non-inactivating and TEA-sensitive (I_{Kv}). This current was assumed not to inactivate and to activate with kinetics modeled as

$$\tau_{mKv} = \tau_0 + \frac{\tau_1}{1 + e^{((V+V_\tau)/k_\tau)}}, \tag{3.6}$$

compatible with voltage clamp experiments. Activation function parameters were taken from [50] without modification, while conductance was estimated from the

data [50].

The TEA-insensitive current was reported to have the characteristics of an A-type current (I_{KA}). Inactivation parameters were used from [50] without modification, while inactivation time constant was estimated from voltage-clamp current traces. Conductance and activation function were obtain from the experimental I-V relationship.

In response to hyperpolarizing voltage steps, a time- and voltage-dependent, non-inactivating current was observed [50]. Current characterization was taken from [50], with an activation time constant of 500 ms, compatible with voltage-clamp experiments in [50].

In the primary murine L-cells, K^+-currents (mainly delayed-rectifiers, I_{Kv}) exhibit voltage-dependent activation kinetics, which was modeled similarly to Eq. 3.6, but with different parameters value compatible with voltage clamp experiments in [53].

K^+-channels were assumed not to inactivate, given their slow inactivation [53]. Activation parameters were used from [53] without modification, while conductance was slightly (∼10%) decreased compared to the value reported in [53], but the resulting I-V relationship was within errorbars.

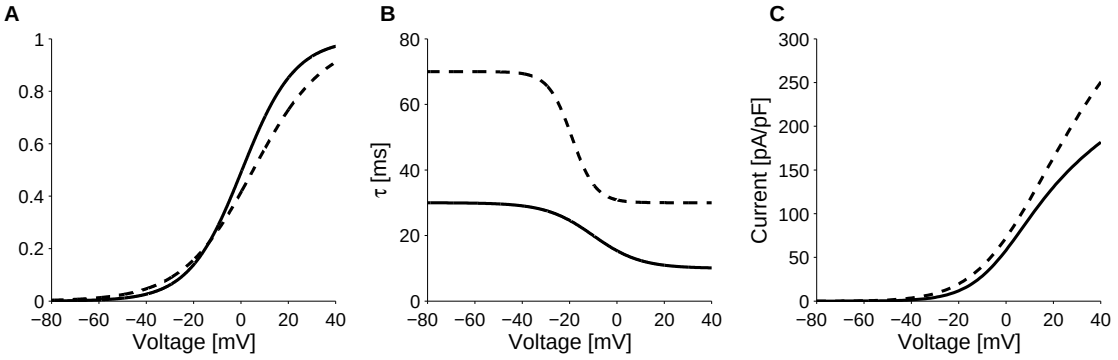

Figure 3.3: **Potassium currents.** Comparison of K^+ current (I_{Kv}) activation function (A), time constant (B) and IV relationship (C) between GLUTag (solid line) and primary L-cells (dashed line).

ATP-sensitive Potassium-channels

The ATP-sensitive potassium (K(ATP)) current was modeled as

$$I_{K(ATP)} = g_{K(ATP)} \left(V - V_K\right),$$

where $g_{K(ATP)}$ represents the equivalent conductance of the ATP-sensitive potassium channels and varies according to the percent of open channels.

K(ATP) current was detected in the GLUTag cell line [49]. Its amplitude was estimated from the immediate whole-cell current of ∼0.6 pA/pF in response to 20 mV pulses from −70 mV. Assuming a potassium reversal potential of $V_K = -70$ mV, we obtain a conductance of $g_{K(ATP)} = 30$ pS/pF in the GLUTag cells.

Similarly, functional K(ATP) channels in primary L-cells were identified in [51], by the presence of a tolbutamide-sensitive current. The endogenous K(ATP) conductance was estimated from the measured slope conductance just after whole-cell mode [51]. The obtained value was $g_{K(ATP)}$ ∼3 pS/pF.

Thus, the ATP-sensitive potassium current resulted to be an order of magnitude bigger in GLUTag compared to primary L-cells.

Sodium/glucose Co-transporter Model

SGLT1 utilizes a concentration gradient of Na^+ to transport glucose from the intestine into the L-cells. Experimental measurements showed that two Na^+ are required to transport one molecule of glucose into the cell. Moreover, in absence of sodium in the external medium, glucose is not transported [59].

These observations lead to a six-state model (Fig. 3.4) [42]. Starting with the empty carrier outside the cell (state 1), the first step is the association of two sodium ions with the carrier (state 2), that allows the subsequent association of glucose (state 3), the third step corresponds to the translocation of the carrier from outside to inside the cell (state 4), symmetrical steps take place inside the cell consisting in successive dissociation of glucose (state 5) and sodium (state 6), a final step bring the empty carrier back the initial state outside the cell. The experimental values of rate constants for the six-state model have been assigned in [42], and are given in Table 3.2.

A small current is associated with sodium/glucose co-transport, attributable to the translocation of the negatively charged carrier [42]:

$$I_{SGLT} = -\frac{2F}{C}\frac{n}{N_A}\left[\alpha(k_{12}C_1 - k_{21}C_2) + \delta(k_{61}C_6 - k_{16}C_1)\right] \tag{3.7}$$

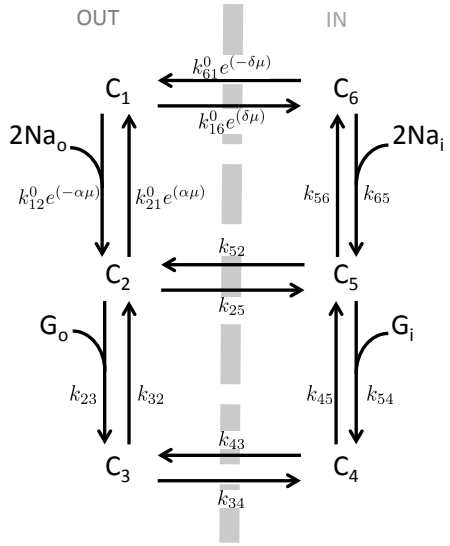

Figure 3.4: Six-state model of sodium/glucose cotransporter SGLT1.

where F is the Faraday constant, C the cell capacitance, n the number of transporters, N_A the Avogadro's number, k_{xy} is the rate constant describing the transition between state x and state y, C_z is the fraction of carriers in state z, and α and δ are phenomenological coefficients representing fractional dielectric distances. Finally, μ is the reduced potential FV/RT, where R is the gas constant and T is the temperature.

The SGLT1 current depends on glucose and sodium concentration inside and outside the cell, as well as on the membrane voltage, given the dependence of the rate constants on this factors. Simulated depolarization steps cause an outward transient current and an inward steady-state current.

The magnitude of the SGLT1 current is directly proportional to the number of transporters n in the cell. In GLUTag cells, the SGLT1 current was calibrated using the change in the holding current at -70 mV, when αMG was applied at saturation level (20 mM) [48], which led to $n = 7.7 \times 10^6$. No corresponding data are available for the primary murine L-cells. We assumed that the SGLT1 current was smaller in primary compared to GLUTag cells, similarly to the difference in K(ATP) conductance, since the balance between the SGLT1 and K(ATP) currents determines

whether the cell is excitable. These currents should therefore be of comparable magnitude in order to allow the cell to switch from quiescence to action potential firing and vice versa. For the primary murine L-cells we used $n = 4 \times 10^6$.

Parameter	Primary	Ref	GLUTag	Ref	Unit
V_{Na}	69		69		mV
g_{Na}	2.1	R11	1.7		nS/pF
V_{mNa}	-19	R11	-9.5		mV
k_{mNa}	-5	R11	-6.7		mV
V_{hNa}	-46	R11	-39.7	R05	mV
k_{hNa}	6	R11	9.2	R05	mV
τ_{hNa}	3		1.5		ms
V_{Ca}	65		65		mV
g_{CaHVA}	0.29	R11	0.24		nS/pF
V_{mCaHVA}	-5	R11	-13.7		mV
k_{mCaHVA}	-6	R11	-9.4		mV
V_{hCaHVA}	-23	R11	-25	R05	mV
k_{hCaHVA}	13	R11	8.5	R05	mV
τ_{hCaHVA}	100		40		ms
A	0.38		0.5	R05	ms
g_{CaT}	0.075	R11	0		nS/pF
V_{mCaT}	-40	R11	-		mV
k_{mCaT}	-7	R11	-		mV
V_{hCaT}	-62	R11	-		mV
k_{hCaT}	20	R11	-		mV
τ_{hCaT}	20		-		ms
V_K	-70		-70		mV
g_K	2.5	R11	1.7	R05	nS/pF
V_{mK}	5.2	R11	0.5	R05	mV
k_{mK}	-15	R11	-11.2	R05	mV
τ_0	30		10		ms
τ_1	40		20		ms
V_τ	20		10		mV
k_τ	5		10		mV
g_A	0		0.65		nS/pF
V_{mA}	-		3.9		mV
k_{mA}	-		-23.5		mV
V_{hA}	-		-61	R05	mV
k_{hA}	-		7.5	R05	mV
τ_{hA}	-		30		ms
g_{Hyper}	0		0.1	R05	nS/pF
V_{Hyper}	-		-40.2	R05	mV
V_{mHyper}	-		-85.7	R05	mV
k_{mHyper}	-		9.2	R05	mV
τ_{mHyper}	-		500		ms
$g_{K(ATP)}$	0.003	R08	0.03	RG02	nS/pF

Table 3.1: Default parameters of the different ion channels. References are R11: [53], R05: [50], R08: [51], RG02: [49].

Parameter	Primary	Ref.	GLUTag	Ref.	Unit
n	4e6	R08	7.7e6	RG02	adim
C	8	R11	7		pF
k_{12}^0	8e-5	P92	8e-5	P92	ms^{-1} mM^{-2}
k_{21}^0	0.5	P92	0.5	P92	ms^{-1}
α	0.3	P92	0.3	P92	adim
k_{23}	0.1	P92	0.1	P92	$ms^{-1}mM^{-1}$
k_{32}	0.02	P92	0.02	P92	ms^{-1}
k_{25}	3e-4	P92	3e-4	P92	ms^{-1}
k_{52}	3e-4	P92	3e-4	P92	ms^{-1}
k_{34}	0.05	P92	0.05	P92	ms^{-1}
k_{43}	0.05	P92	0.05	P92	ms^{-1}
k_{45}	0.8	P92	0.8	P92	ms^{-1}
k_{54}	40	P92	40	P92	$ms^{-1}mM^{-1}$
k_{56}	0.01	P92	0.01	P92	ms^{-1}
k_{65}	5e-8	P92	5e-8	P92	$ms^{-1}mM^{-2}$
k_{16}^0	0.035	P92	0.035	P92	ms^{-1}
k_{61}^0	5e-3	P92	5e-3	P92	ms^{-1}
δ	0.7	P92	0.7	P92	adim

Table 3.2: Default parameters of the SGLT1 model. References are R11: [53], R08: [51], RG02: [49], P92: [42].

3.2 Simulation Results of Electrical Activity

3.2.1 Glucose-sensing Mechanisms

Experimentally, it is possible to stimulate the two glucose-sensing mechanisms individually by using different sugar types. For example, α-methyl-D-glucopyranoside (αMG) is a non-metabolizable glucose analogue that is co-transported by SGLT1 and can depolarize the cell by the SGLT1-associated current without inducing K(ATP)-channel closure. Fructose, on the other hand, does not enter via SGLT1, but is metabolized and the resulting ATP increase closes K(ATP)-channels. Finally, a glucose stimulus might be sensed by the two different pathways simultaneously, and the model could help in differentiating the contribution of each pathway. Instead of fructose, the K(ATP)-channel blocker tolbutamide is commonly used to target K(ATP)-channels without affecting the SGLT1-associated current.

To simplify the notation, in the following SGLT1-substrate will represent any substance that is co-trasported by SGLT1 and induces the associated current. In the model described in the previous Section, a SGLT1-substrate corresponds to the parameter G_o, which represents the extracellular concentration of e.g. glucose or αMG.

GLUTag cells

In GLUTag cells electrical activity was promoted by stimulation with glucose [48–50]; αMG [48], acting on SGLT1 only; or with tolbutamide [49] or fructose [48], which affect K(ATP)-channels only. In contrast to the primary L-cells, a glucokinase activator (GKA50) augmented GLP-1 secretion from GLUTag cells at 1 or 10 mM glucose [55]. These experiments showed that although both electrogenic SGLT1 uptake and sugar metabolism independently can trigger action potential firing in GLUTag cells, the two mechanisms interact and both play a direct role in glucose sensing in the cell line.

It was investigated whether electrogenic glucose uptake alone can evoke electrical activity in the mathematical model of the GLUTag cell line. In order to simulate SGLT1-mediated glucose uptake, with no effect on metabolism, it is sufficient to change extracellular SGLT1-substrate concentration and keep K(ATP)-conductance unchanged. At low G_o (0.5 mM), the cell is in a silent state, and an elevation of G_o (1.5 mM or 10 mM) induces an inward transport of the SGLT1-substrate that generates a fast increase in the associated inward current, which is sufficient to depolarize the cell and initialize electrical activity (Fig.3.5A,B).

The model also reproduces the induction of electrical activity as a consequence of K(ATP)-channel block in response to tolbutamide [49] or fructose [48] (Fig. 3.5C). In this case, the reduction in the outward potassium current is sufficient to allow depolarization and electrical activity.

The SGLT1-associated current becomes positive during the action potential (see Fig. 3.5B), and therefore contributes to cell repolarization. This two-fold role of the SGLT1-associated current, the depolarization effect to initiate the action potential and the repolarizing effect to terminate it, was further analyzed with the model. In response to depolarizing pulses, the SGLT1 co-transporter generates a fast transient outward current followed by a sustained inward current, whose magnitude depends both on the voltage of the pulse (see Fig. 3.6A) and on extracellular

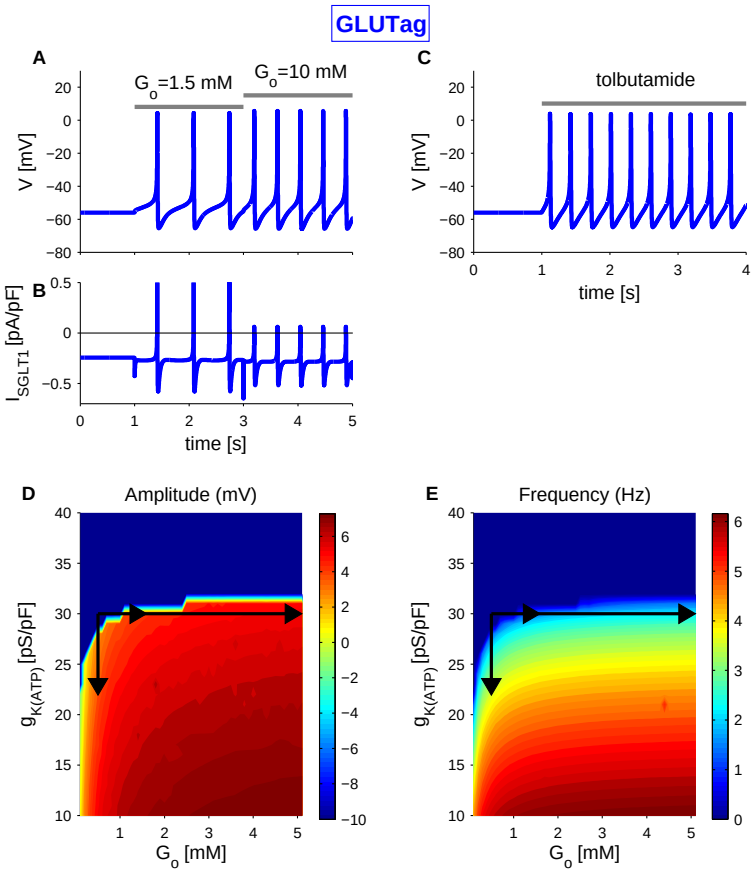

Figure 3.5: **Simulated electrical activity in the GLUTag cell line**. A) Simulation of electrical activity triggered by SGLT1-substrate uptake, corresponding to αMG application, with default parameters and extracellular SGLT1-substrate concentration, G_o, changing from 0.5 mM to 1.5 mM and 10 mM as indicated. B) SGLT1-associated current corresponding to the simulation in (A). C) Simulation of electrical activity triggered by the K(ATP)-channel blocker tolbutamide with default parameters and K(ATP)-channel conductance, $g_{K(ATP)}$, changed from from 30 pS/pF to 23 pS/pF as indicated by the bar. D) Voltage peak amplitude as a function of extracellular SGLT1-substrate concentration G_o and K(ATP)-conductance, $g_{K(ATP)}$. E) Spike frequency as a function of G_o and $g_{K(ATP)}$. In panels (D) and (E), the arrows indicate the parameter changes in (A), (B) and (C).

SGLT1-substrate concentration (see Fig. 3.6B). At low SGLT1-substrate concentrations, the simulated transient outward current is bigger for more positive pulse potentials (V_{pulse}), while the inward current current becomes smaller with increasing V_{pulse}. As the SGLT1-substrate concentration increases, the transient outward current decreases, eventually becoming negligible, whereas the steady-state inward current increases with high affinity for the substrate (see Fig. 3.6C,D). As a consequence, at high SGLT1-substrate concentrations the cell can initiate electrical

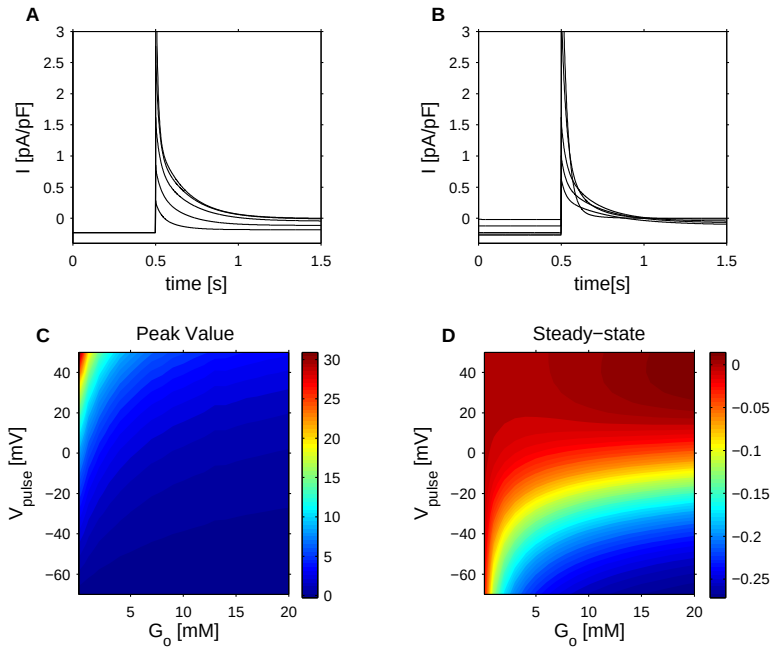

Figure 3.6: **Model characterization of SGLT1-associated currents during voltage clamp as a function of SGLT1-substrate concentration, G_o, and voltage pulse, V_{pulse} and parameters as for GLUTag model**. The voltage-clamp protocol consisted in applying 1 s depolarization at t = 0.5 s from a holding potential of -70 mV. A)Simulated SGLT1-associated current in response to different voltage pulses (V_{pulse} = -50, -30, -10, 10, 30 mV) and constant G_o= 5 mM. B) Simulated SGLT1-associated current in response to a voltage pulse (V_{pulse} = -10) and different G_o= 0.1, 1, 5, 10, 20 mM. C) Simulated peak SGLT1-associated current in response to voltage pulses as a function of G_o and V_{pulse}. D) Simulated steady-state SGLT1-associated current in response to voltage pulses as a function of G_o and V_{pulse}.

activity thanks to the increased inward current, and the action potentials can reach slightly higher values because of the reduced outward current (see Fig. 3.5A,B).

In the simulations above, only one possible glucose-sensing mechanism is involved, i.e. either extracellular SGLT1-substrate concentration, having an effect on SGLT1 current, or $g_{K(ATP)}$, corresponding to the closure/opening of K(ATP)-channels. However, to better understand the interaction between the two glucose-sensing mechanisms, the model response should be analyzed by varying the two parameters simultaneously. Different combinations of the two parameters lead to different electrical activity responses, which can be characterized by the peak value of the membrane potential during spiking activity and the spiking frequency. The results are shown in Figure 3.5D for peak membrane potential and in Fig. 3.5E for the frequency. Looking at the pictures, the region in which the cell is electrically

active becomes evident. Furthermore, simulations showed that, action potential amplitude is almost constant, if the cell is electrically active, while frequency can be modulated by different combinations of G_o and $g_{K(ATP)}$.

Figure 3.5D,E becomes an useful tool to understand the simulations of electrical activity in GLUTag cells (Fig. 3.5A,C). A cell in the silent state can become active as a result of an increase in extracellular SGLT1-substrate, which corresponds to the rightwards arrows in Figure 3.5D,E. Given the high affinity of SGLT1 to its substrate, a higher concentration would not result in a significant effect on electrical activity (see Fig. 3.5D,E). Alternatively, the cell might become active as a result of K(ATP)-channel closure, which is represented by a downwards arrow in the picture. A further decrease in $g_{K(ATP)}$, would result in an increase of both spiking amplitude and frequency.

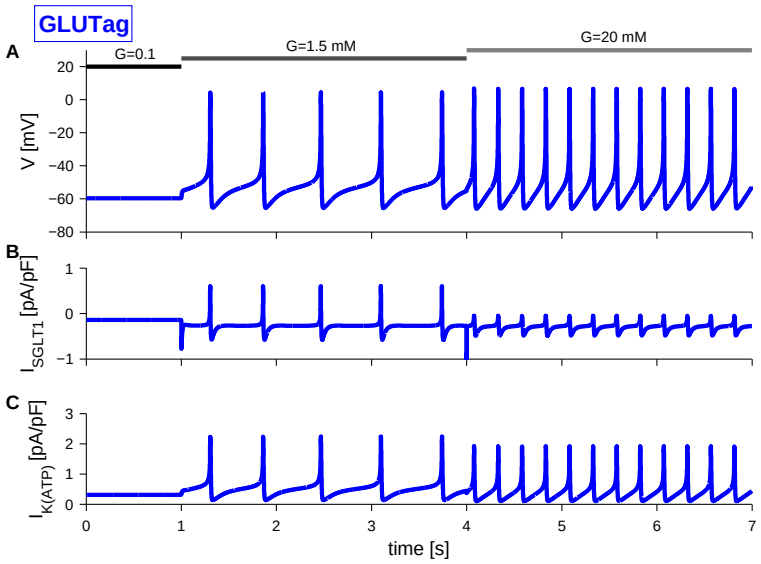

Figure 3.7: **Effect of stimulation with glucose at different concentrations (indicated by grey bars) on GLUTag electrical activity**. The stimulation with 1.5 mM glucose was simulated by changing extracellular SGLT1-substrate concentration, G_o, from 0.1 mM to 1.5 mM, while $g_{K(ATP)}$ remained unchanged from its default value. Subsequent 20 mM glucose application was simulated by changing G_o from 1.5 mM to 20 mM, and $g_{K(ATP)}$ from 30 pS/pF to 25 pS/pF.

Glucose stimulation would have an effect on both variables depending on its concentration. In particular, the ability of GLUTag cells to sense low concentrations of sugars might be attributable to the SGLT1-associated current, given the high glucose affinity of SGLT1, which in the model corresponds to a change in G_o with unchanged $g_{K(ATP)}$. At higher glucose concentrations (>5 mM), there could be an

effect of metabolism and closure of K(ATP)-channels, besides an increase in the SGLT1-associated current. The resulting membrane potential simulation is shown in Figure 3.7. The higher glucose concentration resulted in a small increase in the peak of the action potential and a greater increase in spiking frequency, in agreement with experiments [49]. The increased peak and frequency is due to a combination of the closure of K(ATP)-channels (Fig. 3.7C) and a reduction in the transient outward SGLT1-current (Fig. 3.7B), given its two-fold role explained above (Fig. 3.6).

Primary L-cells

As for the GLUTag cell line, similar simulations can be performed to analyze the contribution of the two sensing mechanisms in primary L-cells. To our knowledge, no experimental data on electrical activity with αMG, acting on SGLT1 transport alone, are available in the literature. However, with the mathematical model, we can now test directly whether electrogenic glucose uptake is sufficient to trigger electrical activity in primary L-cells. Similarly to the GLUTag cells, at low G_o (0.1 mM), the cell is in a silent state, and an elevation of G_o (1 mM or 20 mM) generates an increase in the SGLT1-associated inward current, causing cell depolarization and electrical activity (Fig.3.8A,B). A further increase in G_o does not affect electrical activity significantly because of the high affinity of SGLT1 to its substrate.

The model also reproduces the induction of electrical activity by the K(ATP)-channel antagonist tolbutamide [52] (Fig. 3.8C). However, it is worth noting that the starting point for the primary L-cells corresponds to $g_{K(ATP)}$= 3 pS/pF, which means that on average only a single K(ATP) channel is open [60]. In contrast, the GLUTag cells have a ten-fold higher K(ATP) conductance, which might explain how stimulated metabolism by fructose [48] or glucosekinase activators [55] can have an effect in GLUTag cells but not in primary L-cells: in the latter almost all K(ATP)-channels are already closed and further physiological inhibition is therefore not possible. Nonetheless, pharmacological closure of K(ATP)-channels by tolbutamide can trigger electrical activity and GLP-1 secretion [51, 52, 61], and our model shows that although the exogenous K(ATP)-channels activity is very low, a further reduction is sufficient to allow electrical activity.

The simulated electrical responses are summarized in Figure 3.8D,E showing voltage peak and frequency, respectively, as a function of G_o and $g_{K(ATP)}$. Similarly to the GLUTag cell line, it is easy to identify the region in which the cell is electrically

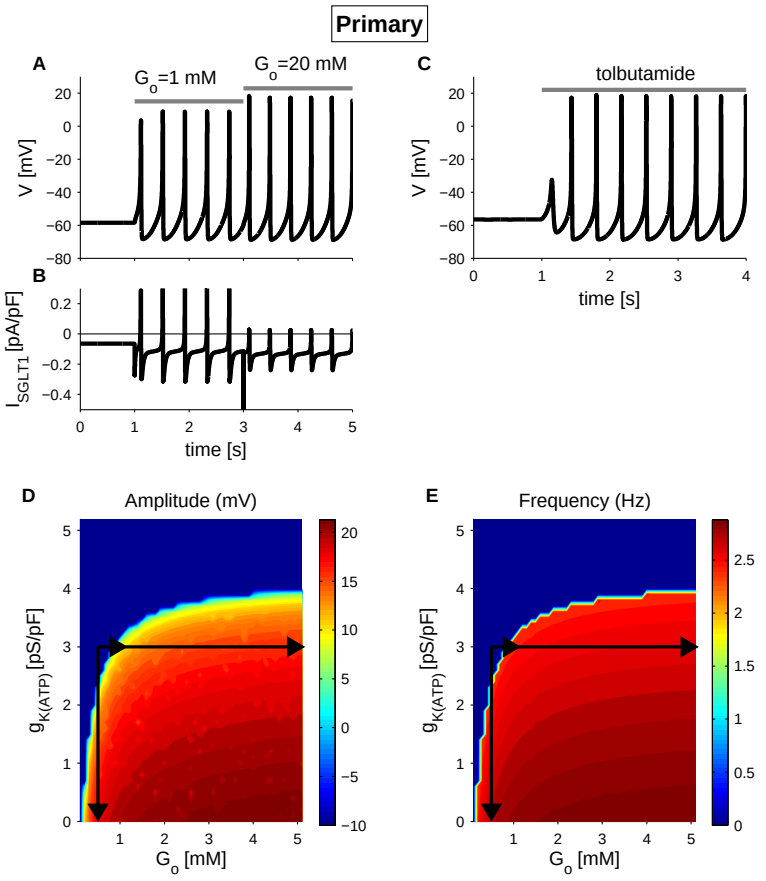

Figure 3.8: **Simulated electrical activity in primary L-cells** . A) simulation of electrical activity triggered by SGLT1-substrate uptake, corresponding to αMG application, in primary L-cells with default parameters and extracellular SGLT1-substrate, G_o, changing from 0.1 mM to 1 mM and 20 mM as indicated. B) SGLT1-associated current corresponding to the simulation in (A). C) Simulation of electrical activity triggered by K(ATP)-channel blocker, tolbutamide. Default parameters and K(ATP)-channel conductance, $g_{K(ATP)}$ changing from from 3 pS/pF to 0 pS/pF. Grey bars indicate application of the substances. D) Voltage peak as a function of extracellular SGLT1-substrate G_o, and K(ATP)-channel conductance, $g_{K(ATP)}$. E) Spiking frequency as a function of G_o and $g_{K(ATP)}$. The arrows indicate the parameter changes in (A) and (B).

active. In that area, the electrical activity changes by different combinations of G_o and $g_{K(ATP)}$. Contrarily to an active GLUTag cell line, whose frequency can be finely modulated mainly by changing $g_{K(ATP)}$ in the presence of G_o, in the primary L-cell model, the spiking frequency is only slightly affected by a further change in the parameters. Action potential amplitude can be increased by different combinations of G_o and $g_{K(ATP)}$. The increase is bigger ($\sim$10 mV) compared to the one obtain in the GLUTag model ($\sim$3 mV) with similar parameter changes. Thus, the model

suggests that primary L-cells use action potential amplitude rather than frequency to transduce glucose-sensing to Ca^{2+} influx.

3.2.2 Role of Sodium-channels

GLUTag

Experimentally, the application of the Na^{+}-channel blocker TTX in the GLUTag cell line blocks action potentials evoked by 10 mM glucose completely, but did not prevent glucose-triggered rise in intracellular Ca^{2+} and had no effect on GLP-1 secretion [50]. These results are likely due to the ability of glucose to depolarize the cell, both in presence and absence of TTX, which may cause a sustained Ca^{2+} current [50]. This explanation could be verified using the model by comparing three conditions: 0.1 mM glucose and no TTX (G_o=0.1 mM and $g_{K(ATP)}$=0.03 nS/pF), 10 mM glucose stimulation and no TTX (G_o=10 mM and $g_{K(ATP)}$=0.015 nS/pF), and 10 mM glucose stimulation with TTX present (G_o=10 mM, $g_{K(ATP)}$=0.015 nS/pF and g_{Na} = 0 nS/pF). Now, we can directly compare the mean voltage and mean Ca^{2+} current, represented by a dashed line during electrical activity, in the different conditions (Fig. 3.9A,B). Glucose depolarizes the cell by ∼10 mV, both in absence and in presence of TTX. The mean Ca^{2+} current is highest during electrical activity in presence of glucose and absence of TTX. However, while TTX application reduces the current, it is still higher than in the absence of glucose, which might explain why glucose simulates GLP-1 secretion also in the presence of TTX in spite of the absence of action potential firing.

Primary L-cells

The important role of Na^{+}-channels in the upstroke of the action potentials in primary L-cells was confirmed by the model. An example of electrophysiological response to TTX was reported in [53]. The primary L-cell, maintained in a depolarized state by continuous injection of a small depolarizing current, fired spontaneous action potentials that were dramatically reduced in frequency, but not completely abolished by TTX. Simulation of Na^{+}-channel block in similar conditions, and with default parameters, completely abolished electrical activity (Fig. 3.9C). However, given that only one example was reported in [53] and considering heterogeneity between cells, we further analyzed the model response to TTX, varying the parameters

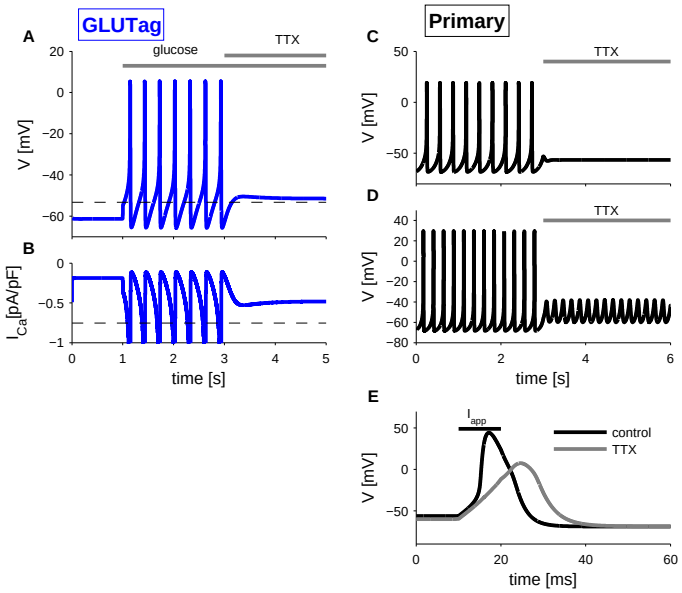

Figure 3.9: **Simulation of application of Na^+-channel blocker TTX.** A) Simulation of glucose-induced electrical activity (G_o = 10 μM and $g_{K(ATP)}$ = 0.015 nS/pF) and subsequent application of TTX in GLUTag cells with default parameters. Dashed line represent mean voltage during electrical activity. B) Calcium current corresponding to the simulation in (A). Dashed line represent mean calcium current during electrical activity. C) Simulation of current-induced electrical activity (I_{app} = 0.1 pA/pF, G_o = 1 mM and $g_{K(ATP)}$ = 0.0035 nS/pF), and subsequent application of TTX in primary L-cells . D) As in (C), except g_{CaT} = 0.11 nS/pF. E) Simulation of current-evoked action potential in primary L-cells in control case (black line) and in presence of TTX (grey line). Black bar indicates the current application I_{app} = 5 pA/pF. Grey bars indicate glucose and TTX application as indicated.

within the physiological limits. For example, by increasing T-type Ca^{2+}-channel conductance from 0.075 nS/pF to 0.11 nS/pF, TTX application resulted in membrane potential oscillations between -60 mV and -40 mV (Fig. 3.9D), which is close to the threshold for the action potential generation. As a consequence, the very low frequency recorded experimentally after TTX application, might be the result of noise, which occasionally allows the membrane potential to cross the threshold and fire an action potential.

Furthermore, in presence of TTX, action potentials could still be evoked by current injection, but compared to the control case, they were wider, elicited at a higher threshold and had a smaller amplitude [53]. The model predicts a threshold of ∼-40 mV for initiation of action potentials, which is close to the one found experimentally of ∼-36 mV [53]. Blocking Na^+-channels in the model, a membrane

potential of ∼-10 mV should be reached to activate sufficient Ca^{2+} channels to continue the depolarization trend, even after the applied current is removed (Fig. 3.9E) Also the decrease in the action potential amplitude caused by TTX is quite similar (∼40 mV) compared to the experimental example reported in [53].

3.2.3 Role of Calcium-channels

GLUTag

The evaluation of the role of Ca^{2+}-channels is fundamental, given the association of calcium concentration with the exocytotic process. In experiments with GLUTag cells, the application of the L-type calcium channel blocker nifedipine in presence of 10 mM glucose caused a reduction in action potential frequency [50]. The GLUTag mathematical model has a single calcium current, and does not differentiate between calcium channel types. To simulate the nifedipine effect, Ca^{2+}-channel conductance was reduced from 0.24 to 0.14 nS/pF, which is comparable to the barium current inhibition caused by nifedipine application in GLUTag cells [50]. The resulting model simulation in Figure 3.10A showed both a lower peak amplitude and a dramatic reduction in action potential frequency.

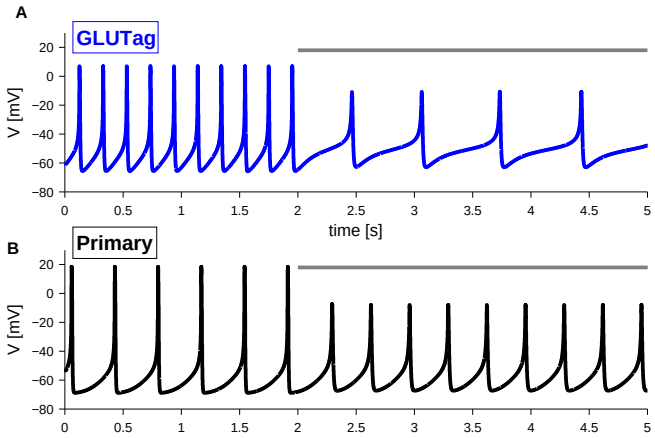

Figure 3.10: **Simulation of application of Ca^{+}-channel blocker.** A) Simulation of application of the L-type Ca^{2+}-channel blocker, nifedipine, in GLUTag cells, with default parameter except G_o=10 mM, $g_{K(ATP)}$ = 0.015 nS/pF. B) Simulation of application of partial block of HVA Ca^{2+}-channels in primary L-cells , with default parameters except G_o=10 mM. Grey bars indicate Ca^{2+}-channel blocker application.

Primary L-cells

Experimentally, the block of L-type or Q-type Ca^{2+}-channels in primary L-cell preparations caused a similar and significant reduction in GLP-1 secretion, both under basal and glutamine-stimulated conditions [51]. Simulation of partial block of HVA Ca^{2+}-channels, which are a combination of L-type and Q-type Ca^{2+}-channels, significantly reduced the peak amplitude of glucose stimulated electrical activity, which might underlie the reduction of secretion found experimentally (Fig. 3.10B).

3.3 Discussion

The relative contribution of SGLT1 and GLUT2 glucose transporters to glucose sensing in the intestinal L-cells has been a matter of debate [56]. Whereas SGLT1 transporters are electrogenic and could promote electrical activity on their own, glucose transported via GLUT2 should be metabolised to increase the ATP/ADP ratio and close K(ATP)-channels, which could lead to action potential firing as in pancreatic β-cells. Glucose entering via SGLT1 could also reduce K(ATP)-channel activity. However, accumulating evidence support the main role of the SGLT1-mediated current in primary L-cells [54–57, 62], whereas both SGLT1 currents and K(ATP)-channel closure contribute to stimulus-secretion coupling in GLUTag cells [48, 55]. The theoretical analyses presented here provide new insight into how the electrophysiological differences between primary L-cells and the GLUTag cell line lead to their diverse glucose-sensing mechanisms. The model further suggests that the two cell types encode the glucose signal in electrical activity in diverse ways: primary L-cells appear to use action potential amplitude (cf. Fig. 3.8D,E) to transduce glucose sensing to Ca^{2+} influx and exocytosis, while we propose that GLUTag cells rely mainly on changes in firing frequency (Fig. 3.5D,E).

In the isolated intestine, reflecting the situation *in vivo*, SGLT1 transporters are located on the luminal, apical side of the L-cells, and are therefore exposed directly to glucose in the intestine [56]. In contrast, the GLUT2 transporters are located on the basolateral, vascular side of the L-cells [56], where they allow glucose to pass between the cytosol of L-cells and the plasma. There are reports of GLUT2 protein being transported to and inserted in the luminal membrane of enterocytes in response to glucose [54, 63] (but see [56]). We note that although GLUT2 knockout mice have less GLP-1 release, the reduced secretion can be explained entirely

by lower GLP-1 expression, since both GLP-1 secretion and expression are reduced by ∼50 % compared to control animals [64]. Hence, no role for GLUT2 in glucose sensing in L-cells can be inferred from the knock-out animals. In contrast, luminal GLUT2 inhibition by phloretin has been shown to reduce but not abolish GLP-1 secretion in the perfused rat small intestine [57]. GLUT2 inhibition also abolished a SGLT1-independent component of GLP-1 secretion in isolated loops of small rat intestine [63], but of note this SGLT1 independent component was not observed in isolated rat small intestine [57] or *in vivo* in mice [62], where the SGLT1 inhibitor phloridzin abolished glucose induced GLP-1 secretion.

Interestingly, vascular perfusion with high glucose concentrations in the presence of 3.5 mM luminal glucose triggered GLP-1 secretion in the isolated porcine intestine [65], but in the isolated rat intestine vascular glucose did not lead to GLP-1 release in the absence of luminal glucose [57]. Besides species differences, these conflicting results can be explained as follows. In the presence of 3.5 mM luminal glucose, the SGLT1 current is operating, and vascular glucose can augment GLP-1 secretion by entering the L-cells via basolateral GLUT2 leading to metabolism and closure of K(ATP)-channels. In contrast, in the absence of intestinal glucose and SGLT1 current, the closure of K(ATP)-channels is insufficient to trigger electrical activity and GLP-1 secretion. In terms of our model, the presence of luminal glucose allows the L-cells to operate further to the right in Fig. 3.8D,E where small downward movements due to reduced K(ATP)-conductance more easily lead to electrical activity.

These various experiments points to a mechanism where SGLT1 is the major glucose-sensing component in primary L-cells, but glucose metabolism leading to K(ATP)-channel closure might play a modulating role. The theoretical results presented here support this picture. Pharmacological modulation of K(ATP)-channels can overwrite glucose-sensing, i.e. K(ATP)-channel closure by tolbutamide can trigger electrical activity and secretion in primary L-cells even in the absence of glucose [51, 52, 57], and the K(ATP)-channel agonist diazoxide abolishes glucose-stimulated GLP-1 secretion [53, 57], which can be explained with the model as follows. Pharmacological modification of K(ATP)-channel conductance can push the system in or out or the area with activity, independently of glucose-sensing by SGLT. Such modulation of K(ATP)-channel activity corresponds to large vertical moves in Fig. 3.8D,E such that horizontal movements (SGLT1-mediated sensing) are ineffective.

In the basal state the primary L-cells have a K(ATP)-conductance of <10 pS

[51], which corresponds to just a single K(ATP)-channel being open on average [60]. Thus, tolbutamide would have very little K(ATP)-channel conductance to act upon. Nonetheless, the simulations presented here showed that a further reduction in K(ATP)-channel conductance is sufficient to allow electrical activity. In contrast, the GLUTag cells have K(ATP)-channel conductance an order of magnitude larger than the primary L-cells [49]. This fact means that physiological modulation of K(ATP)-channel activity becomes a more reliable glucose-sensing mechanism in the GLUTag cell line, as highlighted by the findings that stimulated metabolism by fructose [48] or glucosekinase activators [55] stimulate secretion in GLUTag cells but not in primary L-cells. During an oral glucose tolerance test, tolbutamide does not trigger further GLP-1 release [66]. In this condition, the luminal glucose concentration is high, meaning that the L-cells are active and operating far to the right in Fig. 3.8D,E. A reduction in K(ATP)-channel conductance because of tolbutamide application, corresponding to a downward movement in Fig. 3.8D,E, will therefore have very little effect.

While the role for Na^+-channels in the generation of action potentials is clear in both GLUTag [50] and primary L-cells [53], their importance for GLP-1 secretion is – surprisingly – less evident. The addition of the Na^+-channel blocker TTX does not change glucose-stimulated GLP-1 secretion from GLUTag cells [50], while both basal and glutamine-stimulated GLP-1 secretion from primary L-cell cultures are lowered slightly and to the same extent by TTX [53]. Another Na^+-channel blocker, lidocaine, did not lower glucose-stimulated GLP-1 secretion from perfused rat intestines [57].

The model simulations presented here showed that, in line with experiments, glucose was able to depolarize both GLUTag and primary L-cells, but demonstrated also that the mean Ca^{2+} current in simulated GLUTag cells was greater during electrical activity in the absence of TTX than in the presence of TTX (Fig. 3.9). If the modest elevation in Ca^{2+} current in the presence of TTX is sufficient to trigger maximal secretion, for example because of depletion of the pool of releasable secretory vesicles, then secretion in presence or absence of TTX would be similar, in line with experiments [50]. However, this interpretation is at odds with the fact that glucose-evoked Ca^{2+} elevations in GLUTag cells were unaffected by TTX [50]. It might be that the small Ca^{2+} current evokes Ca^{2+}-induced Ca^{2+} release, which then is responsible for triggering exocytosis, suggesting that it is the depolarization

of the base-line rather than action potential firing that causes GLP-1 secretion. Clearly, the importance of Na^+ channels and electrical activity in L-cells needs further investigation.

The model presented here should be valuable also for understanding glutamine-stimulated GLP-1 secretion, since glutamine is cotransported with Na^+ by the electrogenic glutamine cotransporter [67], and the stimulus pathway is therefore similar to glucose-sensing by SGLT1 investigated here.

4

Modeling Electrical Activity in Human Pancreatic Beta-Cells

The central role of electrical activity in pancreatic β-cells is highlighted by the excellent correlation between the fraction of time with electrical activity and insulin secretion [68]. The plasma membrane potential in rodents shows complex bursting electrical activity with active phases where action potentials appear from a depolarized plateau, interspaced by silent, hyperpolarized phases [68–70]. Mathematical modeling of electrical activity has for nearly 30 years accompanied the experimental investigations of the mechanisms underlying bursting electrical activity, starting with the work by [71] on which virtually all subsequent models, even the most recent, are based [72–75]. β-cell models have been used to test, support and refute biological hypotheses [72, 74, 76], but frequently restricted to rodent, due to the availability of electrophysiological data.

However, human β-cells show important differences to β-cells from mice, for example with respect to the patterns of electrical activity observed, which consist of very fast bursting or spiking in human cells [77–81], and never the classical slower burst pattern observed in rodents. This difference could be due to the involvement of different ion channels in human β-cells compared to rodents [78–81] or to differences in islet organization [82, 83].

Electrophysiological responses in human β-cells to a range of ion channels antagonists are heterogeneous. In some cells, inhibition of small-conductance potassium

currents has no effect on action potential firing, while it increases the firing frequency dramatically in other cells. Furthermore, in contrast to L-type Ca^{2+}channels, P/Q-type Ca^{2+}currents are not necessary for action potential generation, and, surprisingly, a P/Q-type Ca^{2+}channel antagonist even accelerates action potential firing. The heterogenous electrophysiological responses in human β-cells must be taken into account for a deeper understanding of the mechanisms underlying insulin secretion in health and disease.

This Chapter will be focused on the modeling of electrical activity in human β-cells. In particular, the first human model will be presented briefly. Afterwards, my contribution to the further development of the model will be described. The model was also used to study paracrine signals, and to simulate slow oscillations by adding a glycolytic oscillatory component to the electrophysiological model. The last part of the Chapter is dedicated to a further development of the model, which led to interesting but mostly speculative results.

4.1 First Model of Human Beta-cells

In this Section the first published mathematical model of electrical activity in human β-cells [84] will be presented. It was based entirely on published ion channel characteristics of human β-cells and electrical activity was modeled by a Hodgkin-Huxley type model, as has been done for rodent β-cells [71–76, 85]. Most voltage-gated membrane currents (measured in pA/pF) are modeled based on the results of [81], who carefully assured that investigated human islet cells were β-cells. Human Ether-a-go-go-Related Gene (HERG) potassium currents in human β-cells were described in [86] and are modeled accordingly.

The membrane potential V (measured in mV) develops in time (measured in ms) according to

$$\begin{aligned}\frac{dV}{dt} = -(&I_{HERG} + I_{BK} + I_{Kv} + I_{Na} \\ &+ I_{CaL} + I_{CaPQ} + I_{CaT} + I_{K(ATP)} + I_{leak}).\end{aligned} \tag{4.1}$$

In the following, the modeling of the currents on the right-hand side of Eq. 4.1 is explained in detail.

The leak current summarized all currents not modeled explicitly, such as currents mediated by exchangers, pumps and, e.g., chloride and nonselective, non-voltage

dependent cation channels, and was modeled as

$$I_{leak} = g_{leak}(V - V_{leak}). \tag{4.2}$$

The ATP-sensitive potassium current is described by

$$I_{K(ATP)} = g_{K(ATP)}(V - V_K). \tag{4.3}$$

Here, V_{leak} and V_K are the respective Nernst reversal potentials. In [78] it was estimated that at 6 mM glucose, the conductances g_{leak} and $g_{K(ATP)}$ contribute to a similar extent to the total membrane conductance of ∼0.3 nS. With a cell capacitance of ∼10 pF [81], values of $g_{leak} = 0.015$ nS/pF and $g_{K(ATP)} = 0.015$ nS/pF were obtained for a glucose stimulated β-cell. These values were used as default, and can be found with all other default parameter values in Table 4.1.

Voltage-gated membrane currents were modeled as

$$I_X = g_X m_X h_X (V - V_X), \tag{4.4}$$

where X denotes the type of channels, V_X the reversal potential of the ion conducted by the channels, while m_X describes activation and h_X describes inactivation of the channels. As described in the following, some channels were assumed not to inactivate (i.e., $h_X = 1$), some activate instantaneously ($m_X = m_{X,\infty}(V)$), but in general, activation (and similarly inactivation, h_X) was supposed to follow a first-order equation

$$\frac{dm_X}{dt} = \frac{m_{X,\infty}(V) - m_X}{\tau_{mX}}, \tag{4.5}$$

where τ_{mX} (respectively τ_{hX}) is the time-constant of activation (respectively inactivation for h_X), and $m_{X,\infty}(V)$ (respectively $h_{X,\infty}(V)$) is the steady-state voltage-dependent activation (respectively inactivation) of the current. The steady-state activation (and inactivation) functions were described with Boltzmann functions,

$$m_{X,\infty}(V) = \frac{1}{1 + \exp((V - V_{mX})/n_{mX})}, \tag{4.6}$$

except for calcium regulated currents as explained below. For activation functions, the slope parameter n_{mX} is negative, while the corresponding slope parameter n_{hX} is positive for inactivation functions (see Section 2.3.1).

A detailed description of the currents of the model is given in the following.

Voltage-gated Calcium-channels

In [81] three types (T-, P/Q- and L-type) of voltage-gated Ca^{2+}-channels in human β-cells were found. The total Ca^{2+}-current activated very rapidly (<1 ms), and no difference in activation kinetics is apparent from the data using various Ca^{2+}-channel blockers [81, Fig. 5]. It was therefore assumed that all Ca^{2+}-channels activate instantaneously. The activation functions were estimated from the voltage-dependence of peak Ca^{2+}-currents reported by [81], and are given in Figure 4.1A.

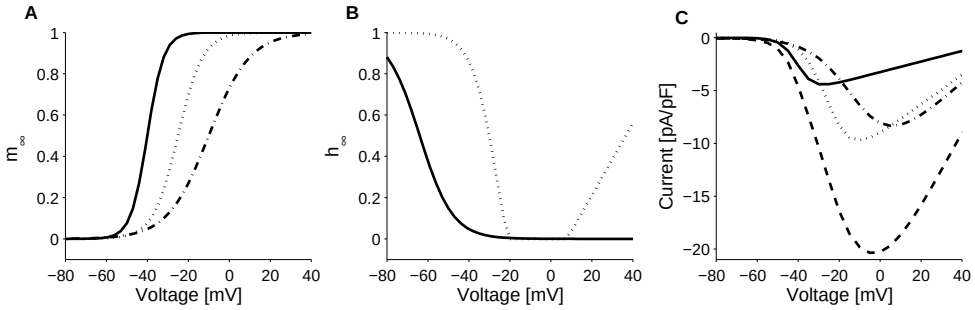

Figure 4.1: **Characterization of Ca^{2+}-channels.** A) Activation functions of T-type (full), P/Q-type (dash-dotted) and L-type (dotted) Ca^{2+}-channels with parameters as in Table 4.1. B) Inactivation functions of Ca^{2+}-channels, legends as in panel (**a**). C) IV-relationship of all Ca^{2+}-currents. The dashed curve shows the total Ca^{2+}-current.

The low-voltage activated T-type channels were found to inactivate faster than the L- and P/Q-types [81, Fig. 5], and it was therefore assumed to be responsible for the fastest component of total Ca^{2+}-current inactivation with a time constant of $\tau_{hCaT} = 7$ ms. The parameters of the Boltzmann function describing steady-state inactivation were used without modification from [81].

The high-voltage activated P/Q-type channels were assumed not to inactivate, since they inactivate much more slowly than the other Ca^{2+}-currents and the duration of action potentials [81].

Finally, the high-voltage activated L-type Ca^{2+}-channels inactivate with a time-constant of $\tau_{hCaL} = 20$ ms.

The parameters of the inactivation function for L-type Ca^{2+}-channels in human beta-cells were unknown. However, the inactivation function of the total Ca^{2+}-current has been investigated [87]. Inactivation showed a U-shaped voltage dependence with maximal inactivation of ∼50% seen at -10 mV. Since L-type currents make up ∼50% of total peak Ca^{2+}-currents in human β-cells [81], and T-type Ca^{2+}-

channels were completely inactivated at -10 mV, while P/Q-type channels do not inactivate substantially [81], it was assumed that the U-shaped inactivation function reflects inactivation of the L-type Ca^{2+}-current with almost complete inactivation at -10mV. Inactivation of the L-type Ca^{2+}-current was assumed to be Ca^{2+}-dependent and caused mainly by Ca^{2+} in microdomains below the L-type channels [87, 88], which is approximately proportional to the L-type Ca^{2+}-current [37]. The amount of inactivation $(1 - h_{CaL,\infty})$ was therefore assumed proportional to the activated L-type Ca^{2+}-current $m_{CaL,\infty}(V)(V - V_{Ca})$, which yields the following expression for the inactivation function

$$h_{CaL,\infty}(V) = \max\left(0, \min\left\{1, 1 + [m_{CaL,\infty}(V)(V - V_{Ca})]/\Phi\right\}\right), \tag{4.7}$$

with normalization factor $\Phi = 57$ mV (adjusted) and is shown in Figure 4.1B. The max-min construction confines h_{CaL} to the interval $[0, 1]$.

Voltage-gated Sodium-channels

Based on the rapid kinetics of the Na^+-currents [81], the voltage-gated sodium channels were assumed to activate instantaneously, and to inactivate with a time constant of 2 ms. The activation function was estimated from the voltage-dependence of peak Na^+-currents reported in [81], and are given in Figure 4.2A. The parameters of the Boltzmann function describing steady-state inactivation were used without modification from [81]. Both set of parameters were in good agreement with estimates in [80].

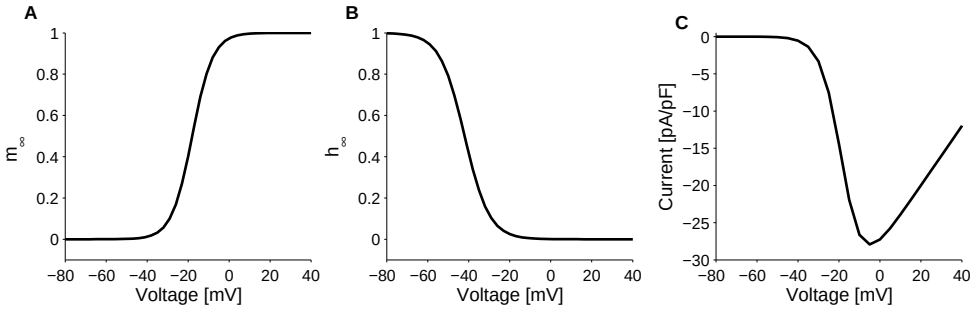

Figure 4.2: **Characterization of Na^+-channels.** A) Activation and B) Inactivation functions of voltage gated Na^+-channels. C) IV-relationship of Na^+-current.

Delayed Rectifying Potassium-channels

The delayed rectifying potassium (Kv) channels were assumed to activate on a voltage-dependent time-scale [81, 89] as shown in Figure 4.3B. with expression

$$\tau_{mKv} = \begin{cases} \tau_{mKv,0} + 10 \exp\left(\frac{-20 \text{ mV} - V}{6\text{mV}}\right) \text{ ms}, & \text{for } V \geq -26.6 \text{ mV}, \\ \tau_{mKv,0} + 30 \text{ ms}, & \text{for } V < -26.6 \text{ mV}, \end{cases} \tag{4.8}$$

where (as default value) $\tau_{mKv,0} = 2$ ms [81]. Note that in [89] Kv-channels were found to activate more slowly with $\tau_{mKv,0} \approx 10$ ms. The Kv-current was assumed not to inactivate, because of its slow (seconds) inactivation kinetics [81, 89].

The activation function was estimated from the voltage-dependence of the Co^{2+}-resistant peak K^+-currents reported by [81], and is given in Figure 4.3A. The estimated values were in general agreement with [87, 89].

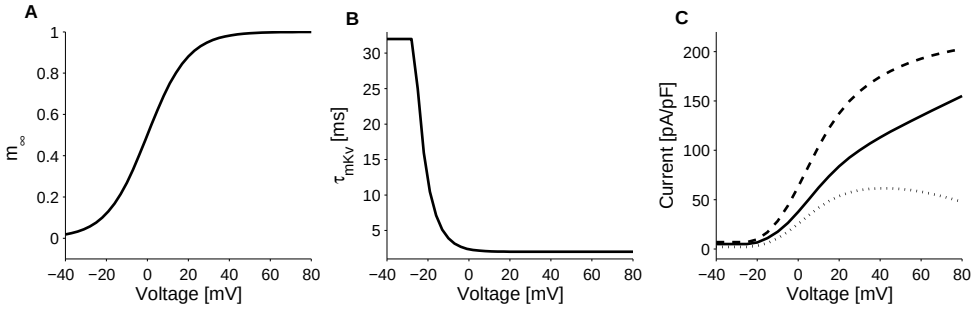

Figure 4.3: **Characterization of K^+-channels.** A) Activation function for both Kv-channels and BK-channels. B) Time constant functions of voltage gated Kv-channels. C) IV-relationship of Kv-current (solid), BK-current (dotted) and total K^+-current (dashed).

Large-conductance BK Potassium-channels

BK-channels show both voltage- and Ca^{2+}-dependence [90]. However, since BK- and Ca^{2+}-channels are colocalized and BK-channel activation is regulated by local, microdomain Ca^{2+} below Ca^{2+}-channels [90], a simplification as done for L-type Ca^{2+}-channel inactivation can be done [37]. The microdomain Ca^{2+}-concentration was assumed to be proportional to the total Ca^{2+}-current $I_{Ca} = I_{CaL} + I_{CaPQ} + I_{CaT}$. The steady-state activation function for BK-channels was therefore assumed to depend on V only, since it was assumed proportional to the product

$$[-I_{Ca}(V) + B_{BK}] \cdot m_{BK,\infty}(V)$$

where B_{BK} denotes "basal", Ca^{2+}-independent, V-dependent activation, and $m_{BK,\infty}$ is a Boltzmann function as in Eq. 4.6. It was assumed that Ca^{2+}-dependent activation occurs instantaneously, while voltage-dependent activation follows Eq. 4.5 with time-constant $\tau_{mBK} = 2$ ms [81]. BK-currents were assumed not to inactivate. This was done partly since the inactivation function of BK channels in human β-cells is unknown, and partly since BK-currents rapidly repolarize the membrane potential in most simulations, hence deactivation due to repolarization happens faster ($\sim$10 ms) than inactivation at depolarized membrane potentials ($\sim$22 ms, [81]).

The BK-current is then expressed as

$$I_{BK} = \bar{g}_{BK} m_{BK} (V - V_K)(-I_{Ca}(V) + B_{BK}), \tag{4.9}$$

with parameters chosen to reproduce the I-V relationship for the iberiotoxin (a specific BK-channel blocker) sensitive K^+-current reported by [81] and shown in Figure 4.3C.

HERG Potassium-channels

The voltage-gated HERG potassium channels are present in human β-cells [86, 91]. The parameters of the Boltzmann activation and inactivation functions in [86] were used without modification. The time-constant of inactivation was estimated from [86] to be $\sim$50 ms, while activation was slower. Based on data from ERG channels expressed in Xenopus oocytes [92], the activation time-constant was set to 100 ms. From results in [86] a conductance of g_{HERG} $\sim$0.5 nS/pF can be calculated. However, g_{HERG} increases with the extracellular K^+ concentration [93]. Since in the experiments in [86] a relatively high extracellular K^+ concentration (40 mM) was used, a lower value of $g_{HERG} = 0.2$ nS/pF was used in the model.

4.2 My Contribution to the Model

In the previous Section, the first model of electrical activity in human β-cells was presented. The model included Na^+-channels, three types of Ca^{2+}-channels, an unspecified leak-current, and several K^+-channels: delayed rectifier (Kv) K^+-channels, large-conductance (BK) Ca^{2+}-sensitive K^+-channels, HERG K^+-channels as well as K(ATP)-channels. Recently evidence for small conductance (SK) Ca^{2+}-sensitive K^+-channels in human β-cells was published [9, 94], a current not included in the mathematical model.

Parameter			Ref.	Parameter			Ref.
V_K	-75	mV	[81]	V_{Na}	70	mV	$*$
V_{Ca}	65	mV	$*$	$g_{K(ATP)}$	0.015	nS/pF	[78]
g_{leak}	0.015	nS/pF	[78]	V_{leak}	-30	mV	+
g_{CaT}	0.050	nS/pF	[81]	τ_{hCaT}	7	ms	[81]
V_{mCaT}	-40	mV	[81]	n_{mCaT}	-4	mV	[81]
V_{hCaT}	-64	mV	[81]	n_{hCaT}	8	mV	[81]
g_{CaPQ}	0.170	nS/pF	[81]				
V_{mCaPQ}	-10	mV	[81]	n_{mCaPQ}	-10	mV	[81]
g_{CaL}	0.140	nS/pF	[81]	τ_{hCaL}	20	ms	$*$
V_{mCaL}	-25	mV	[81]	n_{mCaL}	-6	mV	[81]
V_{hCaL}	-42	mV	+ [87]	n_{hCaL}	6	mV	+ [87]
g_{Na}	0.400	nS/pF	[81]	τ_{hNa}	2	ms	[81]
V_{mNa}	-18	mV	[81]	n_{mNa}	-5	mV	[81]
V_{hNa}	-42	mV	[81]	n_{hNa}	6	mV	[81]
g_{Kv}	1.000	nS/pF	[81]	$\tau_{mKv,0}$	2	ms	[81]
V_{mKv}	0	mV	[81]	n_{mKv}	-10	mV	[81]
$\bar{g}_{BK}$	0.020	nS/pA	[81]	τ_{mBK}	2	ms	[81]
V_{mBK}	0	mV	[81]	n_{mBK}	-10	mV	[81]
B_{BK}	20	pA/pF	[81]	τ_{mHERG}	100	ms	[92]
g_{HERG}	0.200	nS/pF	+ [86]	τ_{hHERG}	50	ms	[86]
V_{mHERG}	-30	mV	[86]	n_{mCaL}	-10	mV	[86]
V_{hCaL}	-42	mV	[86]	n_{hCaL}	17.5	mV	[86]

Table 4.1: Default parameters for the first human β-cells model. ($*$ M. Braun, University of Oxford, UK, personal communications, 2010; + Adjusted.)

The previous model was shown to reproduce, depending on parameter values, spiking or rapid bursting electrical activity, which could be modified in accordance with a series of experiments by simulating pharmacological interventions such as ion channel blocking. These experiments were in general straightforward to interpret, also without a model. For example, the facts that blocking depolarizing Na^+- or Ca^{2+}-currents slowed or abolished electrical activity [81] are as one would expect.

The previous model for human β-cells was extended by including SK-channels and Ca^{2+} dynamics. The new model allowed to get insight in less intuitive experimental findings. The new model is then used to investigate paracrine effects of γ-aminobutyric acid (GABA) and muscarinic signaling on electrical activity. Finally, experimentally slow oscillations in electrical activity that might underlie pulsatile insulin secretion from human pancreatic islets will be shown, and by adding an oscillatory glycolytic component [95] to the electrophysiological model, such slow bursting patterns will be simulated.

4.2.1 Methods

Mathematical Modelling

The previously published Hodgkin-Huxley type model for human β-cells [84], explained in detail in the previous Section, was built on by including SK-channels. Since these channels are Ca^{2+}-sensitive and located at some distance from Ca^{2+}-channels [90], it was necessary to model Ca^{2+} dynamics in a submembrane layer controlling SK-channel activity.

The membrane potential V (measured in mV) develops in time (measured in ms) according to

$$\begin{aligned}\frac{dV}{dt} = -(&I_{SK} + I_{BK} + I_{Kv} + I_{HERG} + I_{Na} \\ &+ I_{CaL} + I_{CaPQ} + I_{CaT} + I_{K(ATP)} + I_{leak} + I_{GABAR}).\end{aligned} \tag{4.10}$$

All currents (measured in pA/pF), except the SK-current I_{SK} and the $GABA_A$ receptor mediated current I_{GABAR}, were already modeled.

SK-channels were assumed to activate instantaneously in response to Ca^{2+} elevations at the plasma membrane but away from Ca^{2+}-channels [90], and were modeled as [96]

$$I_{SK} = g_{SK}\frac{Ca_m^n}{K_{SK}^n + {Ca_m}^n}(V - V_K). \tag{4.11}$$

In human β-cells, flash-released Ca^{2+} triggered a ~10 pA current at a holding current of -60 mV, presumably through SK-channels [94]. Assuming that SK-channels were nearly saturated by Ca^{2+}, the maximal SK-conductance was estimated to be $g_{SK} \approx$ 10 pA/(-60 mV $-V_K$)/$C_m \approx$ 0.1 nS/pF. Where, C_m =10 pF is the capacitance of the plasma membrane [81].

In Eq. 4.11, Ca_m is the submembrane Ca^{2+} concentration ($[Ca^{2+}]_{mem}$; measured in μM), which was described by a single compartment model [97]

$$\begin{aligned}\frac{dCa_m}{dt} = f\alpha C_m(-I_{CaL} - I_{CaPQ} - I_{CaT})/Vol_m \\ - f(Vol_c/Vol_m)\left[B(Ca_m - Ca_c) + (J_{PMCA} + J_{NCX})\right],\end{aligned} \tag{4.12}$$

where f = 0.01 is the ratio of free-to-total Ca^{2+}, a = 5.18x10^{-15} mmol/pA/ms changes current to flux, and Vol_m and Vol_c are the volumes of the submembrane compartment and the bulk cytosol, respectively. B describes the flux of Ca^{2+} from the submembrane compartment to the bulk cytosol, J_{PMCA} is the flux through plasma membrane Ca^{2+}-ATPases, and J_{NCX} represents Ca^{2+} flux through the Na^+-Ca^{2+} exchanger.

Cytosolic Ca^{2+} (Ca_c; measured in μM) follows

$$\frac{dCa_c}{dt} = f[B(Ca_m - Ca_c) - J_{SERCA} + J_{leak}], \tag{4.13}$$

where J_{SERCA} describes SERCA pump-dependent sequestration of Ca^{2+} into the ER, and J_{leak} is a leak flux from the ER to the cytosol. Expressions and parameters for the Ca^{2+} fluxes are taken from [98].

The submembrane compartment volume was estimated based on the considerations of Klingauf and Neher [99], who found that a shell model (in contrast to a domain model) describes submembrane Ca^{2+} satisfactorily when the shell-depth is chosen correctly. The Ca^{2+} dynamics between channels can be estimated from a shell model at a depth of ~23% of the distance to a Ca^{2+}-channel. In mouse β-cells the interchannel distance has been estimated to be ~1200 nm [29]. Moreover, SK-channels are located >50 nm from Ca^{2+}-channels [90].

Based on these considerations, the submembrane space controlling SK-channels was modeled as a shell of depth ~190 nm. The radius of a human β-cell is ~13 μm, which gives cell volume (Vol_c), shell volume (Vol_m) and internal surface area (A_m) of the shell, of

$$Vol_c = 1.15 \text{ pL} = 1150\ \mu\text{m}^3, \quad Vol_m = 0.1 \text{ pL}, \quad A_m = 530\ \mu\text{m}^2. \tag{4.14}$$

The flux-constant B can then be calculated as [100]

$$B = D_{Ca}\frac{A_m}{Vol_c d_m}, \tag{4.15}$$

where d_m is a typical length scale. d_m was set to 1 μm, which together with the diffusion constant for Ca^{2+}, $D_{Ca} = 220\ \mu m^2/s$ [99, 101], gives $B = 0.1\ ms^{-1}$.

In human β-cells, GABA activates $GABA_A$ receptors, which are ligand-gated Cl^--channels. The current carried by $GABA_A$ receptor was modeled as a passive current with the expression

$$I_{GABAR} = g_{GABAR}(V - V_{Cl}), \tag{4.16}$$

where g_{GABAR} is the $GABA_A$ receptor conductance, and $V_{Cl} = -40$ mV is the chloride reversal potential [9]. g_{GABAR} was estimated from the findings that 1 mM GABA evokes a current of 9.4 pA/pF (but with substantial cell-to-cell variation) at a holding potential of -70 mV [102], which yields a conductance of ∼0.3 nS/pF. To simulate the changes in firing patterns evoked by lower GABA concentrations (10 or 100 μM) [102], the does-response curve [103] for the $\alpha 2\beta 3\gamma 2$ subunits, which are the most highly expressed subunits in human β-cells [102], were taken into consideration. At 10 μM the GABA-evoked current is >10-fold smaller compared to 1 mM GABA, thus g_{GABAR} was set to 0.02 nS/pF. At 100 μM, the reduction is about 2-fold compared to 1 mM. $g_{GABAR} = 0.10$ nS/pF was used to simulate application of 100 μM GABA.

To investigate slow electrical patterns, a glycolytic component presented in [95] was added. It drives ATP levels and K(ATP) channel activity. The glycolytic subsystem can oscillate due to positive feedback on the enzyme phosphofructokinase (PFK) from its product fructose-1,6-bisphosphate (FBP). The glycolytic equations are

$$\frac{d\ G6P \cdot F6P}{dt} = V_{GK} - V_{PFK}, \tag{4.17}$$

$$\frac{d\ FBP}{dt} = V_{PFK} - V_{FBA}, \tag{4.18}$$

$$\frac{d\ DHAP \cdot G3P}{dt} = 2V_{FBA} - V_{GAPDH}, \tag{4.19}$$

where V_{GK} is the rate of glucokinase, which phosphorylates glucose to glucose-6-phosphate (G6P). G6P is assumed to be in equilibrium with fructose-6-phosphate (F6P), the substrate for PFK, and G6P·F6P is the sum of G6P and F6P. V_{PFK}

is the rate of PFK producing FBP, which is subsequently removed by fructose-bisphosphate aldolase (FBA), which produces glyceraldehyde-3-phosphate (G3P) and dihydroxyacetone-phosphate (DHAP) with rate V_{FBA}. DHAP and G3P are assumed to be in equilibrium, and DHAP·G3P indicates their sum. Finally, G3P serves as substrate for glyceraldehyde-3-phosphate dehydrogenase (GAPDH with rate V_{GAPDH}), which via the lower part of glycolysis eventually stimulates mitochondrial ATP production. A phenomenological variable a that mimics ATP levels was introduced and model by

$$\frac{da}{dt} = V_{GAPDH} - k_A\, a, \tag{4.20}$$

The K(ATP) conductance depends inversely on a, and was modeled as

$$g_{K(ATP)} = \hat{g}_{K(ATP)}/(1+a). \tag{4.21}$$

Simulations were done in XPPAUT with the cvode solver, except the stochastic simulation, which was performed with the implicit backward Euler method.

Default parameters are given in Table 4.2.

Experiments

Human pancreatic islets were obtained with ethical approval and clinical consent from non-diabetic organ donors. All studies were approved by the Human Research Ethics Board at the University of Alberta. The islets were dispersed into single cells by incubation in Ca^{2+} free buffer and plated onto 35 mm plastic Petri dishes. The cells were incubated in RPMI 1640 culture medium containing 7.5 mM glucose for >24 h prior to the experiments. Patch-pipettes were pulled from borosilicate glass to a tip resistance of 6-9 MΩ when filled with intracellular solution. The membrane potential was measured in the perforated-patch whole-cell configuration, using an EPC-10 amplifier and Patchmaster software (HEKA, Lambrecht, Germany). The cells were constantly perifused with heated bath solution during the experiment to maintain a temperature of 31-33^{o}C. The extracellular solution consisted of (in mM) 140 NaCl, 3.6 KCl, 0.5 $MgSO_4$, 1.5 $CaCl_2$, 10 HEPES, 0.5 NaH_2PO_4, 5 $NaHCO_3$ and 6 glucose (pH was adjusted to 7.4 with NaOH). The pipette solution contained (in mM) 76 K_2SO_4, 10 KCl, 10 NaCl, 1 $MgCl_2$, 5 HEPES (pH 7.35 with KOH) and 0.24 mg/ml amphotericin B. β-cells were identified by immunostaining (18 out of 28 cells) or by size when immunostaining was not possible (cell capacitance >6 pF,

Parameter			Ref.	Parameter			Ref.
V_K	-75	mV	[81]	V_{Na}	70	mV	[84]
V_{Ca}	65	mV	[84]	V_{Cl}	-40	mV	[9]
g_{SK}	0.1	nS/pF	[94]	K_{SK}	0.57	μM	[96]
n	5.2		[96]				
$\bar{g}_{BK}$	0.020	nS/pA	[81]	τ_{mBK}	2	ms	[81]
V_{mBK}	0	mV	[81]	n_{mBK}	-10	mV	[81]
B_{BK}	20	pA/pF	[81]				
g_{Kv}	1.000	nS/pF	[81]	$\tau_{mKv,0}$	2	ms	[81]
V_{mKv}	0	mV	[81]	n_{mKv}	-10	mV	[81]
g_{HERG}	0	nS/pF	+ [84, 86]				
V_{mHERG}	-30	mV	[86]	n_{mHERG}	-10	mV	[86]
V_{hHERG}	-42	mV	[86]	n_{hHERG}	17.5	mV	[86]
τ_{mHERG}	100	ms	[92]	τ_{hHERG}	50	ms	[86]
g_{Na}	0.400	nS/pF	[81]	τ_{hNa}	2	ms	[81]
V_{mNa}	-18	mV	[81]	n_{mNa}	-5	mV	[81]
V_{hNa}	-42	mV	[81]	n_{hNa}	6	mV	[81]
g_{CaL}	0.140	nS/pF	[81]	τ_{hCaL}	20	ms	[84]
V_{mCaL}	-25	mV	[81]	n_{mCaL}	-6	mV	[81]
g_{CaPQ}	0.170	nS/pF	[81]				
V_{mCaPQ}	-10	mV	[81]	n_{mCaPQ}	-6	mV	[81]
g_{CaT}	0.050	nS/pF	[81]	τ_{hCaT}	7	ms	[81]
V_{mCaT}	-40	mV	[81]	n_{mCaT}	-4	mV	[81]
V_{hCaT}	-64	mV	[81]	n_{hCaT}	8	mV	[81]
$g_{K(ATP)}$	0.010	nS/pF	[78]	g_{GABAR}	0	nS/pF	[102, 103]
g_{leak}	0.015	nS/pF	[78]	V_{leak}	-30	mV	[84]
$J_{SERCA,\max}$	0.060	μM/ms	+ [98]	K_{SERCA}	0.27	μM	[98]
$J_{PMCA,\max}$	0.021	μM/ms	[98]	K_{PMCA}	0.50	μM	[98]
J_{leak}	0.00094	μM/ms	[98, 104]	$J_{NCX,0}$	0.01867	ms^{-1}	[98, 104]
f	0.01			Vol_c	1.15	$\times 10^{-12}$ L	
B	0.1	ms^{-1}		Vol_m	0.1	$\times 10^{-12}$ L	
α	5.18×10^{-15} μmol/pA/ms						
k_A	0.0001	ms^{-1}	+	$\hat{g}_{KATP}$	0.050	nS/pF	+

Table 4.2: Default parameters of the new model unless mentioned otherwise. Parameter values are based on the indicated literature references (+ indicates adjusted parameters). All glycolytic parameters are taken without modification from reference [95], where a discussion of their values based on experimental data can be found. HERG channel conductance, g_{HERG}, was set to zero in the new model to investigate whether SK-channels can substitute for HERG channels, e.g., in driving bursting.

[81]). Tetrodotoxin (TTX) and ω-agatoxin IVA were purchased from Alomone Labs (Jerusalem, Israel), UCL-1684 was obtained from R&D Systems (Minneapolis, MN), TRAM-34 from Sigma-Aldrich (Oakville, ON, Canada). Figures with experimental responses to ion channel antagonists (Figs. 4.4, 4.6, 4.7 and 4.8) show recordings from the same cell before (ctrl) and after application of the blocker.

4.2.2 Heterogeneous Responses: Experiments and Model Interpretation

SK-Channels

When stimulated by glucose, human β-cells show electrical activity [78, 81]. Human β-cells express SK-channels [9, 94], which might participate in controlling electrical activity.

The new model with standard parameters produces spiking electrical activity (Fig. 4.4A), which is virtually unaffected by setting the SK-conductance g_{SK}=0 nS/pF simulating SK-channels block. This model prediction was confirmed by our experimental data, and was also observed in at least one cell by Jacobson et al. [94]. Fig. 4.4B shows an example of spiking electrical activity in a human β-cell stimulated by 6 mM glucose, where addition of the SK1-3 channel blocker UCL 1684 (0.2 μM) did not affect the spiking pattern. Unchanged or marginal effects on electrical activity were also seen with a specific SK4 channel antagonist, TRAM-34 (1 μM, Fig. 4.4C). However, in some cells TRAM-34 application increased the action potential dramatically (Fig. 4.4D) in agreement with observations with the SK-channel antagonist apamin [94]. Note that before SK-channel block, the cell in Fig. 4.4D was almost quiescent, and fired action potentials very infrequently and randomly. This increase in spike frequency can be simulated by a stochastic version of the model. For the stochastic simulation in Fig. 4.4E, "conductance noise" [105] in the K(ATP) current was included by multiplying $I_{K(ATP)}$ by a stochastic factor (1+0.2 Γ_t), where Γ_t is a standard Gaussian white-noise process with zero mean and mean square $\langle \Gamma_t, \Gamma_s \rangle = \delta(t-s)$, see also [106–108].

By including noise in the K(ATP) current, an otherwise silent cell produces infrequent action potentials evoked by random perturbations (Fig. 4.4E). When the SK-conductance is set to 0 nS/pF, the cell starts rapid action potential firing driven by the underlying deterministic dynamics. The model analysis indicates that this

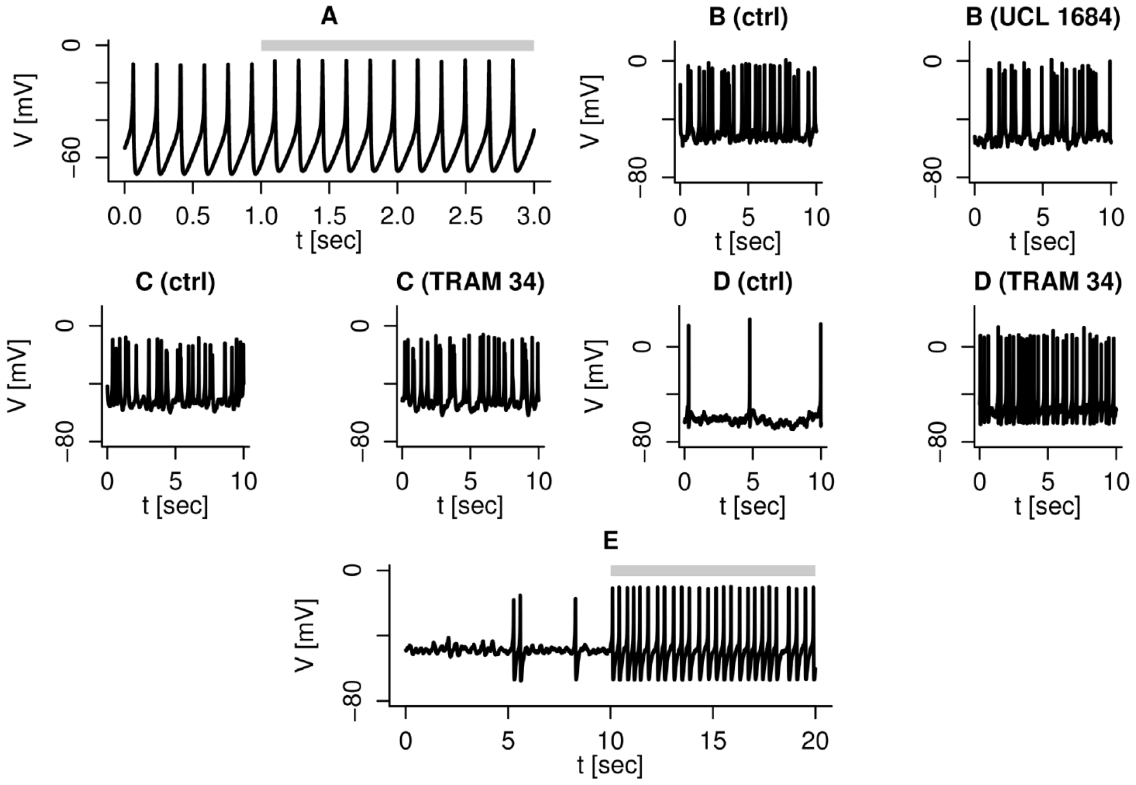

Figure 4.4: **Heterogeneous responses to SK-channel block**. Note the differences in time-scales. A) Simulation, with default parameters, showing no effect of SK-channels block ($g_{SK} = 0$ nS/pF during the period indicated by the gray bar). B) Experimental recording of spiking electrical activity in the same human β-cell before (left) and during (right) application of the SK1-3 channel antagonist UCL-1684 (0.2 μM). C) Experimental recording of spiking electrical activity in the same human β-cell before (left) and during (right) application of the SK4 channel antagonist TRAM-34 (1 mM), which had little effect on the action potential frequency in this cell. D) Experimental recording of spiking electrical activity in the same human β-cell before (left) and during (right) application of the SK4 channel antagonist TRAM-34 (1 μM), which accelerated the action potential frequency in this cell. E) Stochastic simulation reproducing the dramatic effect of SK-channels block ($g_{SK} = 0$ nS/pF during the period indicated by the gray bar). Other parameters took default values, except $g_{KATP} = 0.0175$ nS/pF.

mechanism only works if the cell is very near the threshold for electrical activity in the absence of the SK-channel antagonist. Düfer et al. [109] suggested a similar, important role for SK4 channels in promoting electrical activity in murine β-cells at subthreshold glucose concentrations. Summarizing, cell-to-cell heterogeneity can explain the differences seen in the electrophysiological responses to SK-channel antagonists.

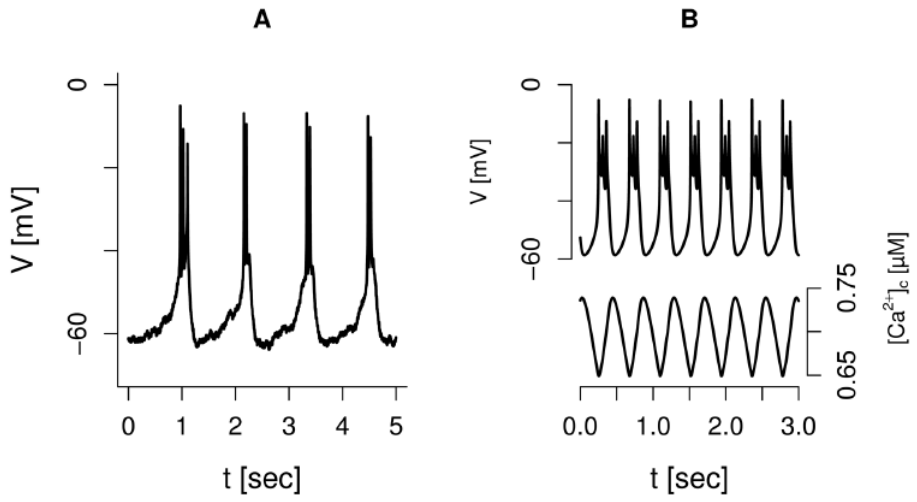

Figure 4.5: **Bursting in human β-cell**. A) Experimental recording of rapid bursting in a human β-cell. B) Simulation of bursting driven by $[Ca^{2+}]_c$ via SK-channels. Default parameters except $g_{SK} = 0.03$ nS/pF, $g_{Kv} = 0.25$ nS/pF, $nx_{PQ} = -10$ mV.

In addition to spiking electrical activity, human β-cells often show rapid bursting, where clusters of a few action potentials are separated by hyperpolarized silent phases [9, 78–80, 110] (Fig. 4.5A). The model presented here can also reproduce this behavior (Fig. 4.5B) as could the previous version of the model, where the alternations between silent and active phases were controlled by HERG-channels. In contrast, in the present version of the model the rapid burst pattern (Fig. 4.5B, upper trace) can be controlled by SK-channels, which in turn are regulated by $[Ca^{2+}]_{mem}$ and ultimately by bulk cytosolic Ca^{2+} levels ($[Ca^{2+}]_c$). The simulated cytosolic Ca^{2+} concentration shows the characteristic sawtooth pattern (Fig. 4.5B, lower trace) of a slow variable underlying bursting [111, 112]. Thus, as in the pioneering model by Chay and Keizer [71], $[Ca^{2+}]_c$ increases during the active phase and activates SK-channels, which eventually repolarize the cell. During the silent phase $[Ca^{2+}]_c$ decreases and SK-channels close, allowing another cycle to occur.

Sodium-channels

Blocking voltage-dependent Na^+-channels in human β-cells showing spiking electrical activity with tetrodotoxin (TTX) typically reduces the action potential amplitude by ∼10 mV, and broadens its duration [80, 81, 110] (Fig. 4.6A).

The previous version of the model could reproduce these results, though the reduction in peak voltage was slightly less than observed experimentally. The inclusion of SK-channels in the model leads to a greater reduction in the spike amplitude (Fig. 4.6B, upper trace) when Na^+-channels are blocked. This improvement is because of a mechanism where the slower upstroke in the presence of Na^+-channel blockers allows submembrane Ca^{2+} to build up earlier and to higher concentrations (Fig. 4.6B, lower trace), and consequently to activate more SK-channels, which in turn leads to an earlier repolarization reducing the action potential amplitude. In other experiments (Fig. 4.6C) [79], TTX application suppresses action potential firing. In agreement, simulated spiking electrical activity can be suppressed by TTX application if the cell is less excitable because of, for example, smaller Ca^{2+}-currents (Fig. 4.6D, upper, black trace). Before TTX application, the simulated cell had less hyperpolarized inter-spike membrane potential (∼-61 mV; Fig. 4.6D) compared to the simulation with default parameters (∼-70 mV, Fig. 4.6B). This finding is in accordance with experimental recordings (compare Fig. 4.6A and 4.6C). The cessation of action potential firing leads to a reduction in simulated $[Ca^{2+}]_{mem}$ (Fig. 4.6D, lower, black trace). The model predicts that spiking, electrical activity can continue in presence of TTX even in less excitable cells, e.g., with lower depolarizing Ca^{2+}-currents, if the hyperpolarizing K(ATP)-current is sufficiently small (Fig. 4.6D, upper, gray trace). In this case, $[Ca^{2+}]_{mem}$ is nearly unchanged (Fig. 4.6D, lower, gray trace). Hence, it is the relative sizes of the depolarizing and hyperpolarizing currents that determine whether TTX application silences the cell or allows the cell to remain in a region where action potential firing continues. The model thus predicts that in some cells, which stop firing action potentials in the presence of TTX, increased glucose concentrations or sulfonylureas (K(ATP)-channel antagonists) could reintroduce spiking electrical activity.

More surprisingly, TTX application can change spiking electrical activity to rapid bursting in some cells (Fig. 4.6E). This behavior can also be captured by the model (Fig. 4.6F). To simulate this behavior it was necessary to increase the size of the Na^+-current. Without TTX, the big Na^+-current leads to large action potentials,

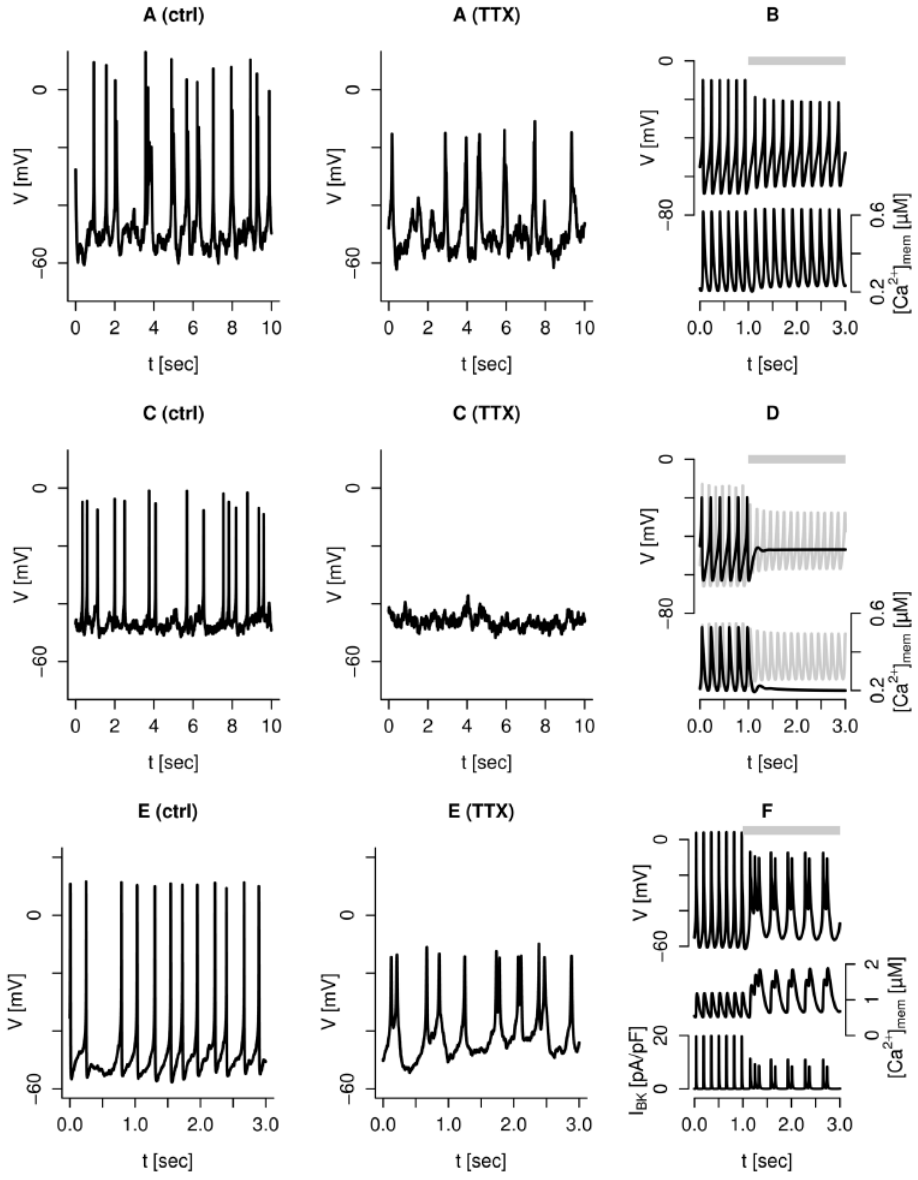

Figure 4.6: **Tetrodotoxin (TTX, 0.1 μg/ml) has different effects on electrical activity in human β-cells**. A) TTX caused a reduction in action potential amplitude in this human β-cell. B) Simulation with default parameters showing V (upper trace, left axis) and $[Ca^{2+}]_{mem}$ (lower trace, right axis), reproducing the data in panel A. C) TTX abolished action potential firing in this human β-cell. D) Simulations of V and $[Ca^{2+}]_{mem}$ with default parameters except $g_{CaL} = 0.100$ nS/pF. With default K(ATP)-channel conductance $g_{KATP} = 0.010$ nS/pF, the simulation reproduces the data in panel C (black traces). When $g_{KATP} = 0.002$ nS/pF, the model shows continued firing with Na^+-channel block (gray traces). E) TTX changed spiking into rapid bursting electrical activity in this human β-cell. F) Simulation showing V (upper), $[Ca^{2+}]_{mem}$ (middle), and I_{BK} (lower), reproducing the data in panel E. Parameters took default values, except $g_{Na} = 0.7$ nS/pF, $\tau_{hNa} = 3$ ms, $g_{Kv} = 0.25$ nS/pF, $g_{SK} = 0.023$ nS/pF, $g_{leak} = 0.012$ nS/pF, and $nx_{PQ} = -10$ mV. The extracellular glucose concentration was 6 mM in all experiments. Each couple of experimental traces (panels A, C and E) is from the same human β-cell before (left) and during (right) application of TTX. In the simulations, the Na^+-channel conductance g_{Na} was set to 0 nS/pF during the period indicated by the gray bars.

which activate sufficient BK-current to send the membrane potential back to the hyperpolarized state, allowing a new action potential to form. With Na^+-channels blocked, there is insufficient depolarizing current to allow full action potentials to develop. In consequence, less BK-current is activated (Fig. 4.6F, lower trace), and the membrane potential enters a regime with more complex dynamics where smaller spikes appear in clusters from a plateau of ∼-40 mV. The change to bursting activity leads to a notable increase in simulated $[Ca^{2+}]_{mem}$ (Fig. 4.6F, middle trace).

Calcium-channels

High-voltage activated L- and P/Q-type Ca^{2+}-currents are believed to be directly involved in exocytosis of secretory granules in human β-cells [78, 81, 97, 113]. Blocking L-type Ca^{2+}-channels suppresses electrical activity [81], which is reproduced by the model (Fig. 4.7A), and the lack of electrical activity is likely the main reason for the complete absence of glucose stimulated insulin secretion in the presence of L-type Ca^{2+}-channel blockers [81]. Thus, L-type Ca^{2+}-channels participate in the upstroke of action potentials and increases excitability of human β-cells.

In contrast, and surprisingly, application of the P/Q-type Ca^{2+}-channel antagonist ω-agatoxin IVA does not block or slow down electrical activity, but leads to an increased spike frequency (Fig. 4.7B). Electrical activity continues also in our model simulations of P/Q-type channel block with slightly increased spike frequency (Fig. 4.7C). Reduced Ca^{2+} entry leads to lower peak Ca^{2+} concentrations in the submembrane space ($[Ca^{2+}]_{mem}$; Fig. 4.7D). As a consequence, less hyperpolarizing SK-current is activated (Fig. 4.7E), which leads to an increase in spike frequency (Fig. 4.7C). Hence, the reduction in excitability caused by blockage of the P/Q-type Ca^{2+}-current can be overruled by the competing increase in excitability due to the smaller SK-current. Experimentally, ω-agatoxin IVA application reduced the action potential amplitude slightly in 3 of 4 cells (by 2.0-4.3 mV), a finding that was quantitatively reproduced by the model, although the reduction was larger (∼7.5 mV in Fig. 4.7C). A direct conclusion from Fig. 4.7B is that the P/Q-type Ca^{2+}-current is not needed for the action potential upstroke, unlike the L-type current, probably because of the fact that P/Q-type channels activate at higher membrane potentials than L-type channels. The fact that electrical activity persists with P/Q-type Ca^{2+}-channels blocked, albeit with lower peak $[Ca^{2+}]_{mem}$, could underlie the finding that ω-agatoxin IVA only partly inhibits insulin secretion [81].

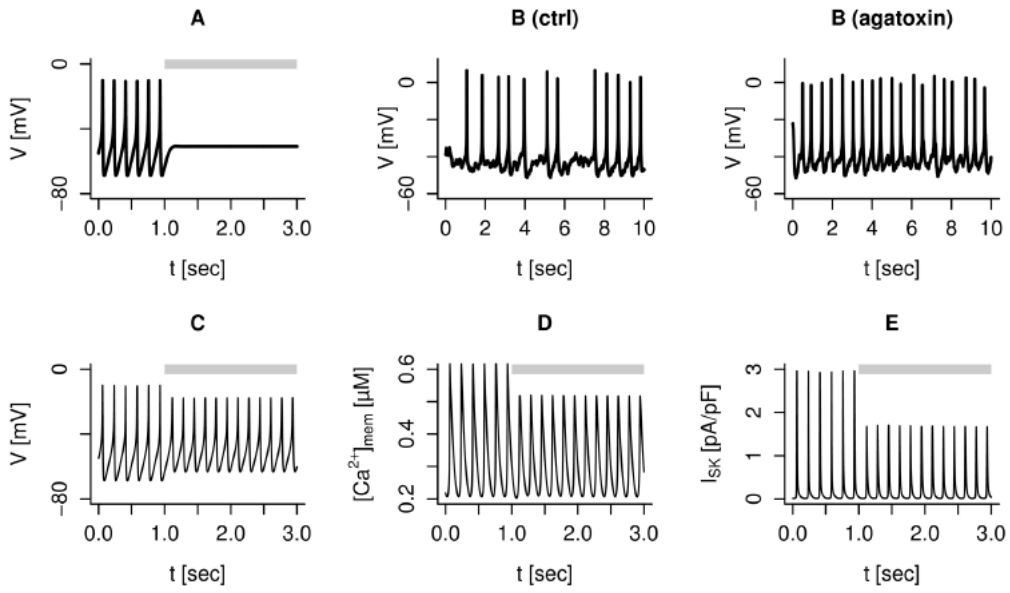

Figure 4.7: **Block of L- and P/Q-type Ca^{2+}-channels affects electrical activity differently**. A) Spiking electrical activity is suppressed by L-type Ca^{2+}-channel block in the model with default parameters, and $g_{CaL} = 0$ nS/pF during the period indicated by the gray bar. B) Spiking electrical activity is accelerated by the application of ω-agatoxin IVA in human β-cells. Recordings from the same human β-cell in 6 mM extracellular glucose before (left) and during (right) application of 200 nM ω-agatoxin IVA. C) Model simulation with default parameters of the membrane potential during spiking electrical activity under control conditions and after blockage of P/Q-type Ca^{2+}-channels ($g_{PQ} = 0$ nS/pF during the period indicated by the gray bar). D) In the model, the peak submembrane Ca^{2+}-concentration $[Ca^{2+}]_{mem}$ is lower when P/Q-type channels are blocked. E) The reduced $[Ca^{2+}]_{mem}$ activate less SK-current when P/Q-type channels are blocked.

Paracrine Effects on Electrical Activity

The neurotransmitter γ-aminobutyric acid (GABA) is secreted from pancreatic β-cells, and has been shown to stimulate electrical activity in human β-cells [102]. In human β-cells, GABA activates $GABA_A$ receptors, which are ligand-gated Cl^- channels, thus creating an additional current. Notably, the Cl^- reversal potential in human β-cells is less negative than in many neurons, and positive compared to the β-cell resting potential, which means that Cl^- currents, such as the $GABA_A$ receptor current, stimulate action potential firing in β-cells. Hence, GABA is a excitatory transmitter in β-cells, in contrast to its usual inhibitory role in neurons. The addition of GABA was simulated by raising the $GABA_A$ receptor conductance.

In a silent model cell with a rather large K(ATP)-conductance, simulated GABA application leads to a single action potential where after the membrane potential settles at ∼-45 mV (Fig. 4.8A), in close correspondence with the experimental results [102]. In an active cell, the simulation of activation of $GABA_A$ receptors leads to a minor depolarization and increased action potential firing (Fig. 4.8B), as found experimentally [102].

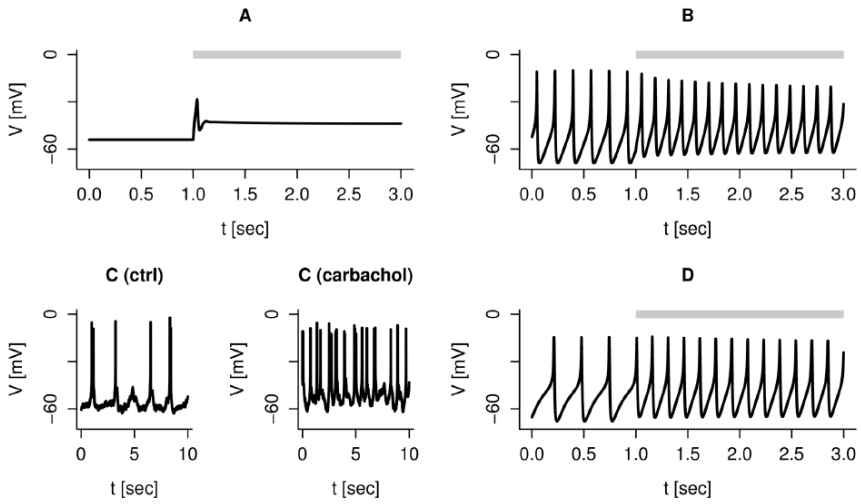

Figure 4.8: **Paracrine effects on electrical activity**. A) Simulation of application of 100 μM GABA to a silent cell (reproducing Fig. 7A in [102]). Default parameters except $g_{KATP} = 0.021$ nS/pF. GABA application was simulated by setting g_{GABAR} to 0.1 nS/pF during the period indicated by the gray bar. B) Simulation of application of 10 μM GABA to an active cell (reproducing Fig. 7B in [102]). GABA application was simulated by setting g_{GABAR} to 0.020 nS/pF during the period indicated by the gray bar. Other parameters took default values. C) Experimental recording of spiking electrical activity in the same human β-cell before (left) and during (right) application of carbachol (20 μM). D) Simulation of accelerated action potential firing due to carbachol application. Default parameters except $g_{KATP} = 0.016$ nS/pF. Carbachol application was simulated by increasing g_{leak} to 0.030 nS/pF during the period indicated by the gray bar.

Another neurotransmitter, acetylcholine, might also play a paracrine role in human pancreatic islets, where it is released from α-cells, and activates muscarinic receptors in β-cells [114]. Muscarinic receptor activation by acetylcholine triggers a voltage-insensitive Na^+-current in mouse pancreatic β-cells [115], and similarly, the muscarinic agonist carbachol activates nonselective Na^+ leak channels (NALCN) in the MIN6 β-cell line [116]. Based on these findings, it was speculated that muscarinic activation of NACLN currents in human β-cells might participate in the positive effect of acetylcholine and carbachol on insulin secretion [9]. Experimen-

tally, carbachol (20 μM) was found to accelerate action potential firing (Fig. 4.8C). The hypothesis of a central role of leak current activation was tested by increasing the leak conductance in the model to simulate carbachol application, which caused accelerated action potential firing. The simulation thus reproduced the experimental data, and lends support to the hypothesis that carbachol and acetylcholine can accelerate action potential firing via muscarinic receptor-dependent stimulation of NALCN currents [9].

Slow Oscillations

The new model was finnaly used to address the origin of slow rhythmic patterns of electrical activity in human β-cells (Fig. 4.9A) [9, 117], which likely underlie slow oscillations in intracellular Ca^{2+} [83, 118] and pulsatile insulin release [119, 120]. Based on accumulating evidence obtained in rodent islets [121, 122], it was speculated that oscillations in metabolism could drive these patterns [84]. In support of this hypothesis, oscillations in ATP levels with a period of 3-5 minutes have been observed in human β-cells [123, 124]. By adding a glycolytic component [95], which can oscillate due to positive feedback on the central enzyme phosphofructokinase (PFK), the new model can indeed simulate such periodic modulation of the electrical pattern, where action potential firing is interrupted by long silent, hyperpolarized periods, which drives slow Ca^{2+} oscillations (Fig. 4.9D-E).

4.2.3 Discussion

Human β-cells show complex and heterogeneous electrophysiological responses to ion channel antagonists. It can therefore sometimes be difficult to reach clear conclusions regarding the participation of certain ion channels in the various phases of electrical activity, in particular since some of the electrophysiological responses are nonintuitive as shown in the previous Section. A deeper understanding of the role of ion channels in electrical activity and insulin secretion could have important clinical benefits, since it might help in the development of new anti-diabetic drugs.

The mathematical modeling can help in interpreting various electrophysiological responses, and in particular, to study the effect of competing effects and cell heterogeneity. The role of SK-channels in human β-cells is still not clear. We (Fig. 4.4) and others [94] have found heterogeneous electrophysiological responses to SK-channel antagonists. Our model suggests that these differences can be caused by underlying

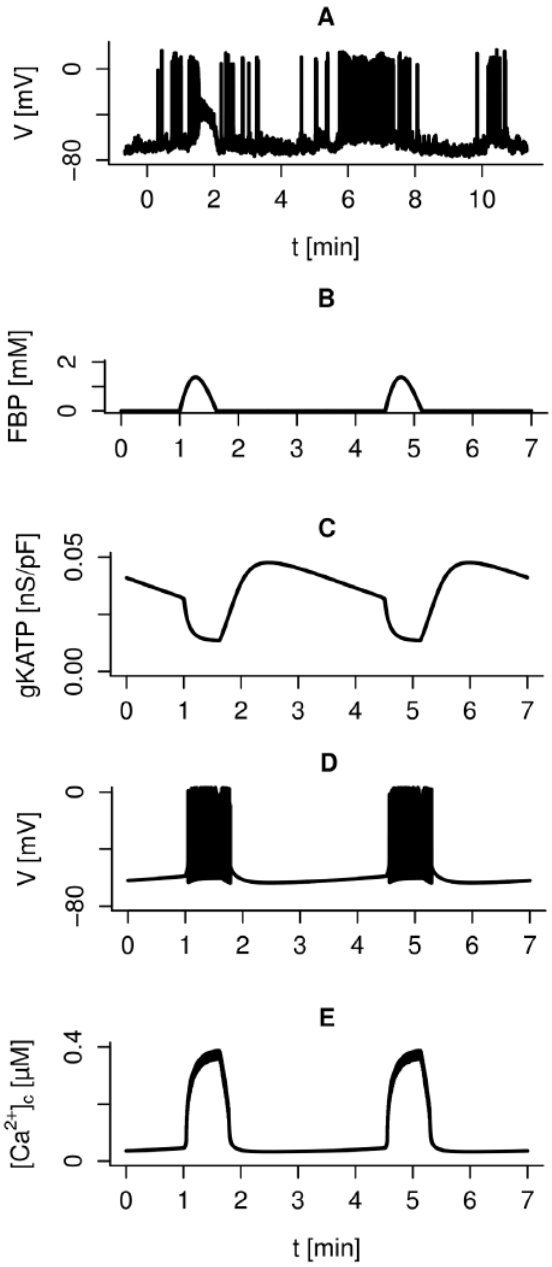

Figure 4.9: **Metabolically driven slow waves of electrical activity and Ca^{2+} oscillations**. A) Experimental recording of slow oscillations in action potential firing in a human β-cell exposed to 10 mM glucose. B-D) Simulation of slow bursting driven by glycolytic oscillations with glucose concentration $G = 10$ mM and default parameters, except $g_{Kv} = 0.2$ nS/pF, $g_{SK} = 0.02$ nS/pF, $g_{BK} = 0.01$ nS/pF. Oscillations in glycolysis create pulses of FBP (B), which via ATP production modulates K(ATP) channels in a periodic fashion (C). The rhythmic changes in K(ATP) conductance drives slow patterns of electrical activity (D), which causes oscillations in the intracellular Ca^{2+} concentration (E).

variations in cell excitability: less excitable β-cells that produce action potentials evoked mostly by stochastic channel dynamics show a clear increase in action potential frequency when SK-channels are blocked (Fig. 4.4DE). In contrast, spiking electrical activity in very active cells is driven by the deterministic dynamics caused by ion channel interactions, and is nearly unchanged by SK-channel blockers (Fig. 4.4A-C). Furthermore, the rapid bursting activity can be driven by $Ca^{2+}$and SK-channels (Fig. 4.5), which could add a complementary mechanism to HERG-channel dynamics, as in the previous version of the model, for the control of rapid bursting.

The wide range of responses to TTX could be accounted for by a single model but with different parameters, i.e., differences in the relative size of the various currents. A peculiar finding is the qualitative change from spiking to rapid bursting seen in some cells (Fig. 4.6E). We suggest that this happens in human β-cells with large Na^{+}-currents. The blockage of this depolarizing current reduces the amplitude of the action potentials, and as a consequence, the size of the hyperpolarizing BK-current. Under the right conditions, the combination of these competing events allows the membrane potential to enter a bursting regime controlled by SK- and/or HERG-channels (Fig. 4.6F). Interestingly, it has been found that TTX reduces insulin secretion evoked by 6 mM glucose greatly, but at glucose levels of 10-20 mM, the effect of TTX on secretion is smaller [80, 81, 110]. Based on the simulations showing that less excitable cells cease to fire in the presence of TTX (Fig. 4.6D, black traces), but that lower $g_{K(ATP)}$ can reintroduce spiking activity (Fig. 4.6D, gray traces), it might be concluded that at low, near threshold glucose levels TTX abolishes electrical activity in many cells, which reduces the $[Ca^{2+}]_{\mathrm{mem}}$ and consequently insulin secretion greatly (Fig. 4.6D, black traces). At higher glucose concentrations, β-cells have lower K(ATP)-conductance and in some of the cells that stop firing in low glucose concentration the effect of TTX on electrical activity and $[Ca^{2+}]_{\mathrm{mem}}$ is smaller (Fig. 4.6D, gray traces). Hence, more β-cells remain active in the presence of TTX at high than at low glucose levels. Consequently, insulin secretion is more robust to TTX at higher glucose concentrations.

Similarly, insulin release is more affected by the P/Q-type Ca^{2+}-channel blocker ω-agatoxin IVA at 6 mM ($\sim$-71%) than at 20 mM ($\sim$-31%) glucose [81]. This is in contrast to L-type Ca^{2+}-channel antagonists, which abolish insulin secretion at both high (15-20 mM) and low (6 mM) glucose concentrations [78, 81, 110]. These results concerning L-type Ca^{2+}-channel block are easily explained by the fact that L-

type channel activity is necessary for action potential generation [81] (Fig. 4.7A). In contrast, we showed that electrical activity in human β-cells not only persists, but is accelerated by ω-agatoxin IVA (Fig. 4.7B). The counter-intuitive finding of increased excitability and electrical activity when the depolarizing P/Q-type Ca^{2+}-current is blocked by ω-agatoxin IVA can be accounted for by an even greater reduction in the hyperpolarizing SK-current due to reduced Ca^{2+}-influx and consequently lower $[Ca^{2+}]_{mem}$.

Our mathematical modeling confirmed that GABA released from human β-cells can have a role as a positive feedback messenger. GABA application has been shown to depolarize both silent and active human β-cells [102], which was reproduced. A detailed characterization of $GABA_A$ receptor currents would refine the analysis presented here.

Data from mouse β-cells [115] and the MIN-6 β-cell line [116] suggest that muscaric agonists such as carbachol and acetylcholine stimulate insulin secretion partly by activating NACLN currents. Using the new version of the model it is possible to translate this finding to the human scenario, thus testing the hypothesis that this mechanism is also operating in human β-cells [9]. The simulations confirmed that increased leak currents can underlie the change in electrical activity found experimentally (Fig. 4.8C). The incretin hormone GLP-1 has also been shown to act partly via activation of leak channels [125], a mechanism which might be involved in activating otherwise silent β-cells [84, 126, 127]. These results suggest that leak currents could play important roles in controlling electrical activity in β-cells, and potentially be pharmacological targets. Further studies are clearly needed to investigate these questions.

By adding an oscillatory glycolytic component to the model, it is also possible to simulate slow rhythmic electrical activity patterns To date, there is no evidence of oscillations in glycolytic variables in human (or rodent) β-cells or islets, but ATP levels have been found to fluctuate rhythmically also in human β-cells [123, 124], supporting the idea of metabolism having a pacemaker role. In agreement, data from rodent β-cells show accumulating evidence for oscillations in metabolism playing an important role in controlling pulsatile insulin secretion [121, 122]. It will be interesting to see if these findings in rodents are applicable to human β-cells.

Regarding the model development, the inclusion of SK-channels in the model provided insight that was not within reach with the previous version of the model

[84]. Besides the direct investigation of the role of SK-channels, the acceleration in action potential firing seen with P/Q-type Ca^{2+}channel blockers (Fig. 4.4) can not be reproduced by the older version of the model without SK-channels [84]. Moreover, considering the effect of TTX on spike amplitude, a better correspondence between experiments and simulations was found with SK-channels included in the model. To model SK-channel activation accurately, a special effort was made to describe $[Ca^{2+}]_{mem}$ carefully. Submembrane Ca^{2+} responds rapidly to an action potential, while $[Ca^{2+}]_c$ integrates many action potentials. The rapid submembrane dynamics has important consequences for the study of the role of SK-channels in spiking electrical activity, e.g., it was crucial for explaining the larger effect of TTX on spike amplitude in this version of the model. Most models of electrical activity in rodent β-cells do not include a submembrane Ca^{2+} compartment, but these models were typically built to explain the slow bursting patterns seen in rodent islets with a period of tens of seconds. For these long time scales, the rapid dynamics in the submembrane compartment is not important. In contrast, the situation is different in human β-cells with their faster dynamics.

4.3 Further Development to the Model

This last Section of the Chapter is dedicated to an interesting and recent further development of the model, which consisted in the inclusion of the inwardly rectifying potassium channels. In particular, the inwardly rectifying Kir2.1 potassium channels are well-known to control cardiac electrical activity, e.g., by stabilizing the interspike interval [128]. The KCNJ2 gene coding for Kir2.1 channels is widely expressed [129], also in human pancreatic islets and β-cells (Beta-Cell Gene Atlas, `www.t1dbase.org/page/AtlasHome`, [130]). Hence, Kir2.1 currents might play a role in shaping action potential firing in human β-cells.

The previous versions of the model tended to fire action potentials too rapidly compared to experiments, which might indicate that the model was still incomplete. Since the Kir2.1 current tends to stabilize the interspike potential in cardiomyocytes and neurons, it might improve the performance of the model concerning action potential frequency.

Interestingly, long QT syndrome can be due to loss of functionality in cardiac Kir2.1 channels [128], and recently, it was reported that some patients with the

KCNQ1 long QT syndrome suffer from increased insulin secretion, hyperinsulinemia and symptomatic hypoglycemia [131]. This finding suggests a possible link between loss-of-function abnormalities of Kir2.1 channels, which can cause KCNJ2 long QT syndrome and increased insulin secretion.

In this Section we will investigate the contribution of Kir2.1 currents to electrical activity in human β-cells using a combination of patch-clamp experiments and mathematical modeling.

4.3.1 Methods

Mathematical Modelling

The membrane potential V (measured in mV) develops in time (measured in ms) according to

$$\begin{aligned}\frac{dV}{dt} = -(&I_{SK} + I_{BK} + I_{Kv} + I_{Kir} + I_{Na} \\ &+ I_{CaL} + I_{CaPQ} + I_{CaT} + I_{KATP} + I_{leak}).\end{aligned} \tag{4.22}$$

All currents (measured in pA/pF), except the Kir2.1 current I_{Kir}, are modeled as described in the previous Section.

The Kir2.1 current I_{Kir} was assumed not to inactivate and to activate instantaneously in response to hyperpolarisation. Activation was modeled with a Boltzmann function, i.e.,

$$I_{Kir} = g_{Kir}\ (V - V_K) \Big/ \left(1 + \exp\left(\frac{V - V_{mKir}}{n_{mKir}}\right)\right). \tag{4.23}$$

To model the data, we first fixed the K^+ reversal potential to $V_K = -85$ mV based on visual inspection of the data and the theoretically calculated value $V_K \approx -83$ mV. The other three parameters, g_{Kir}; V_{mKir}, and n_{Kir}, were then obtained by fitting the current expression in Eq. 4.23 to the I-V data in Fig. 4.10B. Since the perforated-patch recordings of electrical activity [81, 86, 110] are typically performed with intra- and extra-cellular K^+ concentrations different from the ones used for the Kir2.1 characterisation, the value of V_K was shifted to -75 mV in our model simulations [84, 132]. The intra- and extra-cellular K^+ concentrations modify not only V_K, but also the location parameter V_{mKir}, which was estimated to $V_{mKir} = -100$ mV based on Fig. 4.10B. Because a 10 mV shift in V_K corresponds to a nearly identical shift in V_{mKir} [133], we used $V_{mKir} = -90$ mV for the simulations of electrical activity.

The maximal conductance $g_{Kir} = 1$ nS ($g_{Kir} = 0.1$ nS/pF when normalized to cell capacitance $\sim$10 pF [81]) and the slope parameter $n_{mKir} = 15$ mV were not changed from their estimated values.

Simulations were done in XPPAUT [134] with the cvode solver.

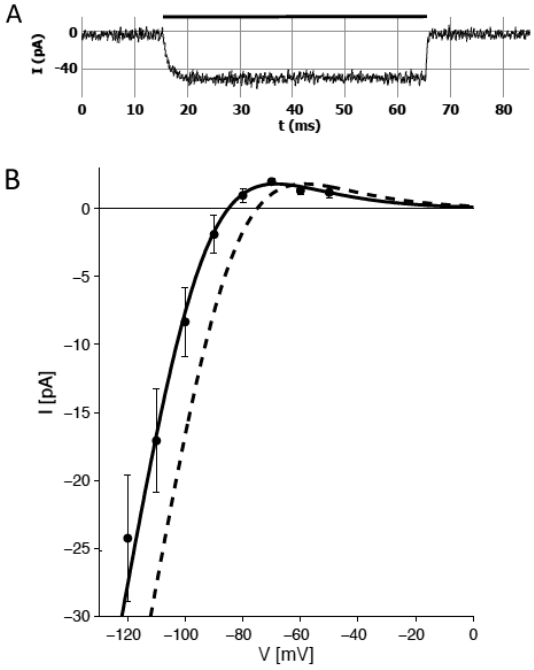

Figure 4.10: A) Example trace of the tolbutamide-insensitive, barium-sensitive K^+ current in a human β-cell in response to a 50 ms depolarisation from -70 mV to -120 mV (black bar). B) Current-voltage relationship of the inwardly rectifying (Kir2.1) K^+ currents in human β-cells (dots and error bars indicate means and standard errors). The full curve shows a fit of Eq. 4.23 to the data points. This curve is right shifted to yield the dashed curve, which is used for the simulations of electrical activity.

Experiments

Human pancreatic islets were obtained with ethical approval and clinical consent from non-diabetic organ donors. All studies were approved by the Human Research Ethics Board at the University of Alberta. The islets were dispersed into single cells by incubation in Ca^{2+} free buffer and plated onto 35 mm plastic Petri dishes. The cells were incubated in RPMI 1640 culture medium containing 7.5 mM glucose for >24 h prior to the experiments. Patch-pipettes were pulled from borosilicate glass to a tip resistance of 6-9 MΩ when filled with intracellular solution. Potassium currents

were measured with the patch-clamp technique in the whole-cell configuration, using an EPC-10 amplifier and Patchmaster software (HEKA, Lambrecht, Germany). The cells were constantly perifused with heated bath solution during the experiment to maintain a temperature of 31-33° C. The extracellular solution consisted of (in mM) 140 NaCl, 3.6 KCl, 0.5 $MgSO_4$, 1.5 $CaCl_2$, 10 HEPES, 0.5 NaH_2PO_4, 5 $NaHCO_3$ and 6 glucose (pH was adjusted to 7.4 with NaOH). The pipette solution consisted of (mM) 130 KCl, 1.0 MgCl2, 1.0 CaCl2, 10 HEPES, 10EGTA, 3.0MgATP, 0.1 Na^+-GTP(pH 7.2 with KOH). β-cells were identified by immunostaining or by size when immunostaining was not possible (cell capacitance >6 pF, [81]).

4.3.2 Results and Discussion

Ion channels are widely expressed, but depending on the cell type they can have different roles in shaping electrical activity. The long QT syndrome can be caused by loss-of-function in potassium channels such as the Kv7.1 channels (KCNQ1 gene) or – more rarely – the Kir2.1 channels (KCNJ2 gene) [128]. Interestingly, patients with the relatively frequent KCNQ1 long QT syndrome exhibit hyperinsulinemia caused by increased secretion of insulin [131].

Experimental Characterisation of Kir2.1 Currents in Human β-cells

The KCNJ2 gene coding for Kir2.1 channels is expressed in human islets and β-cells. Whole-cell voltage-clamp experiments were performed to investigate the Kir2.1 current/voltage (I-V) relationship in human β-cells. We found experimental evidence of a tolbutamide-insensitive, barium-sensitive K^+ current, which activated rapidly and showed little evidence of inactivation (Fig. 4.10A). The current developed at voltages close to the resting potential of human β-cells and at more hyperpolarized voltages, but depolarising pulses deactivated the current (Fig. 4.10B). These characteristics are typical of Kir2.x currents [135, 136].

Besides the Kir2.1 coding gene KNCJ2, the genes KCNJ4 (Kir2.3) and, possibly, KCNJ12 (Kir2.2) are also expressed in human pancreatic islets and β-cells. The available data cannot rule out a contribution from Kir2.2 and Kir2.3 currents since they have I-V characteristics similar to the Kir2.1 current [137]. However, Kir2.1 siRNA knock-down reduced the tolbutamide-insensitive, barium-sensitive K^+ current by $\sim$70% (M. Braun, unpublished), suggesting that the observed current is due to Kir2.1 channels.

Mathematical Modeling of the Role of Kir2.1 Currents in Human β-cells

Kir2.1 current was included in the model of human β-cells based on the I-V curve found experimentally (Fig. 4.10B). The intra- and extracellular K^+ concentrations in the perforated patch experiments measuring electrical activity [81, 86, 110] are different compared to the whole-cell recordings of K^+ currents presented in Fig. 4.10. These changes of K^+ concentrations modify not only the Nernst K^+ potential V_K, but also the activation curve of the Kir2.1 current, which is right-shifted to the same extent as V_K, resulting in a characteristic "cross-over" phenomenon (Fig. 4.10B; [133, 136]).

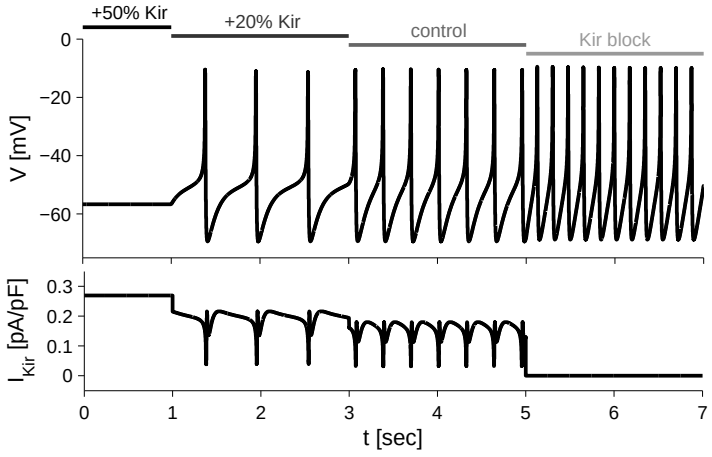

Figure 4.11: Simulation of electrical activity in human β-cells with varying size of Kir2.1 currents as indicated above the bars. "Control" corresponds to the data fit in Fig. 4.10B and corresponding parameters in Table . The case "Kir block" ($g_{Kir} = 0$ nS/pF) corresponds to the previous version of the model.

The previous versions of the model tended to fire action potentials too rapidly ($\sim$5 Hz [132] vs. 1-3 Hz seen experimentally [86, 110]). The simulations showed that the Kir2.1 current stabilises the interspike interval, thus reducing the action potential firing frequency, compared to the previous version of the model (Fig. 4.11). With the Kir2.1 conductance estimated from data, the firing frequency is $\sim$3 Hz, within the range of experimentally observed frequencies [86, 110]. Hence, this last version resulted in a clear improvement of the model behaviour. Of note, the similarity between Kir2.x currents [137] means that the model results are valid also in case Kir2.2 and Kir2.3 channels contribute to the inwardly rectifying current. Blocking the Kir2.1 channels accelerates electrical activity, predicting that KCNJ2

long QT patients, which have reduced Kir2.1 currents, might show increased insulin secretion. Further, increased Kir2.1 conductance, which corresponds to hyperactive channels, reduces the firing frequency, and even abolishes spiking activity at high, which would result in decreased insulin release. We know of no data linking mutations in KCNJ2 to hyperinsulinemia, diabetes or impaired glucose tolerance, but our theoretical results suggest that such connections may exist. Genetic screening could test this hypothesis.

Parameter			Ref.	Parameter			Ref.
V_K	−75	mV	[81]	V_{Na}	70	mV	[84]
V_{Ca}	65	mV	[84]	V_{Cl}	-40	mV	[9]
g_{SK}	0.1	nS/pF	[94]	K_{SK}	0.57	μM	[96]
n	5.2		[96]				
$\bar{g}_{BK}$	0.020	nS/pA	[81]	τ_{mBK}	2	ms	[81]
V_{mBK}	0	mV	[81]	n_{mBK}	-10	mV	[81]
B_{BK}	20	pA/pF	[81]				
g_{Kv}	1.000	nS/pF	[81]	$\tau_{mKv,0}$	2	ms	[81]
V_{mKv}	0	mV	[81]	n_{mKv}	-10	mV	[81]
g_{Na}	0.400	nS/pF	[81]	τ_{hNa}	2	ms	[81]
V_{mNa}	-18	mV	[81]	n_{mNa}	-5	mV	[81]
V_{hNa}	-42	mV	[81]	n_{hNa}	6	mV	[81]
g_{CaL}	0.140	nS/pF	[81]	τ_{hCaL}	20	ms	[84]
V_{mCaL}	-25	mV	[81]	n_{mCaL}	-6	mV	[81]
g_{CaPQ}	0.170	nS/pF	[81]				
V_{mCaPQ}	-10	mV	[81]	n_{mCaPQ}	-6	mV	[81]
g_{CaT}	0.050	nS/pF	[81]	τ_{hCaT}	7	ms	[81]
V_{mCaT}	-40	mV	[81]	n_{mCaT}	-4	mV	[81]
V_{hCaT}	-64	mV	[81]	n_{hCaT}	8	mV	[81]
g_{Kir}	0.1	nS/pF		$g_{K(ATP)}$	0.010	nS/pF	[78]
V_{mKir}	-90	mV		n_{mKir}	15	mV	
g_{leak}	0.015	nS/pF	[78]	V_{leak}	−30	mV	[84]
$J_{SERCA,\max}$	0.060	μM/ms	[98, 132]	K_{SERCA}	0.27	μM	[98]
$J_{PMCA,\max}$	0.021	μM/ms	[98]	K_{PMCA}	0.50	μM	[98]
J_{leak}	0.00094	μM/ms	[98, 104]	$J_{NCX,0}$	0.01867	ms^{-1}	[98, 104]
f	0.01			Vol_c	1.15	$\times 10^{-12}$ L	[132]
B	0.1	ms^{-1}	[132]	Vol_m	0.1	$\times 10^{-12}$ L	[132]
α	5.18×10^{-15} μmol/pA/ms						

Table 4.3: Default model parameters used in the model simulations of electrical activity in Figure 4.11.

5

From Electrical Activity to Exocytosis:
Calcium Diffusion and Buffering

As a result of the β-cell depolarization, Ca^{2+}-channels open, leading to influx and subsequent diffusion of calcium inside the cell, which in turn triggers exocytosis. Hence, from the electrical-activity analysis of the previous Chapters, we will move to the investigation of the relationship between insulin granule exocytosis, calcium levels, distance from Ca^{2+}-channels and channel clustering in pancreatic β-cells.

This subproject is based on Total Internal Reflection Fluorescence (TIRF) microscopy, consisting in simultaneous visualization of two different fluorophores. The first fluorophore is used to label insulin-containing vesicles, and to differentiate them into two groups: the ones that undergo exocytosis in response to depolarization, and the ones that do not. The second fluorophore, a genetically encoded Ca^{2+} indicator (R-GECO), is attached to the plasma membrane and permits visualizing submembrane calcium levels during the stimulus.

Simulations were performed using the modeling program CalC, which implements calcium diffusion and buffering. Simulated calcium levels and the corresponding R-GECO signal were evaluated at different distances from the channel. The comparison of the simulations to the TIRF microscopy data allowed estimating the average distance from the channel of the granules that undergo exocytosis.

The Chapter will begin with a brief introduction to TIRF microscopy, followed by a mathematical description of the diffusion process, along with the important role of calcium buffering. Afterwards, the features of the modeling program CalC will be presented. Finally, after describing the simulation setup, the results of the comparison between experimental data and simulations will be presented.

5.1 TIRF Microscopy

TIRF microscopy, also known as evanescent field microscopy, is used in a wide range of applications, particularly to view single molecules attached to planar surfaces and to study the position and dynamics of molecules and organelles in living culture cells near the contact regions with the glass coverslip.

TIRF provides a means to selectively excite fluorophores in an aqueous environment very near a solid surface ($\leq$100 nm), since the evanescent field does not propagate deeper into the sample. Combined to microscopy, TIRF produces images with high signal-to-noise ratio and very low background fluorescence, by avoiding excitation of fluorophores from out-of-focus planes. Compared with confocal and epifluorescence, TIRF microscopy has the advantage of providing high-resolution, high-contrast images of the region closest to the glass coverslip. As a consequence, it is used for studying processes such as endocytosis, exocytosis, cell adhesion and cytoskeletal dynamics.

This Section will briefly describe the basic optical theory on which TIRF is based, followed by some examples of the current applications in cell biology and the presentation of our data. For a complete review of the technique see [138, 139].

5.1.1 Theoretical Principles

The refractive index, n, of an optical medium represents how electromagnetic waves (e.g. visible light) propagate through it, relative to how it propagates through a perfect vacuum. It is defined as $n = c/v$, where c is the velocity of light in a vacuum and v the velocity of light in the medium.

When a light beam propagating through a transparent medium of high index of refraction (e.g. glass) meet a planar interface with medium of lower index of refraction (e.g. air, water, cytosol), the subsequent direction of the light rays is changed depending on the angle at which the light meets this interface. Some of the

light rays may be reflected from the interface and some may be transmitted into the second medium. If the refractive indices of both media are known, n_1 and n_2, as well as the angle of incidence, θ_1, then Snell's law provides the angle at which light rays are transmitted and/or reflected from this interface, θ_2 (Fig. 5.1):

$$n_1 \sin\theta_1 = n_2 \sin\theta_2. \tag{5.1}$$

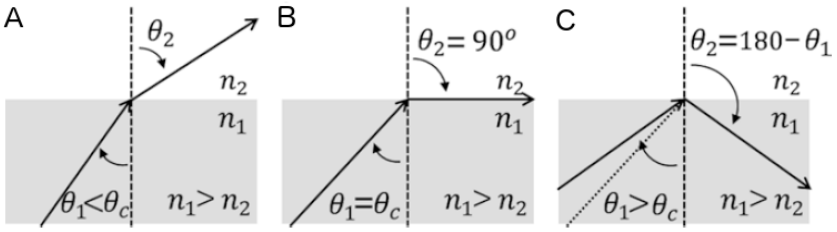

Figure 5.1: The direction of light rays changes when they propagate through one medium (gray) and encounter an interface of a second medium (white), with lower refractive index. A) The angle of incidence is less than the critical angle. B) The angle of incidence is equal to the critical angle. C) The angle of incidence is greater than the critical angle. From [138].

Total internal reflection occurs when the refractive index of the first medium is greater than that of the second, $n_1 > n_2$, and the angle of incidence is greater than what is known as the "critical" angle, θ_c. For "subcritical" incidence angles $\theta < \theta_c$, most of the light propagates through the interface into the lower index material (Fig. 5.1A). When the angle of incidence is equal to the critical angle, $\theta_1 = \theta_c$, light rays emerge into the second medium and propagate tangentially along the direction of the interface, or $\theta_2 = 90^o$ (Fig. 5.1B). So Snell's law gives us:

$$n_1 \sin\theta_c = n_2 \sin 90^o = n_2, \tag{5.2}$$

and therefore

$$\theta_c = \sin^{-1} \frac{n_2}{n_1}. \tag{5.3}$$

For angles of incidence greater than θ_c, light rays are totally reflected back into the first medium (Fig. 5.1C).

The field in the liquid, sometimes called the "evanescent wave" is capable of exciting fluorescent molecules that might be present near the surface, as shown schematically in Figure 5.2B, compared to epifluorescence microscopy where all fluorescent molecules are excited as in Figure 5.2A.

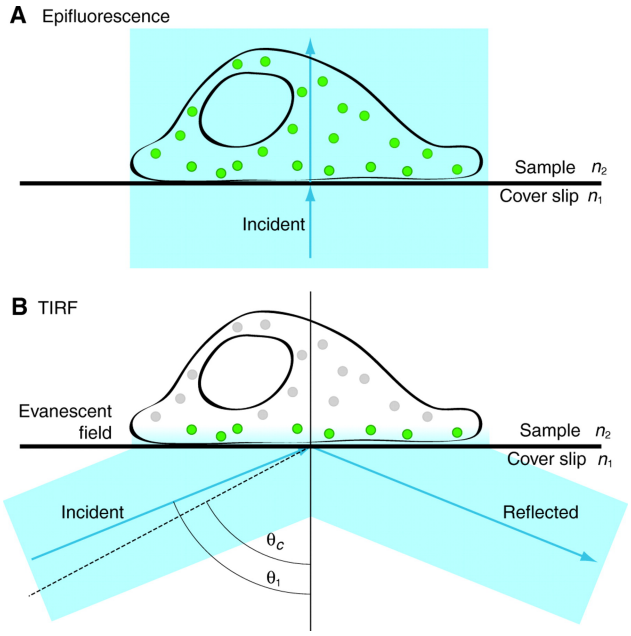

Figure 5.2: A) Epifluorescence, where the excitation beam travels directly through the cover-slip-sample interface exciting the fluorophores in the entire sample. B) TIRF Microscopy, where the excitation beam travels from left at incident angle θ_1 and excites only the fluorophores in the evanescent field. Adapted from [140].

The intensity I of the evanescent field at any position , measured as perpendicular distance z from the interface, exponentially decays with z:

$$I(z) = I_0 \mathrm{e}^{-z/d}, \tag{5.4}$$

where d is the decay constant of the field, and I_0 is the intensity of the field at the interface ($z = 0$).

Local areas of high refractive index within a sample will convert the evanescent field into scattered propagating light which will in turn contaminate images. For that reason, it is often desirable for a TIRF system to have the capability to vary the penetration depth of the evanescent field. The equation below shows what determines the penetration depth:

$$d = \frac{\lambda_0}{4\pi n_1} \left(\sin^2 \theta_1 - \sin^2 \theta_c \right)^{-1/2}. \tag{5.5}$$

Hence, the penetration depth is dependent on the wavelength of the excitation beam, λ_0; the angle of incidence of the excitation beam, θ_1; and the refractive indices of the two media (n_1, n_2). In practice, the refractive index of a biological sample (n_2) is difficult to control, the excitation wavelengths (λ_0) depends on the specific

fluorophore and the refractive index of the imaging surface is fixed (n_1). Therefore, experimentally the penetration depth can only be controlled through variation of the angle of incidence (θ_1).

5.1.2 Applications

TIRF microscopy has been used extensively in the last decade to study cellular organization and dynamics that occurs near the cell culture/glass substrate interface. Some examples will be discussed in this Subsection.

Secretory Granule Tracking and Exocytosis

Secretory granules often reside through the whole depth of a cell. When viewed with standard epifluorescence, marked secretory granules are difficult to distinguish individually (Fig. 5.3A). However, with TIRF the granules closest to the membrane appear very distinctly (Fig. 5.3B). The thin evanescent field allows small motions of individual fluorescence-marked secretory granules to manifest as small intensity changes arising from small motions in the direction normal to the interface (z-direction).

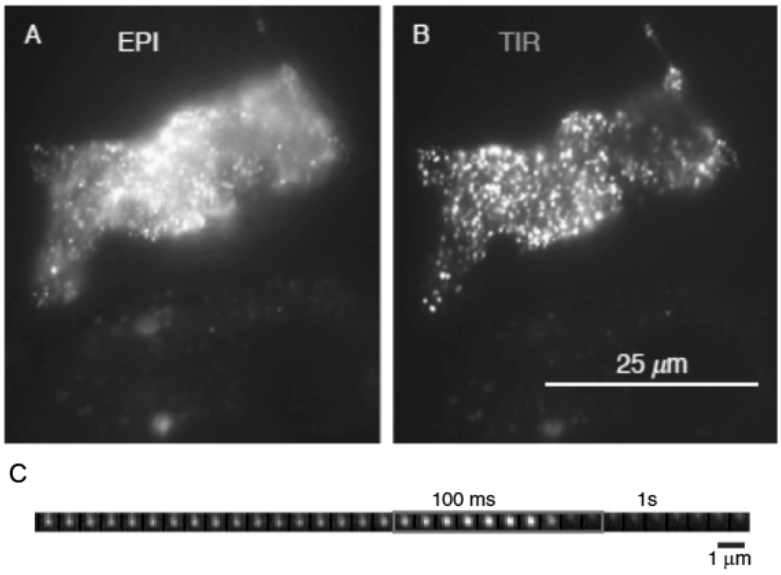

Figure 5.3: Conventional (A) versus TIRF (B) digital images, where bovine chromaffine cell contains secretory granules marked with GFP protein. Adapted from [139]. C) Image sequence showing a single granule undergoing exocytosis [141].

The precision of such axial tracking can be as small as 2 nm, much smaller than the light microscope resolution limit. Because of the high contrast and low background, the position of the centers of granules can be measured with an accuracy down to about 10 nm and motions much smaller than the granule diameter can be followed before and after exocytosis-inducing chemical stimulation [140]. In some cases, dispersal of granule contents can be observed and interpreted as exocytosis and the steps immediately preceding exocytosis characterized.

Figure 5.3C shows the exocytosis of single granule in INS1 cells expressing the granule marker neuropeptide-Y (NPY)-mCherry stimulated via KCl depolarization. The vesicle can be seen to get brighter as it nears the plasma membrane and moves deeper into the evanescent wave. The fluorescence intensity then starts to decline as the granule marker spreads out into the plasma membrane, increasing the width of the intensity profile as this lateral diffusion continues. The exocytic event is usually very fast, so imaging needs to be as rapid as possible.

Endocytosis

There are several endocytic pathways in cells. The most well defined of these is clathrin-mediated endocytosis. Clathrin-coated pits (CCPs) form at the plasma membrane before they are pinched off as vesicles inside the cell through the action of the GTPase dynamin. Fluorescently tagged clathrin and dynamin constructs have been developed and validated for use in live-cell imaging studies [138].

TIRF microscopy can be used to study such processes. When cells express fluorescently labeled clathrin, the CCPs appear as spots at the cell surface. As clathrin-coated vesicles (CCVs) form, they are still seen at the plasma membrane, but as they are pinched off and moved into the cell, and therefore out of the TIRF field, they disappear.

Various criteria need to be met to ascertain that the protein of interest is really undergoing endocytosis. Firstly, the tentative endocytic event must be seen to disappear over successive frames and not move laterally out of the field of view. Secondly, it is necessary to verify that the spot disappearance is not due to photobleaching, by checking that other neighboring spots in the field of view show no change in intensity. Alternatively, a spot is being endocytosed if it disappears from the TIRF image, but is still visible in an epifluorescence image, indicating that it has moved further than 100 nm into the cell.

Cell-Substrate Contact Regions

Focal adhesions (FAs) are large, multiprotein complexes that act to link the actin cytoskeleton of cells to the extracellular matrix through transmembrane proteins called integrins. Regulation of these structures is important for cell migration; new focal contacts, that form at the front of migrating cells, can mature into more stable FAs allowing the cell to transmit traction forces. FAs need to be disassembled at the back of the cell so the rear can be retracted and the cell can move forward. As FAs form at the adherent cell membrane, they are best visualized through the use of TIRF microscopy to eliminate unwanted signal that might obscure their pattern and position in the cell. It is often a topic of investigation for any treatment that affects cell migration and could be acting on the formation or disassembly of FAs.

5.1.3 TIRF DataSet

This subproject is based on TIRF microscopy data consisting in simultaneous visualization of two different fluorophores. The first fluorophore (EGFP) is used to label insulin-containing vesicles, while the second one, a genetically encoded Ca^{2+} indicator (R-GECO), is attached to the plasma membrane and permits visualizing calcium levels during the stimulus.

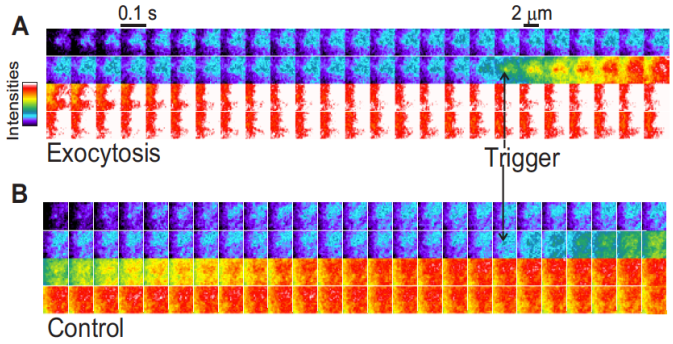

Figure 5.4: INS1 cells transfected with insulin granule marker and Ca^{2+} sensor (R-GECO) were imaged in TIRF microscopy in presence of EGTA-AM. Cells were imaged with short depolarizations with elevated KCl. A) Ca^{2+} levels for the granules which did exocytosis. A) Ca^{2+} levels for the granules which did not do exocytosis. All the images are an average of more than 50 events.

In particular, thanks to the TIRF microscopy it is possible to track insulin granule during stimulus and differentiate them into two groups: the ones that undergo exocytosis in response to depolarization (exo group), and the ones that do not (control group). Thanks to the use of the second fluorophore, it is possible to track the

calcium levels in correspondence to the granule position (Fig. 5.4). Given the division of granules into exo and control groups, it is possible to analyze if there is any difference in calcium seen by the two groups.

The experimental results with different exogenous buffers (EGTA-AM and BAPTA-AM) are shown in Figure 5.5.

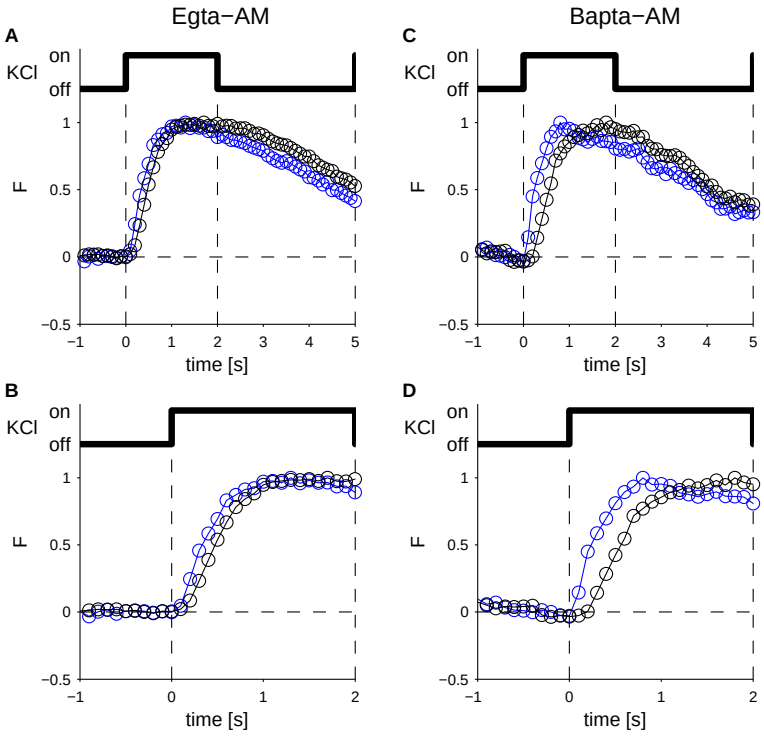

Figure 5.5: The normalized intensities of Ca^{2+} from the exocytosing granule (blue) and control granule (black). A-B) Cells were incubated with EGTA-AM. B) is an enlargement of the depolarizing step in A). C-D) Cells were incubated with BAPTA-AM. D) is an enlargement of the depolarizing step in B).

Experimentally, the exo group exhibits a faster and earlier increase in calcium levels compared to the control group. This likely translates into a closer proximity of the exocytotic granules to the calcium channels. However, it is not possible to quantify that distance. In this context, mathematical simulations of calcium diffusion and buffering inside the cell might help in quantifying the average distance at which exo and control groups are located. Some experimental details are given below.

Cells

INS1-cells clone 832/13 were maintained in RPMI 1640 (Invitrogen) supplemented with 10% fetal bovine serum, streptomycin (100 μg/ml), penicillin (100 μg/ml), Na-pyruvate (1 mM), and 2-mercaptoethanol (50 μM). For experiments, the cells were placed on polylysine-coated coverslips, transfected using Lipofectamine2000 (Invitrogen) and imaged 36-42 hours later.

Solutions

Cells were imaged in solution containing (in mM) 138 NaCl, 5.6 KCl, 1.2 $MgCl_2$, 2.6 $CaCl_2$, 3 D-glucose and 5 HEPES (pH 7.4 with NaOH). For exocytosis experiments the buffer instead contained 10 mM glucose and was supplemented with 200 μM Diazoxide and 2 μM forskolin. Exocytosis was evoked by timed local application of high K^+ (75 mM KCl equimolarly replacing NaCl) through a pressurized glass electrode similar to those used for patch clamp experiments. All experiments were carried out with constant buffer perifusion at 32^{o}C.

Microscopy

Cells were imaged using a custom-built lens-type total internal reflection (TIRF) microscope based on an Axiovert 135 microscope with a 100x/1.45 objective (Carl Zeiss). Excitation was from two DPSS lasers at 473 and 561 nm (Cobolt, Stockholm, Sweden) and a diode laser at 405 nm (Lambda Physik, Göttingen, Germany), controlled with an acousto-optical tunable filter (AA-Opto, France) and using dicroic Di01-R488/561 (Semrock). Cells were found using only 561 nm light, to avoid bleaching of the EGFP signal. The emission light was separated onto the two halves of an EMCCD camera (Roper Cascade 512B) using an image splitter (Optical Insights) with a cutoff at 565 nm (565dcxr, Chroma) and emission filters (FF01-523/610, Semrock; and ET525/50m and 600EFLP, both from Chroma). Scaling was 160 nm per pixel. The alignment of the red and green images was determined once every experimental session using 100 nm beads (Molecular Probes, Eugene, OR) immobilized on the coverslip surface and fluorescing in both channels. An algorithm was then used to shift and shrink (by <4%) the red image to correct for misalignment [142].

Image Analysis

Colocalization of EGFP-labeled proteins with granules was measured as described previously [143]. Briefly, locations of well separated granules were identified by eye (7-36 per cell). An algorithm implemented as MetaMorph journal then read the average pixel fluorescence in a circle of 3 pxl (0.5 μm) diameter and a surrounding annulus with an outer diameter of 5 pxl (0.8 μm) (Fig. 5.6). For comparison, an insulin granule is ∼300 nm in diameter [26]. The circle c represents the granule-associated fluorescence and the annulus a represents local background onto which the cluster is superimposed. The annulus value a was subtracted from that of the circle c to yield the EGFP fluorescence specifically associated with a granule ($\Delta F = c - a$). The cell's average background-corrected annulus value ($S = a - bg$) is linearly related to the expression level of the labeled protein. To account for different expression levels, ΔF was therefore divided by S to yield $\Delta F/S$. In some cases colocalization of EGFP-labeled cluster with granules was also estimated by eye. Granules were tracked using ImageJ particle tracker. Exocytosis events were detected manually based on sudden brightening of a granule (due to pH equilibration and unquenching of EGFP) [144], followed by sudden disappearance of the granule fluorescence. The moment of exocytosis was defined as the first significant change (2 SD) from the pre-exocytosis baseline.

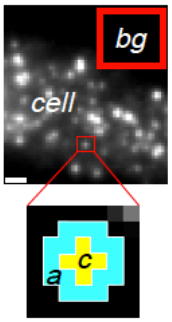

Figure 5.6: Definition of the different areas in the image: a central circle (c) of 3 pxl (0.5 mm) diameter, a surrounding annulus (a) with an outer diameter of 5 pxl (0.8 mm) and a background area not including any cell (bg).

In correspondence to the granule positions, R-GECO fluorescence was analyzed considering the same areas a, c, bg. In particular, the background-corrected circle value $c - bg$ was normalized by the background-corrected pre-stimulus value $c(0) - bg$, where 0 corresponds to the time of depolarization. Finally, since the R-GECO fluorescence can not be easly translated to calcium levels and different cell might have different R-GECO signal but same calcium concentration, the baseline value was subtracted to the curves, and the result normalized to the maximum value. In this way, the resulting curves go from 0 to 1 during depolarization, which allows a direct comparison of the rise times (see Fig. 5.5).

5.2 Calcium Diffusion and Buffering

Diffusion is the process by which random movement of molecules or ions causes an average movement toward regions of lower concentration, which may results in the annihilation of the concentration gradient. The introduction of diffusion into a model raises many issues, such as spatial scale, dimensionality, geometry, and which buffers can be considered immobile. Furthermore, binding sites with different affinities may compete for the diffusing molecule, which leads to a highly non linear dynamics.

In this Section, we will consider the diffusion of Ca^{2+} inside a cell as a result of Ca^{2+}-channel opening, and its interaction with intracellular buffers, which significantly affect the time constant of calcium diffusion.

5.2.1 The Diffusion Process

To describe the basic concepts of diffusion, we will consider the simple case where the spatial variation of Ca^{2+} concentration, c [μM], is restricted to one spatial variable x. This case is represented by Ca^{2+} contained in a long thin tube with constant cross-sectional area A. In any fixed region R along the tube, the conservation of Ca^{2+} states that the rate of change of the total amount of Ca^{2+} within R is equal to the rate at which Ca^{2+} flows in to R minus the rate at which it flows out, plus the difference between its production and its removal.

Now, we will translate this statement into equations. The total amount of Ca^{2+} contained in a region R, whose limits are (x_a, x_b) is:

$$\int_{x_a}^{x_b} c(x,t)Adx. \tag{5.6}$$

By denoting $J(x,t)$ [μM/area/time] as the rate at which Ca^{2+} moves across the boundary at position x from left to right at time t, the net flux of Ca^{2+} into the region R is:

$$AJ(x_a,t) - AJ(x_b,t). \tag{5.7}$$

Finally, by denoting $f(x,t,c)$ [μM/time/volume] the net rate of increase of Ca^{2+} per unit volume at location x and time t, due to the difference between its production and its removal, the total amount of Ca^{2+} produced in the region R at time t is:

$$\int_{x_a}^{x_b} f(x,t,c(x,t))Adx. \tag{5.8}$$

Now, we can translate the conservation law in mathematical symbols as:

$$\frac{d}{dt}\int_{x_a}^{x_b} c(x,t)dx = J(x_a,t) - J(x_b,t) + \int_{x_a}^{x_b} f(x,t,c(x,t))dx, \tag{5.9}$$

where each term was normalized by the area A.

The flux terms can be replaced by

$$J(x_a,t) - J(x_b,t) = -\int_{x_a}^{x_b} \frac{\partial}{\partial x} J(x,t)dx, \tag{5.10}$$

and Eq. 5.9 becomes

$$\frac{d}{dt}\int_{x_a}^{x_b} c(x,t)dx = -\int_{x_a}^{x_b} \frac{\partial}{\partial x} J(x,t)dx + \int_{x_a}^{x_b} f(x,t,c(x,t))dx. \tag{5.11}$$

If the function $c(x,t)$ is smooth enough, then the differentiation and integration can be interchanged

$$\int_{x_a}^{x_b} \left[\frac{\partial}{\partial t} c(x,t) + \frac{\partial}{\partial x} J(x,t) - f(x,t,c(x,t))\right] dx = 0, \tag{5.12}$$

and it is possible to obtain the equivalent conservation law in differential form

$$\frac{\partial c(x,t)}{\partial t} + \frac{\partial J(x,t)}{\partial x} = f(x,t,c(x,t)). \tag{5.13}$$

Note that this equation contains two independent variables (x and t), and partial derivatives with respect to both of these. Such equations are called Partial Differential Equations (PDEs).

Eq. 5.13 is undetermined, because it is a single equation relating two unknowns (c and J). Hence, to resolve this problem, an additional equation is needed. This secondary relation is usually called a constitutive equation, since it must be determined empirically and is not universally valid.

One example is the Fick's law, which states that a substance moves from regions of high to regions of low concentration at a rate proportional to the concentration gradient. Hence, this diffusive flux is:

$$J(x,t) = -D\frac{\partial}{\partial x} c(x,t), \tag{5.14}$$

where the proportionality constant D [length^2/time] is called the diffusion constant. The negative sign signifies that the substance moves spontaneously from high to low concentrations. The value of D depends both on the size of the substance and the properties of the medium in which it is diffusing.

Using Fick's law, Eq. 5.13 becomes the reaction-diffusion equation:

$$\frac{\partial c(x,t)}{\partial t} - \frac{\partial}{\partial x}\left(D\frac{\partial c}{\partial x}\right) = f(x,t,c(x,t)). \tag{5.15}$$

When f is zero, Eq. 5.15 becomes the diffusion equation:

$$\frac{\partial c(x,t)}{\partial t} = \frac{\partial}{\partial x}\left(D\frac{\partial c}{\partial x}\right), \tag{5.16}$$

and if D is constant in space

$$\frac{\partial c(x,t)}{\partial t} = D\frac{\partial^2 c}{\partial x^2}. \tag{5.17}$$

For completeness, the conservation equation in multiple dimension is reported:

$$\frac{\partial c(x,y,z,t)}{\partial t} + \nabla \cdot J = f(x,y,z,t), \tag{5.18}$$

and the corresponding Flick's law

$$J(x,y,z,t) = -D\nabla c(x,y,z,t), \tag{5.19}$$

which combined give the diffusion equation

$$\frac{\partial c(x,y,z,t)}{\partial t} = \nabla \cdot (D\nabla c). \tag{5.20}$$

To solve ordinary differential equations initial data need to be specified. In case of partial differential equations, both initial data and boundary conditions should be given to find a solution. Initial conditions usually specify the values of the dependent variables at some initial time at which the solution is known or specified by experimental conditions. Boundary conditions reflect certain physical conditions of the experiment. For example:

- Dirichlet boundary condition is used when the concentration c is some function $f(t)$ at some boundary point, e.g. $x = x_a$:

$$c(x_a,t) = f(t); \tag{5.21}$$

- Neumann boundary condition is used to specify the flux at a boundary point:

$$-D\frac{\partial c}{\partial x}(x_a,t) = g(t); \tag{5.22}$$

- Robin boundary condition is used when the flux is related to the value of c at the boundary:

$$-D\frac{\partial c}{\partial x}(x_a,t) = h(t) - \alpha c(x_a,t). \tag{5.23}$$

5.2.2 The Role of Buffers

Reaction-diffusion systems have been studied most extensively in the context of buffering and binding of calcium ions. Cells contain an impressive variety of molecules with calcium binding sites, e.g. pumps that remove the intracellular calcium, buffers that bind calcium ions and enzymes activated or modulated by calcium. The interaction of the transient steep calcium concentration gradients with all these binding sites creates complex reaction-diffusion systems, the properties of which are not always completely understood.

Ca^{2+} buffering is an important process in Ca^{2+} signalling because it have been estimated that only about 1-5% of Ca^{2+} ions entering into the cell remain as free Ca^{2+}, which is the physiologically active form [145]. Furthermore, buffers decrease both the peak and equilibrium calcium concentration, slow the diffusion process, and limit the spread of calcium to the submembrane region.

In the cytosol, Ca^{2+} buffering can be mediated by mobile and immobile buffers, keeping under control the diffusion of free Ca^{2+} ions inside the cytoplasm and reducing its diffusion spread. Immobile buffers are represented by molecules of high molecular weight or anchored to intracellular structures, while mobile buffers are molecules of low molecular size, as soluble proteins or small organic anions and metabolites. A mobile Ca^{2+} buffer will disperse domains of elevated calcium concentration, whereas fixed buffers will tend to prolong them. Commonly used buffers for experimental purposes, such as EGTA, BAPTA or fluorescent indicators themselves, must also be considered as competitive buffers.

Here, the macroscopic interaction of Ca^{2+} with buffers will be described using the simple second-order equation:

$$Ca^{2+} + B \underset{k^-}{\overset{k^+}{\rightleftharpoons}} CaB. \tag{5.24}$$

It is only an approximation because most buffers have multiple binding sites with different binding rates and require more complex reaction schemes. However, experimental data for such schemes are often not available. Nevertheless, it is important to express buffer binding with rate equations, in order to consider the effects of the competition between buffers.

At the steady state, the forward flux equals the reverse flux:

$$k^+[Ca][B] = k^-[CaB], \tag{5.25}$$

where k^+ has units of $[\mu\mathrm{M}^{-1}\mathrm{ms}^{-1}]$ and k^- of $[\mathrm{ms}^{-1}]$. Hence, it is possible to define the dissociation constant as:

$$K_D = \frac{k^-}{k^+} = \frac{[Ca][B]}{[CaB]}, \tag{5.26}$$

which has the same unit as concentration. To understand its meaning, let us follow these steps:

$$\frac{K_D}{[Ca]} = \frac{[B]}{[CaB]}, \tag{5.27}$$

$$\frac{K_D}{[Ca]} + 1 = \frac{[B]}{[CaB]} + 1, \tag{5.28}$$

$$\frac{K_D}{[Ca]} + \frac{[Ca]}{[Ca]} = \frac{[B]}{[CaB]} + \frac{[CaB]}{[CaB]}, \tag{5.29}$$

$$\frac{[Ca]}{K_D + [Ca]} = \frac{[CaB]}{[B] + [CaB]}. \tag{5.30}$$

Since the sum $[B] + [CaB]$ corresponds to the total concentration of the buffer B_T, the right side of the equation represents the fraction of buffer, which is bound to calcium:

$$\frac{[Ca]}{K_D + [Ca]} = \frac{[CaB]}{[B_T]}. \tag{5.31}$$

When the calcium concentration equals the dissociation constant K_D, half of the buffer is bound to calcium:

$$\frac{[CaB]}{[B_T]} = \frac{K_D}{K_D + K_D} = \frac{1}{2}, \tag{5.32}$$

which means that the greater the value of K_D is, the greater the calcium concentration should be to occupy half of the buffer present. As a consequence, it is useful to define the affinity constant as the reciprocal of the dissociation constant:

$$K_A = \frac{1}{K_D}. \tag{5.33}$$

While the K_D describes the affinity to calcium at steady state, the dynamic behavior of the buffer is characterized by the rate constants k^- and k^+, i.e. the smaller the constants are, the slower the buffer binds the calcium. Moreover, since affinity is the ratio between the rate constants, two buffers might have the same affinity to calcium, but different kinetics. For example, EGTA and BAPTA have similar affinity, but BAPTA has $\sim$100 times faster kinetics compared to EGTA.

Finally, it is worth defining the buffer capacity, which is the ratio between the inflowing ions that are bound to buffer to those that remain free:

$$\kappa = \frac{d[CaB]}{d[Ca]} = \frac{K_D B_T}{(K_D + Ca)^2}. \tag{5.34}$$

In the case of low calcium concentration, Eq. 5.34 reduces to

$$\kappa = \frac{B_T}{K_D}. \tag{5.35}$$

Buffer capacity in the cytoplasm is high and quite variable among different cell types or even in the same cell depending on host tissue or species, ranging from about 45 in adrenal chromaffin cells [146] to more than 4000 in the Purkinje cell [147].

Genetically Encoded Calcium Indicators

Ca^{2+}-indicators are themselves Ca^{2+} buffers (often highly mobile) that can potentially affect intracellular Ca^{2+} signaling.

After the development of Ca^{2+}-sensitive dyes such as Quin2[148] and fura-2[149], the introduction of genetically encoded Ca^{2+} indicators, GECIs, was preceded by three important steps: the discovery of green fluorescent protein (GFP)[150], the creation of GFP color variants, and the biochemical study of Ca^{2+} binding. An improvement in GECIs was the development of single-fluorescent protein Ca^{2+}-sensors (camgaroos[151], pericams[152], GCaMP[153]).

The strengths of GECIs include the following [154]. The localization of a GECI can be controlled by including a signal sequence as part of the indicator, thus GECIs are preferred for measuring Ca^{2+} in defined subcellular locations, such as the plasma membrane, ER, mitochondria, or Golgi. GECIs can be genetically fused to a protein of interest and therefore can measure Ca^{2+} in micro-domains in the immediate vicinity of a given protein. GECIs can be maintained within cells over days to weeks (in the case of stable incorporation). Hence, GECIs enable extended time-lapse experiments where small molecule indicators would slowly leak out, or be extruded, from the cell. GECIs can be transfected into cells along with other genes such that only the co-transfected subpopulation is monitored.

More recent improvements, involving large-scale screening after random (GECOs [155]) or semi-rational mutation (GCaMP5-indicator family [156]), have led to color and high dynamic range variants of single fluorescent protein-based indicators [157]. In partiuclar, in this subproject the red-shifted fluorescent (R-GECO) was used.

5.3 CalC: the Calcium Calculator

At this point, it becomes easy to imagine that simulating diffusion is in general a computationally expensive process. In my project, the computational program CalC ("Calcium Calculator") was used. It is a free modeling tool for simulating intracellular calcium diffusion and buffering [158, 159]. CalC solves continuous reaction-diffusion PDEs describing the entry of calcium into a volume through channels, and its diffusion, buffering and binding to calcium receptors.

In this Section we will briefly review some of CalC features.

Implemented Geometries

CalC allows simulations in any geometry: cartesian 3D, 2D or 1D, polar, spherical, cylindrical, conical, etc. In the following some examples are given.

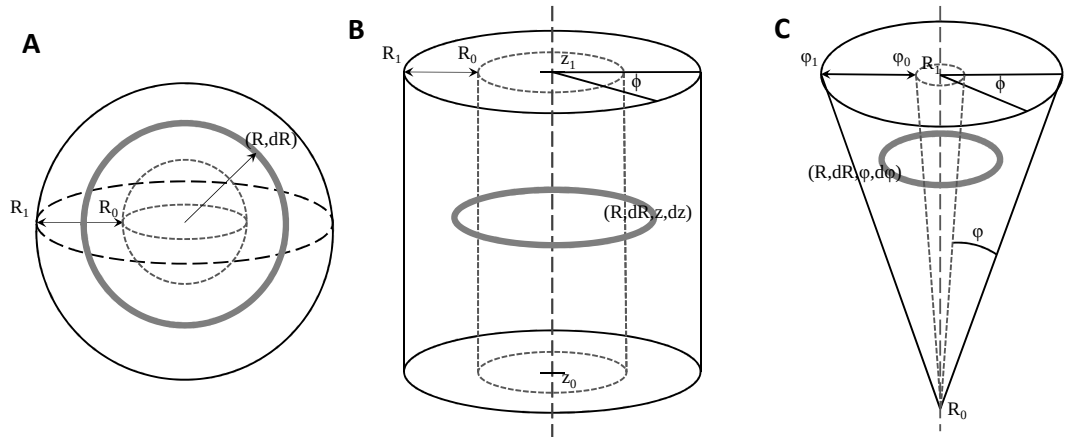

Figure 5.7: **Examples of implemented geometries in CalC.** A) Spherical symmetry. Volume parameters: R_0,R_1. Calcium source in solid grey line, with position described by R and dimension set by dR. B) Cylindrical symmetry with respect to angle ϕ. Volume parameters: R_0,R_1, z_0, z_1. Calcium source in solid grey line, with position described by R,z and dimension set by dR,dz. C) Conical symmetry with respect to angle ϕ. Volume parameters: R_0,R_1,θ_0,θ_1. Calcium source in solid grey line, with position described by R,θ and dimension set by dR,dθ. In all figures the inner surface is represented by dashed grey lines.

When the geometry is *spherically symmetric*, e.g. one source in the center of a sphere or a current uniformly distributed over the surface of a spherical cell, the 3D problem reduces to a 1D problem in spherical coordinates (Fig. 5.7A). In this case it is much more efficient to solve the resulting one-dimensional problem. To define the volume only two parameters are need: R_0 for the inner radius and R_1 for the

outer one of the spherical shell. Similarly, only two boundary conditions need to be defined, corresponding to the two surfaces (inner and outer). Finally, for the calcium source location, R specifies the radius of the spherical surface over which the current is uniformely distributed ($R = 0$ for a source in the center of the sphere), and dR represents the width of the source current layer in radial direction.

If the geometry for the problem is symmetric with respect to the azimuth angle ϕ in *cylindrical coordinates*, the 3D problem reduces to a 2D problem in coordinates r and z(Fig. 5.7B). Four parameters define the volume: R_0 and R_1 represent the inner and the outer radii of the volume, while Z_0 and Z_1 are the limiting z-values, which set the length of the cylinder. In this case, four boundary conditions have to be specified and four parameters describe location (R and z) and dimension (dR and dz) of the calcium source.

Finally, if the geometry for the problem is symmetric with respect to the azimuth angle ϕ in *spherical coordinates*, the 3D problem reduces to a 2D problem in coordinates r and θ [99](Fig. 5.7C). Four parameters define the volume: R_0 and R_1 represent the inner and the outer radii of the volume, while θ_0 and θ_1 are the limiting angle values, which determine the width of the cone base. Similarly to cylindrically symmetric geometry, four boundary conditions have to be specified and four parameters describe location (R and θ) and dimension (dR and dθ) of the calcium source.

The simulation space volume can be composed of an arbitrary number of "boxes", with an arbitrary number of obstacles, i.e. barriers to diffusion of calcium and/or buffers.

Grid Points

Calcium and buffer concentration fields are computed on a mesh of points, covering the entire diffusion space. The grid may be non-uniform too. The advantage of a non-uniform grid is that the accuracy of the computation can be improved by increasing the density of grid points in the vicinity of calcium channels, where the concentration gradients are the greatest.

Boundary Conditions

By default, both calcium and buffers satisfy zero flux boundary conditions at all surface of all geometry elements. However, boundary conditions may be specified

by the user for each volume and for each obstacle. The boundary conditions may be either defined by the user, or be one of the two predefined types, the zero flux and to the boundary value clamped to background concentration. The user defined boundary condition can be in one of these forms:

$$A \cdot Flux + B([Ca] - [Ca]_0) + C\left(\frac{[Ca]^n}{[Ca]^n + K^n} - \frac{[Ca]_0^n}{[Ca]_0^n + K^n}\right) = 0, \quad (5.36)$$

$$A \cdot Flux + B([Ca] - [Ca]_0) = 0, \quad (5.37)$$

$$[Ca] - [Ca]_0 = R, \quad (5.38)$$

where $[Ca]$ is the Ca^{2+} concentration and $[Ca]_0$ is the background concentration. A, B, C, n and K are parameters that can be set by user. In Eq. 5.36 and Eq. 5.37 $Flux$ is the flux per unit area at the boundary, while in Eq. 5.38 R represents the difference between calcium concentration at the boundary and background calcium concentration.

Buffers

CalC allows an arbitrary number of Ca^{2+} buffers, with one-to-one or one-to-two Ca^{2+} binding stoichiometry, to be included in the simulation.

In the case of one-to-one stoichiometry, the following parameters need to be specified to characterize the buffer: total concentration, diffusion (if the buffer is mobile), boundary conditions and calcium binding kinetics, by defining two of the following three parameters: binding rate (k^+), unbinding rate (k^-) or affinity ($K_D = k^-/k^+$). Before the simulation is initiated, the program automatically calculates the initial buffer concentration from its kinetic parameters and total concentration value, assuming an equilibrium with the defined background Ca^{2+} concentration.

To define a buffer with one-to-two calcium binding stoichiometry, the rates of the two reactions in the following diagram should be declared as properties of the buffer B for the first reaction, and of buffer CaB for the second:

$$B + 2Ca^{2+} \underset{k_1^-}{\overset{k_1^+}{\rightleftharpoons}} CaB + Ca^{2+} \underset{k_2^-}{\overset{k_2^+}{\rightleftharpoons}} Ca_2B. \quad (5.39)$$

The diffusion coefficient of a cooperative buffer is allowed to changed upon Ca^{2+} binding, so three diffusivities have to be defined for a buffer B, namely the diffusion for B, CaB and Ca_2B. If the total concentration is defined for the unbound buffer only, then the fully and partial bound states of the buffer are assumed to be in

equilibrium with the background Ca^{2+}. Alternatively, total concentration of each state can be given. In this case, the simulation will start from the defined non-equilibrium initial condition.

Calcium Channels

An arbitrary number of calcium channel can be defined. For each channel, location and width of the spatial distribution of the current need to be defined. The default value for the width parameters is zero, which correspond to a point-like source. Channels can be located either inside the simulation volume or on the boundary.

Simulation Specifications

The simulation run requires specifying the integration time and the value of the calcium channel current during the run. There are two integration methods, the adaptive, corresponding to a variable time step, and the non-adaptive, corresponding to a fixed time-step.

When using the adaptive time-step method, the size of the integration time step is constantly modified to maintain a given level of accuracy. Optional parameters can be used to modify the working setup of the method. For example the initial time-step can be set, and it will be automatically reduced if the error tolerance accuracy is not met. Without going into the details, other parameters can be set in order to obtain the desired accuracy. Accuracy checks are performed every n-steps: if accuracy check is successful, n is increased by one, otherwise the time step is halved, and n is reset depending on the number of steps since last time step reduction. If the error is greater than five times the accuracy tolerance, the integrator takes a reverse step back to the previous successful accuracy check.

The parameters for the non-adaptive method are very simple, since it is sufficient to specify the time-step. The accuracy is an optional parameter.

The simulation may be broken down into an arbitrary number of shorter simulations. In this case, there should be a current definition for each part. Breaking up the simulation into multiple “runs” is desirable when the calcium channel currents change abruptly during the run, as when simulating channel opening and closing events. If an adaptive method is used, it is important that the channel current is continuous during each of the individual “runs”. This will limit the error arising from large current discontinuity.

Finally, the most important hidden parameter controlling the accuracy of the numerical PDE solver specifies how many iterations the numerical engine performs to integrate the non-linear buffering reaction in each time step. The default value is equal to 3, but in the case of very fast Ca^{2+} buffering reactions, its value should be increased to insure accuracy.

Other Features

With proper commands, it is possible to define intracellular calcium uptake into internal stores such as ER or mitochondria. Furthermore, CalC scripts may include ordinary differential equations, for instance to model Ca^{2+}-dependent exocytosis. It is also possible to introduce additional time-dependent variables, that are functions of ODE variables, or a discrete continuous-time stochastic variable.

5.4 Simulation Setup

In the previous Section, CalC general features have been presented. In this Section, the simulation setup for this subproject will be described.

Geometry and Boundary Conditions

For simplicity, the pancreatic β-cell was represented by a sphere with radius 6.5 μm(Fig. 5.8A). The assumption that calcium channels are uniformly distributed on the surface, and that the density of calcium channel in the β-cells is low [29], allowed us to restrict the simulations to a conical region 3 μm in diameter at its base (Fig. 5.8B).

A reflective boundary condition was imposed for both Ca^{2+} and buffers on the sides of the cone. This corresponds to the assumption that the Ca^{2+} and buffer fluxes flowing into the cone from the neighboring Ca^{2+}-channel regions are balanced by the equal fluxes flowing out of the cone. Alternatively, the same boundary condition holds if calcium and buffers levels are at background levels at the boundary.

These assumptions allowed us to simplify the geometry and to perform simulations in rotationally symmetric spherical (r, θ) coordinates, instead of solving the problem in full three dimensions. The reduction from three to two dimensions significantly reduced the computational intensity of the simulations.

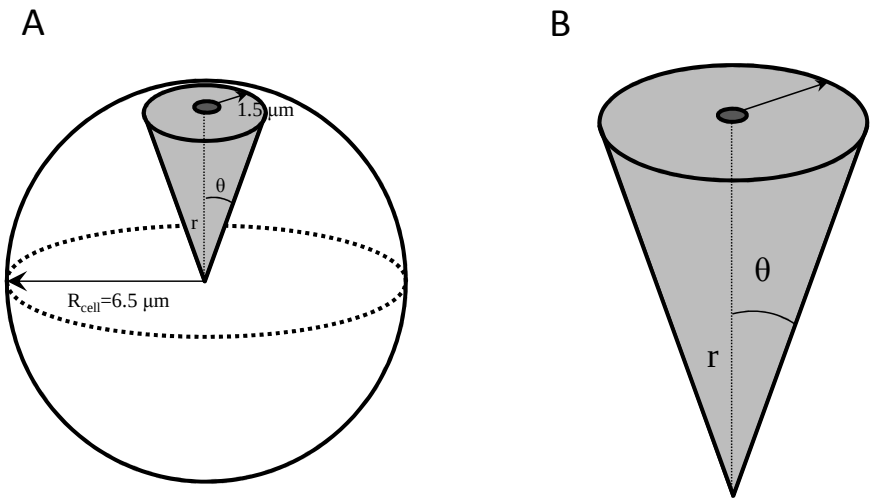

Figure 5.8: A) Schematic representation of the cell. B) Conical symmetry with calcium channel in the enter of the cone base.

Buffers

The calcium simulations included three types of buffers. The R-GECO sensor, which was described in Section 5.2.2 and was used to visualize submembrane calcium levels, responds to the binding of Ca^{2+} by increasing its fluorescence. It is genetically encoded to localize in the plasma membrane, hence it was assumed to be immobile and its distribution was confined to a thin layer under the cone base (50 nm). In CalC the total concentration of the buffer must be fixed. However, in the R-GECO case, it makes more sense to consider its area density to determine if it is a reasonable value. A total concentration, C_T, of 20 μM and a thickness of 50 nm for the layer, in which the buffer is present, were assumed in the simulations. In this case, to convert from total concentration to area density consider the following steps:

$$\begin{aligned} 20\mu\text{M} \cdot 50\text{nm} &= 10^{-21}\text{mol}/\mu\text{m}^2 = \\ &= 6.02 * 10^2\text{molecules}/\mu\text{m}^2 = 1 \text{ molecule}/0.0017\mu\text{m}^2, \end{aligned}$$

which corresponds roughly to the reasonable value (Prof. Sebastian Barg, private communication) of one molecule every 40 nm x 40 nm of square patch. Its kinetics rate constants and affinity was take from the literature [155]. It is worth noting, that R-GECO has slow binding kinetics, similar to EGTA.

The second buffer included in the simulations was the exogenous buffer used during the experiment, which was EGTA-AM or BAPTA-AM. Their characteristics

Parameter	R-GECO	Endogenous	EGTA-AM	BAPTA-AM	Unit
C_T	20	50	50	50	μM
D	0	0	0.22	0.22	$\mu m^2/ms$
k^+	0.01	0.1	0.01	1	$1/(\mu Mms)$
K_D	0.48	2	0.2	0.2	μM

Table 5.1: Default buffer parameters for CalC simulations: C_T total buffer concentration, D diffusion constant, k^+ binding rate constant and K_D affinity.

were taken from the literature [160]. The two buffers have identical diffusion coefficients, and similar affinities to calcium. However, BAPTA-AM binding to calcium is approximately 100 times faster compared to EGTA-AM. To simplify the results analysis, in the simulations the two buffers were assumed to have identical calcium affinity and exactly two orders of magnitude in the difference of binding kinetics. Taking the original values does not affect the results significantly. Little is known about the internal concentrations of the two buffers inside the cell, since they passively move from outside to the inside of the cell. As a consequence, the sensitivity of the results to this parameter was tested.

The last buffer included in the simulations was a generic endogenous buffer. As already discussed in the previous Section, it is a good approximation to consider the endogenous buffer as a fixed one. However, very little is known about its other characteristics. Hence, the sensitivity of the results to these parameters was evaluated.

The default buffer parameters for the CalC simulations are reported in Table 5.1.

Calcium Channels

A Ca^{2+}-channel is not continuously open during stimulation of the β-cell (see Fig. 8 and 10 in [29]). As a consequence besides the magnitude of the single channel current, the opening sequence of the single channel should be defined to perform the simulations.

The single channel current can be calculated as

$$i_{Ca} = \bar{g}_{Ca}(V - V_{Ca}), \tag{5.40}$$

where $\bar{g}_{Ca}$ is single Ca^{2+}-channel conductance, whose value was reported in [60]. Since experiments were performed with 2.6 mM extracellular Ca^{2+}, the corresponding calcium reversal potential V_{Ca} is $\sim$65 mV. Depolarizing the cell with 75 mM

KCl results to a potential of approximately 0 mV [[161]]. This gives a single channel current of ∼2 pS ·(0 − 65) mV= 0.13 pA. Alternatively, the single channel current can be calculated from

$$i_{Ca} = \frac{I_{Ca}}{N_{Ca}}, \tag{5.41}$$

where I_{Ca} is the total calcium current and N_{Ca} is the number of open calcium channels. Since in a β-cell there are ∼450 calcium channel [29], assuming that they are all open at 0 mV, from Figure 1 in [29], one gets:

$$i_{Ca} = \frac{I_{Ca}(0)}{N_{Ca}} = \frac{82}{450}\ \text{pA} = 0.18\ \text{pA}, \tag{5.42}$$

which is in accordance with the previous calculated value.

Regarding the opening sequence, it was reported that depolarization to 0 mV cause an average open time of 1.9±0.3 ms and a mean closed time of 63±20 ms, in recording that contain only a single active channel [29].

For simplicity, in the first part of this subproject the opening sequence was supposed to be deterministic, as a fixed repetition of open and close periods of 2 ms and 63 ms of duration respectively. The magnitude of the current was supposed to be three times bigger than the previous calculated value, given the high probability of triplets of channels in β-cells [29].

5.5 Simulations Results

5.5.1 Calcium Levels and GECO Signal

CalC simulations allow us to track both unbound Ca^{2+} and buffers levels. Unbound Ca^{2+} is the most interesting value, since it has an effect on exocytosis, while the only buffer concentration that has a significant meaning is bound GECO, since it corresponds to the fluorescence data. The concentration of bound GECO is not directly saved from CalC, but it can be easily calculated as the difference between the total concentration and the unbound one, which is directly saved from CalC. The resulting value is normalized by the pre-stimulus bound concentration.

Figure 5.9 shows an example of calcium diffusion simulation during the opening of the Ca^{2+}-channel. In particular, it is possible to see calcium levels both inside the cone (Fig. 5.9A), which represents the inside of the cell, and at the base of the cone (Fig. 5.9B), which represents the submembrane area. The calcium concentration during channel opening reaches high values in close proximity to the channel.

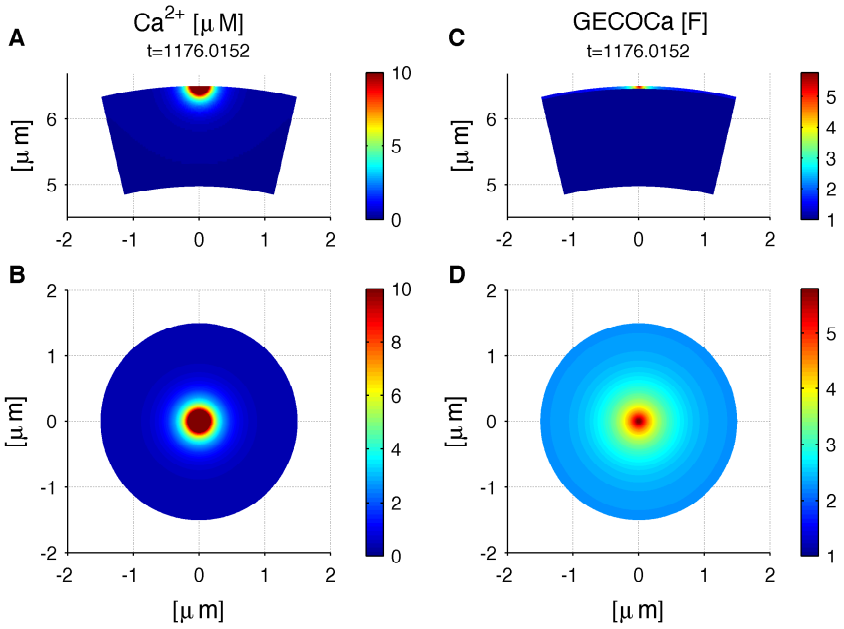

Figure 5.9: **CalC simulation of calcium levels and GECO signal with exogenous buffer EGTA-AM during the opening of the calcium channel.** A) Calcium levels inside the cone . B) Calcium levels at the base of the cone. C) GECO levels inside the cone. D) GECO levels at the base of the cone.

It is worth analyzing how the calcium concentrations translate to the GECO signal. For example, since GECO is membrane-bound, its signal does not spread inside the cell, but it is confined to a thin layer (50 nm) representing the submembrane area (Fig. 5.9C). In this area GECO signal looks quite different compared to the calcium levels (Fig. 5.9B,D). As GECO has high affinity to calcium ($K_D = 0.48$ μM), it is easily saturated by the high concentrations close to the channel. Furthermore, GECO is able to detect also the small changes at some distance from the channel.

In Figure 5.9 only one time instant is considered. However, we are interested in the time changes in calcium levels. To visualize them at different distances from the calcium channel, it is advantageous to consider the conical symmetry and take a line passing through the calcium channel on the cone base. It is possible to evaluate what happens along that line during the entire simulation as a 2D matrix. In particular, putting the simulation time on the x-axis, calcium levels and GECO signal close to the channel (y-axis =0) and far from the channel can be observed simultaneously (Figure 5.10).

In Figure 5.10A, the short opening of the channel are observable as small red

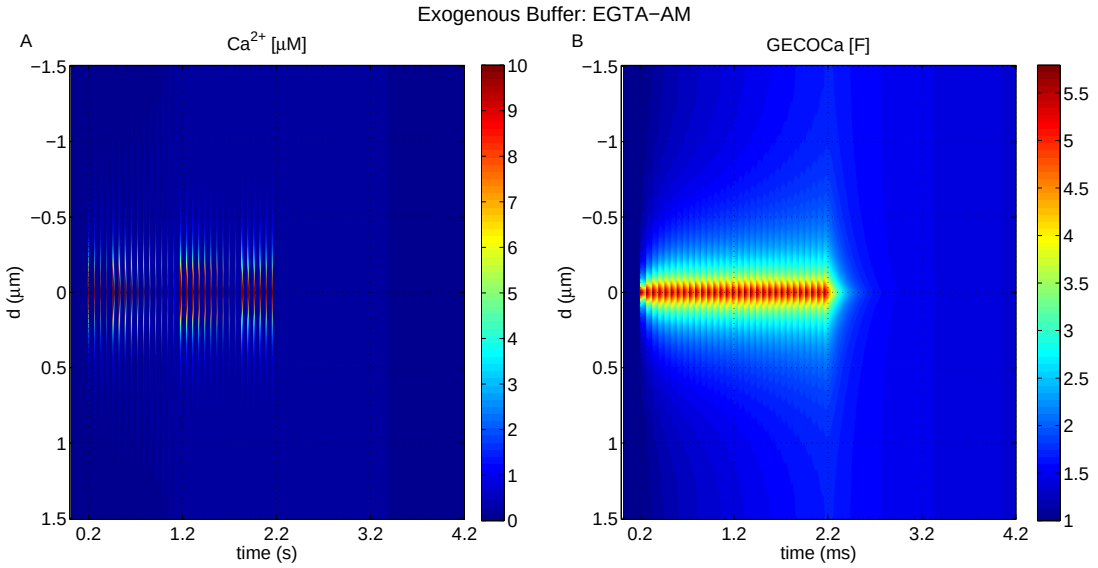

Figure 5.10: **CalC simulation of calcium levels and GECO signal during KCl depolarization stimulus between 2.2 and 4.2 seconds and exogenous buffer EGTA-AM.** A) Calcium levels during stimulus as a function of time and distance from the calcium channel. B) GECO signal during stimulus as a function of time and distance from the calcium channel.

areas, which rapidly vanished as the channel closes. In this case too, it is worth to compare calcium simulations to the corresponding GECO signal (Fig. 5.10B). Since GECO has slow binding kinetics, the short openings of the channel are not clearly observable. Moreover, the high affinity of GECO to calcium allows us to visualize small changes in calcium levels even far from the channel.

So far we visualized simulations of calcium levels and GECO signal without considering the experimental influence. Two aspects should be considered and will be briefly mentioned here without going into the details, which are beyond the scope of this Thesis. The first aspect to be considered is the point spread function of the microscope, which describes the response of an imaging system to a point source. This means that a real point light source would be seen as a blob in the image, which exactly corresponds to the point spread function. Mathematically, the acquired image is the results of the convolution between the real source and the point spread function, which depending of the form of the point spread function would result in an attenuation of the steep spacial gradients in the image.

The second aspect is the fact that the microscope does not capture the image instantly, but it needs ∼50 ms to capture a sufficient number of photons to produce the image, and has a sampling time of 100 ms. As a consequence, the second post-

processing to the simulation was to down-sample the simulation every 100 ms and, instead of taking the instant simulation value, the average over the previous 50 ms was calculated.

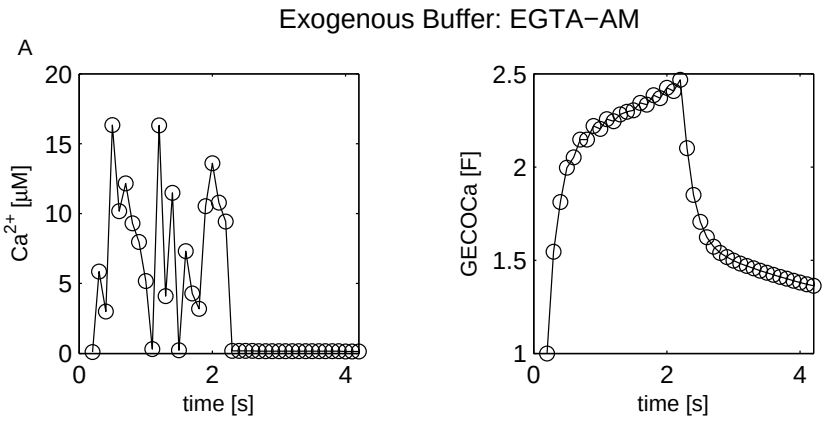

Figure 5.11: CalC simulation of calcium levels (A) and GECO signal after the post-processing steps (B) at 0.3 μm from the calcium channel. KCl depolarization stimulus between 2.2 and 4.2 seconds and EGTA-AM as exogenous buffer.

Since the GECO signal is the light source for our TIRF data, these two post-processing steps were applied to the GECO signal only.

In Figure 5.11, calcium levels and GECO signal after the post-processing steps at a fixed distance from the channel as a function of time are shown. However, to compare the results to the available data, one should take into account that the granules that undergo exocytosis are not all located at the same distance from the channel, but most likely are spread at different distances. As a consequence, instead of plotting the calcium levels at a fixed distance from the channel, it is reasonable to divide the area around the calcium channel in regions with different distances to the channel: around the Ca^{2+}-channel (0-0.16 μm), close to the Ca^{2+}-channel (0.16-0.32 μm or 0.32-0.48 μm), and far from the Ca^{2+}-channel (0.48-1.5 μm). Results are shown in Figure 5.12.

As said before, calcium reaches high concentrations only close to the channel. In particular, simulations predict that between 0 and 0.16 μm from the Ca^{2+}-channel an average concentration of 15-20 μM is reached during the opening of the channel, while further from the channel concentrations do not exceed 2 μM (Fig. 5.12A). On the other side, given its high affinity, GECO levels are easily saturated by high concentrations of calcium. As a consequence, differences between groups can be

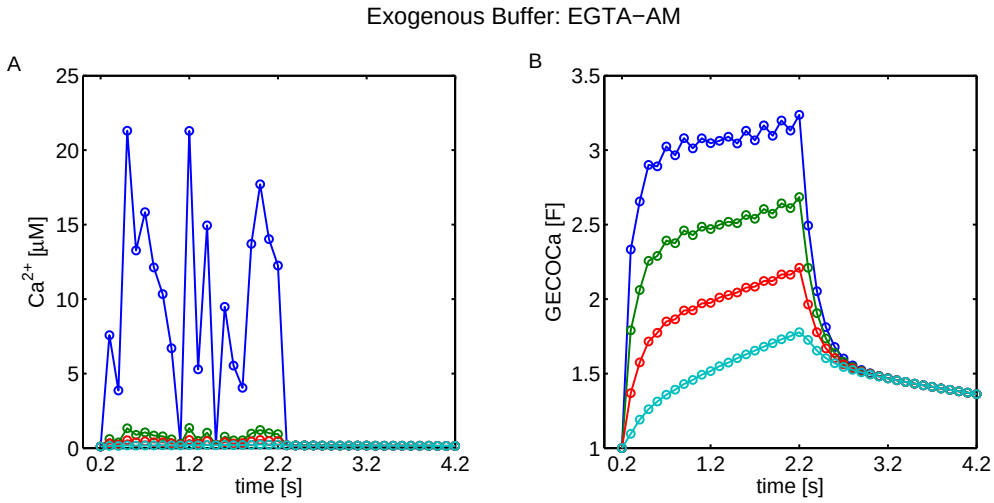

Figure 5.12: CalC simulation of calcium levels (A) and GECO signal after the post-processing steps (B) and EGTA-AM as exogenous buffer. KCl depolarization stimulus between 2.2 and 4.2 seconds. The different groups represent the average of calcium levels or GECO signal in regions with different distances from the channel: 0-0.16 μm (dark blue), 0.16-0.32 μm (green), 0.32-0.48 μm (red) and 0.48-1.5 μm (light blue).

detected even further of 0.16 μm from the channel (Fig. 5.12B). Moreover, the calcium levels are very irregular, due to the short opening and the longer closing of the channel. Contrarily, given the slow kinetics of GECO, its levels are regular since the closing time is too short for calcium to unbind from GECO. As a consequence, GECO signal is almost monotonically increasing and eventually saturated.

Similar figures can be obtained when the exogenous buffer EGTA-AM is substituted with the BAPTA-AM, as for the experimental data. A summary of the results is reported in Figure 5.13.

In the simulations where EGTA-AM is used, the exogenous buffer competes with GECO for binding Ca^{2+}, since they have similar kinetics. Contrarily, BAPTA-AM, which has 100 times faster binding kinetics, tends to overrule GECO limiting its fluorescence closer to the channel (compare Fig. 5.10A,B with Fig. 5.13A,B). Accordingly, the group closest to the channel (0-0.16 μm) has lower GECO signal compared to the EGTA case (compare Fig. 5.12B with Fig. 5.13D), while calcium levels are more similar (compare Fig. 5.12A with Fig. 5.13C). As a consequence, the use of BAPTA-AM as endogenous buffer in the simulations allows to differentiate better the regions closer to the Ca^{2+}-channel, while it tends to flatten the difference for further groups.

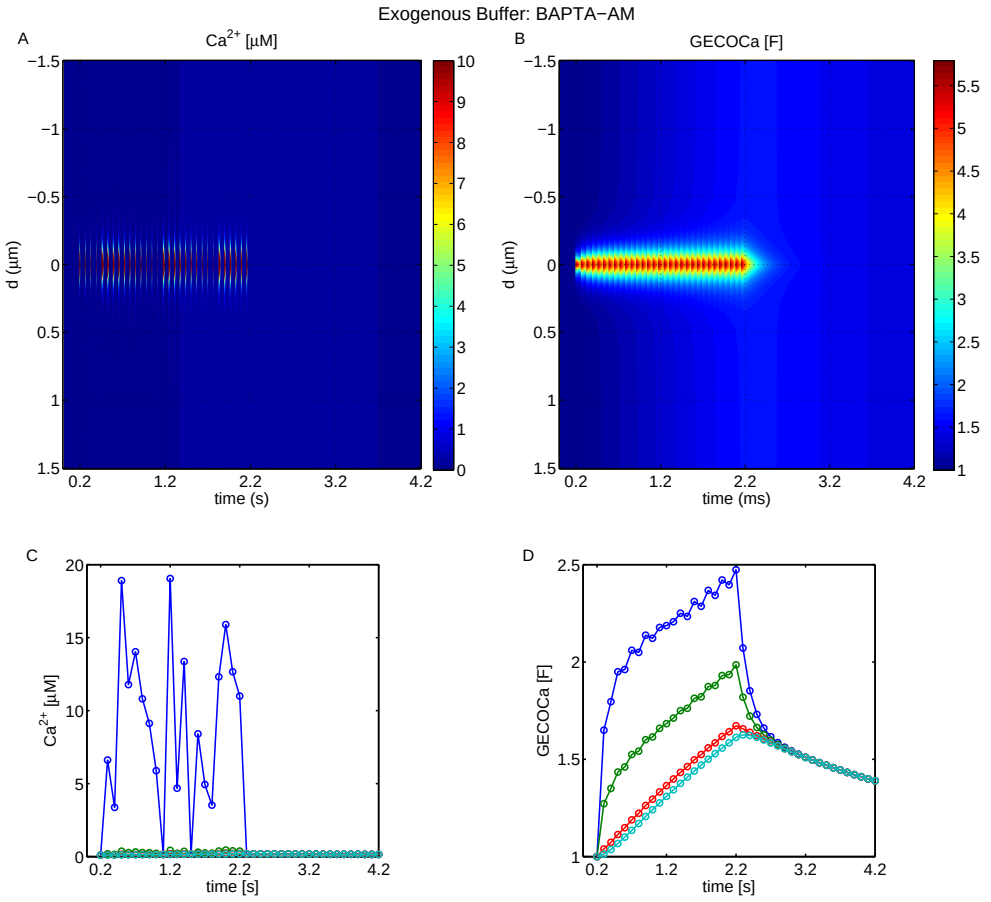

Figure 5.13: CalC simulation of calcium levels and GECO signal with exogenous buffer BAPTA-AM. KCl depolarization stimulus between 2.2 and 4.2 seconds. A) Calcium levels during stimulus as a function of time and distance from the calcium channel. B) GECO signal during stimulus as a function of time and distance from the calcium channel. CalC simulation of calcium levels (C) and GECO signal after the post-processing (D) grouped by distance. The different groups represent the average of calcium levels or GECO signal in regions with different distances from the channel: 0-0.16 μm (dark blue), 0.16-0.32 μm (green), 0.32-0.48 μm (red) and 0.48-1.5 μm (light blue).

5.5.2 Examples of Results Sensitivity to Parameter Changes

In Section 5.4, it was pointed out that little is known about some parameters of the buffers included in the simulations. Here, for completeness some examples of parameter changes will be presented in the case of EGTA-AM as exogenous buffer. Such analysis is usually performed to evaluate which parameter value has greater influence on the results, and consequently should be carefully set. Alternatively, it helps in identifying the parameters, whose value is not necessary to know precisely.

Endogenous Buffer Concentration

Very little is known about the characteristic of the endogenous buffer. However, the buffer capacity ($\kappa = B_T/K_D$) can help in finding a reasonable value for total concentration, even if it is very variable between cells. With the default parameters, the buffer capacity was 25, which is in the lower range for physiological cytoplasmic buffer capacity. As a consequence, it was worth to analyzed what happens if the total concentration of the endogenous buffer is increased 10 times. The comparison of this situation with the default simulation is reported in Figure 5.14B and A respectively, where GECO signal is shown.

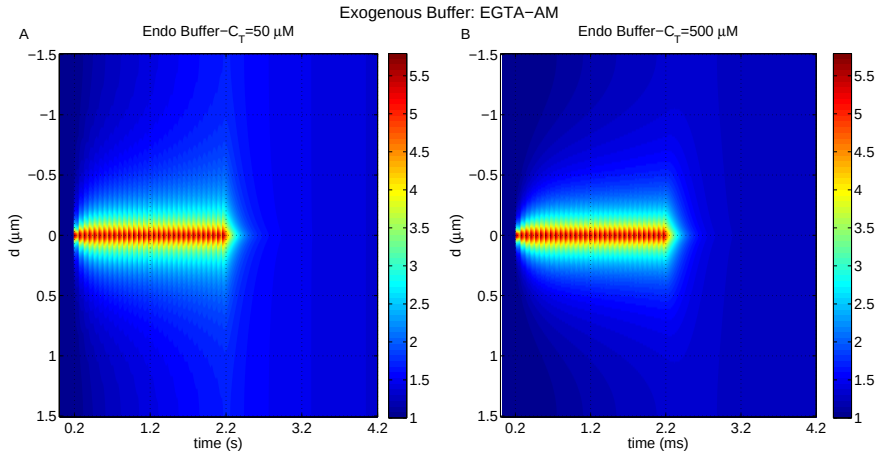

Figure 5.14: CalC simulation of GECO signal with exogenous buffer EGTA-AM, default parameters (A) and a 10 times bigger total concentration (C_T=500 μM) of the generic endogenous buffer (B). KCl depolarization stimulus between 2.2 and 4.2 seconds.

From Figure 5.14, it is possible to notice that the increased concentration of the endogenous buffer causes slightly lower values of GECO signal far from the Ca^{2+}-channel. However, the global results are not significantly affected by a 10 times change in the concentration of the endogenous buffer. As a consequence, it can be concluded that even if the total concentration of the endogenous buffer is not known precisely, its value will probably not affect the results.

R-GECO Density

In Section 5.4, the GECO superficial density was discussed. The expression of the GECO sensor is not controllable and varies from cell to cell. Nevertheless, a range of reasonable values is known (Prof.Sebastian Barg, private communication).

In some cells, it might happen that GECO expression is lower compared to the default value in the simulations. Hence, we analyzed what happens if GECO density (or alternatively GECO concentration, since thickness of the layer of GECO was kept constant) was reduced 10 times.

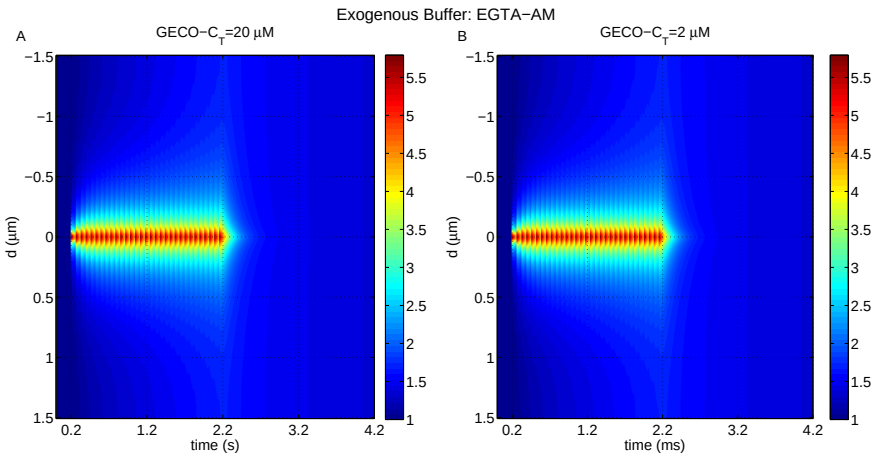

Figure 5.15: CalC simulation of GECO signal with exogenous buffer EGTA-AM, default parameter (A) and a 10 times smaller total concentration (C_T=2 μM) of R-GECO (B). KCl depolarization stimulus between 2.2 and 4.2 seconds.

In Figure 5.15 the two situations are compared. The two figure are almost identical, probably thanks to the high affinity of GECO to calcium. As a consequence, also GECO density do not affect the results.

Virtually Playing with the GECO Sensor

Finally, an interesting application of the simulations will be presented. Experimentally, it is very difficult to change the properties of the sensor. Would it be possible to know in advance if all these efforts in changing the sensor are worth? Changing the properties of the sensor in the simulations can be a fast and easy way to check, if they will improve the data based on the aims of the problem.

Above, it was observed that GECO has slow kinetics. How will the results change if a faster sensor was available? The results are shown in Figure 5.16, where the GECO binding constant, k^+, was increased 10 times, obtaining a fast "virtual" GECO sensor.

With a faster kinetics, the "virtual" GECO sensor would be able to detect the short opening of the Ca^{2+}-channel. Furthermore, the "virtual" GECO sensor would

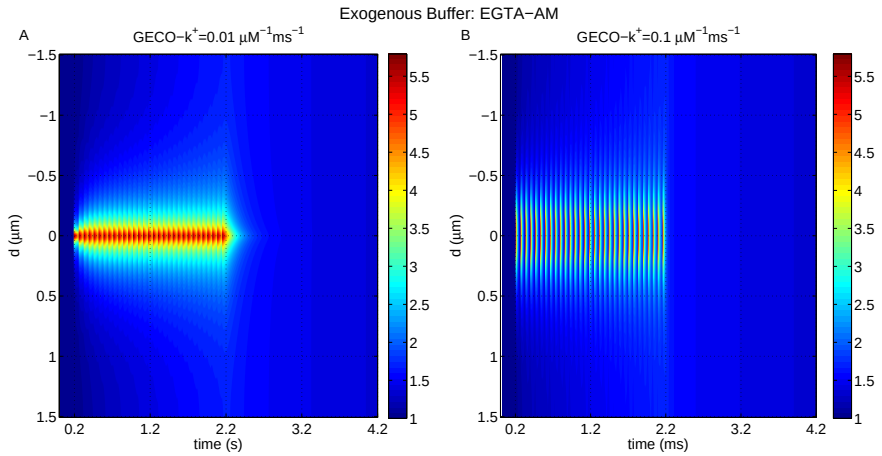

Figure 5.16: CalC simulation of GECO signal with exogenous buffer EGTA-AM, default parameter (A) and a 10 times faster "virtual" GECO sensor (k^+=0.1 μM^{-1}ms^{-1}) (B). KCl depolarization stimulus between 2.2 and 4.2 seconds.

be able to bind Ca^{2+} far from the channel already from the first opening of the channel, probably thanks to the overruled competition with the slower EGTA-AM.

5.6 Comparison TIRF Data and Discussion

While in the previous Section, the CalC simulations results were presented, in this Section they will be compared to the TIRF data, which were described in Subsection 5.1.3. In particular, the data will be compared to the GECO signal simulations grouped by distance, in order to determine if the rise time can give some information about the location of the exocytotic granules.

To allow a direct comparison of the simulation with the data, the different groups in Figure 5.12B and in Figure 5.13D, for exogenous buffer EGTA-AM and BAPTA-AM respectively, were similarly normalized by subtracting the baseline pre-stimulus value and dividing by the maximum value, obtaining curves between 0 and 1 for each group. The normalized groups are shown in Figure 5.17B,D, for exogenous buffer EGTA-AM and BAPTA-AM respectively.

First, let us analyze the TIRF data, where cells were incubated with EGTA-AM (Fig. 5.17A). The exo and the control group exhibit similar rise times, with a slightly earlier increase for the exo group. Similarly, during the repolarization step, the control group decreases with a slightly slower kinetics than the exo group. These two characteristics are captured by the two groups, which are closest to the calcium

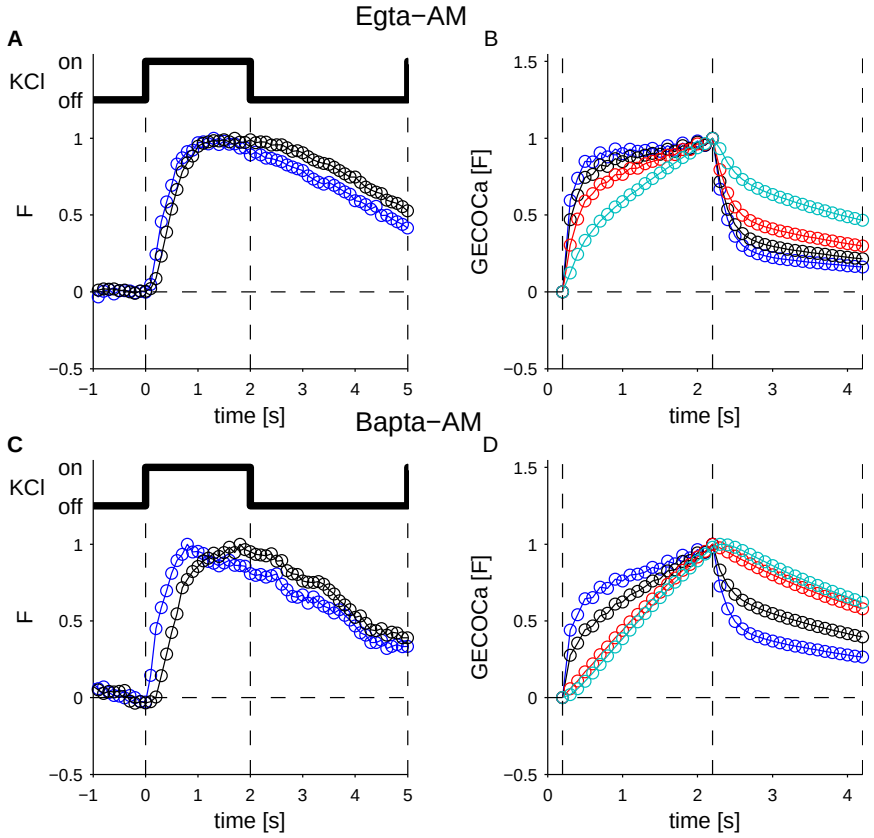

Figure 5.17: Comparison of TIRF data with CalC simulations. A) TIRF data, where cells were incubated with EGTA-AM. Exo group in blue and control group in black. B) CalC simulation with EGTA-AM as exogenous buffer. The different groups represent the average of calcium levels or GECO signal in regions with different distances from the channel: 0-0.16 μm (dark blue), 0.16-0.32 μm (black), 0.32-0.48 μm (red) and 0.48-1.5 μm (light blue). C) TIRF data, where cells were incubated with BAPTA-AM. Exo group in blue and control group in black. D) CalC simulation with BAPTA-AM as exogenous buffer. Groups as in B).

channel: 0-0.16 μm for the exo group in blue and 0.16-0.32 μm for the control group in black. The two groups have similar rise times during depolarization, and similar decrease during repolarization (Fig. 5.17B). However, the simulations in both groups have faster increase compared to the data. This can be due to different aspects, that were not considered in the simulations: the time required by KCl to depolarize the cell, or Ca^{2+}-channel inactivation, which can both affect the opening and closing times of the Ca^{2+}- channel.

The TIRF data, where cells were incubated with BAPTA-AM (Fig. 5.17C), can be used as a test set, i.e. considering the same groups as in the simulations with

EGTA-AM as exogenous buffer, to check if the changes in the simulations with different exogenous buffers are similar to the difference in the experimental data. The two groups, which are closest to the calcium channel (0-0.16 μm in blue and 0.16-0.32 μm in black), exhibit a bigger difference in the rise times when BAPTA-AM is used, instead of EGTA-AM (Fig. 5.17B,D). Similarly, the TIRF data, where BAPTA-AM is used as exogenous buffer, present a bigger difference in the rise time in the exo and control group compared to the data were EGTA-AM is used.

However, the results presented here are only preliminary and need further investigation. For example, both TIRF data and simulations were normalized by the maximum value of each group. This normalization was done since GECO level is not easily translated to calcium concentrations, since GECO expression might differ significantly between cells. As a consequence, we can compare rising times but it does not make sense to compare levels. Moreover, the time at which the granules undergo exocytosis was not taken into account here. It would be interesting to evaluate if there is any difference between the granules that do exocytosis in the first half second of depolarization and the ones that do it later.

6

From Electrical Activity to Exocytosis:

Calcium-Channels Clustering

Calcium diffusion simulations presented in the previous Chapter were coupled to a simple model for insulin granule exocytosis to investigate different pools of granules, in terms of vicinity to the Ca^{2+}-channel and Ca^{2+} affinity. Furthermore, the fusion probability was evaluated both for a single channel, and in a cluster-of- channels context.

This Chapter will firstly present the model of exocytosis and focus will be given to the various steps of exocytosis. Then, after having presented the aim of the coupling of diffusion to the exocytosis model, the implementation of the stochastic channel gating will be described. The Chapter will be concluded with the discussion of the simulation results.

6.1 Model of Exocytosis in Pancreatic Beta-cells

In this Section the mathematical model of exocytosis in pancreatic β-cells developed by Chen at al. will be briefly presented. For the details of the model and its applications see the original article [104].

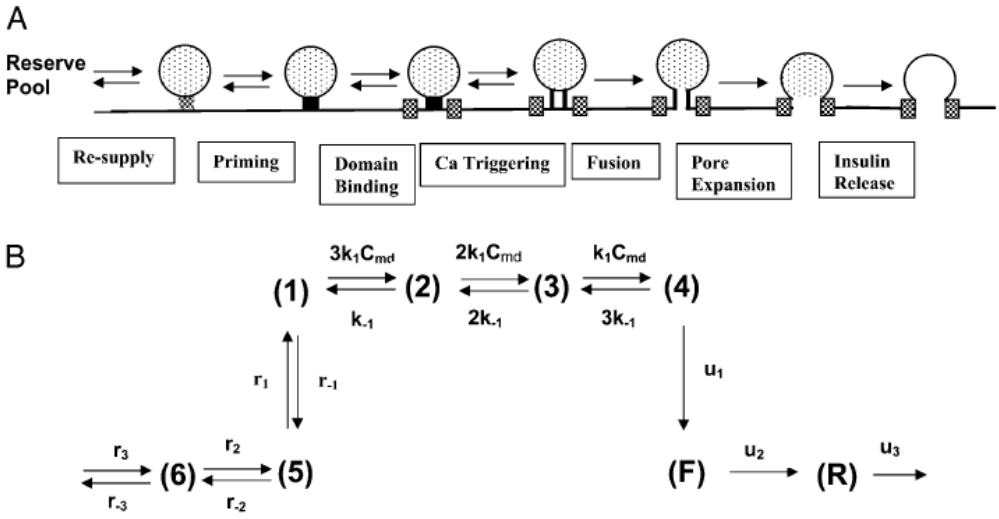

Figure 6.1: Steps of the exocytosis modeled in [104].

Chen's model uses a multi-state kinetic model to represent the various exocytotic reactions, which is combined with a simple two-compartment model to handle the temporal distribution of Ca^{2+} between the microdomain and the cytosol.

Granules in the cell are divided into a large reserve pool and a smaller pool of docked granules, which can be further subdivided according to different fusion competencies. Granules from the reserve pool have to undergo maturation before becoming exocytosable. In particular the exocytotic cascade is divided schematically into seven steps, as shown in Figure 6.1. These steps correspond to the fact that a granule has to dock to the membrane from a reserve pool, be primed, and move to the microdomain at an L-type Ca^{2+}-channel before it can bind with Ca^{2+} and fuse with the cell membrane.

The simplest kinetic scheme for this exocytotic cascade is given in Figure 6.1B, where each step in the cascade is represented by a single chemical reaction except the Ca^{2+} triggering step, which is described by three Ca^{2+} binding reactions as proposed for chromaffin cells [162]. The three pre-triggering ($\rightleftarrows(6)\rightleftarrows(5)\rightleftarrows(1)$) steps are assumed to be reversible, whereas the three post-triggering steps ($\rightarrow(4)\rightarrow(F)\rightarrow(R)$) are assumed to be irreversible. Due to the existence of these irreversible steps, the rates of fusion and insulin secretion of the system are always nonzero, even at the resting steady state.

The time-dependent distribution of the pool population in Figure 6.1B can be

described by following differential equations:

$$\begin{aligned}
\frac{dN_1}{dt} &= -\left[3k_1\mathrm{Ca_{md}}(t) + r_{-1}\right]N_1 + k_{-1}N_2 + r_1N_5,\\
\frac{dN_2}{dt} &= 3k_1\mathrm{Ca_{md}}(t)N_1 - \left[2k_1\mathrm{Ca_{md}}(t) + k_{-1}\right]N_2 + 2k_{-1}N_3,\\
\frac{dN_3}{dt} &= 2k_1\mathrm{Ca_{md}}(t)N_2 - \left[k_1\mathrm{Ca_{md}}(t) + 2k_{-1}\right]N_3 + 3k_{-1}N_4,\\
\frac{dN_4}{dt} &= k_1\mathrm{Ca_{md}}(t)N_3 - \left[3k_{-1} + u_1\right]N_4,\\
\frac{dN_5}{dt} &= r_{-1}N_1 - \left[r_1 + r_{-2}\right]N_5 + r_2N_6,\\
\frac{dN_6}{dt} &= r_3 + r_{-2}N_5 - \left[r_{-3} + r_2\right]N_6,\\
\frac{dN_F}{dt} &= u_1N_4 - u_2N_F,\\
\frac{dN_R}{dt} &= u_2N_F - u_3N_R, \qquad (6.1)
\end{aligned}$$

where N_i represents the number of granules in pool i, and $\mathrm{Ca_{md}}$ is the Ca^{2+} concentration in the microdomain compartment.

The resupply step is assumed to depend on both ATP and bulk cytosolic Ca^{2+}. The ATP dependency derives from the finding that insulin secretion from single islets drops to a low level after a long depolarization in the absence of glucose.

Both the resupply and priming steps are assumed to depend on Ca^{2+} concentration in the cytosol, $\mathrm{Ca_i}$, using the simple equilibrium binding formulae:

$$r_2 = r_2^0\mathrm{Ca_i}(t)/\left[\mathrm{Ca_i}(t) + K_p\right], \qquad (6.2)$$

$$r_3 = r_3^0\mathrm{Ca_i}(t)/\left[\mathrm{Ca_i}(t) + K_p\right], \qquad (6.3)$$

where K_p is a constant.

The rate of fusion, the rate of pore expansion and the rate of insulin secretion at time t can be calculated as:

$$J_F(t) = u_1N_4(t), \qquad (6.4)$$

$$J_R(t) = u_2N_F(t), \qquad (6.5)$$

$$J_{IS}(t) = u_3N_R(t). \qquad (6.6)$$

Similarly the accumulated total number of granules fused, the total number of gran-

ules ready to release and the total amount of insulin secreted corresponds to:

$$M_F(t) = \int_0^t u_1 N_4(t')dt', \tag{6.7}$$

$$M_R(t) = \int_0^t u_2 N_F(t')dt', \tag{6.8}$$

$$M_{IS}(t) = \int_0^t u_3 N_R(t')dt'. \tag{6.9}$$

The dynamics of Ca^{2+} concentration was modeled by two-compartments. The first compartment is represented by the microdomain, which corresponds to a half-sphere surrounding the inner mouth of an L-type channel. It is a functional microdomain, in the sense that it is the place where a primed granule can form a stable complex with the plasma membrane and execute the Ca^{2+} triggered fusion step. In contrast, the R-type channel is not functional because granules do not form stables complexes with the channel and therefore very few fusion events will occur there.

The calcium entering the first compartment through the L-type Ca^{2+}-channels, can diffuse to the second compartment which corresponds to the cytosol. Another entry source for the second compartment are the non functional R-type Ca^{2+}-channels. The clearance of Ca^{2+} from the cytosol compartment is assumed to be regulated by four types of transporters: SERCA pumps, the plasma membrane ATPase (PMCA), the NCX, and the leak channel. For their characterization and other details see [104].

6.2 Tradeoff between Distance from Calcium Channels and Calcium Affinity

In the previous Chapter, the average distance of exocytotic granules from calcium channel was estimated by comparison of simulations to TIRF microscopy data. However, the calcium levels are only one component in Ca^{2+}-triggered granule exocytosis. The affinity of the Ca^{2+} sensor on the granules plays an important role in regulating the secretion.

In many cell types the affinity is similar (20-30 μM), suggesting the existence of a common low-affinity Ca^{2+} sensor or members of a closely related family of Ca^{2+}-binding proteins with similar properties. However, in certain cell types, there are granules with distinct Ca^{2+} dependencies allowing differential control of their release.

In pancreatic β-cells, it is believed that first-phase secretion is a result of granules already residing at the membrane, whereas enhanced supply of new vesicles to the plasma membrane is responsible for second phase. Traditionally, the newly-arrived vesicles must go through maturation steps such as docking and priming before fusing, although other data suggest that newcomer granules fuse with almost no delay during second-phase secretion [163].

Most immediate exocytosis occurs with a very low affinity for Ca^{2+} from a readily releasable pool (RRP) of granules, showing an affinity to Ca^{2+} of tens of micromolar. Such high concentrations are only attained right below the calcium channels. In addition to the fast microdomain controlled exocytosis, another highly calcium-sensitive pool (HCSP) of granules has been described with an affinity to Ca^{2+} of a few micromolar. The difference in calcium affinity between the RRP and the HCSP might be explained by different isoforms of the Ca^{2+}-sensor synaptotagmin regulating membrane fusion from the two pools. Because both HCSP granules and newcomers fuse away from Ca^{2+}-channels, it was proposed that they might be overlapping sets of vesicle, and consist in granules that are still not completely docked to the cell membrane [163].

In the following Section, the exocytotic machinery will be analyzed as a function of distance from calcium channels and affinity of the calcium sensor.

6.2.1 Impact of Calcium Level versus Opening Time

In this context no experimental data were available to us. Nevertheless, the coupling of the diffusion simulations to the exocytotic model become an useful tool in evaluating the impact of the calcium levels in comparison to the calcium channel opening time.

In particular, under control conditions, the mean open time of the Ca^{2+}-channels during a depolarization is very short ($\sim$2 ms) compared to the delay between calcium elevation and the initiation of exocytosis ($\sim$10 ms). This lead to the idea that Ca^{2+}-channels clustering would be functionally advantageous. Furthermore, it was reported that calcium channels mainly clusters in triplets [29].

In this Chapter, three different situations will be compared: a single channel, a cluster of three channels with synchronized gating (all channels open simultaneously) and a cluster of three channels with independent gating (each channel opens independently from the others).

The difference between the single channel setup and the synchronized gating consists only on the current magnitude. However, the average open time of the cluster is equal to the open time of a single channel. This means, that calcium concentration reaches higher levels but only for a short time. On the contrary, the cluster with independent gating increase the possibility to find at least one open channel, but the probability that the three channels are open simultaneously is very low.

To implement the three different scenarios, stochastic simulation of channel gating was needed. In the following Section, the implementation as a Markov process will be described.

6.3 Stochastic Channel Gating

Consider the transition-state diagram already introduced in Chapter 2:

$$C \underset{k^-}{\overset{k^+}{\rightleftharpoons}} O, \tag{6.10}$$

where C corresponds to the closed state, O to the open state of the channel and the arrows stand for reversible elementary molecular processes regulated by k^- and k^+.

Let us define s as a random variable taking values corresponding to the two states, $s \in \{C, O\}$, and $P_i(t)$, the probability that $s = i$ at time t. If a two-state ion channel is in state O at time t, the probability that it will close in a short interval of time (Δt) is given by $k^- \Delta t$. By multiplying this probability to $P_O(t)$, the probability that the two-state channel is indeed in state O, one obtains the probability that the transition $O \to C$ actually occurs. Moreover, the probability that the channel is open at time $t + \Delta t$ is equal to the probability that it was open at time t minus the probability that it leaves this state plus the probability that has just open. In mathematical form:

$$P_O(t + \Delta t) = P_O(t) - k^- P_O(t)\Delta t + k^+ P_C(t)\Delta t \tag{6.11}$$

taking the limit $\Delta t \to 0$, one gets:

$$\frac{dP_O}{dt} = -k^- P_O(t) + k^+ P_C(t) \tag{6.12}$$

Considering that a channel is either open or close, and therefore:

$$P_C(t) + P_O(t) = 1, \tag{6.13}$$

it becomes:

$$\frac{dP_O}{dt} = k^+(1 - P_O(t)) - k^- P_O(t). \tag{6.14}$$

Since the probability that an open channel will close in Δt is given by $k^-\Delta t$, the probability that it will stay open is $1 - k^-\Delta t$. Similarly for a closed channel. Hence, the transition probability matrix takes this form:

$$Q = \begin{bmatrix} 1 - k^+\Delta t & k^-\Delta t \\ k^+\Delta t & 1 - k^-\Delta t \end{bmatrix}, \tag{6.15}$$

where the elements Q_{ij} of the matrix correspond to the transition probability from state j to state i.

Using the transition probability matrix, the state of the channel at $t + \Delta t$ can be written as:

$$\mathbf{P}(t + \Delta t) = Q\mathbf{P}(t), \tag{6.16}$$

where $\mathbf{P}(t)$ is the vector that contains the current state of the channel $[P_C(t); P_O(t)]$. In the general case:

$$\mathbf{P}(t + n\Delta t) = Q^n\mathbf{P}(t). \tag{6.17}$$

The transition probability matrix is useful to calculate the average amount of time that the channel remains in the open or the closed state, the so called *dwell times*. While the probability that one open channel will stay open in a Δt interval is $1 - k^-\Delta t$, the probability that it will stay open for the following time step is $(1 - k^-\Delta t)^2$. In general:

$$P_O(t + n\Delta t|O, t) = (1 - k^-\Delta t)^n. \tag{6.18}$$

By defining $\tau = n\Delta t$, Eq. 6.18 becomes:

$$P_O(t + \tau|O, t) = \left(1 - \frac{k^-\tau}{n}\right)^n. \tag{6.19}$$

Taking the limit for $\Delta t \to 0, n \to \infty$, one gets:

$$P_O(t + \tau|O, t) = e^{-k^-\tau}, \tag{6.20}$$

which means that the probability that a channel open at time t stays open until $t+\tau$ is a decreasing exponential function of τ. Finally, the probability that a channel open at time t stays open until $t + \tau$ and then close for the first time in the next Δt is given by:

$$P_C(t + \tau|C, t)P_O(t + \tau + \Delta t|C, t + \tau) = e^{-k^-\tau}k^-\Delta t. \tag{6.21}$$

Hence, the average open time corresponds to

$$\langle \tau_O \rangle = \int_0^\infty \tau e^{-k^- \tau} k^- d\tau = \frac{1}{k^-}. \tag{6.22}$$

Similarly, the average closed time is

$$\langle \tau_C \rangle = \int_0^\infty \tau e^{-k^+ \tau} k^+ d\tau = \frac{1}{k^+}. \tag{6.23}$$

6.3.1 Single Channel Setup

To simulate the transitions of a two-state channel, a simple method based on the transition probability matrix can be used. Since the conservation of probability ensures that each column of Q will sum to unity, we can divide the interval $[0, 1]$ into regions, each corresponding to a possible change of state or lack of change of state. Then, using a random number Y uniformly distributed on the interval $[0, 1]$, it is possible to choose if a transition took place or not based upon the interval in which Y falls.

In particular, $Q_{12} = k^- \Delta t$ corresponds to the probability that an open channel closes in the next time step Δt. Hence, if the current state is O, then a transition to the closed state occurs if $0 \leq Y < k^- \Delta t$, while the channel remains open if $k^- \Delta t \leq Y \leq 1$, which is an interval of length $1 - k^- \Delta t$ equal to Q_{22}, the probability that an open channel stays open. Similarly, if the channel is in state C, then a transition will occur if $1 - k^+ \Delta t \leq Y \leq 1$, while it remains closed if $0 \leq Y < 1 - k^+ \Delta$.

Now, if the average open and closed times is known, the rate constants k^+ and k^- can be calculated as the reciprocal values. The average open and close times for a single calcium channel in mouse pancreatic β-cells depolarized to 0 mV was reported in [29] and correspond to $\sim$2 ms and $\sim$63 ms respectively. An example of a simulated single channel stochastic gating is reported in Figure 6.2A.

6.3.2 Cluster: Synchronized Gating

The implementation of a cluster with synchronized gating is straightforward. Since the cluster gating dynamics is the same as for a single channel, it is sufficient to change the magnitude of the current depending on the number of channels in the cluster. An example is shown in Figure 6.2B, where the cluster is formed by three channels.

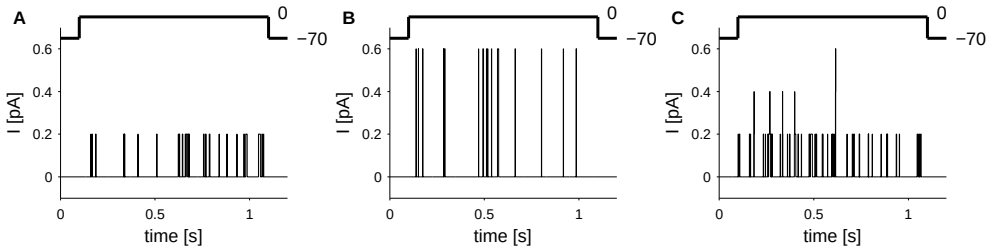

Figure 6.2: Examples of simulation of stochastic gating in a single channel (A), a cluster with synchronized gating (B) and a cluster with independent gating (C)

6.3.3 Cluster: Independent Gating

Finally, the gating of multiple independent channels can be simulated in several ways. The most intuitive method for simulating a small number of independent two-state ion channels is to implement N stochastic simulations of a single channel and just take their sum.

Alternatively, under the assumption of identical and independent channels, it is worth mentioning an alternative method, which consists to simulate a single Markov process that tracks the number of open channels. For simplicity, consider an example of a cluster of three channels. In this case, there are four possibilities for the number of open channels (0, 1, 2 or 3) and thus four distinguishable states for the Markov process. By representing the states as S_0, S_1, S_2 and S_3, the transition state diagram is the following

$$S_0 \underset{k^-}{\overset{3k^+}{\rightleftharpoons}} S_1 \underset{2k^-}{\overset{2k^+}{\rightleftharpoons}} S_2 \underset{3k^-}{\overset{k^+}{\rightleftharpoons}} S_3, \tag{6.24}$$

where the factors modifying the rate constants k^+ and k^- account for the fact that more channels in the same state can make a transition.

The corresponding transition probability matrix is

$$Q = \begin{bmatrix} 1-3k^+\Delta t & k^-\Delta t & 0 & 0 \\ 3k^+\Delta t & 1-k^-\Delta t-2k^+\Delta t & 2k^-\Delta t & 0 \\ 0 & 2k^+\Delta t & 1-2k^-\Delta t-k^+\Delta t & 3k^-\Delta t \\ 0 & 0 & k^+\Delta t & 1-3k^-\Delta t \end{bmatrix}. \tag{6.25}$$

The implementation is quite similar to the single channel case. Since the conservation of probability ensures that each column of Q will sum to unity, we can divide the interval $[0, 1]$ into regions, each corresponding to a possible change in the number of open channels. Then, using a random number Y uniformly distributed on

the interval $[0, 1]$, it is possible to choose if the number of open channels increases, decreases or remains constant.

In particular, supposing that only one channel is open (state S_1), $Q_{12} = k^-\Delta t$ corresponds to the probability that this single channel closes in the next time step Δt. Hence, a transition to the closed state occurs if $0 \leq Y < k^-\Delta t$, reaching state S_0. While one of the two closed channel opens if $k^-\Delta t \leq Y < k^-\Delta t + 2k^+\Delta t$, which is an interval of width $2k^+\Delta t$. In this case the system reaches state S_2. Finally, the system stays in S_1 if $k^-\Delta t + 2k^+\Delta t \leq Y \leq 1$, which is an interval of length $1 - k^-\Delta t - 2k^+\Delta t$, corresponding to Q_{22}. Similarly, if the system is initially in any other state. An example of simulation is shown in Figure 6.2C.

6.4 Comparison and Discussion

In the following, each shown figure is the average on ten stochastic simulations, which was used to get an idea on the average behavior of the model avoiding the misinterpretation of results due to the single specific realization of the stochastic opening sequence. The simulations, whose results are presented in this Section, consists of two seconds depolarization. Moreover, the initial values for the granules in each state was not changed from the one used in Chen's paper. The results presented here can be scaled be any value, keeping the ratio between pools unchanged.

Stochastic versus Deterministic Opening Sequences

In the previous Chapter, the opening of the calcium channel was supposed deterministic for simplicity. For the aim of this analysis, it was more reasonable to consider a stochastic sequence. In particular, the current set in the deterministic context corresponds to a cluster of three channel (0.6 pA). As a consequence, the calcium diffusion simulations obtained in the previous Chapter should be comparable to the stochastic one obtained for a cluster with synchronized gating.

In Figure 6.3, the simulation of GECO signal grouped by distance as a results of a deterministic sequence is compared to the average of ten stochastic simulations for a cluster with synchronized gating. As one would expect, the deterministic sequence and the stochastic one give similar results.

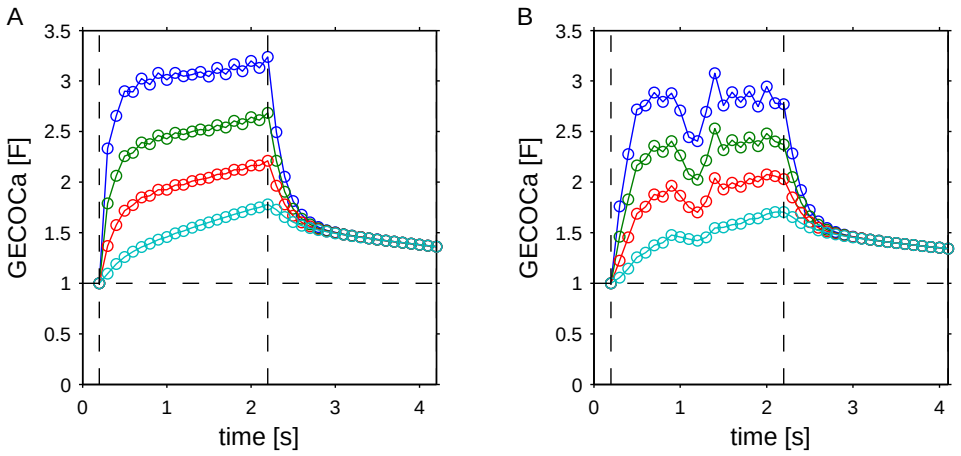

Figure 6.3: Simulation of GECO signal grouped by distance (0-0.16 μm (dark blue), 0.16-0.32 μm (green), 0.32-0.48 μm (red) and 0.48-1.5 μm (light blue)) as a results of a deterministic sequence (A) and the average of ten stochastic simulations for a cluster with synchronized gating (B).

Coupling to the Exocytosis Model

In Chen's model, microdomain calcium levels were calculated as a compartment, whose input was directly proportional to the L-type calcium current and corresponds to an average calcium concentration in close proximity to the Ca^{2+}-channel. With the calcium diffusion simulations described in the previous Chapter, calcium levels at different distances of the channel can be calculated and can substitute the microdomain calcium levels. This substitution allows us to hypothesize different locations for the exocytotic granules, and to use in the model the exact calcium levels corresponding to that distance instead of a mean values as in the microdomain compartment.

The second parameter that controls the exocytotis response is calcium binding affinity. The value for the binding and unbinding calcium rate constants in Chen's model are 20 $ms^{-1}\mu M^{-1}$ and 100 $ms^{-}1$ respectively. Since $K_D = k_{-1}/k_1$, the default parameters correspond to a calcium affinity of 5 μM.

To understand the importance of the distance from the Ca^{2+}-channel, the cumulative total number of granules fused, the total number of granules ready to release and the total amount of insulin secreted are shown in Figure 6.4, in the case of cluster with synchronized gating. Granules were supposed to be at a distance of 30 nm and of 300 nm from the Ca^{2+}-channel for the solid and the dashed line respectively.

If all granules were located at 30 nm, more than half of the ready releasable

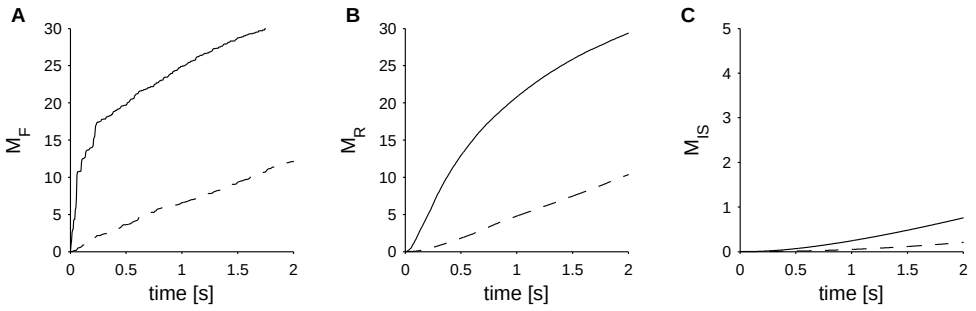

Figure 6.4: Cumulative total number of granules fused (A), the total number of granules ready to release (B) and the total amount of insulin secreted (C), in the case of cluster with synchronized gating. Granules were supposed to be at a distance of 30 nm and of 300 nm from the Ca^{2+}-channel for the solid and the dashed line respectively.

granules will fused with the membrane in half a second. After this first phase, a second slower fusion of granules will take place in the next seconds of depolarization. Contrarily, if the granules were located 10 times further away, at the end of the two second of depolarization almost half of the ready releasable granules would be fused with the membrane (Fig. 6.4A).

Similar considerations can be done for the cumulative total granules ready for release, even if its dynamics is slower and delayed compared to the total fused granules (Fig. 6.4B).

Finally, total amount of secreted insulin is shown in Figure 6.4C. The different behavior between the two assumed distances is still evident. However, in this case it is worth noting the delay for insulin secretion compared to the granule fusion. It is known that insulin is stored into the granules in crystalline form [33] and besides the pore expansion, the insulin-crystal needs time to dissolve, even if the exact mechanisms are not known. This fact is capture by Chen's model by the small value in parameter u_3.

General Case

In the previous example only one affinity and two different distances have been taken into account. However, we are interested to evaluate what happens for different combinations of distances from the Ca^{2+}-channel and calcium affinity of the exocytotic mechanism. To visualize the results, the number of fused granules at the end of the stimulus and the time to reach the half max possible value can be

used to characterize the model response. The first value represents the magnitude of exocytosis, while the second value corresponds to the rapidity of the process.

Moreover, in the previous example only the results relative to the cluster with synchronized gating were shown. What would we expect in the other scenarios? Would it be more functionally advantageous to increase the current magnitude, as in the case of the synchronized gating, or to increase the open time, as in the case of an independent gating?

The results for all the scenarios are shown in Figure 6.5 and Figure 6.6 representing the maximum value and the time for half maximum respectively.

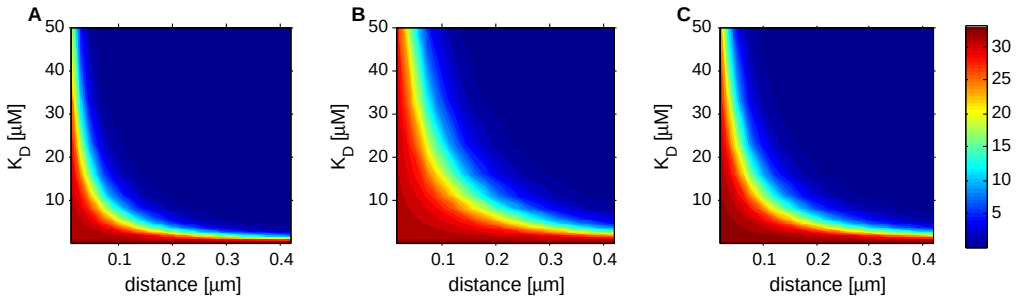

Figure 6.5: Total number of granules fused at the end of two seconds depolarization as a function of distance from calcium channel and calcium affinity in a single channel setup (A), in a cluster with synchronized gating (B) and in a cluster with independent gating.

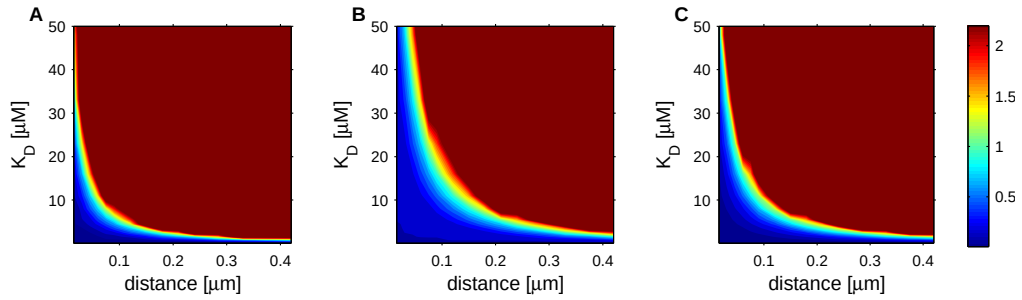

Figure 6.6: Time to reach the half maximum of total number of granules fused as a function of distance from calcium channel and calcium affinity in a single channel setup (A), in a cluster with synchronized gating (B) and in a cluster with independent gating. If the half maximum of total fusible granules is not reached at the end of two seconds of depolarization, the value 2 seconds is displayed.

It is evident that, compared to the single channel, the cluster setup is functionally advantageous both in terms of total number of fused granules at the end of the two

second depolarization and in terms of velocity of the process. The area where all the granules fused after two seconds depolarization is larger in the cluster setup compared with the single channel, with the cluster with synchronized gating having a slightly greater area.

The dependence of total fused granules is exponential both in respect on distance from the calcium channel and on the calcium affinity, in agreement with the exponential decay of calcium concentrations from the Ca^{2+}-channel. This means that if the granules were located close to the channel, the affinity would not have an influence on their fusion, but they will fuse in a short time anyway. However, if we hypothesize that they are located a bit further from the channel, the minimal necessary affinity to get maximal possible fusion decreases exponentially. Similarly, if affinity is considered the granules can be located anywhere to get maximal possible fusion if the affinity is high, while if the affinity is decreased the maximal possible distance decreases exponentially.

To better visualize this characteristic, it is useful to fix calcium affinity at 3.5μM ad see how the number of total fused granules at the end of two seconds depolarization depends on distance. The results are shown in Figure 6.7,light blue line.

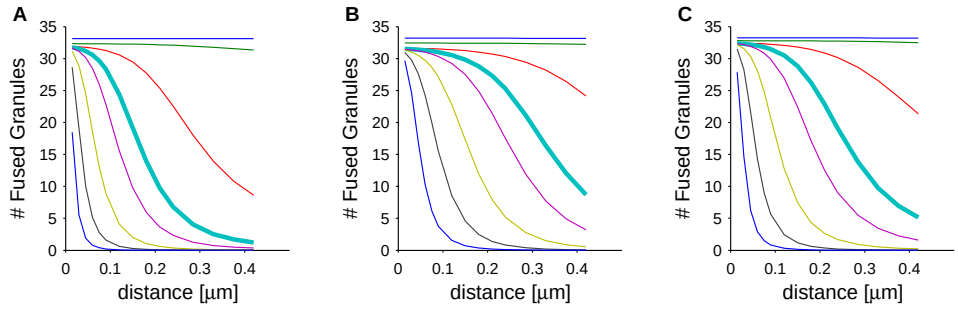

Figure 6.7: Total number of granules fused at the end of two seconds depolarization as a function of distance from calcium channel and calcium affinity in a single channel setup (A), in a cluster with synchronized gating (B) and in a cluster with independent gating. The different color corresponds different to affinities (0.1, 0.4, 1.6, 3.5 (light blue), 5.5, 11, 23, 48 μM)

In the single channel setup, the total number of fused granules remains maximal till ∼100 nm from the calcium channel, then it decrease as we move far from the channel, reaching half maximal value at ∼ 190 nm, and going to zero in correspondence to ∼ 400 nm (Fig. 6.7A). In the cluster with synchronized gating, the number of fused granules remains high till ∼200 nm, and does not go to zero at the furthest

distance $\sim$ 400 nm (Fig. 6.7B). Similarly, in the cluster with independent gating, the number of fused granules remains high till $\sim$150 nm and decreases to zero slower compared to the single channel setup (Fig. 6.7C).

Similar curves can be obtained by varying the calcium affinity. In particular, if the calcium affinity is increased the curves tend to stay at the maximal value for bigger distances, while if the calcium affinity is decreased the curves go to zero for smaller distances (Fig. 6.7).

Concluding Remarks

Under control conditions, the mean open time of the Ca^{2+}channels during a depolarization is very short ($\sim$2 ms) compared to the delay between calcium elevation and the initiation of exocytosis ($\sim$10 ms). This lead to the idea that Ca^{2+}channels clustering would be functionally advantageous [29]. Furthermore, it was reported that the frequency of multi-channel openings far exceeded the probability of observing simultaneous openings of independently gating channels, suggesting that a group of several L-type Ca^{2+}channles may activate and inactivate in a synchronous manner [164].

In this context, the analysis presented previously becomes an useful tool in understanding the impact of different channel organization, i.e. single channel, cluster with synchronized gating and cluster with independent gating.

Our results confirm the functional advantage of a cluster scenario compared to a single channel setup, and the synchronized gating showed the best performance in the exocytotic machinery. Hence, the simulations presented here might suggest that there is a certain degree of interplay between the channel forming the cluster, in accordance with [164].

7

From Exocytosis to Secretion:
Minimal Model of Insulin Secretion in the Perfused Rat Pancreas

So far we analyzed cellular mechanisms, which translate in insulin secretion. Hence, the natural step is to move from a cellular point of view to a bigger scale considering the whole pancreas. In this context, the so called minimal model approach might become useful, by allowing the determination of indexes to assess β-cell function in different experimental groups. In this Chapter a minimal model specific for the perfused pancreas experimental will be described. It was built adapting the C-peptide minimal model previously applied to the intravenous glucose tolerance test. An useful application of the model will be presented: the quantitative assessment of pharmacologically relevant agents.

7.1 Insulin Secretion and the Perfused Rat Pancreas

In the isolated perfused rat pancreas, the biphasic nature of insulin secretion in response to an increase in glucose levels was first observed by Curry et al. [165]. Later experiments have shown that in type 2 diabetes the amount of insulin secreted during the first phase, in particular, is severely reduced . It is now generally accepted that deficient insulin secretion plays a crucial role in the pathogenesis of diabetes

[11]. Thus, reliable methods to investigate and quantify insulin secretion both in clinical and experimental settings are desirable.

The perfused rat pancreas, performed either isolated or in situ, is commonly used for different kinds of investigations, whose aim is the evaluation of β-cell function and the effect of various factors on insulin secretion. The most common application of this experimental setting is the analysis of the effect of drugs or other secretagogues [166][167], in some cases both in normal and diabetic rats [168]. Furthermore, it can also be used to assess the effect of fat content in diet [169][170] or the influence of exercise on insulin secretion and β-cell function [171].

Minimal models, by postulating a specific glucose-insulin secretion functional relationship, are able to provide indices describing β-cell responsivity to glucose of first and second phase secretion. Minimal models describing the glucose/insulin system have been successfully applied for the estimation of indices in a clinical setting (e.g. intravenous and oral glucose tolerance tests) [172]. However, a minimal model applicable to the isolated perfused rat pancreas was unavailable so far. Here, we adapt the C-peptide minimal model, previously applied to the intravenous glucose tolerance test [173], to obtain a specific model for the experimental settings of the perfused pancreas.

Insulin secretion is mainly regulated by glucose through intracellular metabolism of the sugar, and is additionally modulated by other factors such as incretin hormones and fatty acids by stimulation via G Protein-Coupled Receptors (GPCRs). In particular, the activation of specific receptors, that enhance insulin secretion only in presence of stimulatory glucose levels, is therapeutically appealing since they increase insulin levels with minimal risk of hypoglycaemia.

Glucagon-Like Peptide-1 (GLP-1) acts on the pancreatic β-cell through a $G_{\alpha s}$ coupled GPCR. Another potential treatment of type 2 diabetes is the activation of G protein-coupled receptor 40 (GPR40), also known as Free Fatty Acid Receptor 1 (FFAR1), a GPCR that is found in pancreatic β-cells [174]. Several drug candidates addressing this receptor are currently in clinical development, with TAK-875 being the most advanced compound having just entered phase III clinical trials [175]. At Sanofi the compound SAR1 has been identified as a potent and selective GPR40 agonist, which is currently in preclinical development. SAR1 clearly demonstrated a glucose dependent mechanism in increasing the intracellular Ca^{2+}-signal and a resulting increase in insulin secretion under elevated glucose concentrations in the

perfused rat pancreas [176].

The model was applied for the assessment of pharmacologically relevant agents (GLP-1, the synthetic GLP-1-receptor agonist, lixisenatide, and the compound SAR1), with the aim to quantify and differentiate their effect on insulin secretion.

7.2 Materials and Methods

Animals and Housing

Animal studies were performed according to German animal protection law as well as according to international animal welfare legislation and rules, and our experiments were approved by the Federal Authority for Animal Research at the Regierungspräsidium Darmstadt. Male Sprague-Dawley rats were purchased at a body weight of 200-220 g from Harlan-Winkelmann (Borchen, Germany). The animals were acclimatized for $\geq$1 wk and housed under controlled environmental conditions (temperature 22$\pm$2řC, humidity 55$\pm$10%, 12:12-h dark-light cycle, lights on at 0600) with free access to standard laboratory chow (ssniff R/M-H 1534) and tap water. Animals were housed in Macrolon cages size IV-S (1400 cm^2, 2-4 rats/cage) on softwood granulate. For environmental enrichment, all cages were equipped with wood shavings and a wooden gnawing block. All manipulations were performed at the same time in the morning.

Experimental Protocol

Male fed Sprague-Dawley rats weighting 200-220 g were used throughout the experiments and were anesthetized with pentobarbital sodium (80-100 mg/kg body wt). The pancreas was isolated as described previously [177] and placed into the perfusion chamber, which was constantly gazed with a humidified mixture of O_2 and CO_2 (ratio 95:5; Carbogen) and was kept at a constant temperature of 37řC. The organ was perfused (perfusion rate: 1.5 ml/min) with a modified solution of Krebs-Henseleit Buffer (KHB; in mM: 118 NaCl, 4.7 KCl, 25 $NaHCO_3$, 1.2 NaH_2PO_4, 1.25 $CaCl_2$, 1.2 $MgSO_4$) containing 1% bovine serum albumin and glucose as indicated, which was permanently gazed with Carbogen and kept at a temperature of moment 37řC. The solution entered the organ via the aorta abdominalis, circulated through the pancreas, and exited via the portal vein. Insulin was measured from frozen

samples using the fluorescent immunoassay (order no. 10-1248-10) from Mercodia according to the manufacturer's instructions.

This experimental setting was used to test the effect of pharmacologically relevant agents, namely GLP-1, lixisenatide, and SAR1, on insulin secretion. The isolated pancreas was perfused with a buffer (KHB) containing different concentrations of glucose. Initially, the pancreas was perfused with 5.6 mM glucose to ensure that any soluble protease in the pancreas was washed out. To investigate the drug effect, the test compound was added after 6 min at low glucose by switching to a reservoir containing the compound. After 15 min, the concentration of glucose was increased to 16.5 mM by switching to a reservoir with high glucose concentration under the same conditions (testing compound or no drug). The increase to 16.5 mM in glucose concentration induces glucose-stimulated insulin secretion of the isolated organ. The effluent was collected in ice-cooled tubes for the measurement of insulin concentration.

Mathematical Model of Insulin Secretion in the Perfused Pancreas

Pancreatic secretion above basal secretion (SR) is assumed proportional to the amount X (pmol) of readily releasable insulin in the β-cells [178]:

$$SR(t) = mX(t). \tag{7.1}$$

The change in the insulin amount in the RRP X results from the balance between the insulin secretion rate, the provision Y (pmol/min) of insulin refilling the RRP, and recruitment of readily releasable insulin X_D (pmol/min):

$$\frac{\mathrm{d}X(t)}{\mathrm{d}t} = -mX(t) + Y(t) + X_D(t) \qquad X(0) = 0, \tag{7.2}$$

X_D is responsible for the first phase of secretion and is assumed to be proportional to the rate of increase of glucose via the constant parameter K_D:

$$X_D(t) = \begin{cases} K_D \frac{\mathrm{d}G(t)}{\mathrm{d}t}, & \text{if } \frac{\mathrm{d}G(t)}{\mathrm{d}t} > 0; \\ 0, & \text{otherwise.} \end{cases} \tag{7.3}$$

Further explanations for the constraint can be found in [127, 179].

The provision Y generates the slower second phase and is controlled by glucose according to the equation

$$\frac{\mathrm{d}Y(t)}{\mathrm{d}t} = -\alpha \left[Y(t) - \beta \left(G(t) - Gb \right) \right], \qquad Y(0) = 0, \tag{7.4}$$

where Gb represents the basal value of glucose.

It is worth noting that the provision is not linearly related to glucose concentration, but it tends, with a time constant of $1/\alpha$ (min), toward a steady-state value linearly related through the parameter β [pmol/(mmol/l)= 10^9/l] to glucose concentration G (mM) above the basal level Gb.

A direct measurement of glucose concentration inside the pancreas was not feasible. Therefore, it was modeled using a sigmoidal function trying to mimic the experimental protocol:

$$G(t) = Gb + \frac{G_{\max} - Gb}{1 + e^{-n(t-th)}}, \tag{7.5}$$

where $G_{\max}$ 16.5 mM represents the maximum glucose stimulus during the experiment, Gb 5.6 mM represents the glucose level during the first part of the experiment, n controls the steepness of the function, and th is the time at which the switch from Gb and $G_{\max}$ is centred. Parameters were based on the following considerations. We calculated that the solution at high glucose requires ∼0.5 min to reach the aorta abdominalis through the tubing. Additionally, isolated islets show a delay around 1 min before the initiation of insulin secretion by a step increase in extracellular glucose concentration [8] [180]. Thus, the function $G(t)$ (Fig. 7.1A) was chosen to be very steep (n =6) and centred at th =16.5 min, accounting for the delay of 1.5 min due to the sources explained above.

Using a mathematical equation for the glucose concentration allows for an analytic calculation of the glucose derivative without approximations or delays:

$$\frac{\mathrm{d}G}{\mathrm{d}t} = \frac{n\,(G_{\max} - Gb)\,e^{-n(t-th)}}{\left(1 + e^{-n(t-th)}\right)^2}. \tag{7.6}$$

Model Identification

All secretory parameters (m, K_D, α, and β) are a priori uniquely identifiable. The parameters were estimated for each perfused rat pancreas, together with a measurement of their precision, by applying weighted nonlinear least square methods to insulin data using the SAAM II software.

Weights were chosen optimally, i.e., equal to the inverse of the variance of the measurement errors, which were assumed to be independent, Gaussian, and zero mean with unknown constant standard deviation. The variance of the measurement errors was estimated a posteriori.

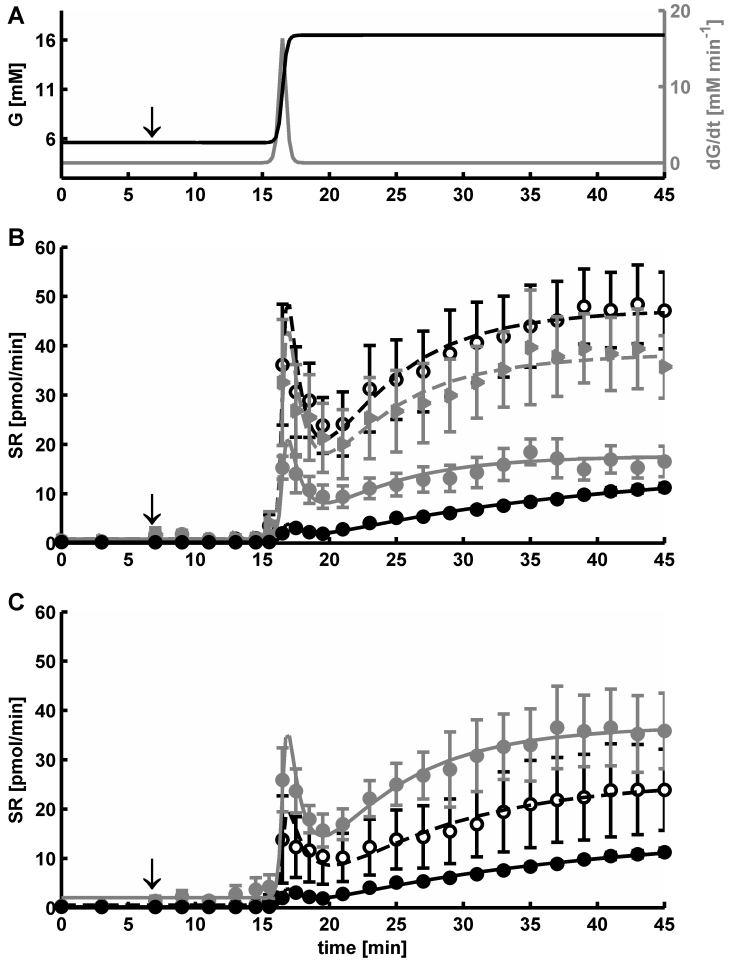

Figure 7.1: A) glucose function (black, left axis), along with its derivative (gray, right axis), using the selected parameters (Gb = 5.6 mM, $G_{\max}$ = 16.5 mM, n= 6 and th = 16.5 min). B) means of estimated insulin secretion profiles with reference data and standard deviation bars in control (black solid line), glucagon-like peptide-1 (GLP-1; 10 nM, black dashed line), lixisenatide (10 nM, gray dashed line, gray triangles), and SAR1 (1 μM; gray solid line, gray circles) groups. C) means of estimated insulin secretion profiles with reference data and standard deviation bars in control (black solid line), GLP-1 (10 pM, black dashed line), and GLP-1 (10 pM)+SAR1 (0.1 μM, gray solid line, gray circles) groups. The arrows indicate the time at which the drug was added.

A Bayesian approach was used when the parameter m was estimated with insufficient precision to avoid compensatory issues with the anticorrelated parameter K_D. Because the parameter m in the control group was estimated with good precision without the Bayesian term, its mean value was used as the prior in the treated groups when required.

Indices Definition and Interpretation

Indices of responsivity to glucose of the first (dynamic) and second (static) phases were also calculated.

The dynamic sensitivity [Φ_D (10^9/l)] is defined as the amount of insulin released during the first phase normalized by the glucose increment $\Delta G = (G_{\max} - Gb)$ during the experiment. To calculate the amount of insulin secreted during the first phase, it is useful to divide compartment X into two components responsible for first and second phases

$$\begin{aligned} X(t) &= X_{\mathrm{I}}(t) + X_{\mathrm{II}}(t), && (7.7)\\ \frac{\mathrm{d}X_{\mathrm{I}}(t)}{\mathrm{d}t} &= -mX_{\mathrm{I}}(t) + K_D\frac{\mathrm{d}G(t)}{\mathrm{d}t}, && (7.8)\\ \frac{\mathrm{d}X_{\mathrm{II}}(t)}{\mathrm{d}t} &= -mX_{\mathrm{II}}(t) + Y(t). && (7.9) \end{aligned}$$

and integrate over time both sides of Eq. 7.8 between 0 and T_{end}, representing the end of the experiment when $X_{\mathrm{I}}(t)$ is back to the steady-state condition:

$$\int_0^{T_{\mathrm{end}}} \frac{\mathrm{d}X_{\mathrm{I}}(t)}{\mathrm{d}t}\mathrm{d}t = \int_0^{T_{\mathrm{end}}} \left(-mX_{\mathrm{I}}(t) + K_D\frac{\mathrm{d}G(t)}{\mathrm{d}t}\right)\mathrm{d}t. \tag{7.10}$$

Alternatively,

$$\int_0^{T_{\mathrm{end}}} \mathrm{d}X_{\mathrm{I}}(t) = -\int_0^{T_{\mathrm{end}}} mX_{\mathrm{I}}(t)\mathrm{d}t + \int_0^{T_{\mathrm{end}}} K_D\mathrm{d}G(t), \tag{7.11}$$

which gives

$$X_{\mathrm{I}}(T_{\mathrm{end}}) - X_{\mathrm{I}}(0) = -\int_0^{T_{\mathrm{end}}} mX_{\mathrm{I}}(t)\mathrm{d}t + K_D(G(T_{\mathrm{end}}) - G(0)). \tag{7.12}$$

Since at T_{end} the system is back to the steady state condition, $X_{\mathrm{I}}(0) - X_{\mathrm{I}}(T_{\mathrm{end}}) = 0$. We can obtain the quantity of insulin secreted during the first phase from Eq. 7.12:

$$\int_0^{T_{\mathrm{end}}} SR_{\mathrm{I}}(t)\mathrm{d}t = \int_0^{T_{\mathrm{end}}} mX_{\mathrm{I}}(t)\mathrm{d}t = K_D(G_{\max} - Gb). \tag{7.13}$$

Finally, normalizing by the glucose increment $\Delta G = G_{\max} - Gb$, we get

$$\Phi_D = \int_0^{T_{\mathrm{end}}} SR_{\mathrm{I}}(t)\mathrm{d}t/\Delta G = K_D. \tag{7.14}$$

The dynamic index is a measurement of the stimulatory effect of the increased rate of glucose on the secretion of readily releasable insulin.

The static sensitivity [Φ_S (10^9 min/l)] is defined as the ratio between the provision and the glucose concentration (above the basal level) at the steady state. Starting from Eq. 7.4, it is possible to calculate the provision at the steady state:

$$Y_{\mathrm{SS}} = \beta(G_{\mathrm{SS}} - Gb). \tag{7.15}$$

Hence, normalizing by the glucose step, and since $G_{\mathrm{SS}} = G_{\max}$, we obtain the following:

$$\Phi_S = Y_{\mathrm{SS}}/\Delta G = \beta. \tag{7.16}$$

The model also allows us to quantify the delay time of the second phase T (min). It is

$$T = \frac{1}{\alpha}, \tag{7.17}$$

simply, the time constant with which the provision reaches its steady state value, and it is related to the time required for new granules to become ready for release.

Statistical Methods

Indices of β-cell function were compared between groups with two-sided t-tests using Microsoft Excel, and P values were Bonferroni corrected to adjust for multiple comparisons. Linear statistical modeling (using r) was used to assess whether SAR1 (0.1 μM) had an effect in the presence of physiological GLP-1 levels (10 pM) by including an interaction term in the linear models of the form

$$Z_j = \beta_0 + \beta_1 GLP1_j + \beta_2 (GLP1 \cdot SAR1)_j + \epsilon_j, \tag{7.18}$$

where j identifies the experiment, Z is one of the estimated β-cell indices (Φ_D, Φ_S, T), β_0 is the estimate of the index in the control group, β_1 indicates an additional effect of 10 pM GLP-1, and β_2 estimates how much SAR1 further modifies the index. $GLP1_j$ is a factor indicating whether the pancreas was exposed to GLP-1, and $(GLP1 \cdot SAR1)_j$ indicates whether both GLP-1 and SAR1 were present. Two-sided t-tests were used to evaluate whether the regression coefficients β_1 and β_2 were significantly different from zero for each β-cell index.

7.3 Results: Drug Effect Quantification

Mean insulin secretion profiles of control and treated groups are shown in Figure 7.1B,C along with their standard errors. After a silent phase in which secretion is at basal values, each profile exhibits the typical biphasic insulin secretion pattern in response to the glucose step. In some groups the addition of the compound alone perturbs the basal secretion. This effect was measured by the area under the curve (between minutes 6 and 15) above basal (before minute 6) of insulin secretion in the prestimulus state. If it was >9 pmol, corresponding to an average flux of 1 pmol/min above basal, the perturbation was considered significant. In the SAR1 and GLP1+SAR1 groups, the compound significantly perturbed more than half of the individual pancreases in the basal state.

Individual secretion parameters for each group are summarized in Tables 7.1,2 together with their precision. The ability of the model to fit the data is shown in Figure 7.1B,C. Precise estimates were obtained for all pancreases in each group.

A significant difference was found in presence of 10 nM GLP-1 compared with control for all of the responsivity indices (dynamic Φ_D, static Φ_S, time delay T); 10 nM lixisenatide had a significant effect on all three indices relative to the control, whereas SAR1, at a concentration of 1 μM, exhibits a significant difference compared with the control for the dynamic index Φ_D and the time delay T but not for the static index Φ_S (P=0.90) (Fig. 7.2).

Physiological levels of GLP-1 (10 pM) had a significant effect on all three indices compared with control (Fig. 7.3). SAR1, when administered in presence of 10 pM GLP-1, was found to have a significant additional effect on both dynamic and static β-cell responsivity indices. In contrast, no further significant decrease in the time delay was detectable (Fig. 7.3).

7.4 Discussion

In this Chapter, a mathematical model of insulin secretion for the isolated perfused rat pancreas was presented. This type of experiment is used in different kinds of investigations aimed at evaluating the effect on β-cell functionality of several factors, such as drugs and secretagogues, but also diet composition and exercise. Hence, mathematical models that are able to characterize insulin secretion phases and quantify β-cell function may be useful tools for the analysis of the perfused rat

	$\Phi_D(10^9\text{l})$	$\Phi_S(10^9\text{l/min})$	$T(\text{min})$	$m(\text{min}^{-1})$
Control				
Rat 1	0.753 (11)	1.072 (10)	23.652 (15)	0.605 (18)
Rat 2	0.809 (11)	1.101 (10)	20.547 (16)	0.892 (18)
Rat 3	1.034 (15)	1.694 (6)	16.273 (13)	0.713 (32)
Rat 4	0.536 (16)	1.566 (10)	26.103 (16)	0.818 (28)
Rat 5	0.701 (14)	1.584 (13)	30.111 (20)	0.636 (30)
Rat 6	0.408 (18)	3.044 (29)	62.383 (34)	1.368 (29)
Rat 7	0.584 (19)	0.767 (5)	12.129 (14)	0.536 (38)
Rat 8	0.854 (14)	1.187 (13)	12.809 (23)	0.698 (26)
Rat 9	0.373 (24)	1.480 (17)	31.211 (24)	1.010 (40)
Rat 10	0.730 (13)	1.585 (6)	19.724 (11)	0.720 (23)
Rat 11	0.660 (15)	1.739 (5)	19.080 (10)	0.757 (24)
MEAN	0.677	1.529	24.911	0.796
SD	0.195	0.589	13.922	0.232
GLP-1 (10 nM)				
Rat 1	5.609 (9)	3.419 (4)	8.757 (11)	0.587 (13)
Rat 2	9.735 (8)	4.220 (3)	4.767 (12)	0.758 (14)
Rat 3	10.482 (9)	4.405 (3)	5.617 (10)	0.509 (15)
Rat 4	10.253 (8)	4.140 (3)	3.750 (14)	0.856 (13)
Rat 5	6.488 (8)	4.260 (4)	7.933 (12)	0.858 (10)
Rat 6	10.664 (6)	5.244 (3)	4.968 (10)	0.911 (9)
MEAN	8.872	4.281	5.965	0.747
SD	2.226	0.585	1.956	0.163
Lixisenatide (10 nM)				
Rat 1	6.673 (8)	3.074 (3)	5.821 (10)	0.593 (12)
Rat 2	7.791 (11)	3.579 (3)	5.581 (12)	0.610 (18)
Rat 3	10.280 (9)	4.152 (4)	4.493 (18)	0.888 (10)
Rat 4	6.044 (12)	3.198 (5)	6.604 (16)	0.775 (21)
Rat 5	11.281 (10)	4.234 (4)	5.444 (14)	0.577 (15)
Rat 6	2.754 (13)	3.426 (11)	19.350 (19)	0.903 (21)
Rat 7	9.904 (8)	3.707 (3)	3.562 (14)	0.884 (12)
Rat 8	8.665 (29)	2.831 (11)	3.395 (49)	0.746 (51)
MEAN	7.924	3.525	6.781	0.747
SD	2.755	0.498	5.199	0.139

Table 7.1: Individual secretion parameters. Data in parentheses are precision of parameter estimates, expressed as % coefficient of variation. Φ_D, dynamic responsivity index; Φ_S, dynamic responsivity index; T, dynamic responsivity index; m, secretion rate.

	$\Phi_D(10^9\text{l})$	$\Phi_S(10^9\text{l/min})$	$T(\text{min})$	$m(\text{min}^{-1})$
SAR1 (1 μM)				
Rat 1	3.445 (8)	1.267 (3)	3.324 (14)	0.900 (13)
Rat 2	2.574 (9)	1.594 (8)	6.678 (17)	0.906 (10)
Rat 3	3.193 (6)	1.601 (4)	9.112 (9)	0.832 (9)
Rat 4	2.828 (7)	1.188 (4)	7.547 (13)	0.846 (12)
Rat 5	5.536 (5)	1.692 (2)	5.374 (9)	0.614 (7)
Rat 6	3.419 (10)	1.538 (5)	4.312 (20)	0.815 (12)
Rat 7	3.929 (11)	2.004 (8)	6.572 (23)	0.899 (18)
MEAN	3.561	1.555	6.131	0.830
SD	0.976	0.272	1.964	0.102
GLP-1 (10 pM)				
Rat 1	4.215 (9)	2.433 (7)	13.534 (14)	0.507 (14)
Rat 2	7.247 (10)	2.426 (3)	4.952 (13)	0.495 (16)
Rat 3	8.060 (9)	3.146 (4)	7.578 (13)	0.623 (14)
Rat 4	4.219 (10)	3.537 (8)	13.233 (17)	0.800 (11)
Rat 5	2.790 (9)	1.771 (4)	9.797 (10)	0.577 (14)
Rat 6	4.447 (12)	2.886 (6)	11.545 (14)	0.511 (19)
Rat 7	0.992 (13)	1.007 (8)	13.702 (16)	0.710 (14)
Rat 8	1.336 (11)	1.635 (7)	13.998 (13)	0.708 (13)
MEAN	4.163	2.355	11.042	0.616
SD	2.528	0.845	3.332	0.113
GLP-1 (10 pM)+SAR1 (0.1 μM)				
Rat 1	5.584 (8)	3.301 (2)	5.799 (8)	0.669 (14)
Rat 2	7.588 (7)	4.674 (4)	9.173 (11)	0.878 (9)
Rat 3	6.533 (7)	2.745 (4)	6.555 (14)	0.953 (8)
Rat 4	4.566 (6)	2.419 (3)	6.585 (10)	0.868 (9)
Rat 5	5.217 (5)	2.539 (3)	7.817 (10)	0.909 (8)
Rat 6	5.032 (9)	3.415 (3)	6.873 (11)	0.729 (12)
Rat 7	5.217 (9)	3.314 (3)	5.103 (12)	0.856 (11)
MEAN	5.677	3.201	6.843	0.837
SD	1.038	0.763	1.332	0.101

Table 7.2: Individual secretion parameters. Data in parentheses are precision of parameter estimates, expressed as % coefficient of variation. Φ_D, dynamic responsivity index; Φ_S, dynamic responsivity index; T, dynamic responsivity index; m, secretion rate.

pancreas experiment.

The C-peptide minimal modeling approach has been applied successfully in humans to a variety of glucose stimuli, e.g., intravenous glucose tolerance test (IVGTT) [178], oral glucose tolerance test (OGTT) [181], and up- and downgraded infusion [173]. Since the change from low to high glucose concentration is very fast, as during an IVGTT, we start from the C-peptide minimal model used previously in this experimental setting and built a new version of the model suitable for the perfused pancreas protocol. The model is simpler in the sense that there is no need to include the C-peptide dynamics, since the insulin secretion profile is measured directly. The model assumes that glucose can stimulate pancreatic insulin secretion via both a dynamic control proportional to its rate of change and a static control related to its concentration. The dynamic control is connected to the model assumption of the presence in the β-cell of a pool of readily releasable insulin, which can be promptly secreted when glucose increases above its basal value and whose recruitment is proportional via the parameter K_D to the glucose increase rate. From Eq. 7.10, is easy to verify that the product of K_D and the total increase in glucose concentration in the rising portion of the glucose function measures the total amount of releasable insulin stored in the β-cell before the experiment, which corresponds to the variable X_0 in the IVGTT model (C-peptide total amount). The static control is related to an insulin secretion provision process, which accounts for a slower and delayed component of secretion.

The time course of insulin secretion in response to a glucose stimulus is biphasic, and each phase can be described by a β-cell responsivity index. A dynamic responsivity index (Φ_D; describing the first phase) reflects the ability of the β-cell to respond to the rate of an increase in glucose levels, whereas the static responsivity index (Φ_D; describing the second phase), together with the time constant T, depicts the response to above-basal blood glucose.

Drug Effect Case Study

We applied the model for the assessment of pharmacologically relevant agents, namely the gut hormone GLP-1, a potent synthetic GLP-1 receptor agonist (lixisenatide), and a GPR40 agonist (SAR1). This particular case study becomes meaningful considering that drug development has the need to assess and quantify the action of antidiabetic drugs in earlier preclinical phases, when the experimental setting of

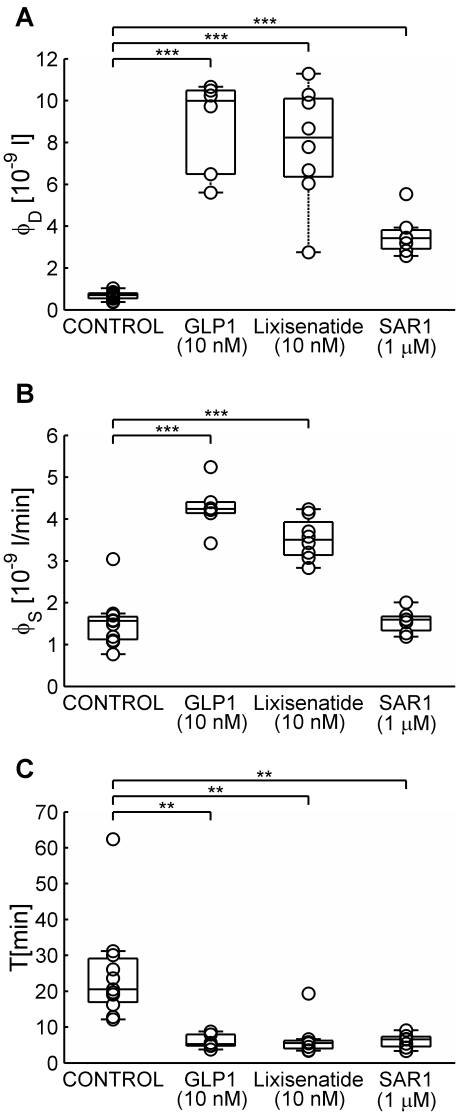

Figure 7.2: Boxplot of responsivity indices dynamic (Φ_D; A), static (Φ_S; B), and time delay (T; C), for control, GLP-1 (10 nM), and SAR1 (1 μM). Superimposed individual values. On each box, the central mark is the median, and the edges of the boxes are the 25th and 75th percentiles. Most extreme data points non considered outliers are delimited by horizontal lines. Difference between groups was assessed using a t-test with Bonferroni correction for multiple test. $\star\star P < 0.0033(0.01/3); \star\star\star P < 0.00033(0.001/3)$.

the perfused rat pancreas is often used.

Our data show that GLP-1 amplifies both the static and dynamic β-cell responsivity in a dose-dependent fashion. At the higher dose applied (10 nM), we found a 13.1-fold increase in Φ_D and a 2.8-fold increase in Φ_S relative to the control. Our results show that lixisenatide at the same concentration (10 nM) of GLP-1 reaches an improvement of β-cell function that is similar to GLP-1 (improvement of 11.7- and 2.3-fold in Φ_D and Φ_S, respectively). Since type 2 diabetes is characterized by a loss of the early phase of insulin secretion [10], the treatment may benefit especially from the pronounced enhancement of the first phase, as reflected by the dynamic responsivity index.

Compared with the control experiment, 1 μM SAR1 showed a 5.3-fold improvement in Φ_D, whereas no effect on Φ_S could be detected. However, it should be noted that the delay constant T was reduced from 25 to 6 min. Thus, 1 μM SAR1 has an effect on the second phase, but this is apparent only in its faster onset and not in the magnitude. Other studies using rat [182] or mouse [183] islets found that GPR40 agonists stimulated the magnitude of the second phase. The perfused rat pancreas in control conditions presents a larger second phase compared with the isolate islet data (Fig. 7.1) [165]. The magnitude of a small second phase, as seen in the isolated islets, might be readily increased by GPR40 agonists. This may explain the discrepancy between our results and those in [182, 183].

Under physiological conditions, in the postprandial state, incretin levels increase and will have an effect on the insulin secretion from the pancreatic islets. This enhancement is not reflected in the basic control experiment, where only the glucose but not the incretin concentration is increased. To approximate the physiological situation, we added 10 pM GLP-1 to the perfusate during the experiment. This GLP-1 concentration is approximately the one found postprandially in the rat [184]. Already under this condition, a substantial increase in β-cell function compared with the incretin-free experiment is observed (6.2-fold increase in Φ_D and 1.5-fold increase in Φ_S, whereas T was reduced to 11 min).

In a previous work [185], where glycemic profiles in an OGTT were matched in the same human subjects by means of an intravenous glucose infusion, an increase of 58% for the static index due to incretin effect was found, which is similar to the 54% increase with 10 pM GLP-1 in the perfused rat pancreas found here. The changes to Φ_D are not directly comparable due to the different patterns of the glucose profiles

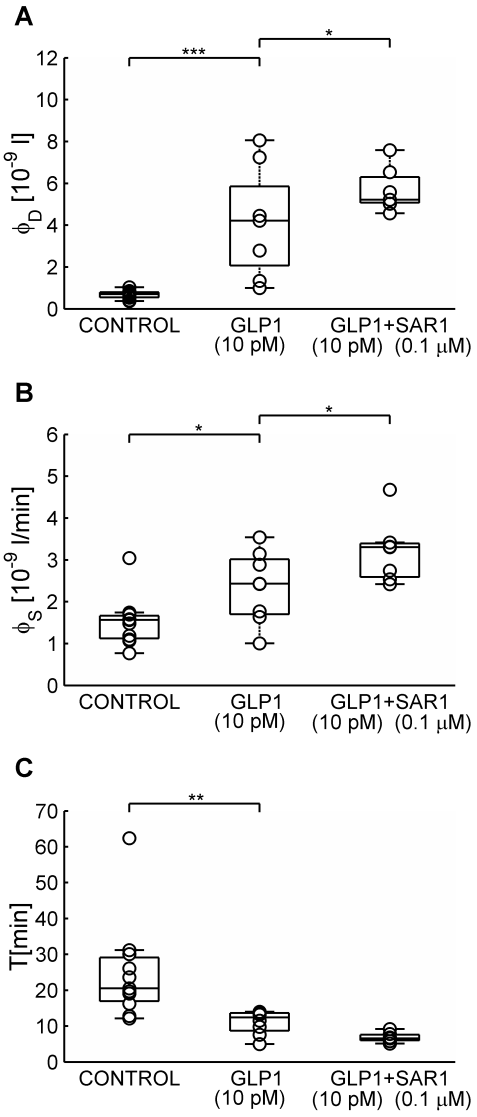

Figure 7.3: Boxplot of responsivity indices dynamic (Φ_D; A), static (Φ_S; B), and time delay (T; C), for control, GLP-1 (10 pM), and GLP-1 (10 pM)+SAR1 (0.1 μM). Superimposed individual values. On each box, the central mark is the median, and the edges of the boxes are the 25th and 75th percentiles. Most extreme data points non considered outliers are delimited by horizontal lines. Difference between groups was assessed using a linear model, as explained in *Statistical methods*. $\star P < 0.05$ $\star\star P < 0.01$;$\star\star\star P < 0.001$.

during an OGTT and in the perfused pancreas experiment.

What effect could we expect if we were to add SAR1 on top of 10 pM GLP-1? Using the 10 pM GLP-1 experiment as a control, we see a 1.4-fold increase in static and a 1.4-fold increase in dynamic responsivity by SAR1. It is interesting to note that SAR1 (1 μM) is not able to improve static β-cell responsivity in the absence of a physiological GLP-1 receptor stimulation, whereas even 0.1 μM SAR1 has an effect on Φ_S in the presence of 10 pM GLP-1. This could indicate a synergistic effect of the $G_{\alpha s}$-coupled GLP-1 receptor and the $G_{\alpha q}$-coupled GPR40 on the second phase of insulin secretion, although care must be taken because of the different SAR1 concentrations used. Overall, this analysis demonstrates that, even in the presence of postprandial GLP-1 levels, SAR1 leads to an additional improvement of β-cell function in the isolated perfused pancreas.

The work presented here, illustrates how the mathematical model is able to assess the ability of a compound to improve β-cell function in an ex vivo experiment, as it is used in the early phases of drug development. The parameter estimates obtained here represent valuable information to rank and classify compounds in development (e.g., by the ability of acting predominantly on one type of β-cell responsivity). Moreover, these values (or their relative changes) can be transferred to a mathematical model of the human glucose insulin system, e.g., the meal simulation model in [186] that also contains parameters for static and dynamic β-cell responsivities. Here, the effect of the new compound on insulin secretion and postprandial glucose lowering can be simulated, thereby translating results from an animal experiment into the human situation (certainly taking into account the uncertainty arising from the species difference). Including the pharmacodynamics of the compound into the model could then make the simulations even more relevant for the assessment of a potential drug. Such a process would then give valuable guidance for the design of first clinical trials.

8

Conclusions

Diabetes is a worldwide problem and the number of people with diabetes is constantly increasing due to several reasons including population growth, age, and increasing prevalence of obesity and physical inactivity. In particular, the long-term complications make diabetes a social and economical problem, since they have great impact on subject daily life and its management is financially expensive. As a consequence, considerable efforts have been made to understand better different aspects of this disease.

Glucose regulations is the result of a complex regulatory network in which different hormones are involved. The focus of this Thesis was on two hormones involved in this regulation: insulin, secreted by pancreatic β-cells, and GLP-1, secreted by intestinal L-cells. In advanced type-2 diabetes, both insulin and GLP-1 secretion is attenuated. In this Thesis, a combination of experimental data and mathematical modeling was used to get a deeper insight into the cellular mechanisms involved in insulin and GLP-1 secretion.

Insulin and pancreatic beta-cells

The stimulus-secretion pathway in pancreatic β-cells is well established, with electrical activity playing a pivotal role. Following metabolism of the sugars, ATP-sensitive potassium channels (K(ATP)-channels) close in response to the elevated ATP/ADP-ratio, which triggers action potential firing and Ca^{2+}-influx through voltage-gated calcium channels. The resulting increase in intracellular calcium leads to insulin release by Ca^{2+}-dependent exocytosis.

However, human β-cells show complex and heterogeneous electrophysiological responses to ion channel antagonists. Therefore, sometimes it is difficult to reach clear conclusions regarding the participation of certain ion channels in the various phases of electrical activity, in particular when electrophysiological responses are non-intuitive. A deeper understanding of the role of ion channels in electrical activity and insulin secretion could have important clinical benefits, since it might help in the development of new anti-diabetic drugs. The mathematical modeling can help in interpreting various electrophysiological responses, and in particular, to study the effect of competing effects and cell heterogeneity.

The first model of electrical activity in human β-cells was presented in [84]. In this Thesis, SK-channels and Ca^{2+} dynamics were included in the previous mathematical to investigate the heterogeneous and non-intuitive electrophysiological responses to ion channel antagonists. By using the model paracrine signals were also studied, and slow oscillations were simulated by adding a glycolytic oscillatory component to the electrophysiological model. The model was further developed by including Kir channels, which resulted in a clear improvement of the model behavior.

From the modeling of electrical activity we moved to the modeling of calcium diffusion and buffering. The TIRF microscopy data allowed us to monitor calcium levels during stimulus in two groups: the granules that undergo exocytosis in response to depolarization and the ones that do not. Simulations were performed using the modeling program CalC, which implements calcium diffusion and buffering. Calcium levels and the corresponding R-GECO signal were evaluated at different distances from the channel. The comparison of the simulations to the TIRF microscopy data allowed estimating the average distance from the channel of the granules that undergo exocytosis.

The calcium diffusion simulations were coupled to a model for insulin granule exocytosis to investigate exocytosis in terms of vicinity of granules to the Ca^{2+}-channel and affinity to calcium. The fusion probability was evaluated both in a single channel, and in a cluster-of-channels context, to assess the importance of channel opening time versus current intensity. Simulations confirmed that the hypothesis of a cluster significantly increases the fusion probability and a certain dependence between the channels in the cluster is functional advantageous.

In a multiscale context, the natural step was to move from a cellular point of view to a bigger scale considering the whole pancreas. A minimal model specific for

the perfused pancreas experimental setting was built and used for the assessment of pharmacologically relevant agents to quantify and differentiate their effect on insulin secretion.

GLP-1 and intestinal L-cells

Contrarily to the β-cells, the stimulus-secretion pathway in L-cells is still poorly understood, although it is known that GLP-1 secreting cells use SGLT1 and K(ATP)-channels to sense intestinal glucose levels. Electrical activity then transduces glucose sensing to Ca^{2+}-stimulated exocytosis. This particular glucose-sensing arrangement with glucose triggering both a depolarizing SGLT current as well as leading to closure of the hyperpolarizing KATP current is of more general interest for our understanding of glucose-sensing cells.

In this Thesis, the first mathematical model of electrical activity underlying GLP-1 secretion was presented and used to dissect the interactions between the two glucose-sensing mechanisms in primary mouse colonic L-cells and in GLUTag.The results illuminate how the two glucose-sensing mechanisms interact, and suggest that the depolarizing effect of SGLT currents is modulated by K(ATP)-channel activity.

Future Developments

Models of electrical activity in β-cell have been frequently restricted to rodents, due to the availability of electrophysiological data. However, human β-cells show important differences to β-cells from mice, for example with respect to the patterns of electrical activity observed, which consist of very fast bursting or spiking in human cells and never the classical slower burst pattern observed in rodents. Consequently, models of human β-cells are in an early stage compared to models of rodent β-cells. However, the former are likely to evolve rapidly and contribute to the understanding of the pathogenesis of type 2 diabetes.

Recently, thanks to the new available techniques, furthers insights into the exocytotic mechanisms in β-cells have been obtained. However, still many aspects remain unknown. The results presented here aims at investigating the location of granules and their affinity to calcium with the modeling support. However, it is only a preliminary analysis, which needs further evaluation. For example, in the TIRF microscopy data, the time at which granules undergo exocytosis was not taken into account. It would be interesting to evaluate if there is any difference between the

granules that do exocytosis in the first half second of depolarization and the ones that do it later. Finally, the coupling of diffusion simulations to the exocytosis model need experimental data, to reach more precise conclusions.

As previously said, the stimulus-secretion pathway in L-cells is still poorly understood. Hence, there are still many areas to investigate and model.

For example, as for the pancreatic β-cells it would be interesting to model the exocytotic steps in L-cells. This becomes even more intriguing considering that L- cells, contrarily to β-cells, are polarized cells, featuring distinct plasma membrane domains: apical, lateral and basal. The apical domain corresponds to the one that faces the intestine lumen, and its function is to sense luminal glucose. The lateral domain represents the connection to other epithelial cells. Finally, the basal domain is the one facing the blood capillary, where GLP-1 should be released. As a consequence, the exocytotic process becomes a spatial problem too, where the glucose sensing in one compartment should be transferred and translated into exocytosis in another compartment. The modeling of L-cells within an epithelial layer, with different ionic and nutrient concentration gradients across the apical and basolateral surfaces, might help in understanding the diversity in response between in vivo and in vitro experiments, where the cell polarity is lost.

Furthermore, intestinal L-cells are not uniformly distributed along the long intestinal tract, but they are primarily found in the ileum and colon, while few are in the duodenum and jejunum. In this context, modeling of the whole intestinal tract with different time for the glucose increase would be an intriguing issue.

This modeling could be the bridge between the cellular mechanism and the whole body GLP-1 secretion. To our knowledge, a minimal model for GLP-1 secretion is still not available. In fact, to better understand the glucose regulatory network, the different hormones should be considered and the development of a minimal model for the GLP-1 secretion could help in understanding the interplay between the different hormones.

Acknowledgements

First of all, I would like to thank my advisor and mentor Dr. Morten Gram Pedersen, I owe him everything I learned about cellular modeling during these years. When I started my Ph.D. project, I knew almost nothing about cellular processes, experiments and cellular modeling. Gratefully, I have been able to make my way through this field supported by his knowledge and help.

Secondly, I would like to thank Dr. Artie Sherman for his hospitality during my visit at NIH. It gave me the opportunity to improve my modeling abilities and to have precious discussions connected to beta-cell modeling and diabetes in general. I would like to thank him and his wife as well, for all their help, making my stay more easy and pleasant.

Then, I would like to thank the experimental groups that made my modeling work possible (modeling is nothing without experiments!). Dr. Matthias Braun, who I did not have the honor to meet before he passed away unexpectedly, for the beta-cell electrophysiology data. Prof. Sebastian Barg's group in Uppsala, Sweden for the TIRF microscopy data: I did not imagine that it would be possible to see exocytosis in real time (it was an exciting experience). Sanofi's research group in Frankfurt, Germany for the perfused rat pancreas data and for teaching me what drug development is like.

I would like to thank Prof. Claudio Cobelli for introducing me into the research world and for helping me during the development of the minimal model.

Outside the working context, I would like to thank my family and my boyfriend for their constant support and for cheering me up during challenging periods even when I was far away. Without doubt I can always rely on that, and I will never thank them enough.

Finally, I would like to thank my "Ph.D. colleagues" for the different ways in which they have made my Ph.D. journey an unique one. A journey can be more joyful if made in good company, especially beside old friends, even more so, when an acquaintance becomes a valuable friendship. Moreover, I would like to thank my colleagues for sharing ideas and for giving advice that made me grow up both professionally and personally.

Bibliography

[1] J. E. Gerich, "Physiology of glucose homeostasis," *Diabetes Obes Metab*, vol. 2, no. 6, pp. 345–350, 2000.

[2] R. Unger and L. Orci, "The essential role of glucagon in the pathogenesis of diabetes mellitus," *Lancet*, vol. 305, no. 7897, pp. 14–16, 1975.

[3] D. F. Kruger, C. L. Martin, and C. E. Sadler, "New insights into glucose regulation," *The Diabetes Educator*, vol. 32, no. 2, pp. 221–228, 2006.

[4] S. L. Aronoff, K. Berkowitz, B. Shreiner, and L. Want, "Glucose metabolism and regulation: beyond insulin and glucagon," *Diabetes Spectr*, vol. 17, no. 3, pp. 183–190, 2004.

[5] J. E. Gerich, C. Meyer, H. J. Woerle, and M. Stumvoll, "Renal gluconeogenesis its importance in human glucose homeostasis," *Diabetes care*, vol. 24, no. 2, pp. 382–391, 2001.

[6] A. R. Saltiel and C. R. Kahn, "Insulin signalling and the regulation of glucose and lipid metabolism," *Nature*, vol. 414, no. 6865, pp. 799–806, 2001.

[7] P. Bansal and Q. Wang, "Insulin as a physiological modulator of glucagon secretion," *Am J Physiol Endocrinol Metab*, vol. 295, no. 4, pp. E751–E761, 2008.

[8] P. Rorsman and E. Renström, "Insulin granule dynamics in pancreatic beta cells," *Diabetologia*, vol. 46, no. 8, pp. 1029–1045, 2003.

[9] P. Rorsman and M. Braun, "Regulation of insulin secretion in human pancreatic islets," *Annu Rev Physiol*, vol. 75, pp. 155–179, 2013.

[10] J. E. Gerich, "Is reduced first-phase insulin release the earliest detectable abnormality in individuals destined to develop type 2 diabetes?," *Diabetes*, vol. 51, no. suppl 1, pp. S117–S121, 2002.

[11] S. Kahn, "The relative contributions of insulin resistance and beta-cell dysfunction to the pathophysiology of type 2 diabetes," *Diabetologia*, vol. 46, no. 1, pp. 3–19, 2003.

[12] A. Lund, J. I. Bagger, M. Christensen, F. K. Knop, and T. Vilsbòll, "Glucagon and type 2 diabetes: the return of the alpha cell," *Curr Diab Rep*, vol. 14, no. 12, pp. 1–7, 2014.

[13] J. J. Holst, "The physiology of glucagon-like peptide 1," *Physiol Rev*, vol. 87, no. 4, pp. 1409–1439, 2007.

[14] R. Burcelin, A. Da Costa, D. Drucker, and B. Thorens, "Glucose competence of the hepatoportal vein sensor requires the presence of an activated glucagon-like peptide-1 receptor," *Diabetes*, vol. 50, no. 8, pp. 1720–1728, 2001.

[15] J. J. Holst, M. Christensen, A. Lund, J. de Heer, B. Svendsen, U. Kielgast, and F. Knop, "Regulation of glucagon secretion by incretins," *Diabetes Obes Metabol*, vol. 13, no. s1, pp. 89–94, 2011.

[16] M. Salehi and D. A. D'Alessio, "Effects of glucagon like peptide-1 to mediate glycemic effects of weight loss surgery," *Rev Endocr Metab Disord*, vol. 15, no. 3, pp. 171–179, 2014.

[17] I. M. Stratton, A. I. Adler, H. A. W. Neil, D. R. Matthews, S. E. Manley, C. A. Cull, D. Hadden, R. C. Turner, and R. R. Holman, "Association of glycaemia with macrovascular and microvascular complications of type 2 diabetes (UKPDS 35): prospective observational study," *BMJ*, vol. 321, no. 7258, pp. 405–412, 2000.

[18] M. Christensen, J. I. Bagger, T. Vilsboll, and F. K. Knop, "The alpha-cell as target for type 2 diabetes therapy," *Rev Diabet Stud*, vol. 8, no. 3, pp. 369–381, 2011.

[19] W. Kim and J. M. Egan, "The role of incretins in glucose homeostasis and diabetes treatment," *Pharmacol Rev*, vol. 60, no. 4, pp. 470–512, 2008.

[20] M. A. Nauck, "Incretin-based therapies for type 2 diabetes mellitus: properties, functions, and clinical implications," *Am J Med*, vol. 124, no. 1, pp. S3–S18, 2011.

[21] F. Gribble, "Targeting GLP-1 release as a potential strategy for the therapy of Type 2 diabetes," *Diabet Med*, vol. 25, no. 8, pp. 889–894, 2008.

[22] N. J. W. Albrechtsen, R. E. Kuhre, C. F. Deacon, and J. J. Holst, "Targeting the intestinal L-cell for obesity and type 2 diabetes treatment," *Expert Rev Endocrinol Metab*, vol. 9, no. 1, pp. 61–72, 2014.

[23] `http://www.nobelprize.org/nobel_prizes/medicine/laureates/2013`.

[24] R. D. Burgoyne and A. Morgan, "Secretory granule exocytosis," *Physiol Rev*, vol. 83, no. 2, pp. 581–632, 2003.

[25] P. S. Abbineni, J. E. Hibbert, and J. R. Coorssen, "Critical role of cortical vesicles in dissecting regulated exocytosis: Overview of insights into fundamental molecular mechanisms," *Biol Bull*, vol. 224, no. 3, pp. 200–217, 2013.

[26] C. S. Olofsson, S. O. Göpel, S. Barg, J. Galvanovskis, X. Ma, A. Salehi, P. Rorsman, and L. Eliasson, "Fast insulin secretion reflects exocytosis of docked granules in mouse pancreatic β-cells," *Pflügers Archiv*, vol. 444, no. 1-2, pp. 43–51, 2002.

[27] E. Neher and R. Zucker, "Multiple calcium-dependent processes related to secretion in bovine chromaffin cells," *Neuron*, vol. 10, no. 1, pp. 21–30, 1993.

[28] J. Rizo and T. C. Südhof, "The membrane fusion enigma: SNAREs, Sec1/Munc18 proteins, and their accomplices-guilty as charged?," *Annu Rev Cell Dev Biol*, vol. 28, pp. 279–308, 2012.

[29] S. Barg, X. Ma, L. Eliasson, J. Galvanovskis, S. O. Göpel, S. Obermüller, J. Platzer, E. Renström, M. Trus, D. Atlas, *et al.*, "Fast exocytosis with few Ca^{2+} channels in insulin-secreting mouse pancreatic β cells," *Biophys J*, vol. 81, no. 6, pp. 3308–3323, 2001.

[30] Y. S. Ermolyuk, F. G. Alder, R. Surges, I. Y. Pavlov, Y. Timofeeva, D. M. Kullmann, and K. E. Volynski, "Differential triggering of spontaneous glutamate release by P/Q-, N-and R-type Ca^{2+} channels," *Nat Neurosci*, vol. 16, no. 12, pp. 1754–1763, 2013.

[31] Z. P. Pang and T. C. Südhof, "Cell biology of Ca^{2+}-triggered exocytosis," *Curr Opin Cell Biol*, vol. 22, no. 4, pp. 496–505, 2010.

[32] A. S. Verkman, "Solute and macromolecule diffusion in cellular aqueous compartments," *Trends Biochem Sci*, vol. 27, no. 1, pp. 27–33, 2002.

[33] H. Lodish, A. Berk, S. L. Zipursky, P. Matsudaira, D. Baltimore, and J. Darnell, *Molecular Cell Biology*. New York: Scientific American Books, 2000.

[34] C. Fall, E. Marland, J. Wagner, and J. Tyson, *Computational Cell Biology*. Springer, 2002.

[35] K. S. Cole, *Membranes, ions, and impulses: a chapter of classical biophysics*, vol. 5. Univ of California Press, 1968.

[36] D. C. Gadsby, "Ion channels versus ion pumps: the principal difference, in principle," *Nat Rev Mol Cell Biol*, vol. 10, no. 5, pp. 344–352, 2009.

[37] A. Sherman, J. Keizer, and J. Rinzel, "Domain model for Ca^{2+}-inactivation of Ca^{2+} channels at low channel density," *Biophys J*, vol. 58, no. 4, pp. 985–995, 1990.

[38] F. Wuytack, L. Raeymaekers, and L. Missiaen, "Molecular physiology of the SERCA and SPCA pumps," *Cell Calcium*, vol. 32, no. 5, pp. 279–305, 2002.

[39] D. L. Nelson, A. L. Lehninger, and M. M. Cox, *Principles of biochemistry*. Macmillan, 2008.

[40] G. E. Lienhard, J. W. Slot, D. E. James, and M. M. Mueckler, "How cells absorb glucose," *Sci Am*, vol. 266, no. 1, pp. 86–91, 1992.

[41] L. Parent, S. Supplisson, D. D. Loo, and E. M. Wright, "Electrogenic properties of the cloned Na^+/glucose cotransporter: I. Voltage-clamp studies," *J Membr Biol*, vol. 125, no. 1, pp. 49–62, 1992.

[42] L. Parent, S. Supplisson, D. D. Loo, and E. M. Wright, "Electrogenic properties of the cloned Na^+/glucose cotransporter: II. A transport model under nonrapid equilibrium conditions," *J Membr Biol*, vol. 125, no. 1, pp. 63–79, 1992.

[43] K. Tran, N. P. Smith, D. S. Loiselle, and E. J. Crampin, "A thermodynamic model of the cardiac sarcoplasmic/endoplasmic Ca^{2+}(SERCA) pump," *Biophys J*, vol. 96, no. 5, pp. 2029–2042, 2009.

[44] A. L. Hodgkin and A. F. Huxley, "A quantitative description of membrane current and its application to conduction and excitation in nerve," *J Physiol*, vol. 117, no. 4, p. 500, 1952.

[45] B. Thorens, "Glucose sensing and the pathogenesis of obesity and type 2 diabetes," *Int J Obes*, vol. 32, pp. S62–S71, 2008.

[46] P. Rorsman, M. Braun, and Q. Zhang, "Regulation of calcium in pancreatic α- and β-cells in health and disease," *Cell Calcium*, vol. 51, no. 3-4, pp. 300–308, 2012.

[47] D. J. Drucker, T. Jin, S. L. Asa, T. A. Young, and P. L. Brubaker, "Activation of proglucagon gene transcription by protein kinase-A in a novel mouse enteroendocrine cell line.," *Mol Endocrinol*, vol. 8, no. 12, pp. 1646–1655, 1994.

[48] F. M. Gribble, L. Williams, A. K. Simpson, and F. Reimann, "A novel glucose-sensing mechanism contributing to glucagon-like peptide-1 secretion from the GLUTag cell line," *Diabetes*, vol. 52, no. 5, pp. 1147–1154, 2003.

[49] F. Reimann and F. M. Gribble, "Glucose-sensing in glucagon-like peptide-1-secreting cells," *Diabetes*, vol. 51, no. 9, pp. 2757–2763, 2002.

[50] F. Reimann, M. Maziarz, G. Flock, A. Habib, D. Drucker, and F. Gribble, "Characterization and functional role of voltage gated cation conductances in the glucagon-like peptide-1 secreting GLUTag cell line," *J Physiol*, vol. 563, no. 1, pp. 161–175, 2005.

[51] F. Reimann, A. M. Habib, G. Tolhurst, H. E. Parker, G. J. Rogers, and F. M. Gribble, "Glucose sensing in L cells: a primary cell study," *Cell Metab*, vol. 8, no. 6, pp. 532–539, 2008.

[52] H. E. Parker, F. Reimann, and F. M. Gribble, "Molecular mechanisms underlying nutrient-stimulated incretin secretion," *Expert Rev Mol Med*, vol. 12, p. e1, 2010.

[53] G. J. Rogers, G. Tolhurst, A. Ramzan, A. M. Habib, H. E. Parker, F. M. Gribble, and F. Reimann, "Electrical activity-triggered glucagon-like peptide-1 secretion from primary murine L-cells," *J Physiol*, vol. 589, no. 5, pp. 1081–1093, 2011.

[54] V. Gorboulev, A. Schürmann, V. Vallon, H. Kipp, A. Jaschke, D. Klessen, A. Friedrich, S. Scherneck, T. Rieg, R. Cunard, *et al.*, "Na^+-D-glucose cotransporter SGLT1 is pivotal for intestinal glucose absorption and glucose-dependent incretin secretion," *Diabetes*, vol. 61, no. 1, pp. 187–196, 2012.

[55] H. Parker, A. Adriaenssens, G. Rogers, P. Richards, H. Koepsell, F. Reimann, and F. Gribble, "Predominant role of active versus facilitative glucose transport for glucagon-like peptide-1 secretion," *Diabetologia*, vol. 55, no. 9, pp. 2445–2455, 2012.

[56] P. V. Röder, K. E. Geillinger, T. S. Zietek, B. Thorens, H. Koepsell, and H. Daniel, "The role of SGLT1 and GLUT2 in intestinal glucose transport and sensing," *PloS One*, vol. 9, no. 2, p. e89977, 2014.

[57] R. E. Kuhre, C. R. Frost, B. Svendsen, and J. J. Holst, "Molecular mechanisms of glucose-stimulated GLP-1 secretion from perfused rat small intestine," *Diabetes*, p. DB_140807, 2014.

[58] T. Budde, S. Meuth, and H.-C. Pape, "Calcium-dependent inactivation of neuronal calcium channels," *Nat Rev Neurosci*, vol. 3, no. 11, pp. 873–883, 2002.

[59] E. M. Wright, D. D. Loo, and B. A. Hirayama, "Biology of human sodium glucose transporters," *Physiol Rev*, vol. 91, no. 2, pp. 733–794, 2011.

[60] F. M. Ashcroft and P. Rorsman, "Electrophysiology of the pancreatic β-cell," *Prog Biophys Mol Biol*, vol. 54, no. 2, pp. 87–143, 1989.

[61] R. E. Kuhre, C. R. Frost, B. Svendsen, and J. J. Holst, "Molecular mechanisms of glucose-stimulated GLP-1 secretion from perfused rat small intestine," *Diabetes*, p. DB_140807, 2014.

[62] R. Moriya, T. Shirakura, J. Ito, S. Mashiko, and T. Seo, "Activation of sodium-glucose cotransporter 1 ameliorates hyperglycemia by mediating incretin secretion in mice," *Am J Physiol Endocrinol Metab*, vol. 297, no. 6, pp. E1358–E1365, 2009.

[63] O. J. Mace, M. Schindler, and S. Patel, "The regulation of K-and L-cell activity by GLUT2 and the calcium-sensing receptor CasR in rat small intestine," *J Physiol*, vol. 590, no. 12, pp. 2917–2936, 2012.

[64] P. D. Cani, J. J. Holst, D. J. Drucker, N. M. Delzenne, B. Thorens, R. Burcelin, and C. Knauf, "GLUT2 and the incretin receptors are involved in glucose-induced incretin secretion," *Mol Cell Endocrinol*, vol. 276, no. 1, pp. 18–23, 2007.

[65] L. Hansen, B. Hartmann, H. Mineo, and J. J. Holst, "Glucagon-like peptide-1 secretion is influenced by perfusate glucose concentration and by a feedback mechanism involving somatostatin in isolated perfused porcine ileum," *Regul Pept*, vol. 118, no. 1, pp. 11–18, 2004.

[66] A. El-Ouaghlidi, E. Rehring, J. J. Holst, A. Schweizer, J. Foley, D. Holmes, and M. A. Nauck, "The dipeptidyl peptidase 4 inhibitor vildagliptin does not accentuate glibenclamide-induced hypoglycemia but reduces glucose-induced glucagon-like peptide 1 and gastric inhibitory polypeptide secretion," *J Clin Endocrinol Metab*, vol. 92, no. 11, pp. 4165–4171, 2007.

[67] F. Reimann, L. Williams, G. da Silva Xavier, G. Rutter, and F. Gribble, "Glutamine potently stimulates glucagon-like peptide-1 secretion from GLUTag cells," *Diabetologia*, vol. 47, no. 9, pp. 1592–1601, 2004.

[68] H. Meissner and H. Schmelz, "Membrane potential of beta-cells in pancreatic islets," *Pflügers Archiv*, vol. 351, no. 3, pp. 195–206, 1974.

[69] P. Dean and E. Matthews, "Electrical activity in pancreatic islet cells," *Nature*, 1968.

[70] P. Rorsman, "The pancreatic beta-cell as a fuel sensor: an electrophysiologist's viewpoint," *Diabetologia*, vol. 40, no. 5, pp. 487–495, 1997.

[71] T. R. Chay and J. Keizer, "Minimal model for membrane oscillations in the pancreatic beta-cell," *Biophys J*, vol. 42, no. 2, pp. 181–189, 1983.

[72] R. Bertram and A. Sherman, "Negative calcium feedback: the road from Chay-Keizer," *The genesis of rhythm in the nervous system*, pp. 19–48, 2005.

[73] R. Bertram, L. Satin, and A. Sherman, "Interaction of glycolytic and mitochondrial dynamics drives diverse patterns of calcium oscillations in pancreatic beta-cells," *Biophys J*, vol. 92, pp. 1544–1555, 2007.

[74] L. E. Fridlyand, N. Tamarina, and L. H. Philipson, "Bursting and calcium oscillations in pancreatic β-cells: specific pacemakers for specific mechanisms," *Am J Physiol Endocrinol Metab*, vol. 299, no. 4, pp. E517–E532, 2010.

[75] M. E. Meyer-Hermann, "The electrophysiology of the β-cell based on single transmembrane protein characteristics," *Biophys J*, vol. 93, no. 8, pp. 2952–2968, 2007.

[76] M. G. Pedersen, "Contributions of mathematical modeling of beta cells to the understanding of beta-cell oscillations and insulin secretion," *J Diabetes Sci Technol*, vol. 3, no. 1, pp. 12–20, 2009.

[77] L. C. Falke, K. D. Gillis, D. M. Pressel, and S. Misler, "Perforated patch recording allows long-term monitoring of metabolite-induced electrical activity and voltage-dependent Ca^{2+} currents in pancreatic islet beta cells," *FEBS letters*, vol. 251, no. 1, pp. 167–172, 1989.

[78] S. Misler, D. W. Barnett, K. D. Gillis, and D. M. Pressel, "Electrophysiology of stimulus-secretion coupling in human β-cells," *Diabetes*, vol. 41, no. 10, pp. 1221–1228, 1992.

[79] D. M. Pressel and S. Misler, "Sodium channels contribute to action potential generation in canine and human pancreatic islet beta cells," *J Membr Biol*, vol. 116, no. 3, pp. 273–280, 1990.

[80] D. W. Barnett, D. M. Pressel, and S. Misler, "Voltage-dependent Na^+ and Ca^{2+} currents in human pancreatic islet β-cells: evidence for roles in the generation of action potentials and insulin secretion," *Pflügers Archiv*, vol. 431, no. 2, pp. 272–282, 1995.

[81] M. Braun, R. Ramracheya, M. Bengtsson, Q. Zhang, J. Karanauskaite, C. Partridge, P. R. Johnson, and P. Rorsman, "Voltage-gated ion channels in human pancreatic β-cells: electrophysiological characterization and role in insulin secretion," *Diabetes*, vol. 57, no. 6, pp. 1618–1628, 2008.

[82] O. Cabrera, D. M. Berman, N. S. Kenyon, C. Ricordi, P.-O. Berggren, and A. Caicedo, "The unique cytoarchitecture of human pancreatic islets has implications for islet cell function," *Proc Natl Acad Sci U S Aa*, vol. 103, no. 7, pp. 2334–2339, 2006.

[83] I. Quesada, M. G. Todorova, P. Alonso-Magdalena, M. Beltrá, E. M. Carneiro, F. Martin, A. Nadal, and B. Soria, "Glucose induces opposite intracellular Ca^{2+} concentration oscillatory patterns in identified α-and β-cells within intact human islets of langerhans," *Diabetes*, vol. 55, no. 9, pp. 2463–2469, 2006.

[84] M. G. Pedersen, "A biophysical model of electrical activity in human β-cells," *Biophys J*, vol. 99, no. 10, pp. 3200–3207, 2010.

[85] L. E. Fridlyand, D. Jacobson, A. Kuznetsov, and L. H. Philipson, "A model of action potentials and fast Ca^{2+} dynamics in pancreatic β-cells," *Biophys J*, vol. 96, no. 8, pp. 3126–3139, 2009.

[86] B. Rosati, P. Marchetti, O. Crociani, M. Lecchi, R. Lupi, A. Arcangeli, M. Olivotto, and E. Wanke, "Glucose- and arginine-induced insulin secretion by human pancreatic beta-cells: the role of HERG K^+ channels in firing and release," *FASEB J*, vol. 14, pp. 2601–2610, Dec 2000.

[87] R. Kelly, R. Sutton, and F. Ashcroft, "Voltage-activated calcium and potassium currents in human pancreatic beta-cells.," *J Physiol*, vol. 443, no. 1, pp. 175–192, 1991.

[88] T. Plant, "Properties and calcium-dependent inactivation of calcium currents in cultured mouse pancreatic β-cells.," *J Physiol*, vol. 404, no. 1, pp. 731–747, 1988.

[89] J. Herrington, M. Sanchez, D. Wunderler, L. Yan, R. M. Bugianesi, I. E. Dick, S. A. Clark, R. M. Brochu, B. T. Priest, M. G. Kohler, *et al.*, "Biophysical and pharmacological properties of the voltage-gated potassium current of human pancreatic β-cells," *J Physiol*, vol. 567, no. 1, pp. 159–175, 2005.

[90] B. Fakler and J. P. Adelman, "Control of K_{Ca} channels by calcium nano/microdomains," *Neuron*, vol. 59, no. 6, pp. 873–881, 2008.

[91] A. B. Hardy, J. E. M. Fox, P. R. Giglou, N. Wijesekara, A. Bhattacharjee, S. Sultan, A. V. Gyulkhandanyan, H. Y. Gaisano, P. E. MacDonald, and M. B. Wheeler, "Characterization of ERG K^+ channels in α-and β-cells of mouse and human islets," *J Biol Chem*, vol. 284, no. 44, pp. 30441–30452, 2009.

[92] R. Schönherr, B. Rosati, S. Hehl, V. G. Rao, A. Arcangeli, M. Olivotto, S. H. Heinemann, and E. Wanke, "Functional role of the slow activation property of ERG K^+ channels," *Eur J Neurosci*, vol. 11, no. 3, pp. 753–760, 1999.

[93] M. C. Sanguinetti, C. Jiang, M. E. Curran, and M. T. Keating, "A mechanistic link between an inherited and an acquird cardiac arrthytmia: HERG encodes the I_{Kr} potassium channel," *Cell*, vol. 81, no. 2, pp. 299–307, 1995.

[94] D. A. Jacobson, F. Mendez, M. Thompson, J. Torres, O. Cochet, and L. H. Philipson, "Calcium-activated and voltage-gated potassium channels of the pancreatic islet impart distinct and complementary roles during secretagogue induced electrical responses," *J Physiol*, vol. 588, no. 18, pp. 3525–3537, 2010.

[95] P. O. Westermark and A. Lansner, "A model of phosphofructokinase and glycolytic oscillations in the pancreatic β-cell," *Biophys J*, vol. 85, no. 1, pp. 126–139, 2003.

[96] J. Maylie, C. T. Bond, P. S. Herson, W.-S. Lee, and J. P. Adelman, "Small conductance Ca^{2+}-activated K^+ channels and calmodulin," *J Physiol*, vol. 554, no. 2, pp. 255–261, 2004.

[97] M. G. Pedersen, G. Cortese, and L. Eliasson, "Mathematical modeling and statistical analysis of calcium-regulated insulin granule exocytosis in β-cells from mice and humans," *Prog Biophys Mol Biol*, vol. 107, no. 2, pp. 257–264, 2011.

[98] L. Chen, D.-S. Koh, and B. Hille, "Dynamics of calcium clearance in mouse pancreatic β-cells," *Diabetes*, vol. 52, no. 7, pp. 1723–1731, 2003.

[99] J. Klingauf and E. Neher, "Modeling buffered Ca2+ diffusion near the membrane: implications for secretion in neuroendocrine cells," *Biophys J*, vol. 72, no. 2 Pt 1, p. 674, 1997.

[100] E. De Schutter and P. Smolen, "Calcium dynamics in large neuronal models," in *Koch C, Segev I, editors, Methods in neuronal modeling: from ions to networks*, ch. 6, pp. 211–250, MIT Press, 1998.

[101] N. L. Allbritton, T. Meyer, and L. Stryer, "Range of messenger action of calcium ion and inositol 1, 4, 5-trisphosphate," *Science*, vol. 258, no. 5089, pp. 1812–1815, 1992.

[102] M. Braun, R. Ramracheya, M. Bengtsson, A. Clark, J. N. Walker, P. R. Johnson, and P. Rorsman, "γ-aminobutyric acid (GABA) is an autocrine excitatory transmitter in human pancreatic β-cells," *Diabetes*, vol. 59, no. 7, pp. 1694–1701, 2010.

[103] J. A. Benson, K. Low, R. Keist, H. Mohler, and U. Rudolph, "Pharmacology of recombinant gamma-aminobutyric acidA receptors rendered diazepam-insensitive by point-mutated alpha-subunits," *FEBS Lett*, vol. 431, pp. 400–404, Jul 1998.

[104] Y. der Chen, S. Wang, and A. Sherman, "Identifying the targets of the amplifying pathway for insulin secretion in pancreatic *beta*-cells by kinetic modeling of granule exocytosis," *Biophys J*, vol. 95, no. 5, pp. 2226–2241, 2008.

[105] J. H. Goldwyn and E. Shea-Brown, "The what and where of adding channel noise to the hodgkin-huxley equations," *PLoS Comput Biol*, vol. 7, no. 11, p. e1002247, 2011.

[106] G. De Vries and A. Sherman, "Channel sharing in pancreatic beta-cells revisited: enhancement of emergent bursting by noise," *J Theor Biol*, vol. 207, pp. 513–530, Dec 2000.

[107] M. G. Pedersen, "A comment on noise enhanced bursting in pancreatic β-cells," *J Theor Biol*, vol. 235, no. 1, pp. 1–3, 2005.

[108] M. G. Pedersen, "Phantom bursting is highly sensitive to noise and unlikely to account for slow bursting in β-cells: considerations in favor of metabolically driven oscillations," *J Theor Biol*, vol. 248, no. 2, pp. 391–400, 2007.

[109] M. Düfer, B. Gier, D. Wolpers, P. Krippeit-Drews, P. Ruth, and G. Drews, "Enhanced glucose tolerance by SK4 channel inhibition in pancreatic β-cells," *Diabetes*, vol. 58, no. 8, pp. 1835–1843, 2009.

[110] S. Misler, A. Dickey, and D. W. Barnett, "Maintenance of stimulus-secretion coupling and single beta-cell function in cryopreserved-thawed human islets of langerhans," *Pflügers Archiv*, vol. 450, no. 6, pp. 395–404, 2005.

[111] J. Rinzel, "Bursting oscillations in an excitable membrane model," in *Ordinary and partial differential equations*, pp. 304–316, Springer, 1985.

[112] A. Sherman, Y. Li, and J. Keizer, "Whole-cell models," in *Fall CP, Marland ES, Wagner JM, Tyson JJ, Computational Cell Biology*, ch. 5, pp. 181–190, Spinger, 2002.

[113] M. Braun, R. Ramracheya, P. R. Johnson, and P. Rorsman, "Exocytotic properties of human pancreatic β-cells," *Ann N Y Acad Sci*, vol. 1152, no. 1, pp. 187–193, 2009.

[114] R. Rodriguez-Diaz, R. Dando, M. C. Jacques-Silva, A. Fachado, J. Molina, M. H. Abdulreda, C. Ricordi, S. D. Roper, P.-O. Berggren, and A. Caicedo, "Alpha cells secrete acetylcholine as a non-neuronal paracrine signal priming beta cell function in humans," *Nat Med*, vol. 17, no. 7, pp. 888–892, 2011.

[115] J. F. Rolland, J. C. Henquin, and P. Gilon, "G protein-independent activation of an inward Na^+ current by muscarinic receptors in mouse pancreatic beta-cells," *J Biol Chem*, vol. 277, pp. 38373–38380, Oct 2002.

[116] L. A. Swayne, A. Mezghrani, A. Varrault, J. Chemin, G. Bertrand, S. Dalle, E. Bourinet, P. Lory, R. J. Miller, J. Nargeot, *et al.*, "The NALCN ion channel is activated by M3 muscarinic receptors in a pancreatic β-cell line," *EMBO reports*, vol. 10, no. 8, pp. 873–880, 2009.

[117] M. Braun, R. Ramracheya, and P. Rorsman, "Autocrine regulation of insulin secretion," *Diabetes Obes Metabol*, vol. 14, no. s3, pp. 143–151, 2012.

[118] F. Martin and B. Soria, "Glucose induced Ca_i^{2+} oscillations in single human pancreatic islets," *Cell Calcium*, vol. 20, no. 5, pp. 409–414, 1996.

[119] P. Marchetti, D. W. Scharp, M. Mclear, R. Gingerich, E. Finke, B. Olack, C. Swanson, R. Giannarelli, R. Navalesi, and P. E. Lacy, "Pulsatile insulin secretion from isolated human pancreatic islets," *Diabetes*, vol. 43, no. 6, pp. 827–830, 1994.

[120] R. A. Ritzel, J. D. Veldhuis, and P. C. Butler, "Glucose stimulates pulsatile insulin secretion from human pancreatic islets by increasing secretory burst mass: dose-response relationships," *J Clin Endocrinol Metab*, vol. 88, no. 2, pp. 742–747, 2003.

[121] R. Bertram, A. Sherman, and L. S. Satin, "Metabolic and electrical oscillations: partners in controlling pulsatile insulin secretion," *Am J Physiol Endocrinol Metab*, vol. 293, no. 4, pp. E890–E900, 2007.

[122] M. J. Merrins, B. Fendler, M. Zhang, A. Sherman, R. Bertram, and L. S. Satin, "Metabolic oscillations in pancreatic islets depend on the intracellular Ca^{2+} level but not Ca^{2+} oscillations," *Biophys J*, vol. 99, no. 1, pp. 76–84, 2010.

[123] E. K. Ainscow and G. A. Rutter, "Glucose-stimulated oscillations in free cytosolic ATP concentration imaged in single islet β-cells evidence for a Ca^{2+}-dependent mechanism," *Diabetes*, vol. 51, no. suppl 1, pp. S162–S170, 2002.

[124] J. Li, H. Shuai, E. Gylfe, and A. Tengholm, "Oscillations of sub-membrane ATP in glucose-stimulated beta cells depend on negative feedback from Ca^{2+}," *Diabetologia*, vol. 56, no. 7, pp. 1577–1586, 2013.

[125] C. A. Leech and J. F. Habener, "A role for Ca^{2+}-sensitive nonselective cation channels in regulating the membrane potential of pancreatic beta-cells.," *Diabetes*, vol. 47, no. 7, pp. 1066–1073, 1998.

[126] P. Gilon and P. Rorsman, "NALCN: a regulated leak channel," *EMBO reports*, vol. 10, no. 9, pp. 963–964, 2009.

[127] M. G. Pedersen, C. D. Man, and C. Cobelli, "Multiscale modeling of insulin secretion," *IEEE Trans Biomed Eng*, vol. 58, no. 10, pp. 3020–3023, 2011.

[128] P. L. Hedley, P. Jòrgensen, S. Schlamowitz, R. Wangari, J. Moolman-Smook, P. A. Brink, J. K. Kanters, V. A. Corfield, and M. Christiansen, "The genetic basis of long QT and short QT syndromes: a mutation update," *Hum Mutat*, vol. 30, no. 11, pp. 1486–1511, 2009.

[129] T. De Boer, M. Houtman, M. Compier, and M. Van der Heyden, "The mammalian KIR2. x inward rectifier ion channel family: expression pattern and pathophysiology," *Acta Physiol*, vol. 199, no. 3, pp. 243–256, 2010.

[130] B. Kutlu, D. Burdick, D. Baxter, J. Rasschaert, D. Flamez, D. L. Eizirik, N. Welsh, N. Goodman, and L. Hood, "Detailed transcriptome atlas of the pancreatic beta cell," *BMC Med Genomics*, vol. 2, no. 1, p. 3, 2009.

[131] S. S. Torekov, E. Iepsen, M. Christiansen, A. Linneberg, O. Pedersen, J. J. Holst, J. K. Kanters, and T. Hansen, "KCNQ1 long QT syndrome patients have hyperinsulinemia and symptomatic hypoglycemia," *Diabetes*, p. DB_131454, 2014.

[132] M. Riz, M. Braun, and M. G. Pedersen, "Mathematical modeling of heterogeneous electrophysiological responses in human β-cells," *PLoS Comput Biol*, vol. 10, p. e1003389, Jan 2014.

[133] B. K. Panama and A. N. Lopatin, "Differential polyamine sensitivity in inwardly rectifying Kir2 potassium channels," *J Physiol*, vol. 571, no. 2, pp. 287–302, 2006.

[134] B. Ermentrout, *Simulating, analyzing, and animating dynamical systems: a guide to XPPAUT for researchers and students*, vol. 14. Siam, 2002.

[135] J. Anumonwo and A. N. Lopatin, "Cardiac strong inward rectifier potassium channels," *J Mol Cell Cardiol*, vol. 48, no. 1, pp. 45–54, 2010.

[136] T.-A. Liu, H.-K. Chang, and R.-C. Shieh, "Extracellular K^+ elevates outward currents through Kir2.1 channels by increasing single-channel conductance," *Biochim Biophys Acta-Biomembr*, vol. 1808, no. 6, pp. 1772–1778, 2011.

[137] A. S. Dhamoon, S. V. Pandit, F. Sarmast, K. R. Parisian, P. Guha, Y. Li, S. Bagwe, S. M. Taffet, and J. M. Anumonwo, "Unique Kir2. x properties determine regional and species differences in the cardiac inward rectifier K^+ current," *Circ Res*, vol. 94, no. 10, pp. 1332–1339, 2004.

[138] N. S. Poulter, W. T. Pitkeathly, P. J. Smith, and J. Z. Rappoport, "The physical basis of total internal reflection fluorescence (TIRF) microscopy and its cellular applications," in *Advanced Fluorescence Microscopy*, pp. 1–23, Springer, 2015.

[139] D. Axelrod, *Biophysical Tools for Biologists: Vol. 2. In Vivo Techniques*, vol. 89 of *Methods in Cell Biology.*, ch. 7: Total Internal Reflection Fluorescence Microscopy, pp. 169–221. Elsevier, 2008.

[140] A. L. Mattheyses, S. M. Simon, and J. Z. Rappoport, "Imaging with total internal reflection fluorescence microscopy for the cell biologist," *J Cell Sci*, vol. 123, no. 21, pp. 3621–3628, 2010.

[141] N. R. Gandasi and S. Barg, "Contact-induced clustering of syntaxin and munc18 docks secretory granules at the exocytosis site," *Nat Commun*, vol. 5, 2014.

[142] J. W. Taraska, D. Perrais, M. Ohara-Imaizumi, S. Nagamatsu, and W. Almers, "Secretory granules are recaptured largely intact after stimulated exocytosis in cultured endocrine cells," *Proc Natl Acad Sci U S A*, vol. 100, no. 4, pp. 2070–2075, 2003.

[143] S. Barg, M. Knowles, X. Chen, M. Midorikawa, and W. Almers, "Syntaxin clusters assemble reversibly at sites of secretory granules in live cells," *Proc Natl Acad Sci U S As*, vol. 107, no. 48, pp. 20804–20809, 2010.

[144] S. Barg, C. S. Olofsson, J. Schriever-Abeln, A. Wendt, S. Gebre-Medhin, E. Renström, and P. Rorsman, "Delay between fusion pore opening and peptide release from large dense-core vesicles in neuroendocrine cells," *Neuron*, vol. 33, no. 2, pp. 287–299, 2002.

[145] J. A. Gilabert, "Cytoplasmic calcium buffering," in *Calcium Signaling*, pp. 483–498, Springer, 2012.

[146] Z. Zhou and E. Neher, "Mobile and immobile calcium buffers in bovine adrenal chromaffin cells," *J Physiol*, vol. 469, no. 1, pp. 245–273, 1993.

[147] I. Llano, R. DiPolo, and A. Marty, "Calcium-induced calcium release in cerebellar Purkinje cells," *Neuron*, vol. 12, no. 3, pp. 663–673, 1994.

[148] R. Tsien, T. Pozzan, and T. Rink, "Calcium homeostasis in intact lymphocytes: cytoplasmic free calcium monitored with a new, intracellularly trapped fluorescent indicator," *J Cell Biol*, vol. 94, no. 2, pp. 325–334, 1982.

[149] G. Grynkiewicz, M. Poenie, and R. Y. Tsien, "A new generation of Ca^{2+} indicators with greatly improved fluorescence properties.," *J Biol Chem*, vol. 260, no. 6, pp. 3440–3450, 1985.

[150] O. Shimomura, F. H. Johnson, and Y. Saiga, "Extraction, purification and properties of aequorin, a bioluminescent protein from the luminous hydromedusan, Aequorea," *J Cell Comp Physiol*, vol. 59, no. 3, pp. 223–239, 1962.

[151] G. S. Baird, D. A. Zacharias, and R. Y. Tsien, "Circular permutation and receptor insertion within green fluorescent proteins," *Proc Natl Acad Sci U S As*, vol. 96, no. 20, pp. 11241–11246, 1999.

[152] T. Nagai, A. Sawano, E. S. Park, and A. Miyawaki, "Circularly permuted green fluorescent proteins engineered to sense Ca^{2+}," *Proc Natl Acad Sci U S A*, vol. 98, no. 6, pp. 3197–3202, 2001.

[153] J. Nakai, M. Ohkura, and K. Imoto, "A high signal-to-noise Ca^{2+} probe composed of a single green fluorescent protein," *Nat biotechnol*, vol. 19, no. 2, pp. 137–141, 2001.

[154] J. E. McCombs and A. E. Palmer, "Measuring calcium dynamics in living cells with genetically encodable calcium indicators," *Methods*, vol. 46, no. 3, pp. 152–159, 2008.

[155] Y. Zhao, S. Araki, J. Wu, T. Teramoto, Y.-F. Chang, M. Nakano, A. S. Abdelfattah, M. Fujiwara, T. Ishihara, T. Nagai, *et al.*, "An expanded palette of genetically encoded Ca^{2+} indicators," *Science*, vol. 333, no. 6051, pp. 1888–1891, 2011.

[156] J. Akerboom, T.-W. Chen, T. J. Wardill, L. Tian, J. S. Marvin, S. Mutlu, N. C. Calderón, F. Esposti, B. G. Borghuis, X. R. Sun, *et al.*, "Optimization of a GCaMP calcium indicator for neural activity imaging," *J Neurosci*, vol. 32, no. 40, pp. 13819–13840, 2012.

[157] A. E. Palmer, Y. Qin, J. G. Park, and J. E. McCombs, "Design and application of genetically encoded biosensors," *Trends Biotechnol*, vol. 29, no. 3, pp. 144–152, 2011.

[158] `http://www.calciumcalculator.org`.

[159] V. Matveev, A. Sherman, and R. S. Zucker, "New and corrected simulations of synaptic facilitation.," *Biophys J*, vol. 83, no. 3, p. 1368, 2002.

[160] M. Naraghi and E. Neher, "Linearized buffered Ca^{2+} diffusion in microdomains and its implications for calculation of $[Ca^{2+}]$ at the mouth of a calcium channel," *J Neurosci*, vol. 17, no. 18, pp. 6961–6973, 1997.

[161] K. Hatlapatka, M. Willenborg, and I. Rustenbeck, "Plasma membrane depolarization as a determinant of the first phase of insulin secretion," *Am J Physiol Endocrinol Metab*, vol. 297, no. 2, pp. E315–E322, 2009.

[162] T. Voets, "Dissection of three Ca^{2+}-dependent steps leading to secretion in chromaffin cells from mouse adrenal slices," *Neuron*, vol. 28, no. 2, pp. 537–545, 2000.

[163] M. G. Pedersen and A. Sherman, "Newcomer insulin secretory granules as a highly calcium-sensitive pool," *Proc Natl Acad Sci U S A*, vol. 106, no. 18, pp. 7432–7436, 2009.

[164] M. A. Nystoriak, M. Nieves-Cintrón, and M. F. Navedo, "Capturing single L-type Ca^{2+} channel function with optics," *Biochim Biophys Acta-Molecular Cell Research*, vol. 1833, no. 7, pp. 1657–1664, 2013.

[165] D. L. Curry, L. L. Bennett, and G. M. Grodsky, "Dynamics of insulin secretion by the perfused rat pancreas," *Endocrinology*, vol. 83, no. 3, pp. 572–584, 1968.

[166] K. Dezaki, H. Sone, M. Koizumi, M. Nakata, M. Kakei, H. Nagai, H. Hosoda, K. Kangawa, and T. Yada, "Blockade of pancreatic islet–derived ghrelin enhances insulin secretion to prevent high-fat diet–induced glucose intolerance," *Diabetes*, vol. 55, no. 12, pp. 3486–3493, 2006.

[167] R. Silvestre, E. Egido, R. Hernández, and J. Marco, "Kisspeptin-13 inhibits insulin secretion without affecting glucagon or somatostatin release: study in the perfused rat pancreas," *J Endocrinol*, vol. 196, no. 2, pp. 283–290, 2008.

[168] T. Edholm, K. Cejvan, S. Abdel-halim, S. Efendic, P. Schmidt, and P. M. Hellström, "The incretin hormones GIP and GLP-1 in diabetic rats: effects on insulin secretion and small bowel motility," *Neurogastroenterol Motil*, vol. 21, no. 3, pp. 313–321, 2009.

[169] R. L. Dobbins, L. S. Szczepaniak, J. Myhill, Y. Tamura, H. Uchino, A. Giacca, and J. D. McGarry, "The composition of dietary fat directly influences glucose-stimulated insulin secretion in rats," *Diabetes*, vol. 51, no. 6, pp. 1825–1833, 2002.

[170] W. Shang, K. Yasuda, A. Takahashi, A. Hamasaki, M. Takehiro, K. Nabe, H. Zhou, R. Naito, H. Fujiwara, D. Shimono, *et al.*, "Effect of high dietary fat on insulin secretion in genetically diabetic Goto-Kakizaki rats," *Pancreas*, vol. 25, no. 4, pp. 393–399, 2002.

[171] S. Park, S. M. Hong, J. E. Lee, and S. R. Sung, "Exercise improves glucose homeostasis that has been impaired by a high-fat diet by potentiating pancreatic β-cell function and mass through IRS2 in diabetic rats," *J Appl Physiol*, vol. 103, no. 5, pp. 1764–1771, 2007.

[172] C. Cobelli, G. M. Toffolo, C. Dalla Man, M. Campioni, P. Denti, A. Caumo, P. Butler, and R. Rizza, "Assessment of β-cell function in humans, simultaneously with insulin sensitivity and hepatic extraction, from intravenous and oral glucose tests," *Am J Physiol Endocrinol Metab*, vol. 293, no. 1, pp. E1–E15, 2007.

[173] G. Toffolo, E. Breda, M. K. Cavaghan, D. A. Ehrmann, K. S. Polonsky, and C. Cobelli, "Quantitative indexes of β-cell function during graded up&down glucose infusion from C-peptide minimal models," *Am J Physiol Endocrinol Metab*, vol. 280, no. 1, pp. E2–E10, 2001.

[174] T. Hara, A. Hirasawa, A. Ichimura, I. Kimura, and G. Tsujimoto, "Free fatty acid receptors FFAR1 and GPR120 as novel therapeutic targets for metabolic disorders," *J Pharm Sci*, vol. 100, no. 9, pp. 3594–3601, 2011.

[175] C. F. Burant, P. Viswanathan, J. Marcinak, C. Cao, M. Vakilynejad, B. Xie, and E. Leifke, "TAK-875 versus placebo or glimepiride in type 2 diabetes mellitus: a phase 2, randomised, double-blind, placebo-controlled trial," *Lancet*, vol. 379, no. 9824, pp. 1403–1411, 2012.

[176] G. Haschke, V. Dietrich, E. Defossa, S. Stengelin, A. Dudda, and A. W. Herling, "Amplification of glucose stimulated insulin secretion by activating the free fatty acid receptor GPR40 in beta-cells and isolated pancreas.," *Diabetes*, vol. 60, no. Suppl 1, p. A534, 2011.

[177] K. E. Sussman, G. D. Vaughan, and R. F. Timmer, "An in vitro method for studying insulin secretion in the perfused isolated rat pancreas," *Metabolism*, vol. 15, no. 5, pp. 466–476, 1966.

[178] G. Toffolo, F. De Grandi, and C. Cobelli, "Estimation of β-cell sensitivity from intravenous glucose tolerance test C-peptide data: knowledge of the kinetics avoids errors in modeling the secretion," *Diabetes*, vol. 44, no. 7, pp. 845–854, 1995.

[179] M. G. Pedersen and C. Cobelli, "Multiscale modelling of insulin secretion during an intravenous glucose tolerance test," *Interface focus*, vol. 3, no. 2, p. 20120085, 2013.

[180] S. G. Straub and G. W. Sharp, "Glucose-stimulated signaling pathways in biphasic insulin secretion," *Diabetes Metab Res Rev*, vol. 18, no. 6, pp. 451–463, 2002.

[181] E. Breda, M. K. Cavaghan, G. Toffolo, K. S. Polonsky, and C. Cobelli, "Oral glucose tolerance test minimal model indexes of β-cell function and insulin sensitivity," *Diabetes*, vol. 50, no. 1, pp. 150–158, 2001.

[182] H. Yashiro, Y. Tsujihata, K. Takeuchi, M. Hazama, P. R. Johnson, and P. Rorsman, "The effects of TAK-875, a selective G protein-coupled receptor 40/free fatty acid 1 agonist, on insulin and glucagon secretion in isolated rat and human islets," *J Pharmacol Exp Ther*, vol. 340, no. 2, pp. 483–489, 2012.

[183] M. Ferdaoussi, V. Bergeron, B. Zarrouki, J. Kolic, J. Cantley, J. Fielitz, E. Olson, M. Prentki, T. Biden, P. MacDonald, *et al.*, "G protein-coupled receptor (GPR) 40-dependent potentiation of insulin secretion in mouse islets is mediated by protein kinase D1," *Diabetologia*, vol. 55, no. 10, pp. 2682–2692, 2012.

[184] Y. Anini, X. Fu-Cheng, J. C. Cuber, A. Kervran, J. Chariot, and C. Rozé, "Comparison of the postprandial release of peptide YY and proglucagon-derived peptides in the rat," *Pflügers Archiv*, vol. 438, no. 3, pp. 299–306, 1999.

[185] M. Campioni, G. Toffolo, L. T. Shuster, R. A. Rizza, C. Cobelli, *et al.*, "Incretin effect potentiates β-cell responsivity to glucose as well as to its rate of change: OGTT and matched intravenous study," *Am J Physiol Endocrinol Metab*, vol. 292, no. 1, pp. E54–E60, 2007.

[186] C. Dalla Man, R. A. Rizza, and C. Cobelli, "Meal simulation model of the glucose-insulin system," *IEEE Trans Biomed Eng*, vol. 54, no. 10, pp. 1740–1749, 2007.